Ice and ocean dynamics at a subglacial river mouth on the Siple Coast, Antarctica

Arran Whiteford

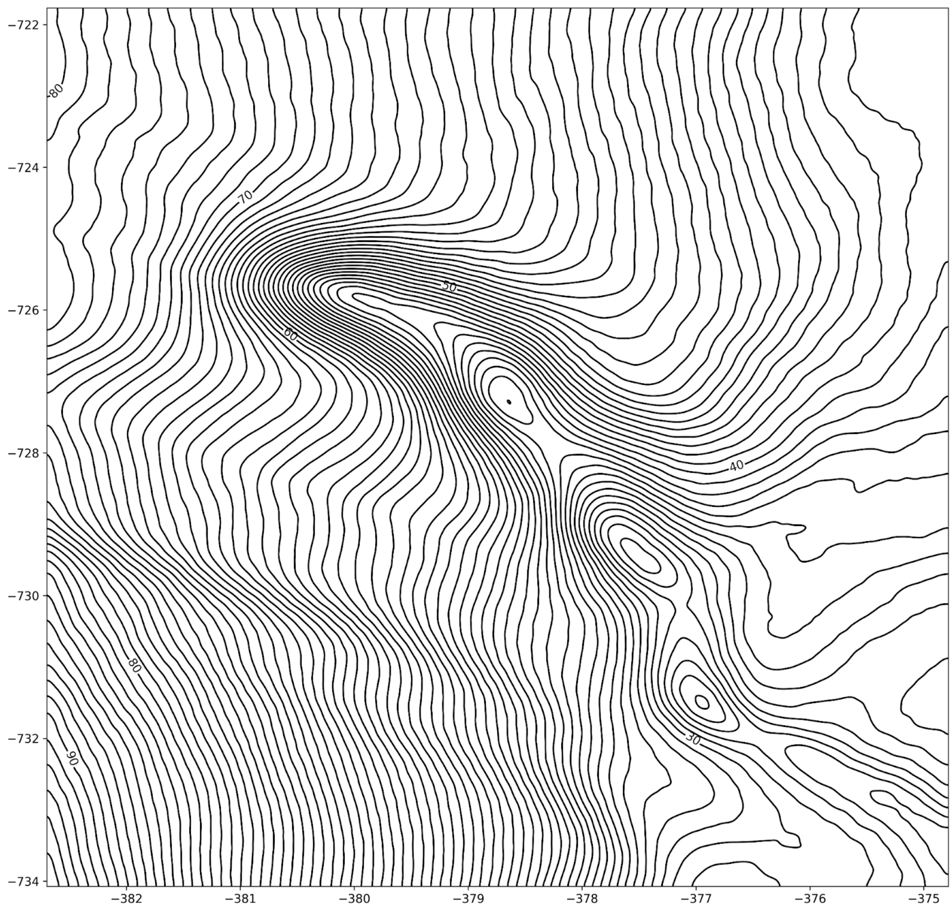

A thesis
submitted to the Victoria University of Wellington
in fulfillment of the requirements for the degree of
Doctor of Philosophy

Victoria University of Wellington
School of Geography, Environment and Earth Sciences
2022

ABSTRACT

Channels melted into the base of ice shelves are thought to influence ice shelf evolution by redistributing melt patterns and reducing their structural integrity. Theories of basal melt and fresh water plume processes which occur in channels are generally poorly constrained by observations. At the grounding line of the Kamb Ice Stream, Antarctica, a distinctive valley in the ice surface topography reveals the location of a subglacial channel. This thesis uses new observations of the ice shelf basal channel to describe processes which cause the formation and growth of the channel. Using a combination of detailed ground–based observations, remote sensing, and interpolation we map the surface and basal topography of the area. The basal channel is observed to have incised up to 50% of the ice thickness and extends 6 km inland from the previously estimated grounding line of the stagnant Kamb Ice Stream. Remote sensing products show that the channel has grown upstream over time, and likely continues to grow. Modern surface lowering at the steep upstream inception of the channel reveals a region of focused melt where a subglacial outlet meets the ocean cavity. We estimate this basal melt to be at least 20 m/yr in a narrow (200 m x 1.5 km) zone. Downstream from the melt region, repeat phase sensitive radar observations reveal a large region of basal marine ice and accretion. A year–long time series of phase sensitive radar observations shows that accretion is generally consistent in magnitude, though oscillates in strength at tidal periods. Using the channel shape mapped by radar surveys as a key constraint, we model ocean circulation and basal ice melt with the MIT Global Circulation Model. The model predicts that ocean circulation in the channel is driven by a melt water plume coupled with estuarine–like dynamics. Predicted melt is strongest at the inception of the channel where the plume ascends the positive gradient of the ice base. The plume causes a strong downstream flow of fresher water in the upper half of the water column, which overlies an upstream flow of salty bottom water from the Ross Ice Shelf ocean cavity. The inflow of salt is entrained into the plume and provides energy to melt the ice base. Higher melt rates, up to 17 m/yr, were only modelled when strong intermittent subglacial drainage flushed the channel and was replaced by salty ocean water in quiescent times. We conclude that the channel is likely formed by an upstream migrating meltwater plume triggered by episodic subglacial drainage.

Contents

List of Tables

List of Figures

ACKNOWLEDGEMENTS

E mihi ana ki ngā tohu o nehe, o Te Whanganui-a-Tara e noho nei au. He mihi ki te iwi e tau nei, Taranaki Whānui me Ngāti Toa tēnā koutou.

This research was part of Antarctic Science Platform Project 1: NZARI Ross Ice Shelf Project and was funded by the Royal Society of New Zealand's Rutherford Discovery Fellowship (Contract: RDF-VUW1602). Additional funding support came from the New Zealand Ministry of Business and Innovation and Employment through the Antarctic Science Platform contract (ANTA1801) Antarctic Ice Dynamics Project (ASP-021-01). Our thanks to Antarctica New Zealand for the field support which was critical to the success of this research.

A humongous thanks to my primary supervisor, Huw Horgan for genuine mentorship, support, encouragement and teaching. Thanks for fostering an environment which left me independent to learn and explore, but well supported when I sought help. Thanks to my secondary supervisor Brian Anderson for constructive guidance and thesis edits. Thank you to all other collaborators who supported and enabled this work. Wei Ji Leong, for remote sensing and python advice, Martin Forbes, for massive efforts collecting data, Alena Malyarenko for being a patient, expert teacher of MITgcm, continuously positive and extremely helpful.

Between waves of lock downs, thanks to the whole crew at the Antarctic Research Centre for fostering such a positive work environment. Thanks to Rob, Dao, Michelle and Aleksander for streamlining running of the ARC, administration and computer systems. Thanks to Meseret and Bereket for keeping the ARC in order, and for conversations and support. Thanks to the other PhD Students for camaraderie and fun times, the originals—Lauren, Wei Ji, and Clarrie, and later—Matt, Fran, Alana.

Very thankful for ongoing, limitless support from Mum and Dad, Andrew, Emma, Lily and Lola. It's no stroke of luck that I ended doing a PhD in Antarctic geophysics, with inspiring and supportive parents who've explored the field. Acknowledging the lockdown workmates—Blake, Henry, Bron, Joane and earlier flatties/friends, Laura, Dhaxna, Meg and Isaac, all cordial cooks, and palatable people. Thanks to the Wellington hills and beautiful southern coast for perfect runs and swims which fostered a good life. Cheers to the adventure mates, the BSR lads, the WoRM crew, and the TTC descendants, running, rogaining, skiing and biking.

Joane, thanks for the nail-on-the-head advice and engagement on completely new topics, but also—hunkering in the storm-battered tent at Tenneson, overlapping on the Tararua Mountain Race, finding a whēke at Taputeranga, or cooking on the fire at Mākara.

P.S. Lastly, six months later, thanks Lael!

DEDICATION

To the howling southerly,

'Blow, Tāwhiri–mātea, and crack your cheeks! rage! blow!'
Kingi Lear

Chapter 1

Introduction

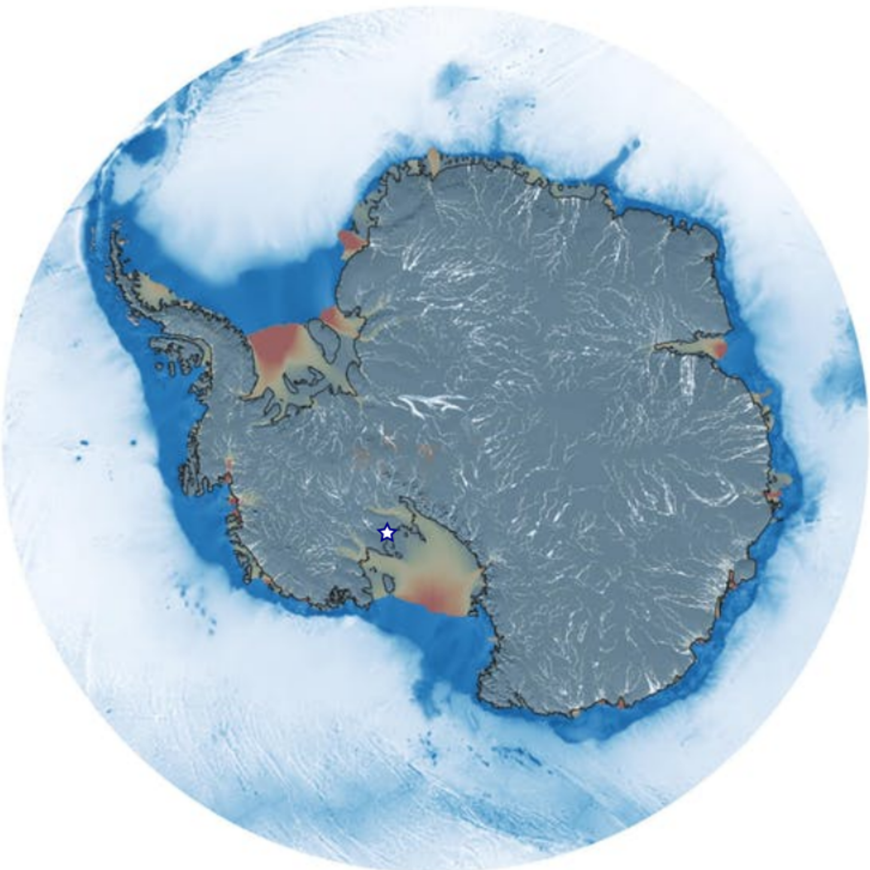

Figure 1.1: Map of Antarctica with subglacial drainage routes in white (Le Brocq et al., 2009), beneath Antarctica's ice sheets in grey. Star shows study location. Warm colours denote regions of fast ice flow (Rignot et al., 2013). Modified from Horgan and Stevens (2022)

1.1 Context

The discharge of ice from the Antarctic Ice Sheet is accelerating, and is projected to contribute to 13–42 cm of sea level rise by the end of the century (Edwards et al., 2021). When ice flows off Antarctica, from sitting grounded on the continent to floating on the ocean, the volume above floatation contributes to the global sea level. The boundary between grounded and floating ice (the grounding line) is therefore an important transition. An increase in the ice flowing over the grounding line, or an inland retreat of the grounding line raises the global sea level. Processes at the grounding line, upstream in the ice sheet, and downstream in ice shelves contribute to total ice discharge (Rignot et al., 2011).

Upstream of the grounding line, the amount of ice which flows from the centre of the ice sheet to the ocean depends on ice velocity. In Antarctica, most ice discharge passes through 'ice streams', which flow at velocities of 100s of metres per year (Rignot et al., 2011) due to low basal friction. Most Antarctic ice flows at much slower velocities of 1-10s of metres per year (Rignot et al., 2011; Morlighem et al., 2013). In slow areas ice is stuck to the bed and flows through viscous deformation. The flow of ice is strongly forced by its coupling with the underlying bedrock (e.g. Rose, 1979; Engelhardt et al., 1990). Changes in friction at this interface can drastically affect ice flux rates by allowing ice to slide (Budd et al., 1979). Water between ice and the bed is thought to be a fundamental factor governing changes in basal friction (Weertman, 1957; Iken and Bindschadler, 1986; Alley, 1989): more subglacial water with higher pressure decouples the ice from the bed, allowing it to slide more easily.

Downstream of the grounding line, ice shelves are an important control on the speed of ice loss from Antarctica. Ice shelves stabilise the inland ice sheet by providing resisting stresses which slow ice discharge at the outlets of glaciers and ice streams (Dupont and Alley, 2005). Over 80% of ice flow off the Antarctic continent drains through floating, but fixed ice shelves (Pritchard et al., 2012). When ice shelves drag past coastlines, islands, and pinning points, they generate back–stresses and buttress against ice flow (Dupont and Alley, 2005; Fürst et al., 2016). The reduction of buttressing when an ice shelf thins or shrinks leads to the acceleration of ice loss (Rignot et al., 2004; Berthier et al., 2012), and further sea level rise. Even highly localised, concentrated thinning over a relatively small area can lead to the upstream acceleration of grounded ice (Reese et al., 2018).

Grounding line dynamics affect the Antarctic contribution to sea-level rise. Processes at the grounding line may impact the stability of an ice sheet (Weertman, 1974). Feedbacks between the grounding line and bed slope are thought to contribute to the movement of the grounding line. Ice which is floated by grounding line retreat contributes to sea level rise (Dowdeswell et al., 2020; Dupont and Alley, 2005). Additionally, basal melt near the grounding line is relatively strong (Rignot et al., 2013; Goldberg et al., 2019).

Melt near the grounding line is highly dependent on local topography (Rignot et al., 2013; Goldberg et al., 2019), which can change rapidly as the grounding line moves.

This thesis is focused on a channel incised into the base of the ice, at the intersection of ice shelf, ice stream and grounding line processes. The channel is at 152.35°E, 82.47°S (Figure 1.1), at the grounding line of the Siple Coast, between the Kamb Ice Stream and the Ross Ice Shelf. The channel's location suggests it is coupled to both ice stream and ice shelf dynamics. Because the channel was likely formed by melt triggered by subglacial outflow (Kim et al., 2016; Alley et al., 2016), better describing the formation of the channel may help to constrain the subglacial drainage system of the Kamb Ice Stream. Additionally, the channel likely changes the local strength of the ice shelf through localised basal melting and a change in melt patterns (as described in model channels by Gladish et al. (2012) and Sergienko (2013)). The channel may funnel plumes of water, causing super–cooling and accretion (Holland and Feltham, 2006). Lastly, the channel is probably an example of localised grounding line retreat. Due to its large size, effective pressure (defined as overburden minus basal water pressure) is likely zero in the channel, as described by Drews (2015). This implies that the channel is filled with ocean water, and is part of the ice shelf cavity. The channel therefore likely forms a local embayment in the grounding line, shaped like a river mouth.

In this introduction chapter, we set the context for research on the subglacial channel by reviewing the literature on sub–ice–shelf channels. Firstly, in Section 1.2 we present an overview of ice shelf basal channels. Next, in Section 1.3 we discuss processes upstream of the grounding line, in ice streams. In Section 1.4 we outline processes at the grounding line. Section 1.5 covers dynamics of the ice shelf cavity, with Section 1.5.1 focused on oceanography in ice shelf cavities, Section 1.5.2 on the theory of basal melt under ice shelves and then Section 1.5.3 describing the Ross Ice Shelf specifically. Lastly, in Section 1.6.1 we outline the objectives of the research, followed by a description of the structure of this thesis (Section 1.6.2)

1.2 Channels

Channels incised into the base of ice shelves have been observed across Antarctica and Greenland (e.g. Alley et al., 2016; Washam et al., 2019). For an inventory and categorisation of ice shelf basal channels in Antarctica see Alley et al. (2016). Ice shelf channels are thought to influence basal melt of ice shelves through redistributing melt patterns (Millgate et al., 2013). Increased melt rates have been observed in channels through satellite and Autonomous Phase-sensitive Radio-Echo Sounder (ApRES) based sensing techniques. For instance, Marsh et al. (2016) and Stanton et al. (2013) used ApRES to detect elevated melt rates ($\approx$ 20 m/yr greater) at channels on the Whillans Ice Stream and Pine Island Glacier respectively, and Chartrand and Howat (2020) used

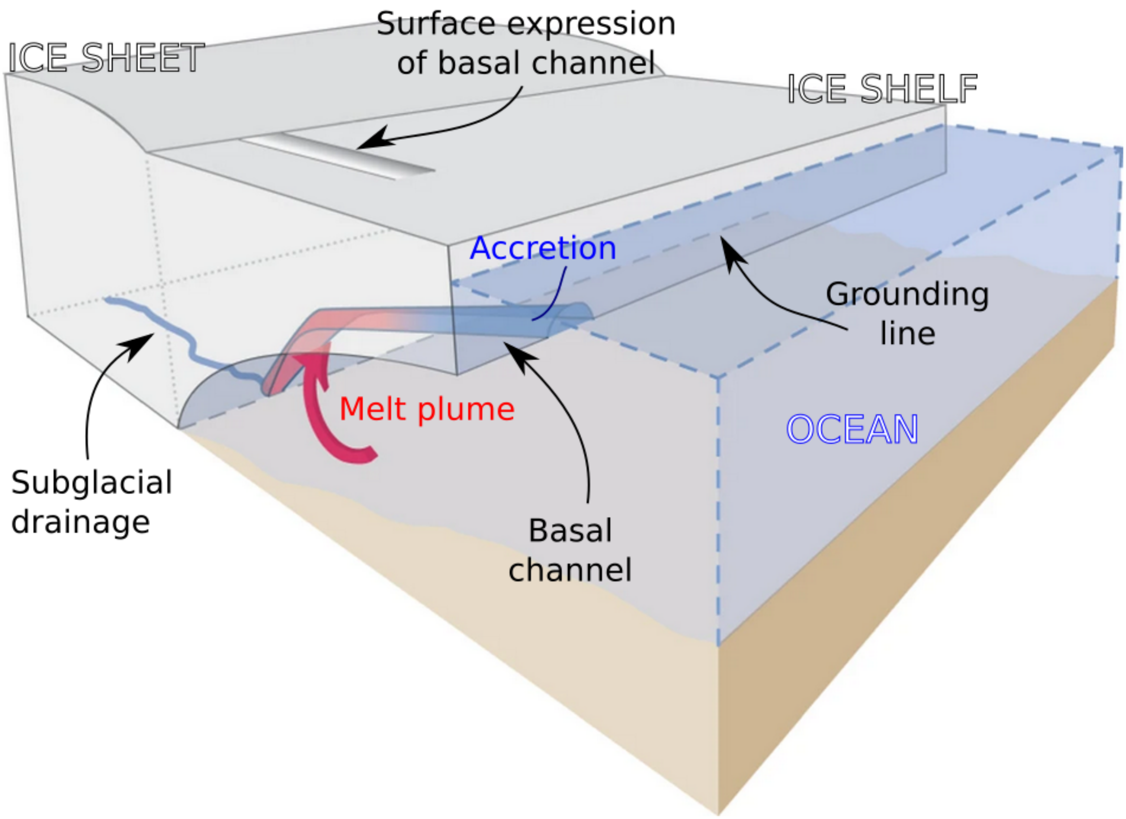

Figure 1.2: Schematic showing the growth of a subglacially sourced sub–ice–shelf channel. (Adapted from Le Brocq et al. (2013).)

satellite observations to find similar increased melt rates in a channel on the Getz Ice Shelf. Modelling results from Gladish et al. (2012) and Millgate et al. (2013) have shown that the increase in melt rates associated with basal channels may cause a decrease in melt rates across the broader ice shelf. However, channels are thought to generally have a destabilising effect on ice shelves, causing their structural weakening (Alley et al., 2019). Channels have been observed to be co-located with crevassing (Stanton et al., 2013; Alley et al., 2016), and it has been suggested that channels could speed up the collapse of ice shelves (Rignot and Steffen, 2008).

Satellite observations (Rignot et al., 2008) and modelling results (Sergienko, 2013) show that ice shelf channels are generally formed in regions of high basal melt, such as the regions close to or inside grounding zones (Alley et al., 2016). The majority of ice shelf channels categorised by Alley et al. (2016) are formed as streak lines which extend downstream of shear margins or obstructions in advecting ice. However, some categorised channels were co–located with subglacial drainage outlets (as modelled by Le Brocq et al. (2013)) and were likely formed by plume melt triggered by subglacial outflow (Alley et al., 2016).

Drilling directly into channels in the Petermann and Pine Island Glacier respectively, Rignot and Steffen (2008) and Stanton et al. (2013) found buoyant plumes of melt water.

Melt water plumes are thought to dominate channel circulation, as described by modelling research by Jenkins (2011), Sergienko (2013) and Gladish et al. (2012) (Figure 1.2). Sergienko (2013) and Gladish et al. (2012) suggested that the growth of channels is driven by feedbacks between the steepness of basal topography and the velocity of melt water plumes. As melt increases at the ice–ocean interface, water becomes fresher and more buoyant, causing a plume to accelerate up the ice gradient. The increase in velocity causes stronger melt as the plume entrains more salt from the deep ocean, and the melt causes a steepening and deepening of the channel such that the melt plume feedback is further stimulated (Sergienko, 2013).

1.3 Ice Streams

In Antarctica, regions of fast flowing 'ice streams' are characterised by low basal friction and velocities of 100s of metres per year. Slower areas where ice is stuck to the bed flow via viscous deformation at velocities of 1-10s of metres per year (Rignot et al., 2011; Morlighem et al., 2013). Although ice streams only make up a small fraction of the area of Antarctica, they contribute 90% of the total dynamical ice loss from the continent (Bamber et al., 2000; Rignot et al., 2011). Consequently, modelling their dynamics is crucial to predicting Antarctic's future ice mass budget. The high velocity of ice streams is associated with the presence of basal melt water, and deformable, saturated sediment slurries, which allow the ice to slide with little friction. This has been confirmed with seismic (Blankenship et al., 1986; Alley et al., 1987) and radio–echo surveys (Robin et al., 1970), borehole observations (Engelhardt and Kamb, 1997), and inferences from sediment cores (Hodson et al., 2016). It follows that some changes in the flow of the Antarctic Ice Sheet can be attributed to changes in subglacial water distribution and drainage systems (e.g. Alley et al., 1994).

Despite understanding the importance of subglacial water in predicting the future of the Antarctic Ice Sheet, no model confidently describes what these waterways look like. When modelling ice flow in the Siple Coast, Bougamont et al. (2015) cites subglacial drainage as a major source of uncertainty in projecting future sea level contributions. Difficult to access beneath hundreds of metres of ice, our knowledge of Antarctic drainage systems comes from observing paleo–ice sheet beds (Hättestrand, 1997; Lewis et al., 2006), remote sensing (Schroeder et al., 2013), inverse modelling (Morlighem et al., 2013) and sparse borehole drilling (Engelhardt and Kamb, 1997). Bed conditions such as intermittent pools of water or saturated sediments, lakes, channelisation of water, and areas with frozen beds with no drainage system have all been found to be widespread (Carter et al., 2009; Schroeder et al., 2013; Young et al., 2016).

Current models of subglacial drainage in Antarctica are based on theories of alpine glacier drainage, as alpine glaciers are generally easier to study due to their accessibility, size, and seasonal change. However, ice stream drainage systems are thought to be different from those in mountain glaciers, in that they are characterised by smaller hydraulic gradients, less water supply, thicker ice and softer bed substrate. To encapsulate varied and often unknown drainage conditions, all large scale models of subglacial drainage in Antarctica have assumed that areas of sliding have sheet or porous flow (Flowers, 2015). This is a broad assumption that aims to approximate bed conditions and is normally based on two findings: Firstly, Alley (1989) predicted that if there was no channelised flow, sheet flow would dominate drainage systems under ice sheets. Later, Alley (1996) showed that in the absence of information about basal conditions, modelling drainage as sheet flow is a reasonable approximation for a wide variety of bed conditions. The Alley (1996) pure sheet flow model can reasonably accurately describe relationships between basal shear stress and water pressure but is too simple to show changes in the subglacial drainage systems, which are believed to exist (e.g. Schroeder et al., 2013).

Canals (channels incised into the bed substrate) are thought to be the most representative model for 'discrete' drainage elements in Antarctica (e.g. Walder and Fowler, 1994; Simkins et al., 2017). Discrete drainage elements like canals or channels are confined to certain routes, and contrast with drainage elements like porous or sheet flow which are modelled across the entire ice base. Compared to other drainage models, the theory of subglacial canals is least developed. Active canals have not been observed, and the models which summarise the erosion dynamics which govern the width of canals have not been robustly compared against observations (e.g. Damsgaard et al., 2017). As opposed to R–channels, (channels incised into the ice base) canals are thought to exist at a low effective pressure (defined as overburden minus basal water pressure) (Walder and Fowler, 1994). Model canals support a relationship with subglacial water pressure increasing as discharge increases (Walder and Fowler, 1994; Ng, 1998), whereas R–channels support the opposite (Röthlisberger, 1972; Shreve, 1972). It is believed that a positive relationship between discharge and water pressure is a requirement for the feedbacks that drive ice streams, whereby low effective pressures (high water pressure) and fast sliding lead to more frictional melt (Fowler and Johnson, 1996). R–channels, because they tend to increase effective pressure as discharge is increased, favour slow ice flow. Additionally, it is not clear that the low hydraulic gradients and low melt rates under Antarctica are sufficient to support persistent R–channels; though R–channels have been argued to exist at the outlets of draining lakes (Evatt et al., 2006; Pattyn, 2008), as well as under the shear margins of ice streams, where there are high melt rates (Perol and Rice, 2011).

Most observations of subglacial water in Antarctica are related to documenting the existence of subglacial lakes (e.g. Carter et al., 2007; Wright and Siegert, 2012; Siegfried and Fricker, 2018). Airborne radar surveys first revealed subglacial lakes in the 70s (Robin et al., 1970). Since then over 400 subglacial lakes have been found (Siegert et al., 2016) with radar–echo sounding reflections (e.g. Carter et al., 2007) or through repeated altimetry that shows localised drops or uplifting in the ice surface that are the result of lakes draining or filling (Wingham et al., 2006; Stearns et al., 2008; Gray et al., 2005; Fricker et al., 2007). Other drainage features have been observed in paleo ice sheet beds, now underwater (e.g. Nitsche et al., 2013; Anderson and Fretwell, 2008). These identify large channels which are hypothesised to be formed from subglacial melt water due to the fact they are parallel to flow or are anastomosing. Using radar in an area of the Antarctic Ice Sheet, Schroeder et al. (2013) found what they believe is a transition from channelised drainage system to a distributed drainage system by observing changes in specularity of a radar reflection. However, the only imaging of active Antarctic subglacial drainage channels comes from Drews et al. (2017), who imaged a subglacial channel near a grounding line. Drews et al. (2017) hypothesise that the channel has formed a large esker, and note that with consistently low effective pressures near a flat grounding line R–channels will grow large.

1.3.1 Kamb Ice Stream

The Kamb Ice Stream once drained the interior of the West Antarctic Ice Sheet to the Ross Ice Shelf (Figure 2.1), flowing faster than 350 m/yr (Ng and Conway, 2004). Around 150 years ago, it stagnated to a speed of around 10 m/yr (Ng and Conway, 2004). As a result of this change in flow, the Kamb Ice Stream is often referenced as an example of internal variability in ice stream flow (e.g. Hulbe and Fahnestock, 2004). The grounding line of the Kamb ice stream is thought to have occupied its current position for around 150 years, prior to which it was downstream (Fried et al., 2014). Horgan et al. (2017) suggest that the grounding line likely retreated to its current location after the stagnation of the Kamb Ice Stream. If the Kamb Ice Stream reactivated, ice discharge would potentially increase by 20 Gt/a (Jacobel et al., 2009). While variability in the flow of the Kamb Ice Stream is attributed to changes in subglacial drainage, there is no clear evidence of how this happened. The leading hypothesis proposes that water was rerouted away from the ice stream leaving its base dry (e.g. Anandakrishnan and Alley, 1997), though observations of water at the base of the ice stream contradict this hypothesis (Engelhardt and Kamb, 1997). A second hypothesis for the slowdown describes changes in the shape of subglacial networks, from an inefficient high–pressure system that fosters sliding to an efficient, low–pressure system that doesn't greatly reduce bed friction (Lelandais et al., 2018; Retzlaff and Bentley, 1993). Other models describe ice stream variability as driven by changes in the thermal regime at the bed, between frozen/stuck and wet/sliding regimes (Robel et al., 2013, e.g.).

The subglacial drainage system (water) of the Kamb Ice Stream was modelled by Le Brocq et al. (2013). While the water flow rates in this model have high uncertainties, the estimated flow routing was mapped directly from relatively accurate pressure gradients based on ice thickness maps. Le Brocq et al. (2013) founds a valley in the hydro–potential field, and predicted the confluence of almost all subglacial drainage. Kim et al. (2016) suggested that there is likely channelised drainage under the Kamb Ice Stream, through finding linked subglacial lakes whereby the flooding of one lake fills downstream lakes. The predicted flow path and potential channelised drainage route meets the grounding line at a large channel feature which is the subject of this thesis.

1.4 The grounding zone

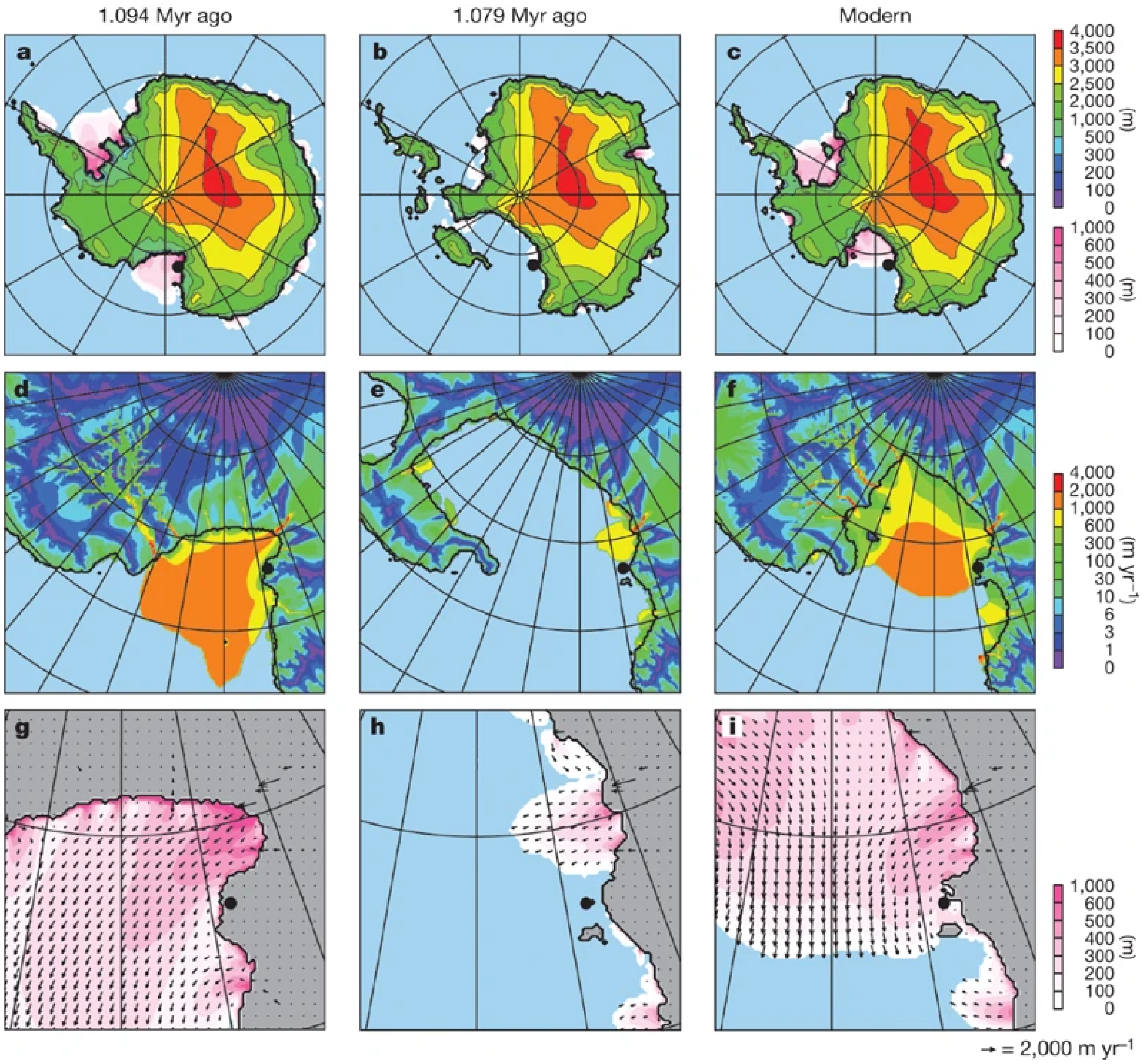

Figure 1.3: From Pollard and DeConto (2009). Grounded ice elevations and floating ice thicknesse from a) 1.094 Myr ago, b) 1.079yr ago (MIS 31 retreat) and c) present day. Surface ice speeds (m/yr), from higher-resolution (10 km) nested runs over the Ross embayment for d) 1.094 Myr ago, e) 1.079yr ago and f) present day. Floating ice thicknesses (m) and velocity vectors from the nested simulations, enlarged over the western Ross embayment for g) 1.094 Myr ago, h) 1.079yr ago and i) present day. The location of the AND-1B drill location is shown by the black dot.

The 'grounding line/zone' is the boundary between grounded and floating ice. For larger scale processes, this boundary is often simplified as a line (e.g Gudmundsson, 2013), though in reality the boundary spans an inter-tidal area (e.g Christianson et al., 2016), termed the grounding zone. Around the grounding zone, the interaction of the ocean and ice sheet base affects ice sheet flow and basal melt. There are numerous observations of ice streams which accelerate and decelerate depending on the tide (e.g. Winberry et al., 2009; Anandakrishnan et al., 2003). When an ice shelf rises and falls with tidal cycles, ice bends at the grounding line. Various modelling approaches agree that tidal bending has the potential to move water and that with each tidal cycle, the ocean extent changes (Sayag and Worster, 2013; Walker et al., 2013). For this reason, the grounding line is commonly termed the grounding zone. Observations confirm that the transition from grounded to floating ice occurs over some distance (e.g. Brunt et al., 2019), and that the transition from fresh water basal hydrology to salt is not clear cut (e.g. Christianson et al., 2016). Ice sheet models are highly sensitive to basal melt at the grounding line, and models show that an increase in basal melt enhanced by the inland intrusion of salt water can cause a large change in the modelled evolution of the volume of an ice sheet (Robel et al., 2022).

1.4.1 West Antarctic Ice Shelf instability

In contextualising paleo ice sheet extent (e.g Naish et al., 2009; Pollard and DeConto, 2009), grounding line location is used as a proxy for the size of an ice sheet. Grounding line location and dynamics are chronicled to identify the past collapse of the ice sheet. The modelled paleo extent of the Ross Ice Shelf and West Antarctic Ice Sheet, 1.094 million years ago, is shown in Figure 1.3.

The West Antarctic Ice Sheet is a marine ice sheet, meaning it is largely grounded below sea level (Fretwell et al., 2013). This is unstable in that if it were to collapse (as in Figure 1.3 b), it would not grow back in modern climate conditions (Oerlemans, 2021). In the present day, snow fall augments ice mass and is balanced by the discharge of ice, which flows from the interior of the continent to the sea (Rignot and Thomas, 2002; Paterson, 2016). However, if the ice sheet were to collapse, snow would fall on the ocean, and would not augment ice mass. The formation of a marine ice sheet relies on lower sea levels with enough landmass to sustain a positive mass balance (Oerlemans, 2021).

The West Antarctic Ice Sheet has retreated quickly in the past (Yokoyama et al., 2016). This observation, along with theoretical ideas of instabilities in marine ice sheets (e.g. Katz and Worster, 2010) has led to a hypothesis that the West Antarctic Ice Sheet could collapse quickly in the future (Vaughan, 2008). The most heavily cited mechanism for describing this collapse is the marine ice sheet instability (Weertman, 1974). The marine ice sheet instability postulates that with no change in accumulation, a reverse bedslope is an unstable grounding line position, while a positive bedslope is stable. This instability theoretically applies to a one dimensional glacier, which is thought to be representative of a glacier with no lateral bounds. If the grounding line retreats on a reverse bed slope, ice thickness increases, which leads to faster ice discharge and further retreat. Stability is only achieved when the downstream flux gradient at the grounding line exceeds the accumulation rate (Haseloff and Sergienko, 2018). On a reverse slope, a perturbed grounding line will advance or retreat until the grounding line reaches a location with a positive slope.

While the marine ice sheet instability is widely cited as a source of concern, with more realistic models Haseloff and Sergienko (2018), Gudmundsson (2013) and Jamieson et al. (2012) all found that marine ice sheets confined laterally or by ice shelves are not necessarily unstable on reverse bed slopes. They found that buttressing can restore stability to marine ice sheets with reverse bed slopes, and that the marine ice-sheet instability may not apply to marine ice sheets with lateral and/or ice shelf buttressing (Haseloff and Sergienko, 2018). It follows that is not clear to what extent the West Antarctic Ice Sheet is unstable (Vaughan, 2008). Some areas of the West Antarctic Ice Sheet like Thwaites Glacier and Pine Island Glacier appear to be collapsing due to a combination of the marine ice sheet instability and the southward intrusion of relatively warm currents of Circumpolar Deep Water (Favier et al., 2014; Joughin et al., 2014). Other areas, such as the Siple Coast, appear to be presently stable (Hindmarsh, 1996), and have retreated relatively slowly in the past (Conway et al., 1999).

1.5 Ice Shelf Cavity

1.5.1 Oceanography

Floating ice shelves which fringe Antarctica provide a direct connection between the world's oceans and the Antarctic Ice Sheet. The coupling between these two important entities can be reduced to processes which occur at the interface between ice shelves and the ocean (Holland et al., 2003a). These processes have large impacts on both the ice sheet and the ocean. As climate change warms the oceans, the heat melts ice shelves which thin and weaken, reducing their restraint on the flow of the ice sheet (Pritchard et al., 2012). Based on climate projections for the twenty-first-century, heating of the oceans is predicted to increase mass loss of Antarctica's ice shelves by between 41% and 129% (Naughten et al., 2018). Conversely, as ice shelves melt they release large quantities of fresh cool water into the ocean (e.g. Holland and Feltham, 2006). This water has a strong effect on the production of sea ice (Langhorne et al., 2015), and is one of the building blocks of the Antarctic Bottom Water which fills the worlds deep oceans (Foldvik et al., 2004).

The Southern Ocean is not blocked by obstacles for its entire 360 degree span around Antarctica, allowing the free flow of wind and seas. The strong westerlies present drive the worlds strongest current, the Antarctic Circumpolar Current which transports a mean 100-150 million m^3/s (Knauss and Garfield, 2016) (Figure 1.4, ACC). The Antarctic Circumpolar Current connects to the Atlantic, Pacific, and Indian Oceans, and propels portions of the principal currents in each ocean, as well as acting as an intersection (a large

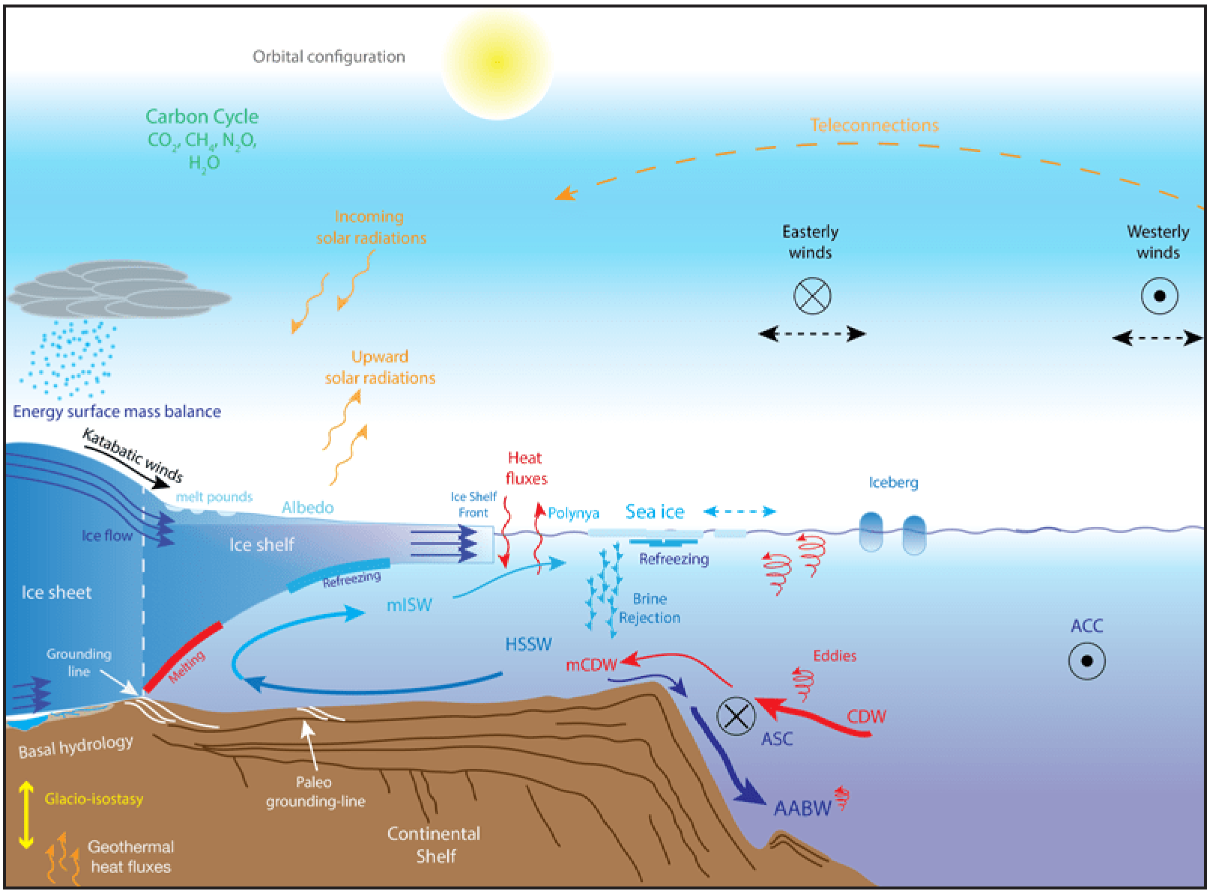

Figure 1.4: Two dimension schematic showing dominant ocean processes linked to the Ross Ice Shelf. Acronyms represent water masses. A circled X means flow into the image, and a circled dot means flow out of the image. Reproduced with permission from De Santis et al. (2018).

round–about) for exchange between them (Knauss and Garfield, 2016). The circumpolar current dominates the Southern Ocean, blocking direct north–south transfer, and driving movement of the relatively warm and salty water mass, named Circumpolar Deep Water, eastward and in places southward (Knauss and Garfield, 2016). Some ice shelves, such as those of the Pine Island and Thwaites Glaciers (Nakayama et al., 2019) in the Amundsen and Bellingshausen Seas, are strongly affected by this warm water which transports heat and salt south (Nakayama et al., 2018), increasing basal ice shelf melt.

Basal melt is driven by the circulation of water under ice shelves, which transports heat and salt from the open ocean to the ice base (Figure 1.4). The largest circulation pattern in ice shelf cavities starts in the open ocean surrounding Antarctica (Jacobs et al., 1992). Sea ice proliferates on the open ocean, growing from a mean summer extent of 3.1 million km^2 to a mean winter extent of 18.5 million km^2 (Hobbs et al., 2016). The formation of sea ice contributes to ice shelf melt through the following process: as sea ice forms, it leaches brine (Figure 1.4, Sea Ice, Refreezing, Brine Rejection). Brine is relatively dense and so sinks, forming the water mass known as High Salinity Shelf Water

(Figure 1.4, HSSW). The dense High Salinity Shelf Water flows inland along the sea floor until it meets ice at the grounding line (Jacobs et al., 1992). There, the availability of salt causes melting of the ice base, releasing fresh water (Figure 1.4, Melting). The buoyant melt water forms a plume which rises up the gradient of the ice shelf (Figure 1.4 , mISW). The plume entrains salty water from the depths of the ocean to mix with the ice boundary layer and melts the ice base (Jacobs et al., 1992). This process is thought to be the dominant source of vertical mixing under ice shelves, essential for the transport of salt through the stable water column from the bottom of the ice shelf cavity to the ice base. A positive feedback between momentum of the plume and melt drives this process. Momentum enhances the entrainment of salt and heat, causing melt which results in a gain in buoyancy, allowing the plume to accelerate up a positively sloped ice base (Jenkins, 1991). The plume continues to ascend away from deep salty waters.

Eventually, entrainment wanes until the plume lacks salt and heat. The plume ceases to melt the ice, but residual momentum and buoyancy propel the plume. The pressure and freezing point of ascending water drops, causing the plume to dip below the freezing point, becoming super–cooled (Holland and Feltham, 2006). Super–cooling is relieved by the growth of frazil ice, small ice crystals suspended in the water column. Eventually, the plume reaches equilibrium height and detaches from the sloped ice base, plateauing into the ice cavity at a constant depth (Hewitt, 2020). The crystals of frazil formed from the super–cooling of water are thought to eventually consolidate at the ice base, forming layers of marine ice (e.g. Fricker et al., 2001) (Figure 1.4 Refreezing). Over time this layer is thought to metamorphose and consolidate, first forming a platelet layer, then continuing to become less porous (Craven et al., 2009). Marine ice is distinct from glacial (meteoric) ice in that it is salty. While accretion may also occur directly on the ice base, some observations (Vaňková et al., 2021b) and modelling (Bombosch and Jenkins, 1995) suggest marine ice forms from the deposition of frazil. Accumulation of marine ice or accretion generally occurs away from the edges of ice shelves, (though there exist exceptions to this broad summarising statement (e.g. Langhorne et al., 2015)).

The dominant circulation pattern in an ice shelf cavity (described above) is driven by density changes through melting and freezing which cause water masses to change salinity (Jacobs et al., 1992). Ice melt causes both cooling and freshening of water, which have opposite effects on the density of water (and in reverse for formation of sea ice). However, the change in salinity has a greater effect on density, so melt water is buoyant (Jenkins, 1991). The circulation pattern described causes a net transfer of ice and energy in two steps. Firstly, the formation of sea ice on the open ocean effectively drives the removal of ice from the ice shelf. Secondly, ice shelf melt near the grounding line drives the formation of marine ice under an ice shelf. The second part of this process is known as the 'ice pump' described by Lewis and Perkin (1986). Following this reasoning, the first part is effectively a 'negative ice pump', as negative potential ice through high salinity water is transported rather than potential ice through relatively fresh water. These processes are visible in satellite observations which confirm a pattern of negative basal mass balance around the perimeter of ice shelves, and positive or zero basal mass balance at the centre (e.g. Rignot et al., 2013).

Additional to these broad distributions of basal melt across ice shelves 10s to hundreds of kilometres wide, large changes in basal melt can be found over spatial scales of hundreds of metres (e.g. Marsh et al., 2016; Stanton et al., 2013; Stewart et al., 2019), which are likely caused by localised circulation (Sergienko and Hindmarsh, 2013). Local variability is particularly visible near the grounding line, for example at topographical features like ice shelf channels, which have been identified as some of the strongest regions of ice shelf melt away from the open ocean (e.g. Marsh et al., 2016; Stanton et al., 2013). Through feedbacks with basal topography (Sergienko and Hindmarsh, 2013), channels stimulate the growth of meltwater plumes. These plumes, driven by buoyancy are an important source of vertical mixing, which transports salt and heat from the ocean bottom to the ice shelf base (MacAyeal, 1984).

Vertical mixing is also enhanced by tidal currents (MacAyeal, 1984). Horizontal tidal currents experience friction on boundaries with the sea floor and ice base. The friction induces shear and turbulence, causing the development of mixed layers at both boundaries. In shallow areas tidal currents are stronger, creating thicker mixed layers which provide greater vertical transport (Makinson, 2002). If the cavity is shallow enough, the top and bottom mixed layers meet and vertical transport is not restricted by a stable middle layer.

The broad theoretical model of ice shelf overturning, as pictured in Figure 1.4, describes vertical and N-S circulation though neglects the complexity of 3D circulation (Holland and Feltham, 2006). In reality, earth's rotation causes austral currents to deflect left, generally resulting in stronger outflow on the western sides of Antarctic ice shelves. As a result, buoyant plumes do not flow up–gradient unless they are constrained by topography. Due to the low-friction of the ice shelf base, plumes are almost geostrophic and are found to contour around ice shelves (Jenkins, 2016). The geostrophic balance is between the Coriolis force and buoyancy force, which is deflected up–gradient by the ice base. Currents follow iso-baths and horizontal movement of water dominates ocean flow. As a result, currents will not rise and become super–cooled under a smooth ice base, topographic roughness or constraints are necessary to force up–welling (Holland and Feltham, 2006).

Up–welling forms cool melt water which flows out of the ice shelf cavity and has a strong impact on global oceans. This very cold water mass, named Ice Shelf Water (Figure 1.4 , mISW), mixes with other water masses to form Antarctic Bottom Water (Figure 1.4 , AABW). Antarctic Bottom Water is a super–dense water mass which sinks and spills off the Antarctic continental slope, spreading northward to fill most of the depths (>4 km) of the worlds oceans (Orsi et al., 1999). Additionally, Ice Shelf Water which reaches the open ocean surface is relatively cold and fresh and often filled with frazil ice, both of which enhance sea ice thickening (Langhorne et al., 2015). Climate models are particularly sensitive to the outflow of Ice Shelf Water. Modelling results suggest that increases in melt water can increase sea ice extent and affect the global climate (e.g Merino et al., 2018; Golledge et al., 2019; Bronselaer et al., 2018), though the treatment of ice shelf melt water flux in these models is not yet realistic (Jourdain et al., 2020).

1.5.2 Basal melt theory

What is generally called 'melt' can be driven by the supply of heat or salt to the ice base (Wells and Worster, 2011). When heat is supplied to the ice base, melting occurs when the ice base is warmed to the freezing point of fresh water. However, 'melt' can also occur with ice below the freezing point of fresh water when salt is transported to the ice base. In this case, the salt locally lowers the salinity–dependent freezing point, allowing ice to change to liquid phase (e.g. McPhee et al., 1987). Strictly, this is the 'dissolving' of ice (e.g Malyarenko et al., 2020), whereby the amount of ice ablated is dependent on the quantity of salt transported to the ice base. Basal ice shelf melt is often driven by salt supply. For example, near the grounding line of the Ross Ice Shelf, 510 m below sea level, Robinson et al. (2020) found sea water was at -2.25 °C and 34.75 psu and predicted melt rates of 0.2 m/yr, which were confirmed independently by observations. This melt falls under the dissolution regime as it is occurring at temperatures beneath the freezing point of fresh water.

As described above, transport of heat and salt to the ice shelf base occurs on a larger (>km) scale from the open ocean to the ice shelf cavity (Holland and Jenkins, 1999). Additionally, the fine scale (<m) is important for melt rates. Salt and heat must be in physical contact with the ice boundary to cause melt (e.g. Jenkins et al., 2010). Melt of a horizontal ice–ocean interface has a stabilising effect on the ocean cavity. Melt contributes to a low density layer at the top of the water column. This isolates the ice boundary from the warmer saltier sea below. At the ice–ocean interface, shear currents driven by buoyancy, pressure gradients or tides produce turbulence, causing mixing and vertical transport of heat and salt to the ice boundary. When modelling melt, the ocean boundary layer adjacent to the ice shelf is generally divided into three sublayers: The inter-facial sub-layer, millimetres to centimetres from the ice boundary, characterised by the fact that transfer of momentum is driven by molecular viscosity and direct interaction with the roughness of ice (Jenkins et al., 2010). The surface layer, metres from the ice boundary, where turbulent mixing is influenced by the boundary. The outer layer, 10s of metres from the boundary, where turbulence is unaffected by the boundary and mixing is determined mainly by Ekman transport and stratification. Observations of these boundary layers

and turbulent processes exist (e.g. Jenkins et al., 2010; Davis and Nicholls, 2019), though they are very sparse and so processes are generally poorly parametrised (e.g. Jenkins et al., 2010; Malyarenko et al., 2020).

1.5.3 Ross Ice Shelf

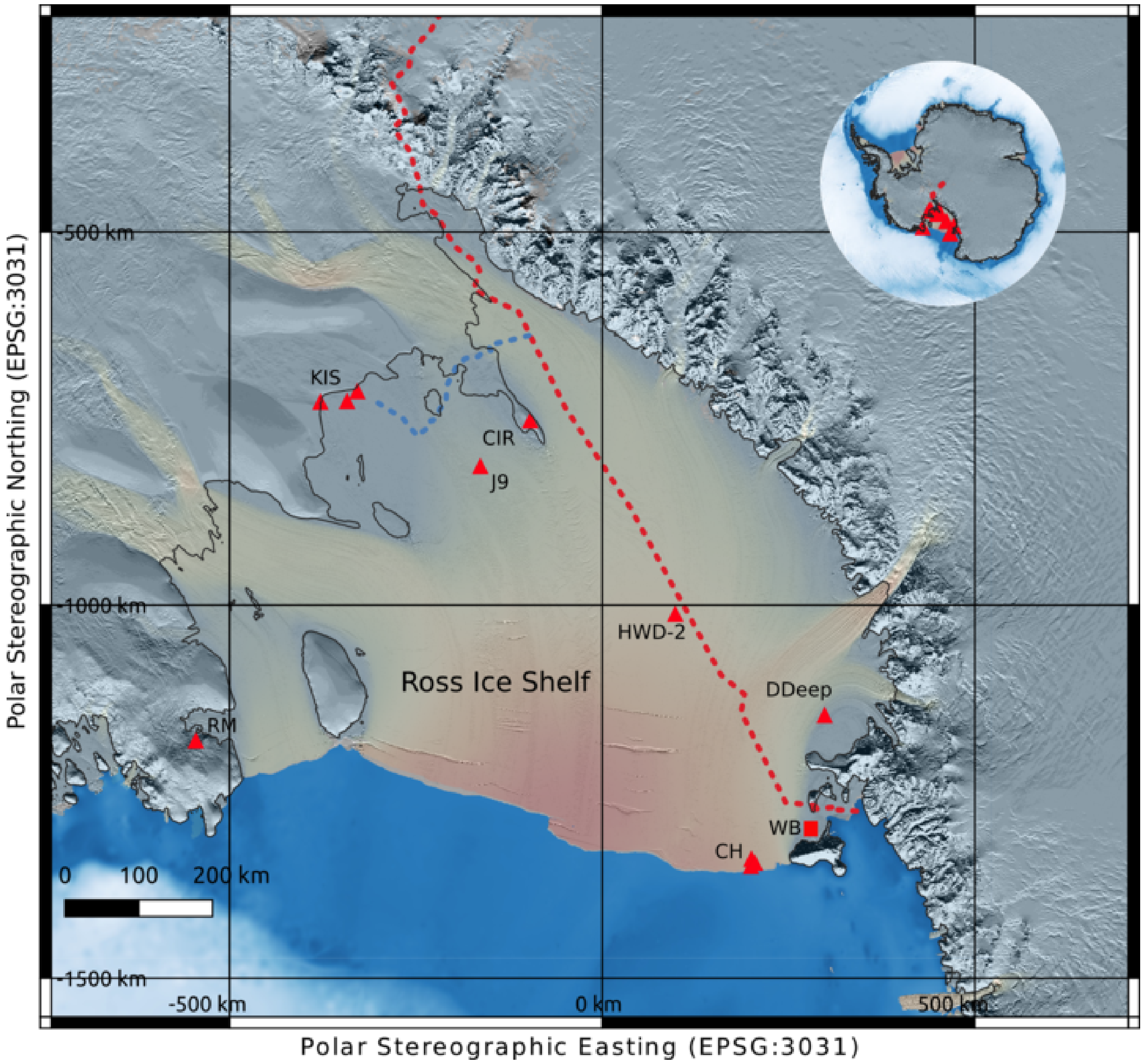

Figure 1.5: Map showing the Ross Ice Shelf. Background image is REMA 100m Mosaic (Howat et al., 2019) overlaid with MEaSUREs Phase-based Ice Velocity Rignot et al. (2011). Red triangles mark the locations of boreholes through the Ross Ice Shelf labelled with the borehole name. KIS is the Kamb Ice Stream. This field location focused on in this thesis is at the left red triangle under the KIS label. Red dotted line shows the South Pole Traverse Route. Blue dotted line shows the traverse to KIS.

The Ross Ice Shelf is the world's greatest ice drainage basin, with around 130 Gt ice/yr discharged through the shelf (Rignot et al., 2008) (Figure 1.5). Spanning around 400,000 km^2, the Ross Ice Shelf is fed by the ice streams of the Siple Coast to the south east, which discharge ice from the West Antarctic Ice Sheet, and glaciers of the Transantarctic Mountains to the west, which drain from the East Antarctic Ice Sheet.

The Ross Ice Shelf loses around 50 Gt/yr of ice through basal melt (Rignot et al., 2013; Moholdt et al., 2014; Das et al., 2020). Basal melt rates average around 12 mm/yr

(Moholdt et al., 2014). Point melt rates have been observed as high as 50 m/yr at the ice front (Stewart et al., 2019), and up to 20 m/yr at localised channel features near the grounding line (Marsh et al., 2016). Unlike the Amery Ice Shelf where 100s of metres of marine ice have been found (Craven et al., 2009), no more than 6 m of marine-ice accumulation has been found underneath Ross Ice Shelf (Zotikov et al., 1980), although no comprehensive survey exists.

There are few observations of circulation under the ice shelf (e.g. Jacobs et al., 1979; Stewart, 2018; Stevens et al., 2020; Robinson et al., 2020), shown in Figure 1.5. Of these campaigns, Jacobs et al. (1979), Foster (1983) and Stevens et al. (2020) profiled ocean structure in the central Ross Ice Shelf. At both sites (named J9 and HWD2 respectively), the basal accretion of crystals was observed. Additionally, both found a mid-column with features which increase fluxes of heat and salt, such as interleaving, intrusion, and overturns (Stevens et al., 2020). In general, the two sites had large differences in ocean structure, for instance, Stevens et al. (2020) found generally greater salinity and additional to the three layers observed by Jacobs et al. (1979) who found a 30 metre thick basal melt layer. These large differences may be due to the fact the two locations were separated by different circulation cells which divide regions of the cavity, as suggested by simulations of the cavity (Pritchard et al., 2012). Similarly, Begeman et al. (2018) made oceanographic observations beneath the Ross Ice Shelf, though at the grounding line in a 10 m deep water column. They observed a region of low basal melt, and little vertical mixing, shown by a vertically stratified water column. Tides in the area did not induce strong currents. These findings were contrary to most theories of conditions at the grounding zone, were strong tides are thought to cause vertical mixing and higher melt rates (e.g. MacAyeal, 1984).

Observations at the ice front (e.g. Smethie Jr and Jacobs, 2005) and physical simulations of ocean circulation in the cavity by Holland et al. (2003b) provide a broad picture of flow in and out of the cavity. Salty warm water flows into the cavity at the western third of the ice shelf, and cool fresh water flows out in the centre. This is a generalisation, finer scale observations reveal more complex dynamics, for example, Robinson et al. (2014) found cool fresh outflow on the Western flank of the cavity. Within the Ross Ice Shelf cavity, the tidal range is predicted to be greatest on the Siple Coast (Padman et al., 2003). There, the peak to peak tidal range is around 3 m. Typical tidal currents are predicted to be around 5 cm/s under the ice shelf (Padman et al., 2003).

The stability of the Ross Ice Shelf is partially dependent on its coupling with the warming ocean. Some heat supplied to the ice shelf cavity originates from the Circumpolar Deep Water (e.g. Rignot and Thomas, 2002). This water mass intrudes across the Ross Sea Break along troughs in the sea floor, becoming mixed with other water masses before flowing under the ice shelf (Castagno et al., 2017). Relative to ice shelves of the Amundsen sea or the Antarctic peninsula, which are thought to be susceptible to break up from the intrusion of warm Circumpolar Deep Water (Favier et al., 2014), the Ross Ice Shelf is less well connected to the warmer saltier waters to the north (Dinniman et al., 2011). In the Ross Sea, the Circumpolar Deep Water is not only cooler initially and travels a longer distance to reach the ice shelf, but it also experiences more vertical mixing with surface waters. This dissipates the heat available to be advected under the ice shelves (Dinniman et al., 2011).

The Ross Ice Shelf is currently stable (Paolo et al., 2015). Its present extent repeatedly arises in model experiments simulating Antarctica's past (Pollard and DeConto, 2009), suggesting that its current configuration is stabilised by bedrock topography such as the pinning points of the Ross and Roosevelt Islands. Surface textures on the Ross Ice Shelf like flow stripes and crevasses record the provenance of modern ice. Analysis of these textures reveals that ice flux through the Transantarctic Mountains has been relatively stable for at least 500 years, while ice supply from individual ice streams has stagnated and reactivated over century timescales (Hulbe and Fahnestock, 2007). Flow lines suggest that about 850 years ago Whillans Ice Stream stagnated, then reactivated 400 years later. Similarly, the MacAyeal Ice Stream stagnated and reactivated around 800-650 years ago, and the Kamb ice stream stagnated around 150 years ago (Hulbe and Fahnestock, 2007).

The stability of the Ross Ice Shelf and the stability of the West Antarctic Ice Sheet are thought to be closely linked. While the Ross Ice Shelf buttresses flow from the West Antarctic Ice Sheet, the West Antarctic Ice Sheet feeds the Ross Ice Shelf. In the past, the West Antarctic Ice Sheet has rapidly disintegrated in sync with the collapse of the Ross Ice Shelf (Pollard and DeConto, 2009). Sediment cores show that over the past 5 million years the location of the present Ross Ice Shelf front has fluctuated between ice shelf, ice sheet and open ocean (Naish et al., 2009). This implies that both the ice shelf and the ice sheet advanced and retreated. Modelling experiments by Pollard and DeConto (2009) extrapolated from the Naish et al. (2009) data suggest that the entire West Antarctic Ice Sheet repeatedly expanded and collapsed over the last 5 million years. At the Last Glacial Maximum ($\approx$20 kyr before present) grounding lines advanced to the continental–shelf edges, 300 km north of Ross Island (McKay et al., 2008) . Beginning around 5000 years ago, the ice shelf suffered a widescale collapse on the continental shelf. This was followed by continuous grounding line retreat until the current ice shelf and ice sheet extent was reached aroun 1500 years ago (Yokoyama et al., 2016). Predictions for the future of the Ross Ice Shelf and West Antarctica show large differences in ice sheet sensitivity to climate forcing because of differences in model parameterisations (DeConto and Pollard, 2016; Golledge et al., 2015; Edwards et al., 2021).

1.6 This Thesis

This thesis is focused on a basal channel at the grounding line where the Kamb Ice Stream meets the Ross Ice Shelf. The channel has been noted previously in literature (Le Brocq et al., 2009; Alley et al., 2016; Kim et al., 2016; Goeller et al., 2015; Horgan et al., 2017), and was profiled by airborne radar as part of the Center for Remote Sensing of Ice Sheets (CReSIS) airborne radar project (Arnold et al., 2020). The channel is migrating upstream at around 1-1.5 m/yr and shows present surface lowering (Kim et al., 2016). While Kim et al. (2016) suggested that the formation of the channel coincides with the ice stream shutdown, Horgan et al. (2017) suggests that the grounding line retreated to its current location after the shut down. Because the channel is at the outlet of an inferred subglacial drainage system, Le Brocq et al. (2009), Alley et al. (2016) and Kim et al. (2016) suggest that the channel is subglacially sourced. This implies that channel growth was triggered by subglacial outflow. The channel does not appear to be a relic streak line formed by the advection of ice past an obstruction, as the channel is not a linear feature but appears to meander downstream.

The channel provides an opportunity to study ice–ocean interaction at the intersection of the ice stream and ice shelf at the grounding line. Constraining a description of the channel and processes associated with the channel and its formation may help to explain and model a variety of important processes upstream and downstream from the channel. Firstly, better quantifying subglacial outflow at the channel may help to constrain Kamb's subglacial drainage system, which has been cited as a major source of uncertainty in projecting future sea level contributions (Bougamont et al., 2015). Secondly, better constraining the processes involved in inland migration of the channel, and the cause of stability or retreat may help to predict future grounding line retreat on the Siple Coast. Lastly, better understanding interaction between the ocean and ice shelf in the channel will improve ice shelf melt predictions. Because ice is not advecting at the channel, the channel is a potential natural experiment in plume driven melt processes. The shape of the channel alone may illuminate plume driven melt processes. Better constrained plume models would improve predictions of basal mass balance and the stability of ice shelves, as well as, Ice Shelf Water production. While the channel is anomalous for the Kamb grounding line, it is likely the region's most dynamic feature, and is not clearly explained by existing data-sets and theoretical models.

1.6.1 Goals

The goal of this thesis is to improve our ability to understand and predict ice ocean interaction both in the channel and in the surrounding ice and ocean cavity. I aim to narrow the possibilities for potential conditions and processes within the channel, constraining processes upstream in the ice stream as well as downstream in the ocean cavity.

The specific objectives outlined by chapter are:

2. Characterise the channel using surface geophysics and remote sensing. Describe ice topography and the temporal gradient in ice topography around the channel, including the subaerial ice surface and base of the ice. Use these results to constrain and better understand ice and ocean interaction in the channel and processes which have formed the channel. Create a map of the ice base topography of the basal channel to guide future research on the channel.

3. Interpret contemporary change in ice base processes in the channel. Identify conditions of the ice–ocean interface, and constrain processes causing these conditions.

4. Constrain ocean circulation and plume dynamics in the channel, extrapolating from channel observations to better estimate melt rates. Better understand the impact of subglacial discharge and ocean dynamics on the basal melting of ice, and compare contemporary ocean circulation to the dynamics which formed the channel.

1.6.2 Structure

This thesis is divided into five chapters, an introduction, three body chapters and a synthesis conclusion.

Chapter Two presents observations of the channel's shape and temporal gradient in topography. We describe surface topography from remote sensing products as well as surface raising and lowering. The ice base topography is estimated over the channel using an interpolation of ground based radar data. Surface elevation and ice thickness are combined to estimate the extent to which ice is floating across the study area. We present two transects of ApRES observations, across and parallel to the channel, which describe the changing ice base topography. Results are used to constrain theories for channel growth and plume processes. We discuss the mechanism which caused the formation of the channel, the impact of bridging of ice stresses on observations, constraints on basal melt rates based on surface observations, and the implications of the channel shape on channel processes.

Chapter Three focuses on an ApRES time series obtained at the apex of the channel. Frequency-Modulated Continuous-Wave Radar techniques are used to process data to obtain basal displacement and strain. Next, amplitude tracking techniques are used to analyse the data-set in greater detail to better constrain basal processes. Lastly, we discuss the implications of the time series, including the properties of the basal environment, its change, and the processes driving the change.

Chapter Four extrapolates from the data presented in Chapters Two and Three using an ocean model with a coupled ice shelf boundary to understand ice-ocean interaction.

The 'Massachusetts Institute of Technology general circulation model' (MITgcm) is used to run simulations of a simplified channel cavity, with prescribed upstream and downstream boundaries designed to emulate the real world channel. Simulations explore the effect of varied subglacial drainage flowing into the model, and varied connections with the larger Ross Ice Shelf cavity. These results are used to explore the sensitivity of the system to processes, such as subglacial drainage, melt water plume dynamics and connection with the ocean.

The final chapter summarises the key findings of the thesis and links between these findings. We discusses their implications and how they lead to future work on the channel. Lastly, we summarise a unified theory describing the channel and associated processes, based on results from this thesis and existing theory.

1.7 Statement of authorship

Chapter Two of this thesis is in review for publication. While this chapter involves collaboration with coauthors, as noted below, the work presented in this thesis is my own. The word 'we' is used throughout this thesis to refer to this work.

Chapter Two is in review as:

Whiteford A, Horgan HJ, Forbes M, Leong WJ (in review, Journal of Geophysical Research: Earth Surface), Melting and refreezing in an ice shelf basal channel at the grounding line of the Kamb Ice Stream, West Antarctica.

I collected and processed field data with input from Horgan and field support from Forbes. I wrote the manuscript. Leong contributed processed Icesat–2 data. All authors contributed editorial input.

Chapter 2

Melting and refreezing in an ice shelf basal channel at the grounding line of the Kamb Ice Stream, West Antarctica

2.1 Abstract

Ice shelves buttress ice streams and glaciers, slowing the rate at which they flow into the ocean. When this buttressing is reduced, either through increased melt or calving, the increased discharge of grounded ice upstream contributes to sea level rise. The thickness, strength, and stability of ice shelves can be influenced by channels in the ice base. Here, we focus on a subglacially–sourced basal channel which is observed to have melted up to 50% of the ice shelf thickness. The channel extends 6 km upstream of the previously estimated grounding line of the stagnant Kamb Ice Stream. Using a combination of ground–based observations and remote sensing, we find that the channel is growing upstream over time. Over–snow radar surveying images the shape of the channel, constrains a steep inception, and shows that not all of the basal shape is manifest at the surface. Modern surface lowering at the upstream head of the channel is interpreted as a region of focused melt where a subglacial outlet meets the ocean cavity. We estimate this basal melt to be at least 20 m/yr in a narrow (200 m x 1.5 km) zone. Downstream from the melt region, repeat phase sensitive radar observations reveal accretion contributing to the growth of a ledge on the true–right side of the channel. We conclude that the channel is likely formed by a retreating subglacial outlet which triggers basal melt in episodic steps.

2.2 Introduction

2.2.1 Ice shelves

Accelerating ice loss from Antarctica's ice sheets is projected to contribute 13–42 cm of sea level rise by the end of the century (Edwards et al., 2021). This contribution is driven by an increase in ice flowing off the continent and into the ocean. Most Antarctic ice discharge becomes part of a floating ice shelf (Rignot et al., 2013), half of which will melt before it reaches the open ocean, while the other half will eventually break off as icebergs (Rignot et al., 2013; Liu et al., 2015). Ice shelves slow the discharge of glacial ice into the ocean. When ice shelves drag past coastlines, islands, and pinning points, they generate back stresses and buttress against ice flow (e.g. Dupont and Alley, 2005; Fürst et al., 2016). This is an important control on the speed of ice loss from Antarctica. The removal of buttressing when an ice shelf retreats or disintegrates leads to the acceleration of ice loss (Rignot et al., 2004; Berthier et al., 2012), and further sea level rise.

Ice shelf melt is largely controlled by ocean circulation in the sub–ice–shelf cavity. Theory of ocean circulation under ice shelves was first developed from interpretations of direct oceanographic observations at ice shelf fronts (e.g. Jacobs et al., 1979). At a large scale, currents under an ice shelf follow a circulation-cell, described in more detail by Jacobs et al. (1992) and well approximated by the ice pump mechanism (Lewis and Perkin, 1986). Sea ice formation releases high salinity water which sinks and flows down–slope along the seafloor into the ice shelf cavity. This relatively dense, warm water comes into contact with the ice shelf at the grounding line, where it melts the ice shelf base and forms a meltwater plume. This relatively fresh, buoyant plume (described in a 1d model by Jenkins (1991)) flows along the ice–ocean interface to the open ocean. This theory predicts ice shelf melt to be strongest at two places: near the ice shelf front where ice is in close contact with the open ocean, and in the region near the grounding line where the relatively warm water from the lowest portion of the water column meets the ice shelf. Near the grounding line, stronger tidal mixing and the development of meltwater plumes also causes vertical mixing which enhances melt (MacAyeal, 1984, 1985). Away from the edges of an ice shelf at its centre, basal ice is either at equilibrium with the ocean or there is accretion at the ice base. This ice shelf melt pattern is supported by indirect observations of ice shelf melt rates (e.g. Rignot et al., 2013; Mankoff et al., 2012; Goldberg et al., 2019), and melt rates predicted by ocean models (e.g. Goldberg et al., 2019).

Indirect estimates of melt-rate patterns are often derived from observations from remote sensing. First, flux divergence is estimated from remote observations and then mass conservation is solved for the basal mass balance. Different approaches to these estimates are outlined in Berger et al. (2017). Such surveys can achieve sub–kilometre scale spatial resolution while covering broad areas. For example, Berger et al. (2017) and Gourmelen et al. (2017) found average melt rates of 0.8 m/yr and 7.8 m/yr on the Roi Baudouin and Dotson Ice Shelf respectively. At a finer scale, direct observations using radar can resolve basal melt with high accuracy (e.g. Vaňková et al., 2020; Young et al., 2018). Starting with Corr et al. (2002), the Autonomous Phase-sensitive Radio-Echo Sounder (ApRES instrument) has been used to make point measurements of melt rates on ice shelves. Developed by Brennan et al. (2014) and Nicholls et al. (2015), ApRES images the ice base and internal ice reflectors, which are used to estimate the vertical strain rate profile. Subtracting vertical strain from the change in ice thickness gives a basal melt or accretion estimate (Brennan et al., 2014). High resolution surveys show large changes in basal melt over small spatial scales (<1 km), particularly near the ice front (e.g. Stewart et al., 2019) and at basal channels (e.g. Stanton et al., 2013; Dutrieux et al., 2014; Marsh et al., 2016).

2.2.2 Basal channels

On ice shelves at both poles, the surface expressions of long linear channels of relatively thin ice are visible from satellite imagery. For an overview of ice shelf channels in Antarctica see Alley et al. (2016). Ice shelf channels influence the mass budget of ice sheets by redistributing melt patterns. Satellite and ApRES observations have shown increased melt rates within some channels. For example, Marsh et al. (2016) and Stanton et al. (2013) used ApRES to measure melt rates of 22.2 $\pm$ 0.2 m/yr and 14.2 to 24.5 m/yr in channels on the ice shelves of the Whillans Ice Stream and Pine Island Glacier respectively. Both studies found that melt rates dropped to near-zero outside of the channel, 1-2 km and 200 m away from the channel apex respectively. Chartrand and Howat (2020) used satellite observations to find similar channel melt rates in the Getz Ice Shelf, estimating melt rates of 22 m/yr at the channel apex and melt rates close to zero 2-3 km away. The impact of ice shelf channels on the whole ice shelf is more complex. Both Gladish et al. (2012) and Millgate et al. (2013) used coupled, numerical ice–ocean models to show that when channels focus melt they prevent melting across the rest of the ice shelf. These authors suggested that by reducing melt over the wider ice shelf, these channels might increase the stability of ice shelves, however, their models did not specifically investigate the structural weakening of the ice shelf. Contrarily, observations support the idea that channels have a destabilising effect on ice shelves (e.g. Alley et al., 2016). Vaughan et al. (2012) directly observed basal and surface crevasses at a channel, and through numerical modelling found that the stress generated from channel melting could trigger crevasse formation. Meanwhile, Alley et al. (2016) found that basal channels are widely associated with areas of crevassing. Alley et al. (2019) emphasised that the common development of basal channels on the margins of ice shelves increases the susceptibility of ice shelves to rapid break–up or retreat. Rignot et al. (2008) also suggested that the break up of ice shelves, caused by warmer ocean waters, may occur sooner than predicted from the mean reduction in ice shelf thickness due to the intense thinning of ice in basal channels.

Direct access and observations of sub–ice–shelf channels beneath Peterman Glacier in Greenland (Rignot and Steffen, 2008) and Pine Island Glacier in Antarctica (Stanton et al., 2013) have revealed buoyant plumes of meltwater. These meltwater plumes are thought to be strengthened by feedbacks between steep slopes, fast plume flow and enhanced melt rates (e.g. Jenkins, 2011; Sergienko, 2013; Gladish et al., 2012). As plume water melts a sloping ice face, the plume becomes fresher, and more buoyant, so accelerates up the ice face. As the plume accelerates it entrains more water from the surrounding ocean, transporting this relatively warm water to the ice face, further contributing to melting. The melt causes the sloping ice face to steepen, enhancing the melt plume feedback, making preexisting basal features more pronounced.

Most observations of sub–ice–shelf channels are restricted to their surface expression, in the form of imagery, elevation, and velocity products from satellites. Comparing surface observations with model outputs has provided some insights into channel formation. For example, Sergienko (2013) modelled channel formation using a fully coupled ice shelf/ocean model, showing a positive feedback between the basal topography of the ice and a meltwater plume. Their study inferred that high melt rates, and existing variability in ice thickness are required to develop a channel. Satellite observations show that basal channels correspond to areas of high basal melt (e.g. Rignot et al., 2008), and confirm that these channels often originate close to or inside grounding zones (Alley et al., 2016).

While channels are thought to be sustained and deepened by meltwater plumes (e.g. Sergienko, 2013), a variety of mechanisms have been proposed to describe their initial formation (e.g. Alley et al., 2019). Channels can be formed from existing valleys in ice thickness. Alley et al. (2019) used satellite data to show that the lateral shearing at ice shelf margins creates a surface valley that when floated past the grounding line initialises a channel. Drews et al. (2017) and Jeofry et al. (2018) used satellite imagery and radio–echo–sounding profiling to show that some channels originate as advection streaks caused by basal topography upstream. Alternatively, Alley et al. (2016) and Le Brocq et al. (2013) identified basal channels co–located with subglacial outflow (as modelled by Le Brocq et al. (2013)), and suggest that subglacial outflow triggers a localised subglacial plume which will form a channel without the requirement of an existing surface valley.

2.2.3 Objectives and outline

This study aims to further our understanding of subglacially–sourced channel formation. We present detailed observations of a basal channel at the grounding line of the Kamb Ice Stream (Figure 2.1). Through these observations we aim to better constrain ice and

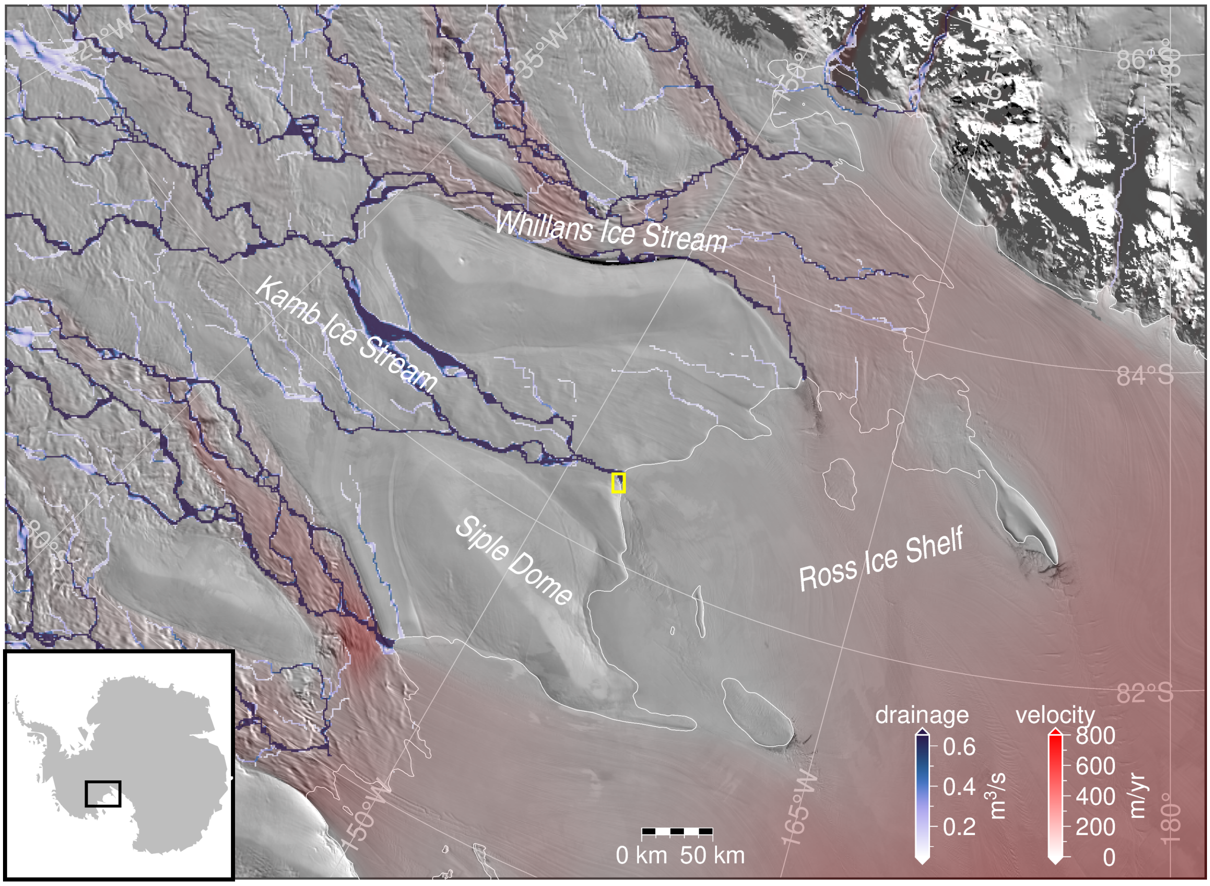

Figure 2.1: Map showing the Siple Coast region. The study area is plotted as a yellow box at the grounding line of the Kamb Ice Stream. Figures 2.3, 2.7, and 2.8 cover this study area. Modelled subglacial drainage of the Siple Coast is in blue (Le Brocq et al., 2009), grounding line and coastline (Depoorter et al., 2013) are plotted as thin white lines. Background image is MODIS MOA 2009 (Haran et al., 2014) overlaid with MEaSUREs Phase-based Ice Velocity (Mouginot et al., 2019). Antarctic place names are labelled in white. Figure produced using PyGMT (Uieda et al., 2021; Wessel et al., 2019) with scientific colour maps (Crameri, 2018). Plotted using an Antarctic Stereographic Projection with a standard latitude of 71°S (EPSG:3031).

ocean interaction in the channel, and processes which have formed the channel. These results be can used as a case study to further constrain models of channel formation and growth, and therefore their impact on ice shelves. The channel has been noted previously in literature (Alley et al., 2016; Kim et al., 2016; Goeller et al., 2015; Horgan et al., 2017), and was profiled by airborne radar during Center for Remote Sensing of Ice Sheets (CReSIS) airborne radar project (Arnold et al., 2020). Because Kamb Ice Stream has little to no ice velocity, this channels is unique in that it is not formed by ice advection or shear. As a result, the channel can be used as a natural experiment in plume-driven melt processes. Kim et al. (2016) and Alley et al. (2016) suggested that the channel is formed from submarine melting from a subglacially sourced buoyant freshwater plume.

We use the terms 'surface valley' and 'basal channel' to distinguish the surface and basal expressions of the channel respectively. 'True left' and 'true right' are from a perspective looking downstream. Channel 'inception' refers to the upstream limit of the basal channel incision. Channel 'apex' is the maximum height of along a lateral transect, while the 'walls' are the channels lateral flanks. The 'apex' and 'walls' run down the length of the basal channel. The surface valley lies at the downstream end of a modelled subglacial drainage path (Figure 2.1), and optical satellite imagery shows the feature is contiguous with a sinuous feature that cross–cuts streaklines upstream of the grounding zone (Figure 2.2). Downstream of the channel, the ice shelf exhibits a damaged zone many tens of kilometres long (Figures 2.1,2.2). In this paper, we start by examining the surface valley of the channel (Section 2.3.1) using satellite imagery (MODIS MOA Haran et al. (2014) and LandSat Roy et al. (2014)) and elevation products (REMA Howat et al. (2019) and ICESat2 Smith et al. (2021)), presenting surface elevation and surface elevation change. In Section 2.3.2.1 we examine the basal channel underlying the surface valley, using low-frequency (7 MHz) radio–echo–sounding from a series of closely spaced (as little as 250 m) cross-channel profiles. Next, repeat phase sensitive radar (ApRES) observations are used to estimate the basal mass balance within the basal channel in Section 2.3.2.4. We then discuss the implications of these results, first constraining the mechanism which creates the channel (Section 2.5), and explaining why we see discrepancies between the ice base and surface (Section 2.5.0.1). We then estimate a lower bound on the melt rate magnitude in the basal channel (Section 2.5.0.2). Lastly, we discuss processes that could explain our observations. In particular, the linear shape of the channel (Section 2.5.1.1), the steep shape of the channel inception (Section 2.5.1.2), and ledges in the channel (Section 2.5.1.3).

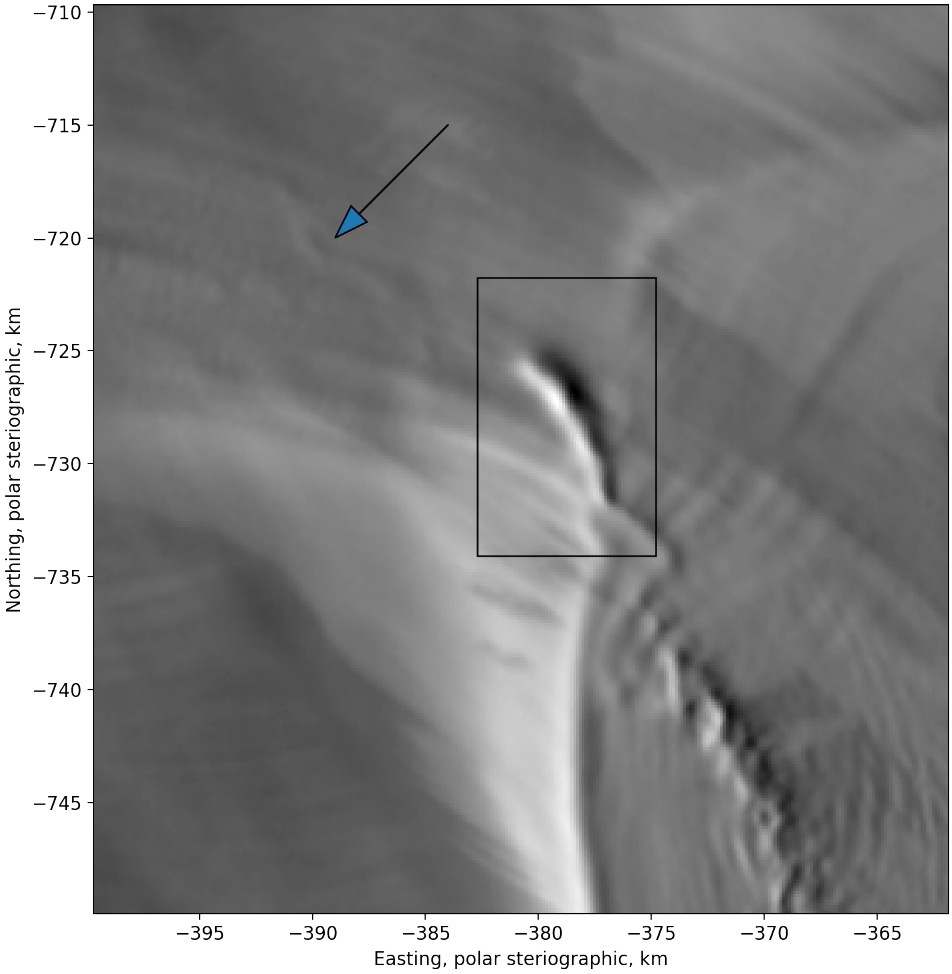

Figure 2.2: MODIS MOA (2009) imagery of wider study area (Haran et al., 2014). Arrow points to continuation of the surface valley upstream of the main study region. Black box outlines the study area shown in Figures 2.3, 2.7, and 2.8.

2.3 Methods

To estimate ice surface elevation and ice thickness in the study area we used a collection of remote sensing products and over-snow radio–echo–sounding. Basal mass balance is estimated at point locations using repeat ApRES. Data coverage is shown in Figure 2.3. This section outlines the remote sensing products used and describes the ApRES and radio–echo–sounding processing along with the interpolation methods used to estimate ice thickness and ice base topography.

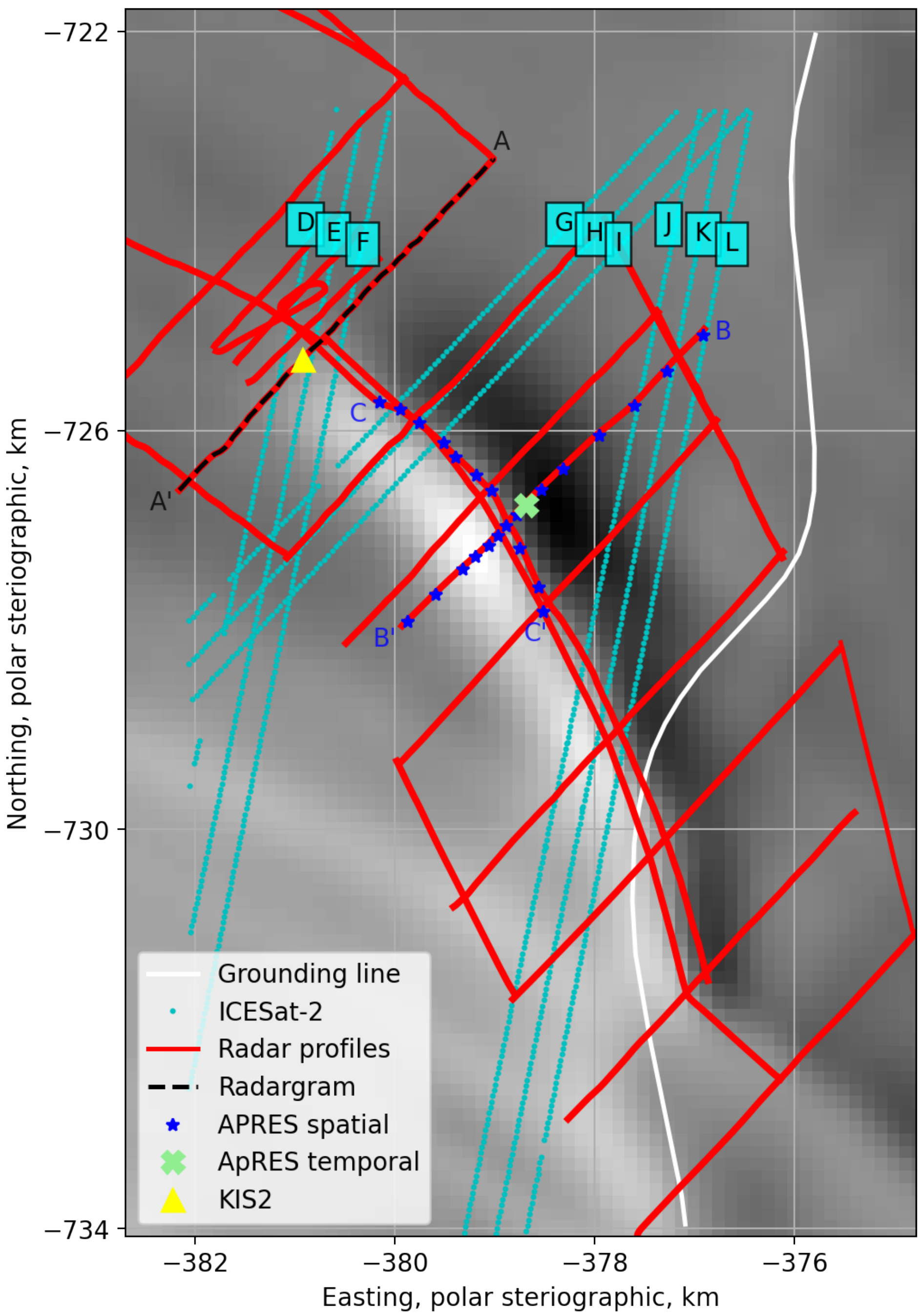

Figure 2.3: Map of study area showing location of data. Ice flow direction is from top left to bottom right. Background image is MODIS MOA 2009 (Haran et al., 2014). Red lines are low–frequency radar profiles, white line is grounding line from Depoorter et al. (2013), black dashed line shows location of radar profile from Figure S6, blue stars are ApRES repeat measurement locations, and light blue dots are ICESat–2 tracks. ApRES was placed continuously recording at the light green ‘X’, and the yellow triangle marks the planned location of a direct access drilling site scheduled for drilling in late 2021. Letters are referred to in subsequent figures.

Product	Data timespan	Site coverage	Reference
REMA 2m strip	12/2012–09/2017	2 m pixels of site area	Howat et al. (2019)
ICESat–2	4/2019–ongoing	6 tracks across channel	Smith et al. (2021)
Landsat	1985–ongoing	20 m pixels covering site area	Roy et al. (2014)
MODIS MOA	-	125 m pixels covering site area	Haran et al. (2014)

Table 2.1: Remote sensing products used in this study.

2.3.1 Surface

2.3.1.1 Remote Sensing

Four different remote sensing products were used to study the surface valley (Table 2.3.1.1). Optical satellite imagery included Landsat 4-8 (Roy et al., 2014) and the 2009 MODIS Mosaic of Antarctica (MOA) (Haran et al., 2014). Landsat 4, 5, 7, and 8 showed temporal change in the surface valley, and showed the earliest image of the valley in 1985. The 125 m spatial resolution MODIS MOA product provided a broader view of the study area and surrounding surface. For surface elevations, we used ICESat–2 and Reference Elevation Model of Antarctica (REMA) strips (Howat et al., 2019; Smith et al., 2021). ICESat–2 track coverage is shown in Figure 2.3. REMA strips provided the most detailed view of surface elevation, with 2 m pixels over the study area. While nine strips from December 2012 to September 2017 pass over the study area, most have some cloud cover or miss a significant portion of the study area. The REMA strip from 9 November 2016 has full coverage, so was used used to calculate ice base elevation from ice thickness. A second REMA strip from 24 December 2012 was differenced from the 2016 strip to calculate the temporal gradient in the ice surface. The 2012 and 2016 REMA strips state a vertical accuracy of 4 m and 3.5 m respectively Noh and Howat (2015); Howat et al. (2019). However, the elevation models are expected to be more accurate over the study area which is relatively stable due to low surface velocity Rignot et al. (2017).

We used ICESat–2 ATL11 point elevations (Smith et al., 2021), which had nine tracks crossing the study area. The reference ground track numbers for these tracks are 114, 175, 349, 410, 617, 852, 1059, 1120, 1294. These were acquired more recently (since 2019) than the REMA elevation strips. Mean surface measurement precision from ATL11 points over the study area was 1.12 cm (Figure 2.4). For ICESat–2 differences a year apart, we double this mean surface precision to get an uncertainty of 0.02 m/yr. All elevations in this paper are referenced to the GL04C geoid datum, which is approximately 47 m below the WGS84 ellipsoid datum in the study area. Elevation differences from ICESat–2 ATL11 point elevations were also compared to differences calculated using debiased REMA strips.

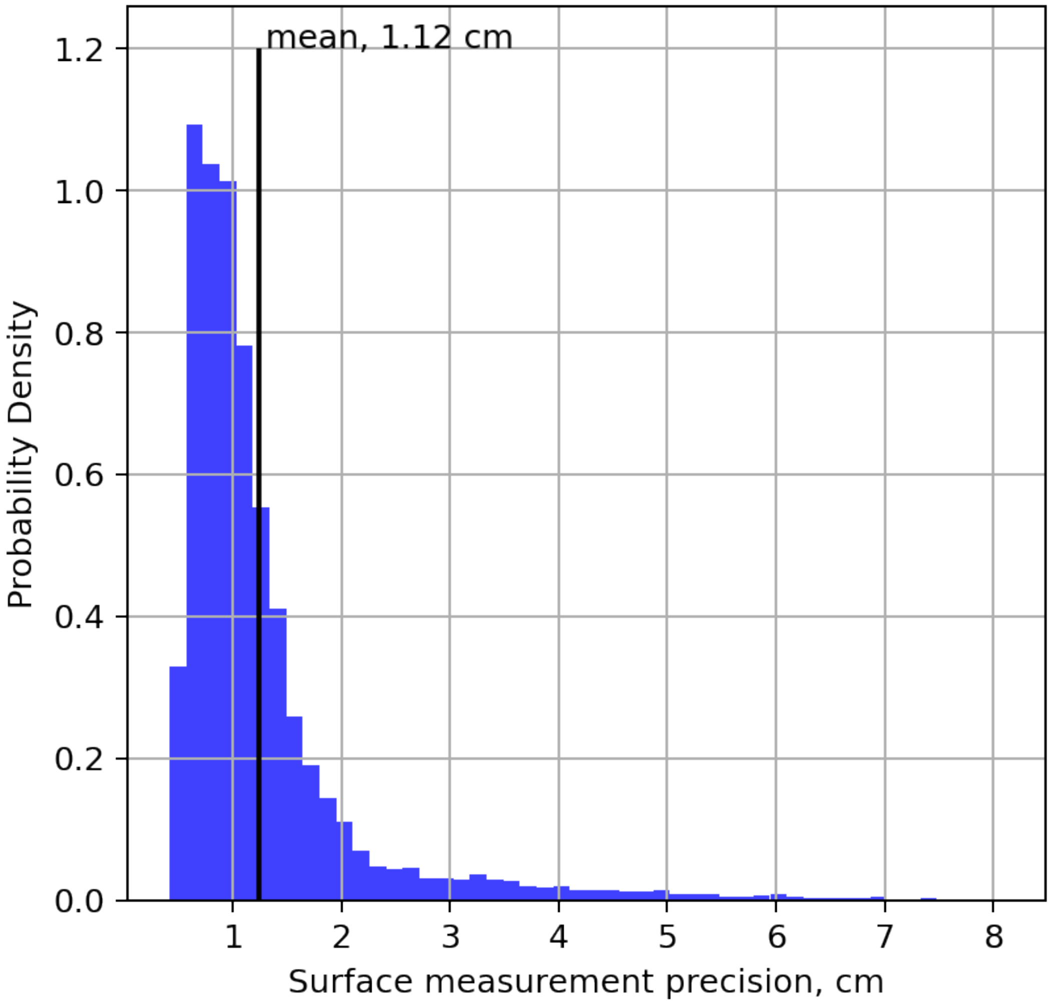

Figure 2.4: Histogram showing the range of ICESAT–2 surface measurement precision in the study area.

2.3.2 Ice thickness

2.3.2.1 Low Frequency Radar

To estimate ice thicknesses over the channel, the study area was profiled using low-frequency (7 MHz) radio–echo–sounding. Radar profiles were 1000-1400 m apart, except at the head of the channel where the spacing between lines was reduced to approximately 200 m to better constrain the inception of the channel (Figure 2.3). Data collection followed Christianson et al. (2016). The radar transmitter and receiver were towed on sleds at approximately 8 km/hr resulting in an average spatial resolution along radar lines of 1.8 m. Data processing included dewowing, bandpass filter (1-2–15-18) MHz, along track spatial stacking into 3 m bins, and debiasing. The data were then finite difference migrated at 169 m/μs, before a final (3-4-15-18) MHz bandpass filter was applied. The resulting profile data in off-nadir reflections (discussed in more detail in Christianson et al. (2016)), which are difficult to interpret but must be considered during analysis.

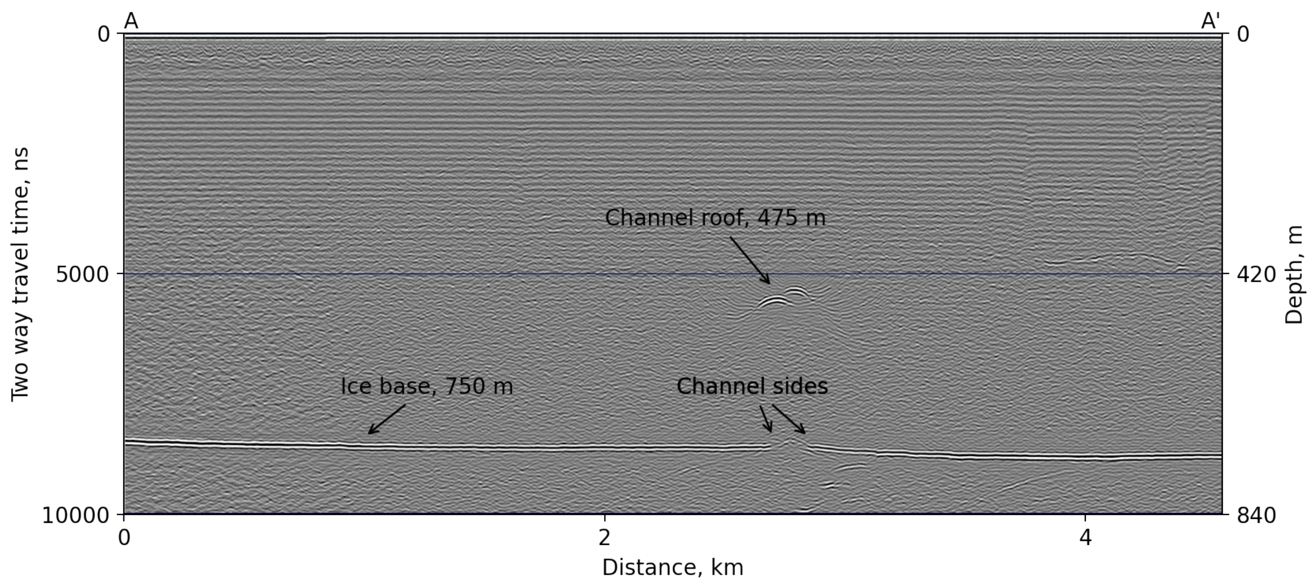

Figure 2.5: Processed radargram showing radar reflection of the basal channel. Profile location is shown as a black dashed line in Figure 2.3.

Radar survey positioning used Global Navigation Satellite Signal (GNSS) observations, post processed using the Precise Point Positioning kinematic method (Natural Resources Canada, 2016). An example processed radar line is shown in Figure 2.5. The location of all radar lines are shown in Figure 2.3. Following Dowdeswell and Evans (2004), a firn correction of +7 m was added to ice thickness. Additionally, a +7 m was added to ice thickness to correct the offset between the single frequency radar and the more accurate ApRES ice thicknesses. This difference is likely caused by the low frequency radar trigger threshold. This correction was calculated as the mean difference between ice thicknesses derived from coincident ApRES and low frequency radar at line BB' shown on Figure 2.3.

2.3.2.2 Ice base DEM

We estimated the three dimensional shape of the basal channel by digitising the base of the ice and then interpolating between radar profiles. Our observations of ice thickness had high spatial sampling across the channel (3 m trace spacing) and low spatial sampling in the downstream direction (profile spacing of 200–1400 m). This meant that conventional interpolation techniques failed to capture the shape of the steep sided narrow channel (Figure 6.3). To overcome this we use an interpolation method that is based on the assumptions that the channel is bounded laterally and has downstream continuity. First, all radar lines crossing the channel were resampled spatially from the channel apex to either side of the channel. Equivalent points from each line were then interpolated downstream with a cubic spline. These along–channel interpolated profiles were then interpolated altogether onto a regular grid. Because radar lines parallel to the channel included some off-nadir reflections that were not correctly repositioned by migration, they were not used in the interpolation. Ice thickness in the study area not over the channel was estimated using linear interpolation of all radar line points outside the channel. The channel thickness interpolation was cropped onto the surrounding ice thickness estimate, and the whole study area was again gridded using a nearest–neighbour interpolation. The resulting estimate of ice thickness (Figure 6.6) was then subtracted from a 2 m REMA surface elevation strip to produce ice-base elevation. Our interpolation technique accounts for the anisotropic resolution of radar data by assuming that the cross section of the channel has downstream continuity. Additionally, it uses the cross-channel radar profiles which unlike downstream profiles can be corrected by 2D migration, and so give a more accurate quantification of ice base elevation. The resulting interpolation of the basal channel shape was compared to independent basal elevation estimations provided by Center for Remote Sensing of Ice Sheets (CReSIS) airborne radar project (Arnold et al., 2020), which had three lines passing over the basal channel in the study area.

One goal of estimating an accurate channel shape is to better constrain the freshwater plume which carves the channel. For this, the gradient of the channel inception is important, as it is a dominant forcing in plume melt rate models (Jenkins, 1991). Locating the inception of the channel, however, is not straightforward due to off nadir reflections. The channel inception is best shown in a radar line parallel to channel direction (Figure A 6.1). From this, we deduce that the farthest upstream radar line which has a reflection crossing the channel, shows an off nadir reflection. This interpretation is confirmed by the fact that this radar data shows a reflection distance equal to the distance to the channel reflection on the next radar line. In the channel interpolation, the channel depth is set to be zero at this off nadir reflection, which constrains the downstream distance or angle over which the channel forms.

2.3.2.3 Hydrostatic Equilibrium

For each pixel from the ice base DEM, we calculated the vertical distance which the ice column is offset from hydrostatic equilibrium. We call this the vertical offset from hydrostatic equilibrium. An offset of zero describes ice at hydrostatic equilibrium (described in Section 2.3.2.3), and a negative/positive offset indicate the ice column is held below/above equilibrium by external forces. To calculate this measure we first estimated average density of the ice column for each pixel, using ice thickness from the interpolated DEM (Section 2.3.2.2) and the density-depth model of Herron and Langway (1980). For the density model, we assumed an accumulation rate of 0.11 m/yr (Stewart, 2021), a mean annual temperature of -27.3 °C, and initial, critial and ice densities of 300, 555 and 917 kg/m^2 respectively. Next, using Archemedis principle, ice thickness and average density, we calculated the theoretical freeboard if the ice column at each pixel were at hydrostatic equilibrium. This is calculated as $h_{freeboard} = h_{thickness}\,(1 - \bar{\rho}_i/\rho_s)$ where $h_{freeboard}$ is the freeboard elevation of the pixel at hydrostatic equilibrium, $\bar{\rho}_i$ is the average density of the ice column for a pixel and ρ_s is the density of displaced seawater which we set to 1030 kg/m^2. We subtracted the resulting freeboard elevation from the REMA elevation of the region corrected to the GL04 geoid to get the vertical offset from floatation (Figure 2.11).

2.3.2.4 ApRES

Basal mass balance was surveyed using ApRES on two profiles, one parallel to the surface valley low, the other crossing the channel (Figure 2.3). ApRES observations were made in Dec 2019 and repeated in Dec 2020 at the same locations, which we marked with flags. The ApRES antennae had a parallel orientation and were spaced 9 m apart. Data collection and processing followed the method described in Stewart et al. (2019). The ApRES surveys are not migrated so results may show off nadir reflections. While the ApRES can observe accretion, quantifying the rate is problematic due to the occurrence of multiple reflections from both the glacial/marine–ice interface and the marine–ice/water interface, and unknown changes in the properties of marine–ice (Vaňková et al., 2021b). The values presented should be interpreted as an 'apparent accretion' rate as described by Vaňková et al. (2021b).

2.4 Results

2.4.1 Topography

2.4.1.1 Surface topography

The surface valley is visible in the first available imagery from Landsat 5 in 1985 and extends further upstream in subsequent Landsat imagery in 1989, 2002, and 2020 (Figure 2.6). While changing illumination angles may affect the apparent migration of the valley, the apparent migration appears to exceed any direct shading effects. By 2020 the channel appears more defined and extends approximately 1.5 km upstream of the 1985 surface channel. The 2016 REMA strip shows that the surface valley was approximately 2 km wide, over 10 km long and had a maximum depth of 15 m relative to the adjacent ice stream (Figure 2.7 B). The valley starts abruptly, 5 km inland from the Depoorter et al. (2013) grounding line (Figure 2.3). The surface gradient at the head of the valley is approximately -1 degree, then the valley is fairly straight and flat–bottomed for around 1.5 km. The valley then becomes moniliform, with three connected distinct basins downstream (labelled B1, B2, B3 in Figure 2.8). The three basins downstream from the surface valley inception correspond to bends in the basal channel. Both the surface valley and basal channel first turn to the true right by 30 degrees (B1), then right by 20 degrees (B2) then left by 60 degrees (B3) at the three basins respectively. On the surface, high points between basins are 3-7 m higher than the basin lows, and the valley is 5-10% wider at the basins. In historic imagery (1985, 1989; see Figure 2.6) the three basins are visible, and the surface valley does not extend upstream from the three basins.

In the 2009 MODIS MOA imagery, a faint trace of the valley continues upstream from its clear head for 10 more kilometres (Figure 2.2). The faint trace of the basal channel upstream is not visible in radar profiles.

2.4.1.2 Ice base topography

The downstream profile of the channel apex is best described from radar lines perpendicular to the channel. Radar lines following the channel do not accurately show channel depth due to off nadir reflections. The bisection of perpendicular radar lines and the channel apex are shown in Figure 2.8 as ‘Surveyed channel apex’ and are interpolated to produce the ‘Interpolated Channel Maximum’ as described in Section 2.3.2.2. The ‘Surveyed channel apex’ show the basal channel starts abruptly, approximately 300 m upstream from the start of the surface valley (Figure 2.8 B). The inception of the basal channel inclines from 0 m to 300 m above the bed over less than 300 m horizontally, constrained by the spacing between parallel radar profiles. Therefore, the initial gradient of the basal channel is constrained as between 45 and 90 degrees from horizontal. Over 500 m downstream the basal channel incises approximately 50% of ice thickness (350 m

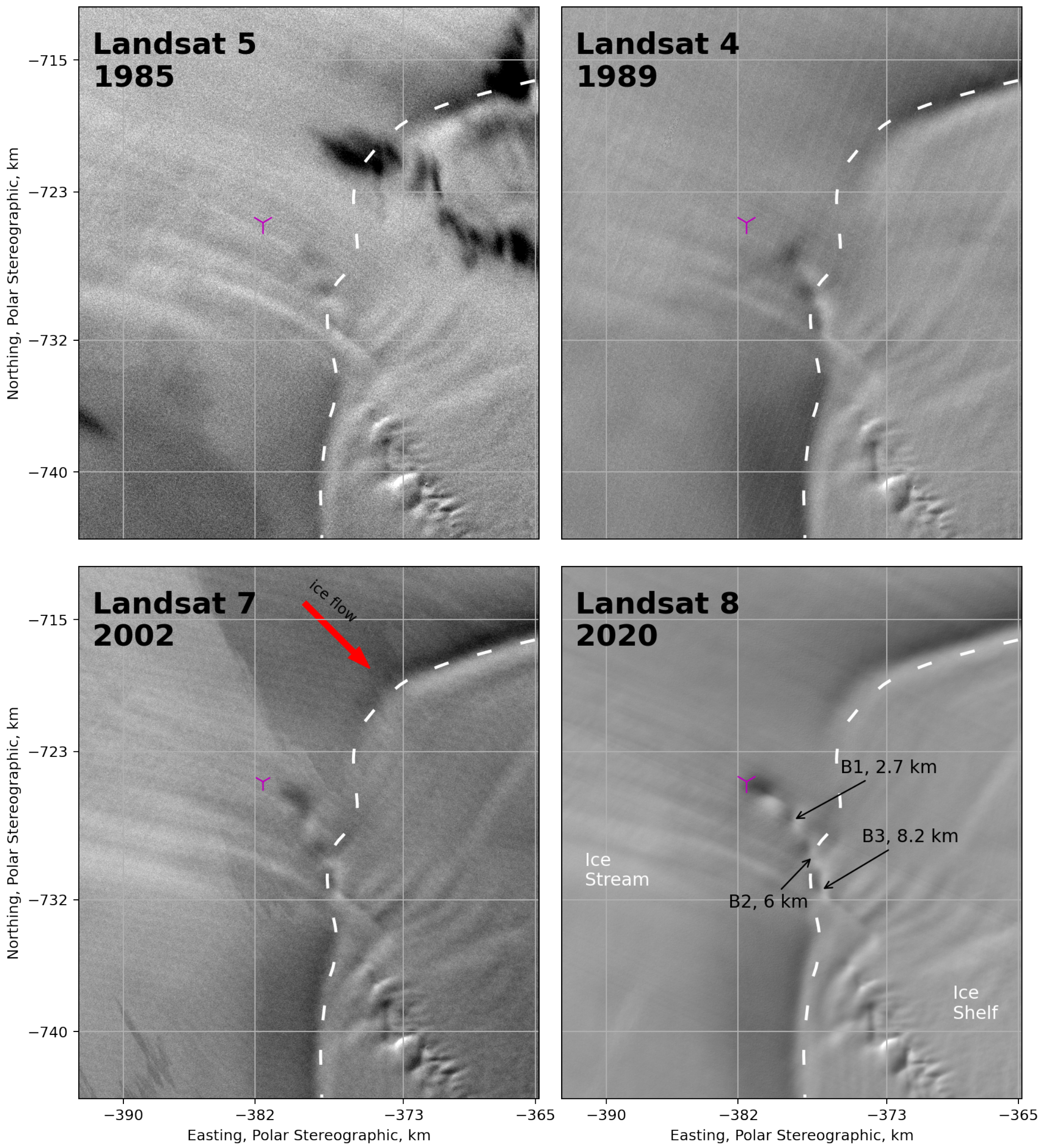

Figure 2.6: Landsat imagery of a visible valley in the ice surface (Roy et al., 2014), shown in the central grid square at (-380,-725 km). The surface valley sits at the outlet of estimated subglacial drainage paths (Figure 2.1), and is the surface expression of a sub–ice–shelf channel. The grounding line (Depoorter et al., 2013) is shown as a white dashed line, which divides the Kamb Ice Stream and the Ross Ice Shelf. Red arrow shows direction of ice flow. Basins B1–3 are topographic lows in the ice surface, distances are from the upstream start of the Interpolated Channel Maximum to each basin centre.

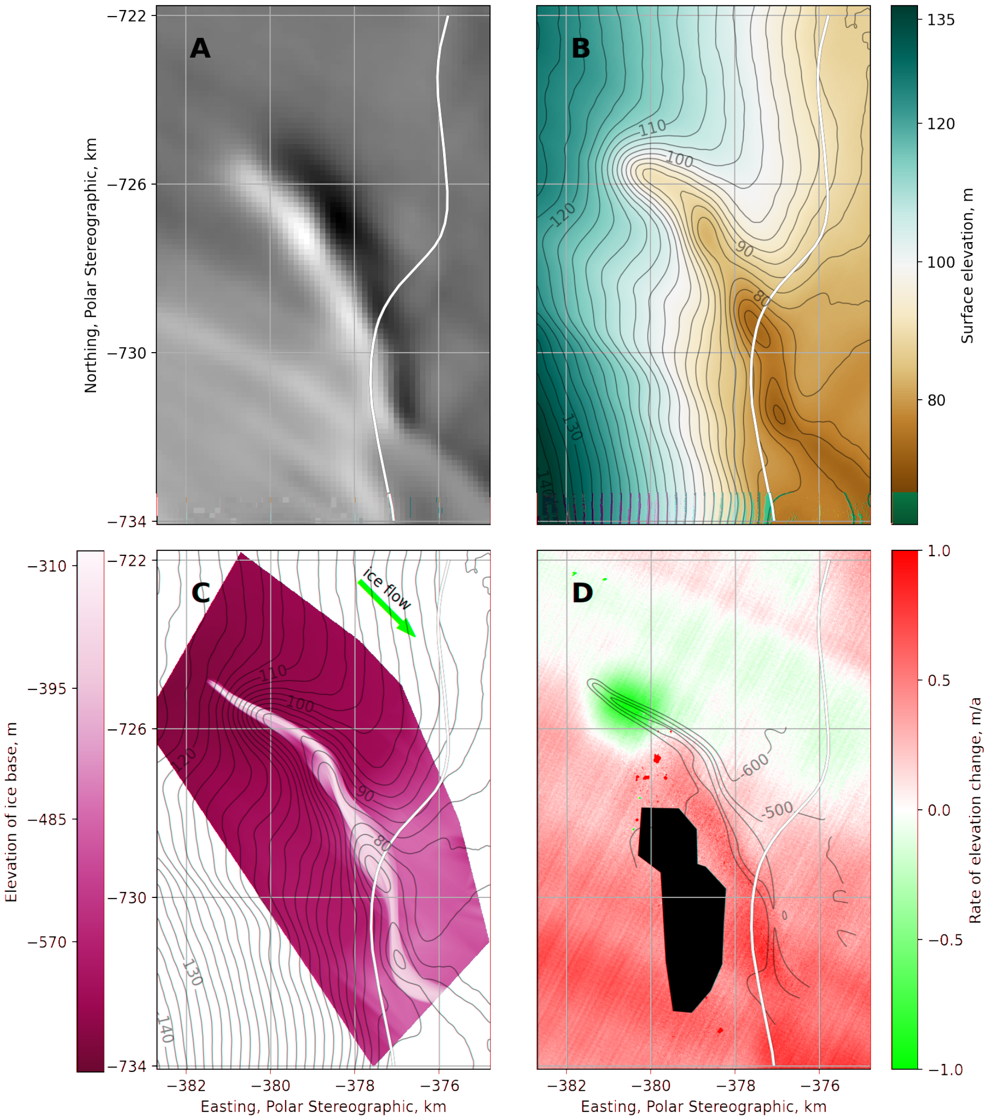

Figure 2.7: A: MODIS MOA optical image of study area (Haran et al., 2014). B: REMA ice elevation, 2 m resolution, (Howat et al., 2019). The white line is the grounding line from Depoorter et al. (2013) C: Estimated ice base elevation interpolated from radar survey, contours of REMA surface elevation. D: Difference between REMA elevation from 2012-12-24 to 2016-11-09, contours show estimated ice base. Red line shows direction of ice flow. Black area is masked out due to clouds.

of 700 m), to a maximum elevation of -325 m (Figure 2.8 A). The 'Surveyed channel apex' then show a reduction in basal channel height of greater than 30 m to an elevation of -330 m at 0.75 km downstream from its inception (Figure 2.8 A). The interpolated

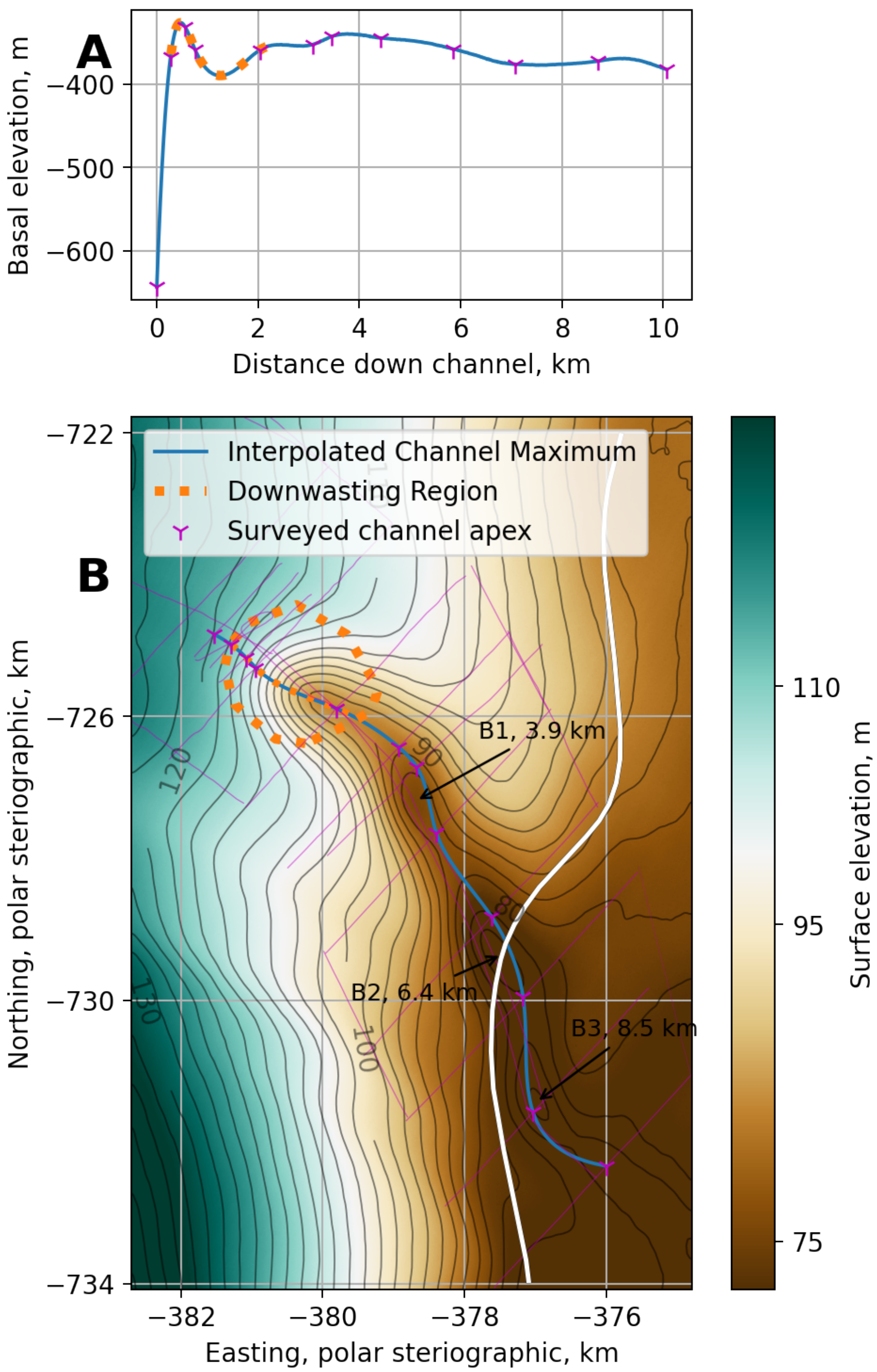

Figure 2.8: A) Estimated ice base elevation along the apex of the channel, calculated by interpolating between the maximum height of each radar line crossing the channel (Surveyed channel apex). B) Estimated channel apex position plotted over REMA surface elevation. Basins B1–3 are topographic lows in the ice surface, distances are from the upstream start of the Interpolated Channel Maximum to each basin centre. The region of surface lowering is delineated by orange dotted region, and coincides with the onset of the surface valley. White line is the grounding line from Depoorter et al. (2013).

channel maximum estimates a local minimum in the downstream channel apex at -390 m elevation, 1.25 km downstream, though this is unsupported by data points. The 'Surveyed channel apex' show that the basal channel apex rises to around -340 m at 3.5 km then lowers to around -380 m at 10 km (Figure 2.8 A) at the edge of the study area. The elevation of the surface valley is at approximately 80 m (Figure 2.8 B).

The basal channel has three bends which correspond to surface basins B1–3 (described in Section 2.4.1.1). The channel is around 200 m wide for almost 1 km from its inception, then widens to 700 m at the first bend (B1) 3.9 km down the channel, narrows to 450 m then widens to 1050 m at the bend (B2) 6.4 km downstream (Figure 2.7). These widths are measured at radar lines and are therefore not a result of interpolation. While there are no radar lines crossing the channel at the third bend (Figure 6.2), the interpolation estimates that the basal channel narrows to 200 m and widens to 600 m at the third bend (B3) 8.5 km downstream (Figure 2.7). While these bends correspond to basins in the surface elevation, they do not correspond discernibly to changes in the ice base elevation.

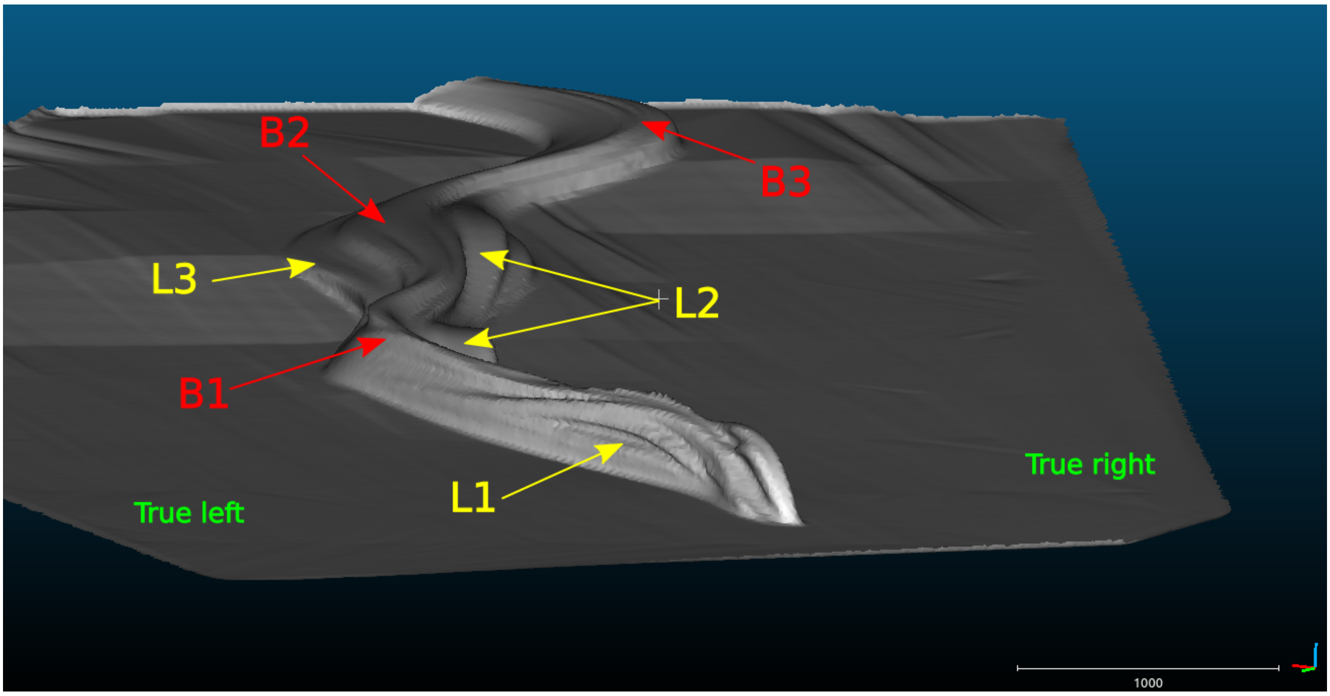

Figure 2.9: Three dimensional view of the ice base map, showing the location of ledges (L1, L2, L3) and bends in the channel (B1, B2, B3). Bends correspond to basins on the subaerial ice surface.

The cross–sectional shape of the basal channel varies along flow. While the basal channel flanks are imaged to be consistently vertical, the channel has distinct ledges along its sides (Figure 2.9). These ledges are separated from the apex of the basal channel by a vertical offset. For around 1 km downstream of the basal channel inception, a ledge is visible on the true left (Figure 2.10, L1), this is separated from the basal channel apex by

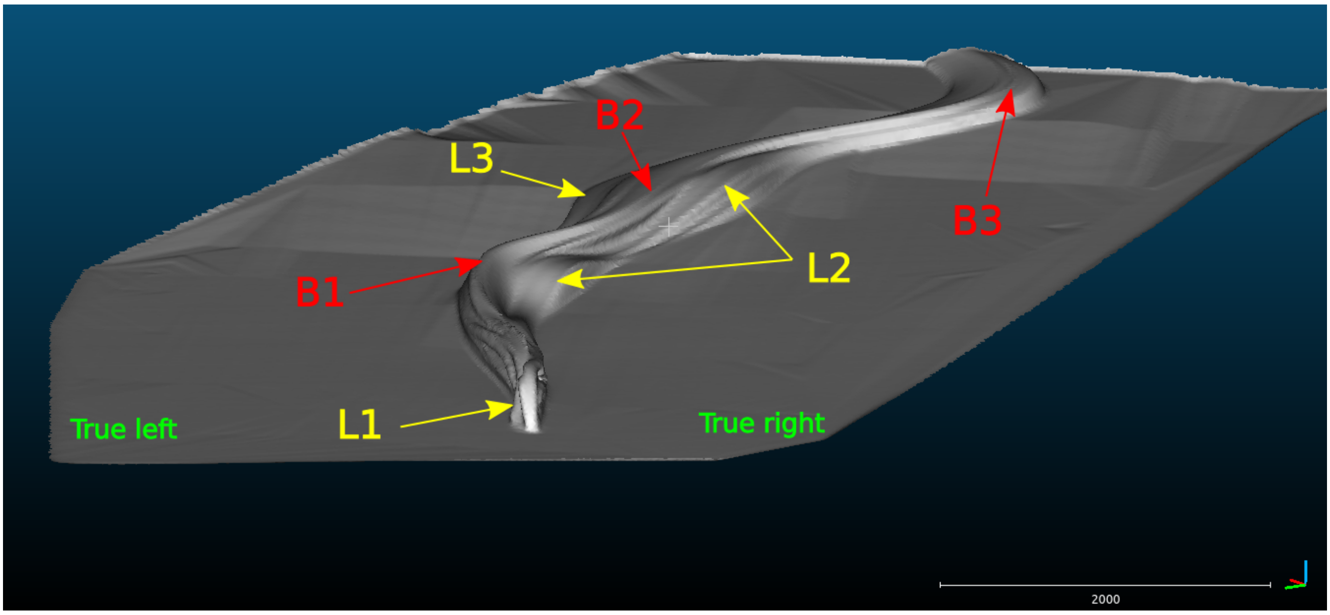

Figure 2.10: Three dimensional view of the ice base map, showing the location of ledges (L1, L2, L3) and bends in the channel (B1, B2, B3). Bends correspond to basins on the subaerial ice surface.

a wall ranging from 200 m at first to 50 m further downstream. A ledge on the true right then appears from around 1 km to 6 km downstream from the channel inception (Figure 2.9, L2). This ledge is widest at the bend (B1) 3.9 km downstream from the channel inception where it is 150 m shallower than the channel apex. A third ledge (Figure 2.9, L3) is visible from 4 to 6.6 km downstream from the channel inception. The last 4 km of the channel has no observable flat ledges and the channel walls appear to have a gentler slope than those upstream.

2.4.1.3 Hydrostatic Equilibrium

The basal channel inception appears approximately 6 km upstream of the grounding line estimated by Depoorter et al. (2013). The vertical offset of the ice column from hydrostatic equilibrium indicates where the ice is freely floating and ranges from -10 to 45 m over the study area (Figure 2.11). A positive vertical offset denotes an ice column which is held above floatation, either by the ground or from internal ice stresses. A vertical offset of zero denotes ice which is floating, and a negative vertical offset denotes an ice column held beneath hydrostatic equilibrium by lateral ice stresses. Upstream of the surface valley, the vertical offset of the ice from equilibrium is positive 20 m, showing that the ice is well grounded. Outside the surface valley, the vertical offset decreases steadily downstream. By 8 km downstream from the channel inception, the ice outside of the surface valley is at hydrostatic equilibrium . The ice column directly over the basal channel has positive vertical offset from floatation, peaking at 45 m above flotation at the upstream end of the basal channel and dropping to 10 m above flotation at the downstream end of basal channel within the study area. Along the length of the channel, the channel apex is offset further above the flotation height than the sides, which are 10-20 m closer to flotation. In areas under the surface valley but not above the sides of the basal channel, the ice column is offset below floatation by up to 10 m. This occurs along the length of the surface valley, and is especially pronounced on the true right. The uncertainty in the vertical offset from equilibrium is 3.5 m, which is propagated from the 2016 REMA surface elevation (Section 2.3.1.1, 2.3.2.3).

2.4.2 Surface elevation change

2.4.2.1 Change in surface topography

Near the inception of the basal channel, a region of modern surface lowering is apparent when differencing REMA elevation strips from 2012-12-24 to 2016-11-09 (Figure 2.7 D). The region of surface lowering is an oval approximately 1.4 km long in the along–channel direction and 1 km wide in the cross-channel direction. This region is centred around the onset of the surface valley (Figure 2.8 B). The first 300 m of the basal channel sits outside of the region of surface lowering (Figure 2.8). Over the full difference image, shown as 'Stable area' in Figures 2.13 and 2.15, the mean is 0.3 m/yr (surface raising) and the standard deviation is 0.2 m/yr, which we use as an estimation of uncertainty in the area.

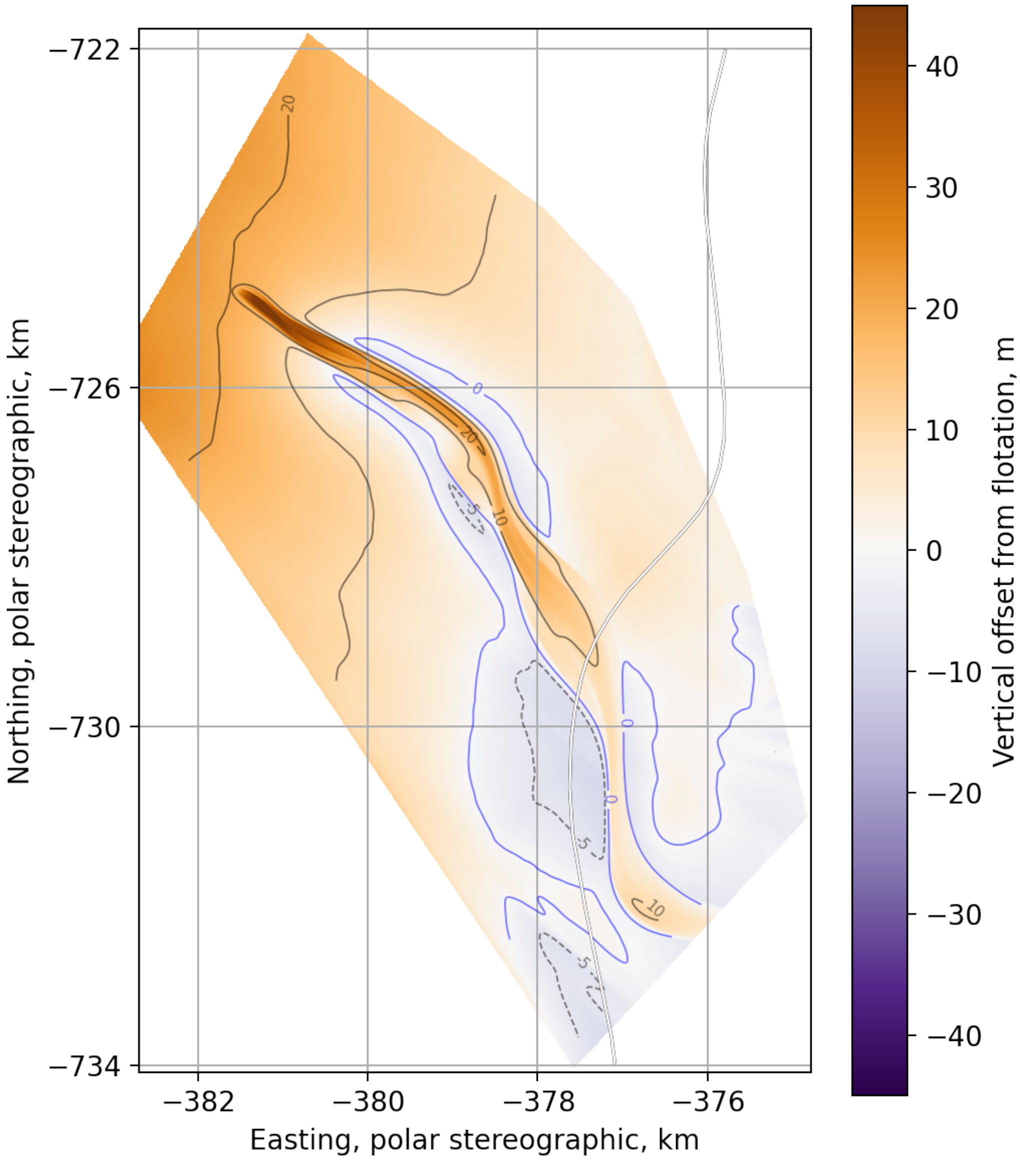

Figure 2.11: Vertical offset from hydrostatic equilibrium. Blue line indicates the zero contour, where ice is estimated to be floating. Positive values indicate ice is held above floatation either by the ground, or by bridging stresses with surrounding ice. Negative values indicate ice is held below floatation by lateral stresses with surrounding ice. White line is the grounding line from Depoorter et al. (2013).

The region of surface lowering is centred approximately 1 km downstream from the onset of the basal channel (Figure 2.7 C, D). This region has a maximum of -1.0 ± 0.2 m/yr at its centre, and has a mean elevation change of -0.4 ± 0.2 m/yr (Figure 2.7 D).

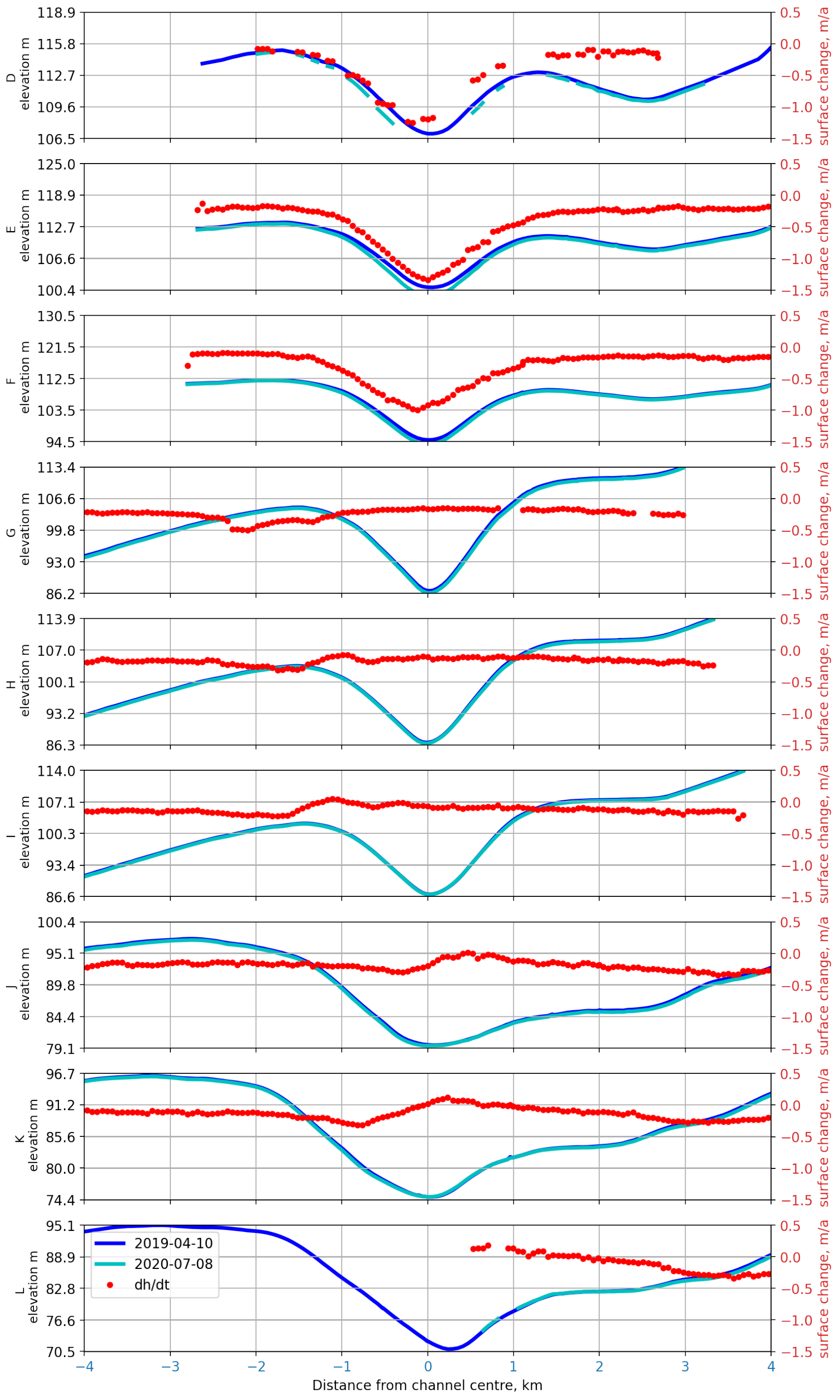

Figure 2.12: ICESat–2 along track elevations and differences for nine tracks which cross the surface valley in 2019 and 2020. Locations of the lines are shown in Figure 2.3 and S4. Lines D to L are in order from upstream to downstream. Lines are shown looking downstream, positive distance from channel centre corresponds to true right.

Differences from ICESat–2 point elevations from 9 May 2019 to 5 August 2020 find the same pattern, showing surface lowering up to -1.25 ± 0.02 m/yr on three upstream lines that cross the circular region (Figure 2.12 D, E, F). One kilometre downstream from this region, ICESat–2 point elevations show more complex changes in surface elevation

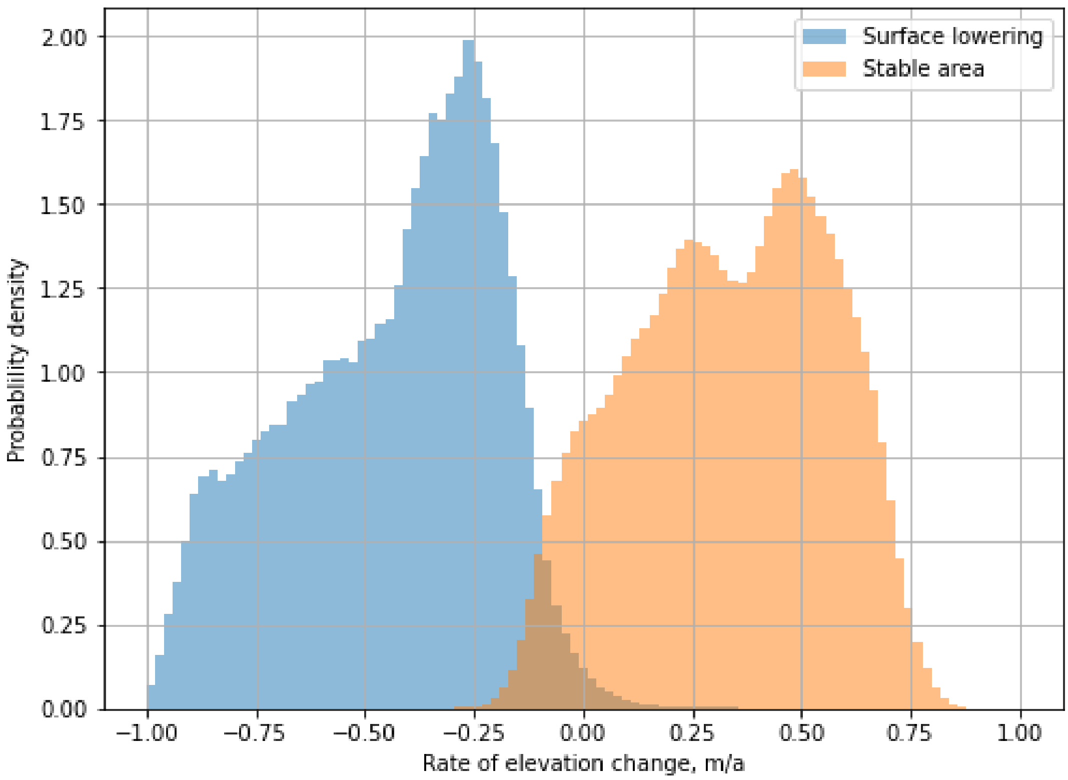

Figure 2.13: Histogram showing the distribution of the REMA rate of surface elevation change in two areas. The distribution of background elevation change distribution is shown in blue ('Stable area' outlined in Figure 2.15), and the region 'Surface lowering' (outlined in Figure 2.15) is shown in peach.

(Figure 2.12 G, H, I). While the background ice stream's surface is lowering at around -0.2 ± 0.02 m/yr, the surface valley's sides are lowering more quickly, with the true right side lowering up to -0.4 ± 0.02 m/yr more than the background ice stream (Figure 2.12 G, H, I). This suggests that the channel is widening, but not deepening in this area. Further downstream, the REMA strip difference shows up to 0.5 ± 0.2 m/yr increase in surface elevation along the true right side of the valley shown in Figure 2.7 D between (-379.5,-727) and (-377.5,-730). While this signal does not dominate uncertainty, the more accurate ICESat–2 differences confirm these elevation changes. At the downstream end of this area (coincident with the basin B2 labeled in Figure 2.8), the later ICESat–2 differences from 2019–2020 (Figure 2.12 J, K, L) show up to 0.1 ± 0.02 m/yr of increase in surface elevation on the true right of the valley and -0.3 ± 0.02 m/yr of lowering on the true left, suggesting that the valley is migrating to the true left. Background surface lowering on ICESat–2 lines J, K and L is between -0.1 ± 0.02 m/yr and -0.2 ± 0.02 m/yr (Figure 2.12 J, K, L). This location is coincident with the location of ledge L2 (Figures S8, S9) discussed in Section 2.4.1.2.

2.4.2.2 Change in ice base topography

While caution should be taken when interpreting accretion rate estimates from repeat ApRES observations, our observations indicate apparent accretion is occurring within the downstream portion of the basal channel (Figure 2.14). On the cross channel profile (see Figure 2.3 for the location), all but one of the ApRES survey sites outside the channel indicate basal melt. In the channel, all sites indicate apparent accretion. Apparent accretion peaks on the true right of the channel, coincident with a ledge (Figure 2.9 L2) and surface raising detected by REMA strip differencing (Figure 2.7 D, Section 2.4.1.2 and 2.4.2.1). ICESat–2 data also show surface raising on the channel right in a similar area (Figure 2.12). Vertical strain rates derived from ApRES observations map roughly to melt rates (Figure 2.14). Strain is most negative where accretion is strongest, and low melt rates map to sites with low strain. Two sites at the channel apex are an exception, where both accretion is strong and strain is close to zero.

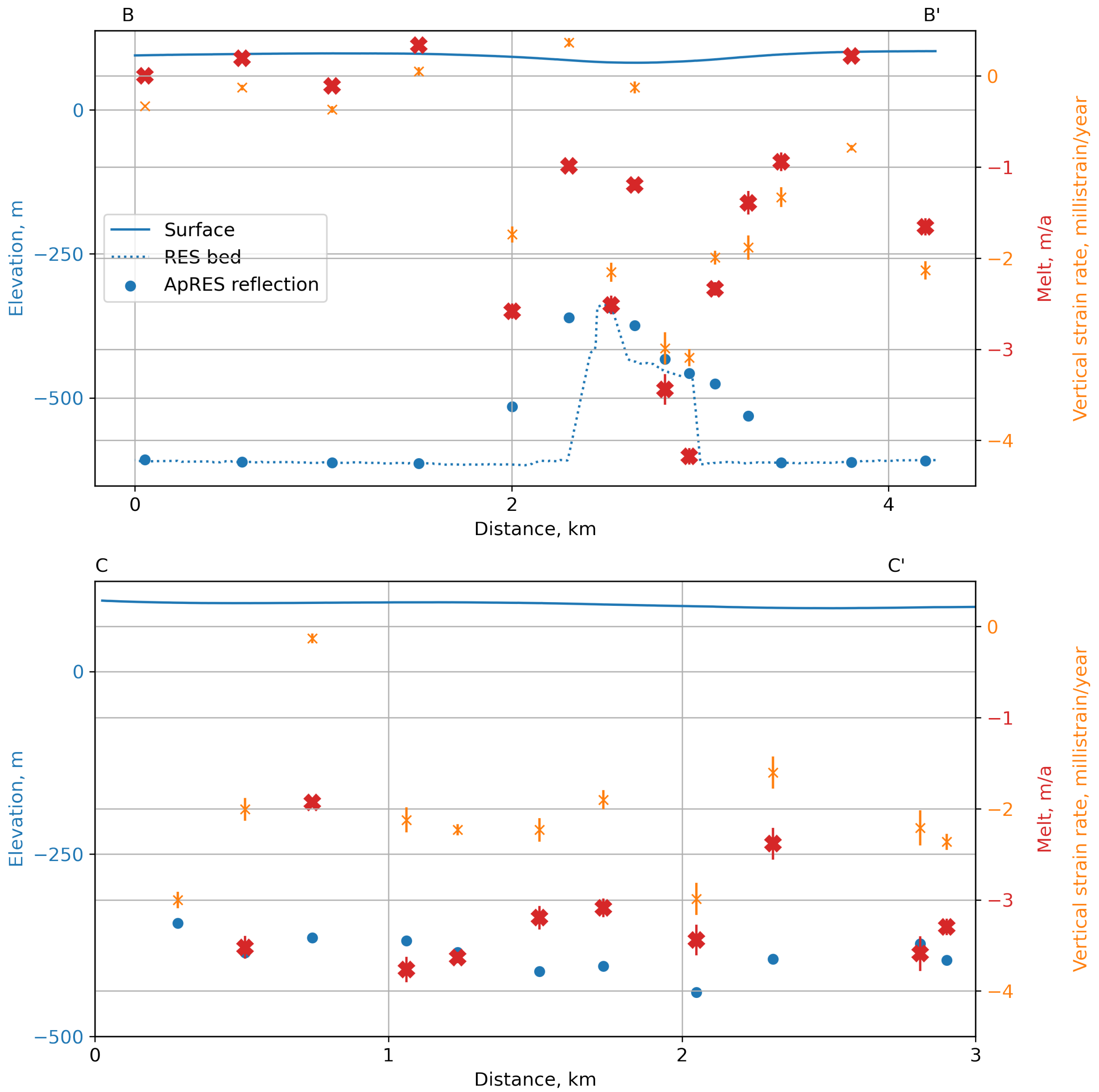

Figure 2.14: ApRES basal mass balance on two profiles the channel shown in (Figure 2.3). 'B' crosses the channel at right angles, 'C' follows the surface valley low. ApRES repeat surveys are from 07/12/2019 to 22/12/2020. Negative melt denotes accretion.

2.5 Discussion

Our observations confirm that the surface valley described in Section 2.4.1 is the expression of a basal channel as concluded by Kim et al. (2016) and Alley et al. (2016) (Figure 2.7C). As the channel's location corresponds to predictions of concentrated subglacial flow (Figure 2.1), it is most likely that the channel has been incised by a subglacially sourced meltwater plume. Under Kamb Ice Stream, subglacial meltwater has been modelled as concentrating in a single hydropotential low before flowing to the sea (Carter and Fricker, 2012; Le Brocq et al., 2013). When this freshwater meets the salty ocean it likely forms a buoyant plume which entrains warmer ocean water (as described by Sergienko

(2013)), and incises the channel into the underside of the Ross Ice Shelf (Figure 2.7). Plume driven melt incises the channel both higher into the ice and upstream following the subglacial drainage route. As the channel grows, the grounding line is shifted locally upstream, and salty bottom water flows upstream to replace fresh plume driven outflow in the top of the water column. The resulting shape and circulation is likely comparable to an esturine river mouth, whereby the sea and fresh water meet in a channel which forms a local deviation from the coast line. In addition to a classic estuary, a melt water plume at the inception of the channel directly couples fresh and salty layers by entraining the upstream flow of salty bottom water and expelling buoyant fresh water.

We interpret the surface lowering (Figure 2.7 D) as caused by submarine melt and subsequent adjustment of the ice towards hydrostatic equilibrium. The region is approximately 2 km^2 and the surface is lowering by up to approximately 1 m/yr. The along–channel orientation of the oval of surface lowering suggests melting is occuring over an elongated region of the channel, though the shape does not directly reflect the shape on the ice base. We attribute the general mismatch of surface and basal topography to bridging stresses in the ice.

2.5.0.1 Bridging

Ice bridging is indicated in Figure 2.7 C, as the basal shape is not mirrored directly at the surface. Surface changes shown in Figure 2.7 D suggest that melt induced changes to the basal shape are also not mirrored directly at the surface, indicating bridging. The rigidity of ice distributes bridging stresses, whereby the weight of ice is partially supported laterally by the surrounding ice and ground. This smooths the surface response to basal changes at a length scale which masks small features. This is shown in Figure 2.11, where in places the surface is above flotation on the channel and close to or below flotation to either side of the channel. Over larger regions ($\approx$ 1x1 km) the ice is adjusting to hydrostatic equilibrium, while over smaller length scales ($\approx$ 100x100 m) the ice is not at flotation. This is well supported by ice dynamics theory, which predicts that the length scale of surface expressions of the basal channel will be no smaller than the ice thickness (shown in Figure 2.7, $\approx$ 700 m at the field site) (e.g. Gudmundsson and Raymond, 2008). Significant bridging has been noted around other ice shelf channels, and used to explain discrepancies between basal and surface topography (e.g. Dutrieux et al., 2013; Chartrand and Howat, 2020; Vaughan et al., 2012). These explanations are supported by ice dynamics modelling by Drews (2015), who found that narrow channels show significant bridging, even at equilibrium.

While further stress modelling would be required to understand in more detail where bridging stresses affect the surface expressions of the basal channel, our observations begin to explain how surface lowering is influenced by bridging. One conclusion is that more basal melt has occurred than that which is manifest in surface lowering. In our study area, ice is furthest from hydrostatic equilibrium at the inception of the channel (Figure 2.11), which is upstream from the surface valley (Figure 2.7C). We expect basal melt to occur at the start of a positive basal gradient of ice, as theoretical models (e.g. Jenkins, 2011) of sub–ice–shelf plumes assume these plumes are generated by buoyancy (Jenkins, 1991). These models predict that positive slopes at the ice base, like that at the head of the channel, will generate melting. However, the region of surface lowering does not overlap the inception of the channel but starts 300 m downstream from the initial channel ramp (Figure 2.8). We attribute this discrepancy to ice bridging and suggest that melt is occurring at the inception of the basal channel but is not expressed at the surface. Significant bridging is expected at the inception as it is just 200 m wide (shown in Figure 2.7, similar to the channel modelled by Drews (2015) and Wearing et al. (2021)). As the channel inception grows wider over time, basal melt will likely be manifest at the surface as surface lowering. The 1000 m wide region of surface lowering (Figure 2.7D) is much wider than the 200 to 400 m wide basal channel below, reflecting the fact that sharp changes to the base will be smoothed at the surface due to bridging stresses which provide lateral support. While the area of the surface lowering may be larger than the area of basal melt, the volume of ice lowered on the surface is expected to be smaller than the basal volume melted due to lateral support in the ice. ApRES surveying shows basal accretion at the edge of the large area of surface lowering (Figures 2.3, 2.7, 2.14). This likely shows that while basal melting and accretion are occurring within close proximity, the melt signal is overwhelmingly larger, and so is smoothed by bridging and masks the accretion signal at the surface.

2.5.0.2 Quantifying basal melt

Despite the distorted representation of basal changes on the surface topography, we know that basal topography will be underrepresented at the surface but not over represented. It follows that we can estimate a minimum melt rate from REMA differences (Sec. 2.4.2.1). REMA and ICESAT–2 differences show surface downwasting of up to 1 and 1.25 m/yr respectively. In the same location Kim et al. (2016) used Landsat imagery to calculate 1.2 m/yr of surface lowering. Integrating over the circular area of surface lowering shown in red in Figure 2.7 C, the ice volume lost is found to be 1,270,000 m^3/yr. Calculating the submarine volume lost (assuming the lowering is from hydrostatic adjustment to equilibrium) and restricting the melted volume to the area of the channel, basal melt rates are estimated as approximately 20 m/yr. Due to uncertainties described below, this estimation is a lower bound on melt rates in the channel. In comparison, Marsh et al. (2016) and Stanton et al. (2013) used ApRES to measure melt rates of 22.2 $\pm$ 0.2 m/yr and 14.2 to 24.5 m/yr in channels on the ice shelves of the Whillans Ice Stream and Pine Island Glacier respectively. Figure 2.11 shows the region of surface lowering (delineated in Figure 2.8 B) is not at hydrostatic equilibrium but is likely close to it, shown by the fact ice < 1 km downstream, on either side of the channel (at -380,-726) is floating. The along-flow strain rate in the area is $< 2 \times 10^{-6}$/yr (Alley et al., 2018), too small to produce such large surface changes. Our initial estimate likely underestimates melt. Firstly, our estimate neglects surface mass balance which is likely positive in the surface valley, due to the fact hollows tend to be filled in by wind driven snow (e.g. Gow and Rowland, 1965). Secondly, due to bridging stresses, the basal melt is understated at the surface (Drews, 2015). If ice is not at hydrostatic equilibrium at the channel ceiling, it is held away from hydrostatic equilibrium. Any melt in the channel will be expressed at the surface less than or equal to if it were at hydrostatic equilibrium, but not more. Thirdly, in calculating a 1D melt rate from a melt volume we assume melt spans the channel area. However, melt is likely restricted to a smaller area due to the Coriolis force which will cause the melt plume to trend to the true left wall (more detail in Section 2.5.1.3). A smaller melt area would correspond to a higher 1D melt rate for the same melt volume. Lastly, if the channel was filled with rock or till, the assumption that the channel roof was supported by bridging or floating may be wrong, and melt rate could be overestimated. However, due to the location of the channel in a drainage outlet, the large magnitude of surface lowering, and the fact that the region of lowering ice is close to flotation (Figure 2.11), it is unlikely that the channel is not water filled. It follows that basal melt is most likely understated here.

REMA strips state a vertical accuracy of 4 m and 3.5 m for 2012 and 2016 strips respectively (Noh and Howat, 2015; Howat et al., 2019). Because the study area is relatively stable due to low surface velocity (Rignot et al., 2017), both strips are expected to be more accurate than the large stated accuracy. This also applies to the uncertainty of the vertical offset from hydrostatic equilibrium (Section 2.4.1.3), which is calculated from the 2016 REMA strip. While 4 m is large relative to the ≈ 5 m range we observe to calculate the rate of surface lowering, it is unlikely we have overstated surface lowering in the accuracy due to the following. Firstly, ICESat–2, with a mean accuracy of 1.12 cm shows a near identical region of lowering, with a similar magnitude (Figure S4). While the lowering shown in ICESat–2 spans a different time period, its similarities suggest that the process observed is ongoing. Secondly, the observed lowering is the opposite sign from the general trends and error in the data. The mean of the difference between REMA strips is positive (surface raising) over grounded ice outside the negative region of surface lowering (Figure 2.13). Over the full difference image, the mean is 0.3 m/yr (surface raising) and the standard deviation is 0.2 m/yr, which we used to estimate uncertainty. In the region of lowering the mean surface change is -0.4 $\pm$ 0.2 m/yr. The mean lowering is therefore out of the range of the uncertainty. Thirdly, artifacts in the REMA difference show patterned bands which are clearly different to the observed surface lowering (Figure

2.15). The region of surface lowering is centred between bands, where background surface change is negative.

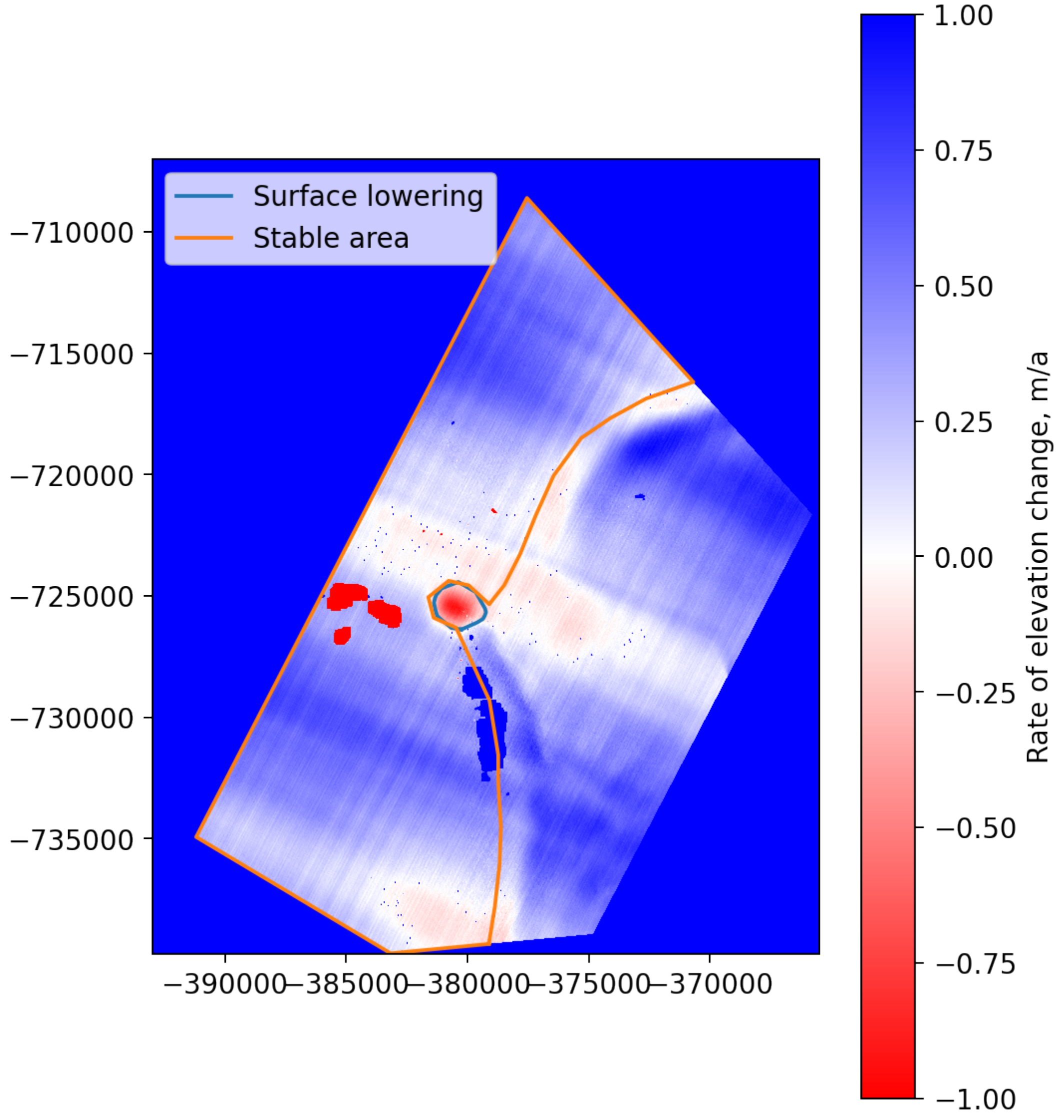

Figure 2.15: Broader view of the difference between REMA elevations from 2012-12-24 to 2016-11-09 (Noh and Howat, 2015; Howat et al., 2019) as in Figure 2.7. Dark blue spots to the true–right of the channel, and red spots upstream of the area 'Surface lowering' are artefacts.

2.5.1 Mechanisms

2.5.1.1 Stepped grounding line retreat

With ice velocity less than 5 m/yr at the channel head (Rignot et al., 2017), there is no clear mechanism to explain why the basal channel is a (10km) long feature. We suggest that the melt plume has migrated upstream, leading to the present linear channel shape. In Section 2.5.0.2 we estimated modern melt rates to be over 20 m/yr vertically. At this rate, the basal channel would take less than 18 years to melt vertically through 350 m of ice to its current height. The fact that melt is ongoing suggests that the channel exhibits large changes in melt rates, and/or channel melt migrates over time. Landsat imagery shows the surface valley migrates upstream (Figure 2.6), and REMA differences reveal modern melt is likely at the head of the channel (Figure 2.7 D). Since 1985, the surface valley has grown upstream by 1.5 km towards the location of modern surface lowering (Figure 2.6, 2020). Similarly, Chartrand and Howat (2020) observed a sub–ice–shelf basal channel migrating upstream towards a grounding line at ≈ 1 km/yr. Surface elevation shows three distinct basins in the surface valley (B1, B2, B3, Figure 2.8). These basins are clear in the oldest satellite imagery of the valley (Figure 2.6, 1985). We interpret the surface basins to be historic plume locations and suggest that the modern grounding line and meltwater plume location is situated just upstream of the surface lowering shown in Figure 2.7 D.

We suggest that the basin features are formed by varying melt from either or a combination of the two processes proposed by Horgan et al. (2017) to describe disjointed channel features in the area. Either melt rates vary in time or the region's grounding line has undergone stepwise retreat. Large changes in melt rates could result from changes in flux in the subglacially sourced meltwater plume. Changes in plume flux could be caused by episodic subglacial drainage events upstream, originating from the flooding of upstream active subglacial lakes as described by Kim et al. (2016), or in changes in flux caused by the rapid rerouting of the subglacial network as described by Carter and Fricker (2012). Maximums in subglacial outflow would cause a strengthening of the subglacial plume, allowing melt to occur higher in the water column. Wider parts of the channel likely form between melt peaks, when a weaker plume melts the channel walls. While changes in ocean conditions could similarly cause fluctuations in melt rates due to the dependance of melt on the amount of heat and salt entrained from the ocean (Jenkins, 1991), conditions in the ice shelf cavity interior are expected to be stable (Stevens et al., 2020). Alternatively, the region's grounding line could be retreating episodically. At each step, the steep plume would melt a hollow, manifest in a basin shape on the ice surface. Stepwise retreat can occur when the grounding line jumps between stable positions usually determined by local bed topography (Haseloff and Sergienko, 2018), and is commonly observed (e.g. Jakobsson et al., 2012).

The channel bends and corresponding changes in channel width could be interpreted as channel meandering, similar to that of a supraglacial river (e.g. Ferguson, 1973). At wider parts of the channel, the ice shelf has less buoyancy and so would locally sink, and would likely manifest as the basins at the surface seen in Figure 2.7. However, we do not think meandering is a robust explanation for the channel shape, as it is unlikely the plume melts down the length of the channel in a manner similar to a supraglacial river. Firstly, the channel walls widen both left and right at bends rather than just on the outside of a bend like a supraglacial river (Ferguson, 1973). Secondly, plume theory predicts that downstream from the initial positive gradient of the channel, the plume will not melt basal ice. Past this point, the plume will either cause accretion, as observed in ApRES observations (Figure 2.14), or detach from the ice. It is possible that downstream from the positive gradient in ice basal slope at the head of the channel, subsequent plumes are generated from ice slopes on the walls or from downstream positive gradients in the channel depicted in Figure 2.8.

The moniliform shape of the surface valley is similar to the shape of a feature observed by Berger et al. (2017) (Figure 7) at the Roi Baudouin Ice Shelf, Antarctica. Radar imagery shows this is the surface expression of englacial lakes found 30 m below the surface. While the basins we see are not formed by englacial lakes, it is interesting to note that this shape of connected basins in ice shelf topography appears to be stable.

Horgan et al. (2017) propose that the grounding line retreated to its current location after the stagnation of the Kamb Ice Stream. The basal channel likely formed after this shift in the grounding line. Due to its location in a hydropotential low (Le Brocq et al., 2009), the basal channel may have existed under grounded ice before Kamb Ice Stream's stagnation. As the grounding line retreated to its current location, feedbacks with the ocean likely allowed it to grow to its current size. Once ice advection stopped, even if melt rates were low, the plume would be concentrated in one location allowing it to incise a deep channel. With no upstream migration of the channel, the observed 10 km long surveyed section of the basal channel would take approximately 2000 years to form with present ice velocity (≈ 5 m/yr). The channel continues downstream from the study area shown in Figure 2.7 C, though surface imagery shown in Figure 2.2 suggests that the basal channel is less pronounced. It is possible that a strengthening of the meltwater plume is related to a proposed reorganisation of the subglacial drainage (e.g. Anandakrishnan and Alley, 1997), which may be associated with the ice stream shut down around 150 years ago. For example, if the subglacial hydrology of the Kamb ice stream became more channelised as proposed by Lelandais et al. (2018), subglacial flux at this location would increase. More buoyant subglacial water would be discharged at the grounding line, which would strengthen the sub–ice–shelf plume.

2.5.1.2 Steep initial channel slope

The initial gradient of the ice base at the inception of the channel in the downstream direction is constrained between $45° - 90°$ by radar echo sounding observations (Figure 2.8). This implies that the plume was flowing upwards at a steep or vertical angle when it incised the head of the channel. We suggest that the channel grows through a positive feedback between basal steepness and melt as described by Sergienko (2013) and Gladish et al. (2012). Through this feedback, steep basal slopes cause the plume flow to accelerate, which causes more melt, making preexisting slopes even steeper. In other observed ice shelf channels (e.g. Drews et al., 2017; Jeofry et al., 2018), the height of incision is moderated by ice advection which restricts the amount of time any region on the ice shelf base experiences melt. In our study location, ice velocity is less than 5 m/yr at the channel head (Rignot et al., 2017). Any notch melted into the ice shelf is not advected downstream but grows deeper over time, resulting in a steep gradient at the channel inception. Unless the plume changes, the feedback between slope and melting can continue until the channel is vertical at its inception (Sergienko, 2013; Gladish et al., 2012). The roof of the basal channel follows roughly the same elevation of around -380 m (Figure 2.8). This may represent a natural limit to which the freshwater plume will rise given the ocean density structure. A natural bound on the thickness of the channel should correspond to the height at which the plume reaches the density of the surrounding ice shelf cavity. Here, melt–water plumes are expected to stop rising and detach from the ice, flowing horizontally into the sea (Jenkins, 2011; Hewitt, 2020).

2.5.1.3 Channel migration

Both REMA (Figure 2.7 D) and ICESat–2 data (Figure 2.12 G–L), shows less negative surface lowering (relative raising) just to the true right of the surface expression apex, and more negative surface lowering (relative lowering) on the true left of the surface apex. The relative rising surface is likely related to the accretion shown at the base of the channel by our ApRES observations (Figure 2.14), which indicate more accretion is occurring on the true right of the channel. This is coincident with a ledge (L2, Figures S8) described in Section 2.4.1.2 . The Coriolis force likely causes the melt plume to follow the true left wall. This may be accompanied by accretion on the true right side, resulting in the leftward migration of the channel. While it is not commonly observed that channels migrate to the left, Gourmelen et al. (2017) and Alley et al. (2016) found steeper walls on the true left of channel profiles and attributed the asymmetry to enhanced melt due to the Coriolis force. Similarly, Chartrand and Howat (2020) observed the leftward migration of a channel at $\approx$ 80 m/yr. Our basal channel profiles show asymmetry in that the channel has large ledges on the right hand side for roughly half of the distance down the channel (Figure 2.9). Ledges (terraces) were also found on an ice shelf channel by Dutrieux et al. (2014). Drews et al. (2020) also observed a pattern of surface lowering and raising across an ice shelf channel, and interpreted this pattern to be caused by wind eroding snow from windward slopes and depositing it on the leeward side of slopes.

Relative to the ApRES data, REMA and ICESat–2 observations of a rising surface span a different time period and location respectively. However, both REMA and ICESat–2 show a consistent trend of a rising surface on the channel right (Figure 2.7 D, and Figure 2.12 G–L). ApRES accretion and the surface rising shown in REMA/ICESat–2 occur downstream from the region of surface lowering we attribute to melt (Figure 2.7D). This agrees with plume theory, which predicts that as a plume loses energy it causes accretion, downstream from where melt is occurring Jenkins (1991). Estimating the location of accretion with the 1D model of Jenkins (2011) is not done here as the oceanographic variables (e.g. ambient stratification in the ocean cavity) are unknown to us, and result in large changes in the length scale over which accretion occurs.

2.6 Conclusion

We have presented a series of observations describing a sub–ice–shelf channel at the grounding line of Kamb Ice Stream, combining remote sensing and field-based geophysical surveying. These observations reveal a channel that is actively melting at its upstream inception and has been growing upstream past the grounding line since at least 1989. The inferred melt is likely driven by a buoyant plume, initiated by freshwater from Kamb Ice Stream's largest subglacial drainage outlet. The channel is asymmetric and tortuous, unlike most observed sub–ice–shelf channels which tend to be linear and symmetric. While most sub–ice–shelf channels are formed as downstream streak lines in advecting ice, the channel we present is situated in stagnant ice, and appears to have developed its elongated shape due to a shift in the melt location. Over–snow radar surveying shows that the channel widens 50%–100% at each bend. The bends correspond to a moniliform series of basins on the surface which we relate to past locations of concentrated melt. We interpret the bends and basins as evidence that the upstream migration of the melt location at the head of the channel is irregular, stepping upstream over time. This irregularity likely stems from episodic subglacial drainage and/or instabilities in grounding line locations associated with bed topography. Radar surveying also reveals that the channel inception extends upstream of its surface expression. Ice above this narrow (250 m wide) part of the channel is not floating but is supported by bridging to the flanks of the channel. Modern melt is manifest as surface lowering. By quantifying this surface lowering, we estimate melt to be at least 20 m/yr. In agreement with channel theory, melt occurs near the upstream inception of the channel, and ice is accreted onto the channel roof downstream. This accretion is verified with ApRES observations and appears to be contributing to the growth of a ledge in the channel. The differences between the surface expression and basal features of this channel are noteworthy for studies of sub–ice–shelf channels using surface observations alone. To predict the stability of ice shelves, it may be important to model sub–ice–shelf channels. Our observations can be used as a case study to further constrain theories of channel formation and growth. As the channel shape is not distorted by advection, it serves as a natural experiment for understanding plume driven melt. The results presented show that melt can form an ice shelf channel in the absence of advection through the inland migration of a focused melt source. Migration has continued upstream from the local grounding line, similar to an esturine river mouth. The focused melt source appears to continue to deepen and steepen the channel at its inception. Future research on this channel could build on the work of this paper by better constraining melt rates and ocean plume properties, which in turn could be used to better understand subglacial outlet flow. This was the objective of a direct access drilling campaign carried out in the austral summer of 2021/2022.

Chapter 3

Phase sensitive radar reveals marine ice at basal channel

3.1 Introduction

3.1.1 Justification

Ice shelves are a control on Antarctica's mass balance, providing resisting stresses which slow ice discharge at the outlets of glaciers and ice streams (De Angelis and Skvarca, 2003; Gudmundsson, 2003; Dupont and Alley, 2005). Melt at the base of ice shelves accounts for roughly half of ice shelf mass loss in Antarctica (Rignot et al., 2013). To constrain and improve the accuracy of forecasts of the mass balance and buttressing ability of ice shelves it is necessary to quantify modern basal melt (e.g. Fürst et al., 2016).

At a large scale, basal ice shelf melt is driven by the circulation of water from the open ocean. This circulation is described in detail by Jacobs et al. (1992) and summarised here. The freezing of sea ice on the open ocean forms dense high salinity water which flows along the bottom of the ice shelf cavity to the grounding line. When this relatively warm, salty layer contacts grounded ice, it melts the ice base and forms melt–water plumes. The fresh plumes, driven by buoyancy, flow seaward along the upward sloping ice shelf base at the ice–ocean interface. As the buoyant plumes continue to rise they decrease in pressure, becoming super cooled, and partially freezing to the ice base (Lewis and Perkin, 1986). Due to this circulation pattern, melting is greatest at the perimeter of an ice shelf: at the ice front where ice is in close contact with the open ocean (e.g. Goldberg et al., 2019), and the grounding line (e.g. Mankoff et al., 2012), where deeper ice is in contact with warm salty water which sits at the bottom of ice shelf cavity. In the centre of an ice shelf, the ice–ocean interface is generally at equilibrium or shows accretion (e.g. Rignot et al., 2013). This pattern is clear in the basal mass balance recorded by a traverse of the Ross Ice Shelf by Snodgrass (2021) shown in Figure 3.1.

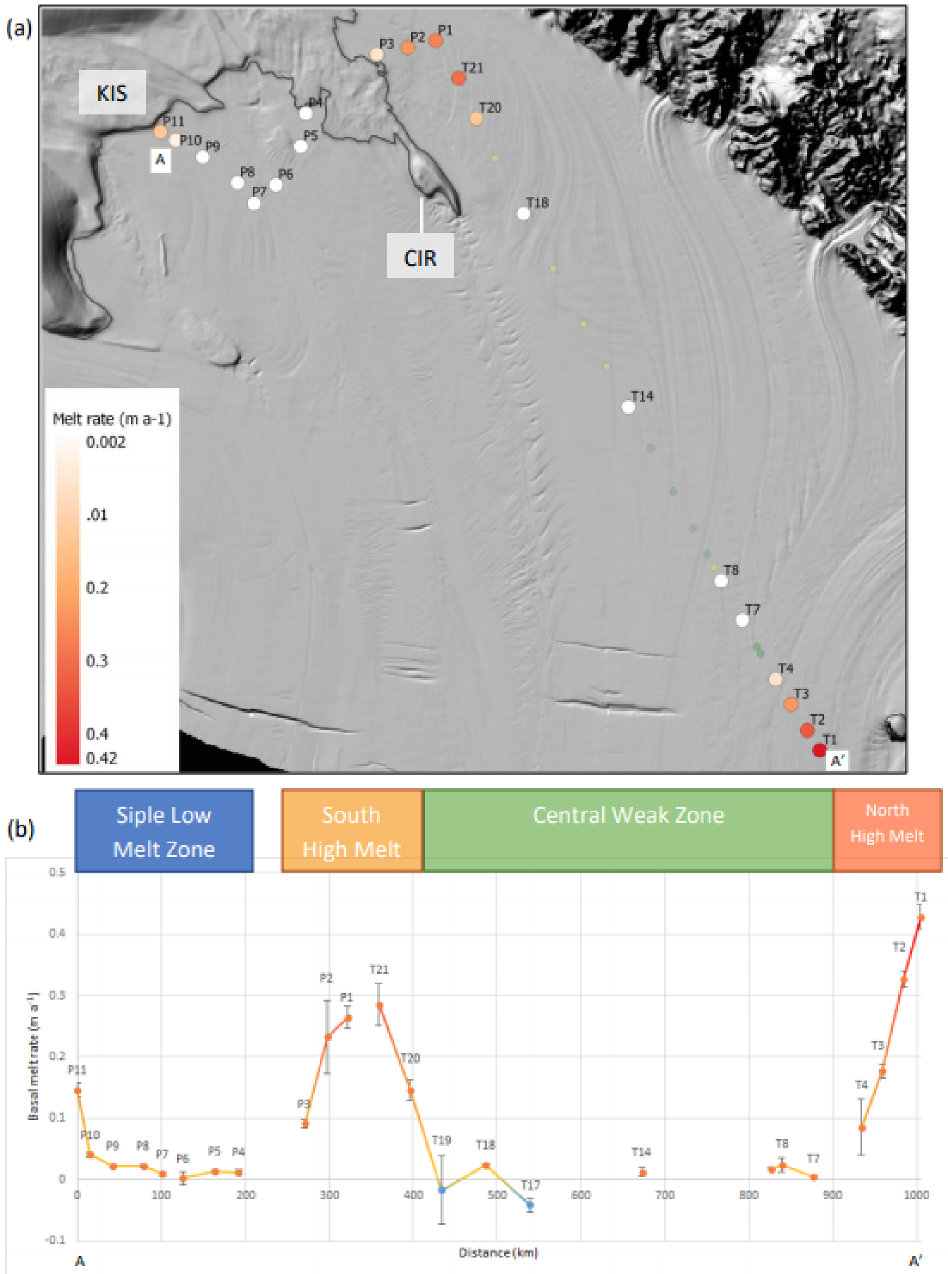

Figure 3.1: From Snodgrass (2021). Basal basal mass balance across the Ross Ice Shelf in (a) map view (b) and by distance along the transect. Error bars indicate ApRES error. Yellow and green markers on the map view indicate site locations where melting could not be quantified.

3.1.2 Observations of ice shelf melt

While these theories of ocean circulation beneath ice shelves are broadly supported by direct observations, such generalisations neglect small scale variations in basal mass balance which are commonly observed, both temporally (e.g. Stewart, 2018) and spatially (e.g. Marsh et al., 2016).

Temporal changes in basal melt can be observed directly using acoustic altimeters (e.g.

Stewart, 2018). Basal accretion is often observed directly, though can be challenging to quantify (Vaňková et al., 2020). In supercooled water oceanographic instruments interfere with accretion, and accretion of ice to sensors disrupts measurements (Robinson et al., 2020). In the centre of the Ross Ice Shelf, Stevens et al. (2020) observed a 10 cm layer of ice crystals during melt conditions, which they interpreted as displaying the ablation phase of intermittent melt and accretion. Similarly, Craven et al. (2014) interpreted the floating and sinking of moored instruments as intermittent accretion and melting.

Alternatively, the surface–based Autonomous Phase-sensitive Radio-Echo Sounder (ApRES) instrument surveys precise measurements of melt rates on ice shelves by comparing small changes in the phase of radar waves reflected off the ice base between repeat radar surveys. Relative to drilling a hole through the ice shelf to access the basal interface directly, ApRES surveys are inexpensive in resources and time. ApRES can be used to better understand processes in ice (e.g. Case and Kingslake, 2022) and at the ice base (e.g. Sun et al., 2019). However, inference of basal processes with ApRES is an estimation which relies on assumptions about the properties of the ice and ocean outlined in Section 3.2 (Brennan et al., 2014). The ApRES was primarily designed for observing negative basal mass balance (melt). Most ApRES surveys observe basal melt, (e.g. Lindbäck et al., 2019; Davis et al., 2018), however, the ApRES has been used to observe accretion (e.g. Stewart, 2018), and new techniques are being developed to improve the interpretation of accretion (Vaňková et al., 2020, 2021b).

ApRES time series of basal melt under ice shelves can reveal connections between certain ocean forcings and the ice–ocean interface. While melt time series close to the front of ice shelves generally show seasonality and relationships with ocean conditions (e.g. Lindbäck et al., 2019), time series from further inland are often difficult to interpret and show little connection to our understanding of ocean circulation (e.g. Davis et al., 2018). Lindbäck et al. (2019) present two ApRES time series of basal melt from the Nivlisen Ice Shelf. The first, 4 km from the ice front, shows seasonality while the second, 35 km from the ice shelf front, does not. Both sites show diurnal periods, semidiurnal periods and a fortnightly period, which the authors attribute to tidal cycles. Similarly, Sun et al. (2019) record basal melt about 90 km from the ice shelf front, near the grounding line of the Roi Baudouin Ice Shelf and see no seasonality though find a diurnal period which they attribute to a tidal cycle. Alternatively, Hirano et al. (2020) see strong seasonality in basal melt at a location 45 km inland from the Shirase Glacier Tongue, 16 km from the north of the southernmost SGT grounding line. At a location hundreds of kilometres from the open ocean, Vaňková et al. (2020) observe little periodicity though see intermittent melt and accretion.

Typically, direct observations of the ice base are restricted to point surveys. Because drilling through an ice shelf is resource intensive, these measurements are sparse. Submarine technology opens up possibilities for spatial surveys of the ice base, but has not yet been used to survey ice base mass balance. As a result, most spatial surveys of basal mass balance come from indirect remote sensing techniques and ApRES.

At a coarse resolution (>1km), basal mass balance has been mapped over large areas of Antarctica's ice shelves using remote sensing techniques (e.g. Rignot et al., 2013; Mankoff et al., 2012; Goldberg et al., 2019). Using velocity data to estimate flux divergence, mass conservation is solved for the basal mass balance. A detailed description of these techniques can be found in Berger et al. (2017). Over large scales these studies have confirmed that melting is greatest at the perimeter of an ice shelf: at the ice front where ice is in close contact with open ocean and the grounding line (e.g. Rignot et al., 2013; Mankoff et al., 2012; Goldberg et al., 2019), and at the grounding line where deeper ice is in contact with warm salty water at the bottom of ice shelf cavity. However these techniques rely on the assumption that ice is at hydrostatic equilibrium, so begin to fail at a length scale where ice is not at equilibrium. Hydrostatic Equilibrium occurs at lengths approximately greater than ice thickness (Gudmundsson and Raymond, 2008), ($\gtrapprox$ 100s of m for ice shelves).

To resolve basal mass balance at a higher spatial resolution it is common to use ground based ApRES, whereby point locations are surveyed twice at different times, and basal mass balance is calculated from the change in radar reflection (Stanton et al., 2013; Dutrieux et al., 2014; Marsh et al., 2016). Such surveys have revealed large changes in basal mass balance over scales of hundreds of metres. These high gradients in basal melt have been found at the ice front (e.g. Stewart et al., 2019) and at basal channels (e.g. Stanton et al., 2013; Marsh et al., 2016). For example, Marsh et al. (2016) and Stanton et al. (2013) used ApRES to measure melt rates of 22.2 $\pm$ 0.2 m/yr and 14.2 to 24.5 m/yr in channels on the ice shelves of the Whillans Ice Stream and Pine Island Glacier respectively. In both cases, melt rates were measured near-zero outside of the channel, 1-2km and 200 m away from the channel apex respectively.

3.1.3 Goal and structure

Here we present a time series of ApRES observations in a location situated at the apex of a basal channel at the grounding line of the Kamb Ice Stream (Figure 3.2). The objective of this chapter is to constrain processes at the ice–ocean interface, and the structure of the interface. We aim to identify changes (or lack of changes) in basal mass balance and associate those changes to large scale processes in the channel, e.g. tides or subglacial drainage. The channel has been identified in previous studies by Alley et al. (2016); Kim et al. (2016); Goeller et al. (2015); Le Brocq et al. (2009) and Horgan et al. (2017). These authors proposed that the channel is sourced by subglacial drainage from the main trunk of the Kamb Ice Stream.

In this chapter, we start by describing data processing which follow the method of

Nicholls et al. (2015), using code from Stewart (2018) and methods to estimate accretion from Vaňková et al. (2021b) (Section 3.2). In Section 3.2 we refer to the basal mass balance observed with the ApRES as 'melt rate' in line with ApRES nomenclature. In Section 3.3, results from the time series are presented, including time series of apparent accretion rates, the amplitudes of the basal reflector, and strain rates. In this section, we use the terminology coined by Vaňková et al. (2021b), referring to the observed basal mass balance as 'apparent accretion'. Apparent accretion refers to the change in basal mass balance estimated using a dielectric constant of glacial ice to convert phase to displacement, substituting the unknown electromagnetic properties of the accreted marine ice (as described in Section 3.2), and neglecting the effects of multiple basal reflections. Lastly, we discuss the physical meaning of apparent accretion rate and the implications of the time series (Section 3.4).

3.1.4 Site description

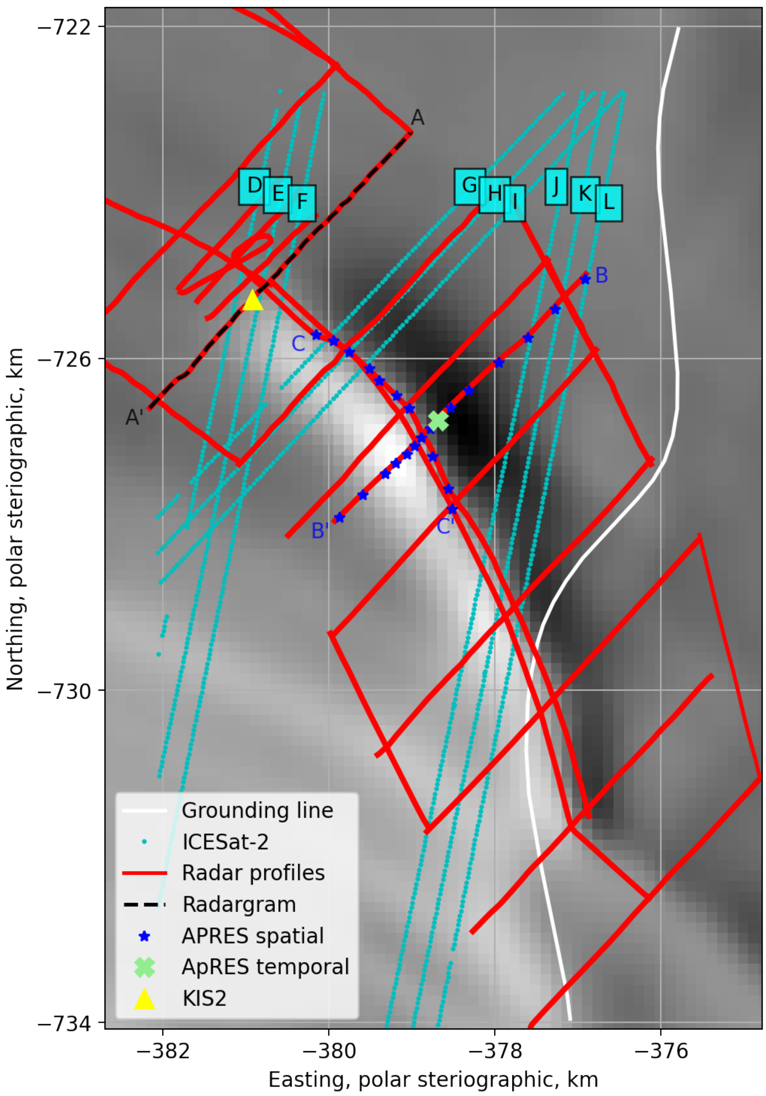

Figure 3.2: Map of study area showing all field data (repeated from Figure 2.3). ApRES was placed continuously recording at the light green 'X'. Background image is MODIS MOA 2009 (Haran et al., 2014).

To estimate basal mass balance at a channel incised into the base of the Ross Ice Shelf, an ApRES instrument was deployed. The channel extends upstream of the grounding line of the Kamb Ice Stream. The site location (Figure 3.2) is at the apex of a basal channel, where ice thickness is 433 metres. The channel is manifest on the ice surface as a 10 km long, 3 km wide, 20 m deep valley and is visible from the ground and in satellite imagery. The ApRES instrument was 3 km downstream from the inception of the channel. The instrument was installed on 31st of December 2019, and retrieved on the 24 December 2020. Radar imagery described in Chapter 2 shows that the basal channel extends 6 km upstream of the previously estimated grounding line of the Kamb Ice Stream and incises up to 50% of the ice thickness. Because the channel is situated at the outlet of estimated subglacial drainage paths (Chapter 2), the channel is likely formed by a buoyant meltwater plume triggered by subglacial discharge (Le Brocq et al., 2009; Kim et al., 2016). Remote sensing data shows present day surface lowering at the head of the channel, which in Chapter 2 we interpret as submarine melt. A cross section of basal mass balance bisecting the channel was presented in Chapter 2.

3.2 Methods

3.2.1 Field measurements

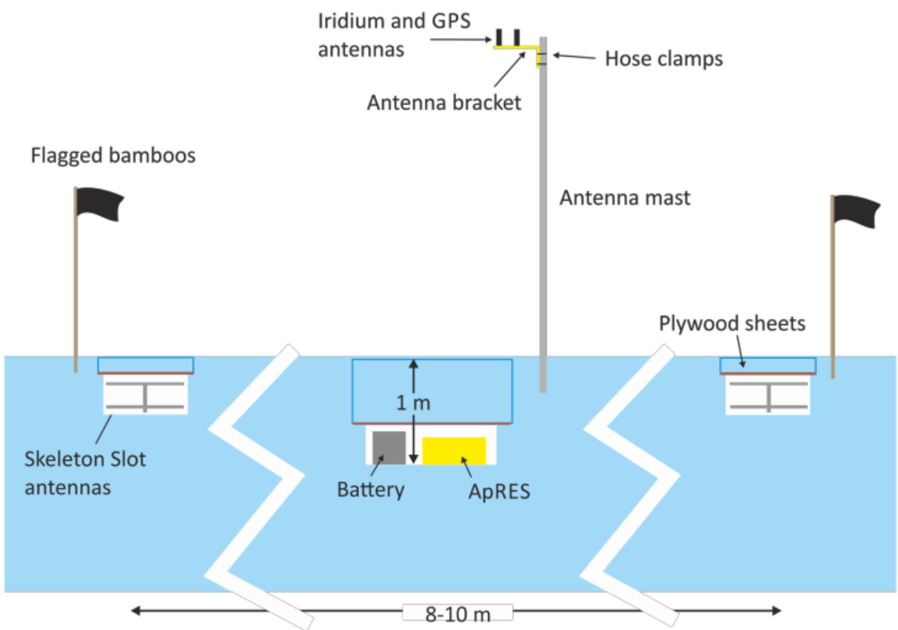

Figure 3.3: Image from Nicholls (2018), ApRES setup with two skeleton slot antennas, a gps on a mast to keep the internal clock synchronised, a battery, and a box labelled 'ApRES' with radar board and radar controller enclosed.

Developed by Brennan et al. (2014) and Nicholls et al. (2015), ApRES uses multiple frequency radio waves to image the ice base and internal ice reflectors to detect high precision mass balance. ApRES is a frequency modulated continuous wave system, which unlike single frequency radar, generates and emits a continuous wave signal. The system's advantage over traditional radar systems is phase coherence and a superior signal to noise ratio. The instrument (Figure 3.3) consists of two skeleton slot antennas, a GPS to keep the internal clock syncronised, a battery, and an enclosed radar board and radar controller, which also logs the data. The ApRES was deployed following Nicholls (2018), with antenna ≈ 9 m apart, 1 m deep and with parallel orientation. The instrument set up is shown in Figure 3.3.

The ApRES was set up to survey the ice every hour through the following on-board procedure: The first antenna transmitted a sequence of 20 chirps of radio waves. Each chirp ramped linearly from 200 to 400 MHz over a 1s period. The second antenna received the signal, first passing it through amplifiers, and an adjustable attenuator set on deployment. The received signal and a copy of the transmitted signal was then multiplied with a frequency mixer, in a process known as deramping. This removed the linear ramp of frequencies produced by a chirp, and produced an output signal with frequencies of the sum and differences of the received and transmitted signal. This was low pass filtered to isolate the difference, which contains a beat frequency proportional to the range, or distance from the antenna to the basal reflector. The signal was then high–pass filtered, amplifying weaker, more distant reflections to correct for effects of geometric spreading and dielectric absorption.

3.2.2 Processing

Data processing followed Brennan et al. (2014) and Nicholls et al. (2015). The methods described by these authors is summarised here.

The frequency of the deramped signal, f_d is given by

$$f_d = \frac{2B\sqrt{\epsilon_r}}{Tc}, \tag{3.1}$$

where T is the pulse duration, c is the speed of light, B is the sweep bandwith and ϵ_r is the dielectric constant of the medium (genrally 3.1 for ice). The range to a reflection is an average across the radar footprint. The range resolution, ΔR, is the minimum vertical distance at which two separate reflections can be resolved. f_d is found using Discrete Fourier Transform of the deramped signal, resulting in a spectral estimate with a resolution of $\Delta f_d = 1/T$. This implies a range resolution between Discrete Fourier Transform bins of

$$\Delta R = \frac{c}{2B\sqrt{\epsilon_r}}, \tag{3.2}$$

and a range to the nth Discret Fourier Transform bin centre of

$$R_{coarse}(n) = \frac{nc}{2B}, \tag{3.3}$$

valid only for bins from $n = 0$ to $n = N/2 - 1$. A typical centre frequency of 300 MHz and a sweep bandwidth of 200 MHz correspond to a deramped frequency of 2.35 Hz/m, with 1 s pulses. This gives a range resolution of 43 cm Brennan et al. (2014). The phase of the deramped signal is also proportional to target range. The phase range estimate can be combined with the frequency-derived range to obtain absolute range measurements with sub-mm precision Brennan et al. (2014). To maintain accurate phase-coherency between signals, the exact time at which the signal is digitised is aligned with the start of each transmitted chirp. The fine range,

$$R_{fine} = \frac{\lambda \phi_d}{4\pi} \tag{3.4}$$

was used to find the difference in phase between a Discrete Fourier Transform bin centre and the reflector (Brennan et al., 2014), where λ is the wavelength in the medium and ϕ_d is the instantaneous phase of the deramped signal at the chirp centre. When combined with the coarse range, total range can be resolved at sub-millimetre accuracy. ApRES was primarily designed to measure melt at the base of ice shelves. For a melt application, it is assumed that a temporal phase shift is caused by a vertical displacement of the basal reflector. This neglects phase changes in the dieletric contrast of the reflector caused by changes in ice or ocean properties at the reflector interface, which are small under melt conditions. Under conditions like at the Ross Ice Shelf, where the salinity is ≈ 34 psu, even a relatively large change of 4 psu would result in an apparent thickness change of less than 0.1 mm. Under conditions of basal accretion changes in the electromagnetic properties of accreted ice affect the phase of the reflection. In this case, it is no longer appropriate to interpret changes in phase solely as changes in ice thickness.

3.2.3 Melt rates

To calculate rates of change, we looked at the differences between two radar returns taken from the same point at different times. The raw recorded data describes amplitude as a function of frequency. These data are Fourier transformed to give a complex signal amplitude in terms of delay time. Assuming a constant velocity of radio waves, delay time is proportional to depth (Nicholls et al., 2015). The two-way travel time between the radar antenna and the ice base reflector is dependent on firn compaction, surface accumulation, vertical strain and hardware changes like instrument performance (Nicholls et al., 2015). To correct for these factors and solve for melt rates, stable internal reflectors are detected for two separate radar returns and used as reference points to track vertical displacement.

To eliminate the effects of hardware changes, surface accumulation and firn compaction, a single stable reflector beneath the firn is needed (Jenkins et al., 2006). We first aligned the two depth–profiles by cross-correlating the amplitudes of the depth–profiles immediately below the firn layer, and subtracted the difference from one return. This provided a vertical correction which accounted for accumulation, firn compaction and changes in hardware.

The left over change in thickness between the firn layer and the base is caused by vertical strain and basal melting (Nicholls et al., 2015). We next estimated vertical strain by comparing the phase of individual internal reflectors beneath the firn layer and calculating their relative motion (Figure 3.4). This was done by cross-correlating 4 m

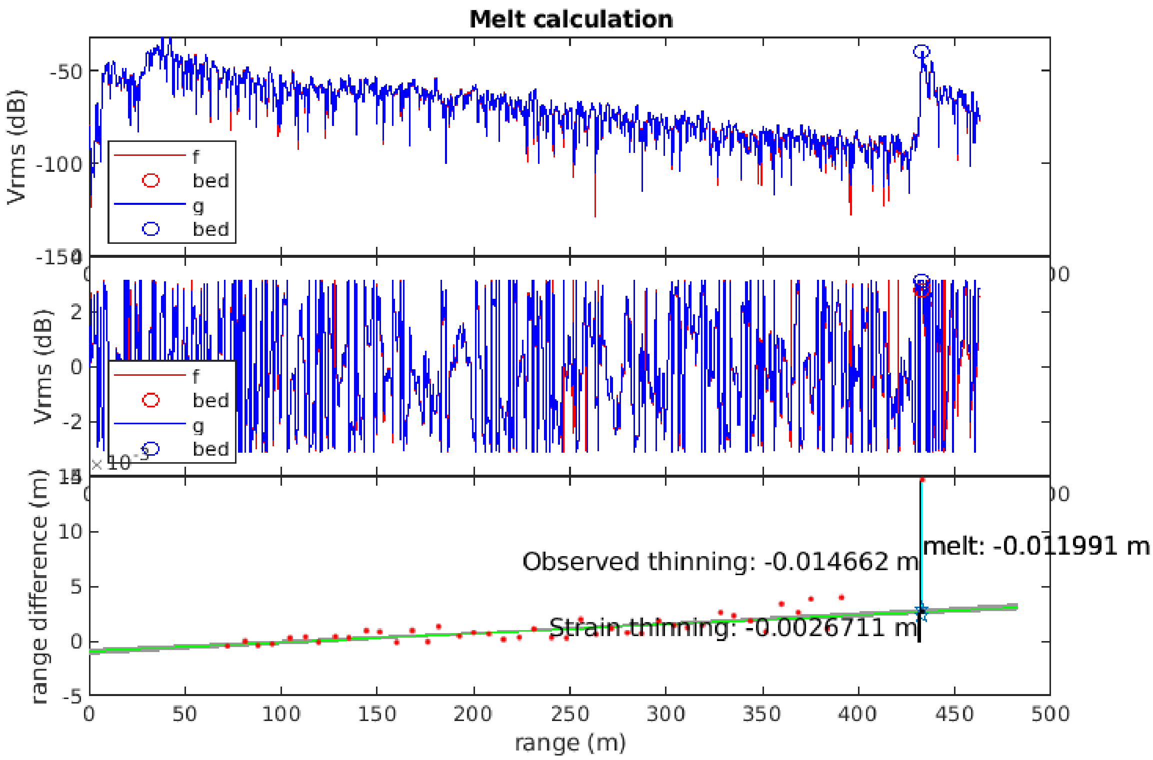

Figure 3.4: Example signals from repeat ApRES radar surveys 140 hours apart, shown as 'f' and 'g'. Top: The Fourier transform of the averaged radar chirp, amplitude of the return signal as a function of depth. The clear basal reflection is at 433 m. Centre: The radar signal. Bottom: Vertical displacement of tracked internal reflectors (red dots). The green line shows the linear fit through internal reflectors, and the red stars show the observed displacement of the shelf base, and the displacement due to vertical strain. The black vertical line shows the distance between extrapolated strain and the basal reflector, representing estimated melt. Blue stars show the bounds of estimated strain error.

segments of the first profile with the complex conjugate of the corresponding segment of the second. Because the two signals had been aligned at a reflector beneath the firn, the displacement was relative to that point (Nicholls et al., 2015). We estimated a strain rate by modelling a linear relationship between displacement and depth. Subtracting the strain rate from the change in depth gave an estimate of the melt rate. The basal mass balance is the distance of the basal reflector off the fitted line though internal reflectors. The strain rate error was calculated as the quality of the fit in the linear regression. To calculate the basal mass balance error, we combined the error in the strain rate with the error in vertical displacement, which is based on the signal to noise ratio of the two basal reflections.

Estimating accurate strain rates is a key challenge in the process of calculating basal melt rates, and is a dominant source of uncertainty (Vaňková et al., 2020). Internal reflectors can be relatively weak, and difficult to track. To accurately estimate strain, these reflectors must show coherent relative displacement (Lindbäck et al., 2019). However, with too much movement reflectors can be difficult to correlate. Various ApRES studies filter out high frequency melt or strain rate changes due to a increase in uncertainty from strain measured over a small period of time. For example, Lindbäck et al. (2019) and Davis et al. (2018) low pass filtered ApRES time series with cutoffs at 36 hours and 48 respectively. We instead follow the method of Sun et al. (2019), using a rolling interval to calculate strain and melt rates. The effects of this method are described in Section 3.3.2.

We estimated basal mass balance every 7 hours by comparing ApRES measurements over 7 hour and 28 hour intervals from the 1st of January 2020 to the 23rd of December 2020. Files were outputted as 7 aggregated 1–hour blocks, resulting in faster processing at 7–hour intervals. Higher frequency estimates were not considered useful due to the increase in uncertainty in estimated strain (described above). The point in time for basal melt calculated over a time interval is set to the centre of the interval (± 3 1/2 and 17 1/2 hours for the 7 and 28 hour sliding intervals respectively).

3.2.4 Accretion

Compared to basal melt, quantifying accretion is problematic due to the occurrence of multiple reflections from both the glacial/marine–ice interface and the marine–ice/ocean interface (Vaňková et al., 2020). If these reflections are close together they cannot be distinguished. The sum of these reflections gives a phase shift depending on the thickness of the layer, its permittivity, and the relative strength of the internal and basal reflections. Additionally, changes in the electromagnetic properties of ice at the interface of the reflection cause changes in the phase of reflection. Vaňková et al. (2021b) developed methods of quantifying intermittent accretion/melt cycles by comparing the amplitude, phase and centre frequency of the radar reflection. When measuring basal mass balance with a base of glacial ice, these problems do not occur as there is a single clear reflection which is always between glacial ice and salt water. Small changes in the salinity of the water cause negligible phase shifts.

3.2.5 Amplitude

Lastly, we estimated higher resolution and accuracy amplitudes, and amplitude based ranges to radar reflections for the time–series. Following Vaňková et al. (2021b), we improved on the accuracy of the picked bed reflector used to find basal mass balance (chosen with the routine as described by Stewart (2018)). We chose three points adjacent to the originally picked bed reflector, and used least squares to calculate a quadratic fit to the three points. The maximum of the quadratic gave the amplitude and the range to the basal reflector. Basal mass balance is calculated from the amplitude based range by subtracting the estimated strain from the difference between two range estimates and dividing by the time period.

3.3 Results

3.3.1 Time series

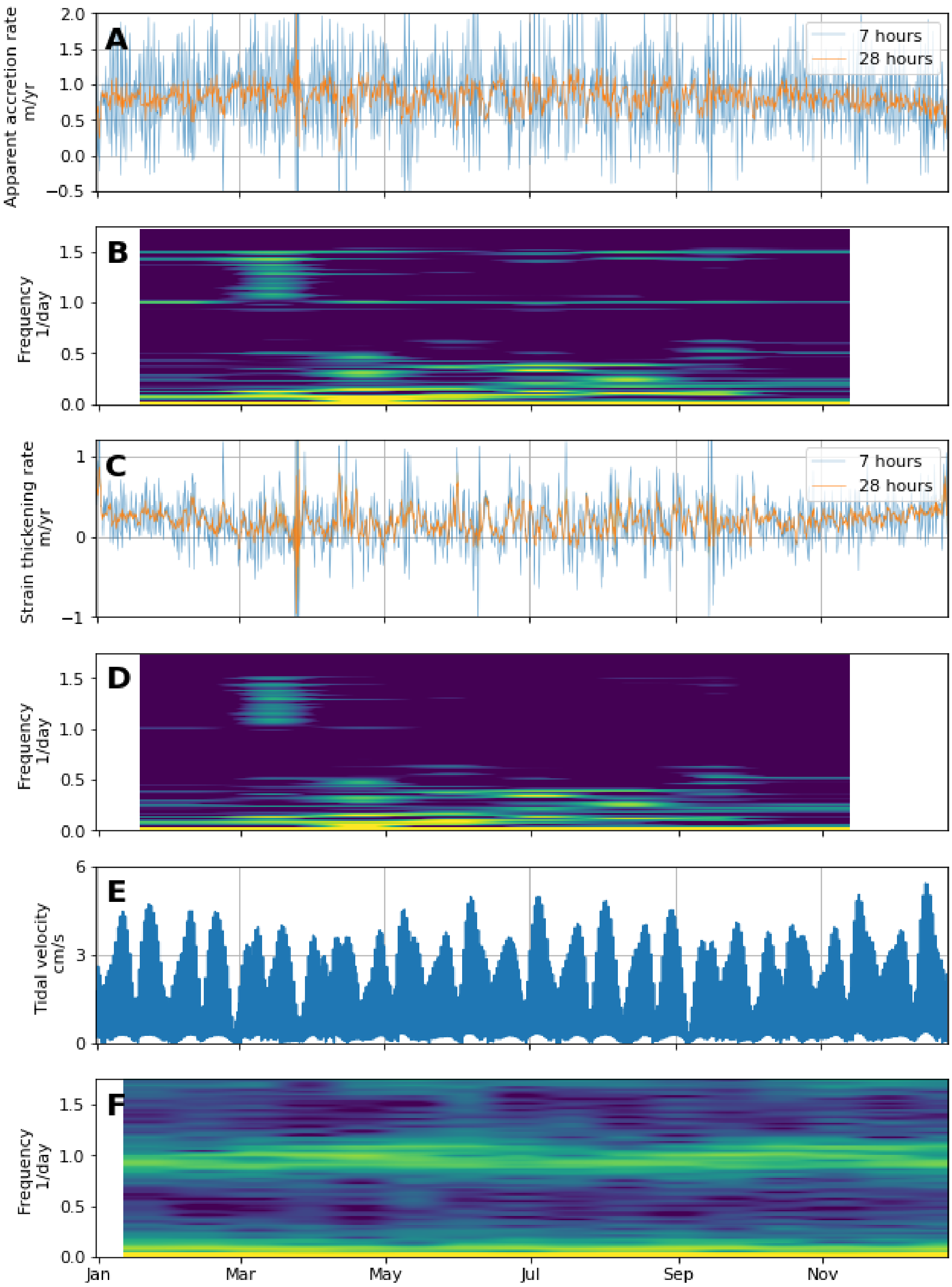

Figure 3.5: A) Time series of apparent accretion calculated at 7–hr intervals (blue line), overlaid by 28 hour intervals (orange line). Errors for the 28 hour interval time series are shown by shaded transparent orange areas (easier to see in Figure 3.6). B) Spectrogram of the time series shown in (A), derived using the 28 hour rolling interval. C) Time series of strain thickening calculated at 7–hr intervals (blue line), overlaid by 28 hour intervals (orange line). Errors for the 28 hour interval time series are shown by shaded transparent orange areas. D) Spectrogram of the strain thickening time series, derived using the 28 hour rolling interval. E) Time series of estimated tidal velocity magnitude at the channel using output provided by Padman et al. (2002). F) Spectrogram of the tidal time series.

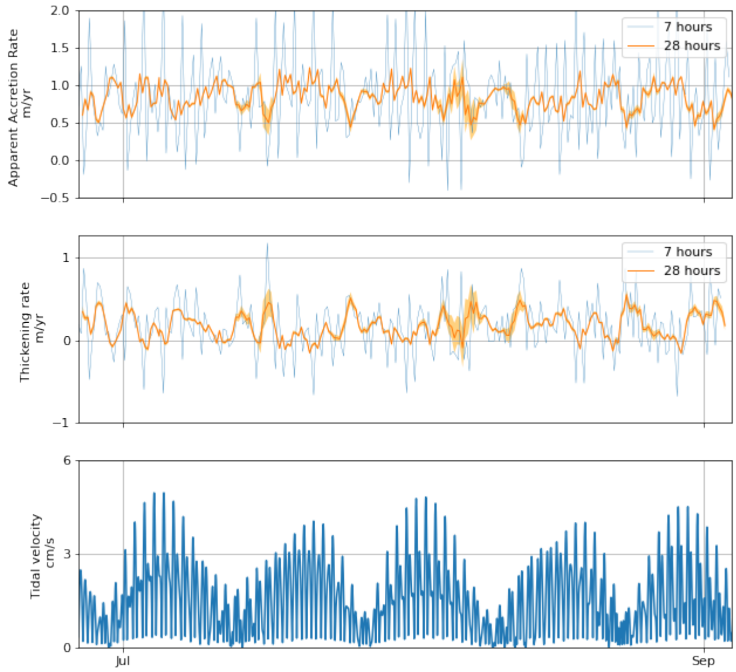

Figure 3.6: Data from time series as in Figure 3.5 zoomed in on the month of July. A) Apparent accretion as in Figure 3.5 A. B) Strain thickening as in Figure 3.5 C. C) Time series of estimated tidal series as in Figure 3.5 E.

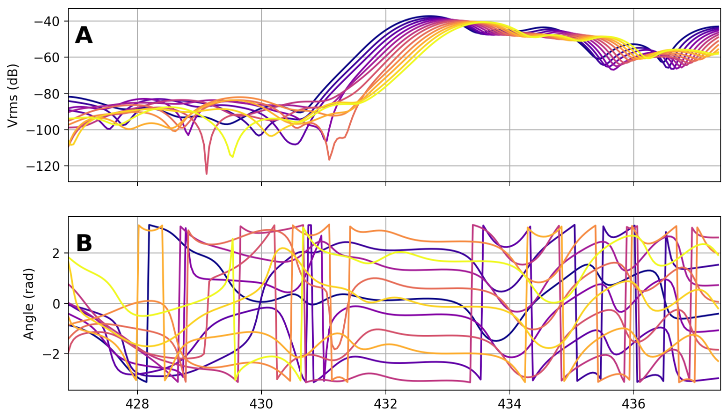

Figure 3.7: 12 separate ApRES observations over 12 months of 2020. A) Range vs Amplitude, B) Range vs Phase. X–axis is zoomed in on the basal reflector at 433 m. Each line is calculated from the 1st of each month of 2020. Cool colours start in January, warm colours end in December.

Figure 3.5 A shows a time series of apparent accretion from the 1 January 2020 to 23 December 2020. Each data point is calculated from two ApRES observations made from

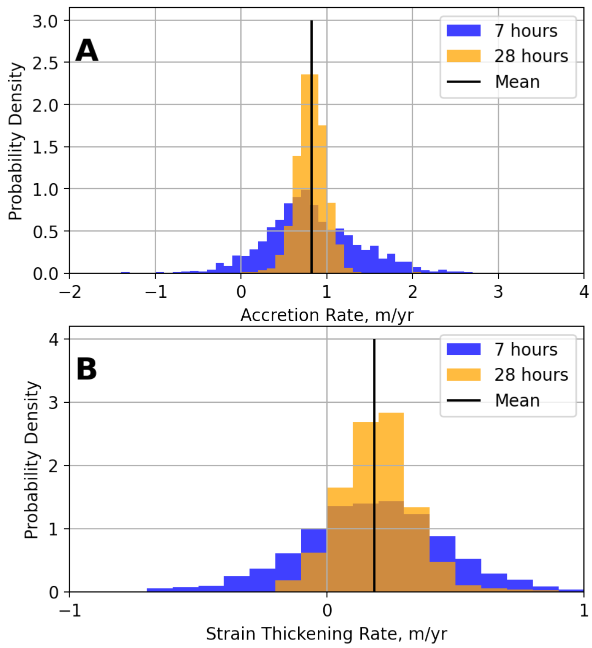

Figure 3.8: Histograms showing the variation in A) Accretion, B) Strain, over the time series.

± 3 1/2 and ± 14 hours for the 7 and 28 hour sliding intervals respectively. Note that 'apparent accretion' represents an increase in thickness and corresponds to the negative of 'melt rate' as described in most ApRES research (e.g. Vaňková et al., 2021b; Lindbäck et al., 2019). For both 7 and 28 hour intervals, apparent accretion fluctuates around an average of 0.81 m/yr for the duration of the time series (Figure 3.8), with median errors of 0.07 and 0.03 m/yr respectively (Figure 3.5 A). The degree of variability is strongly dependent on the interval length, with longer intervals smoothing the apparent accretion in time (Figure 3.6). The 7 hour interval time series has lower and upper quartiles of 0.5 m/yr and 1.1 (Figure 3.8), and the 28 hour interval time series has quartiles of 0.7 and 0.9 m/yr (Figure 3.8) . The spectrogram of apparent accretion (Figure 3.5 C), which is calculated with 28 hour intervals, shows dominant short periods of 16, 18 and 24 hours and a weakly dominant period of 26 hours. Longer 14 day periods are strongly dominant from January until around October, and 2 and 4 day periods are intermittently dominant.

Strain thickening rate varies in amplitude throughout the time series around a mean of 0.2 m/yr (Figure 3.8) with a mean strain rate error of 0.03 m/yr. Strain calculated over 28 hour intervals have lower and upper quartiles of 0.12 and 0.27 m/yr respectively (Figure 3.8). With a mean ice thickness of 433 m, this corresponds to a strain rate of 4.6 x 10^{-4} / yr. Strain is generally positive, showing longitudinal compression or thickening due to strain in the area (Figure 3.4 and 6.7). On average, the strain correction is 24% of the size of the apparent accretion. The periodogram of strain (Figure 3.5 D) shows 14 days periods are strongly dominant from February until around October. Periods of 1, 2 and 4 days are intermittently dominant.

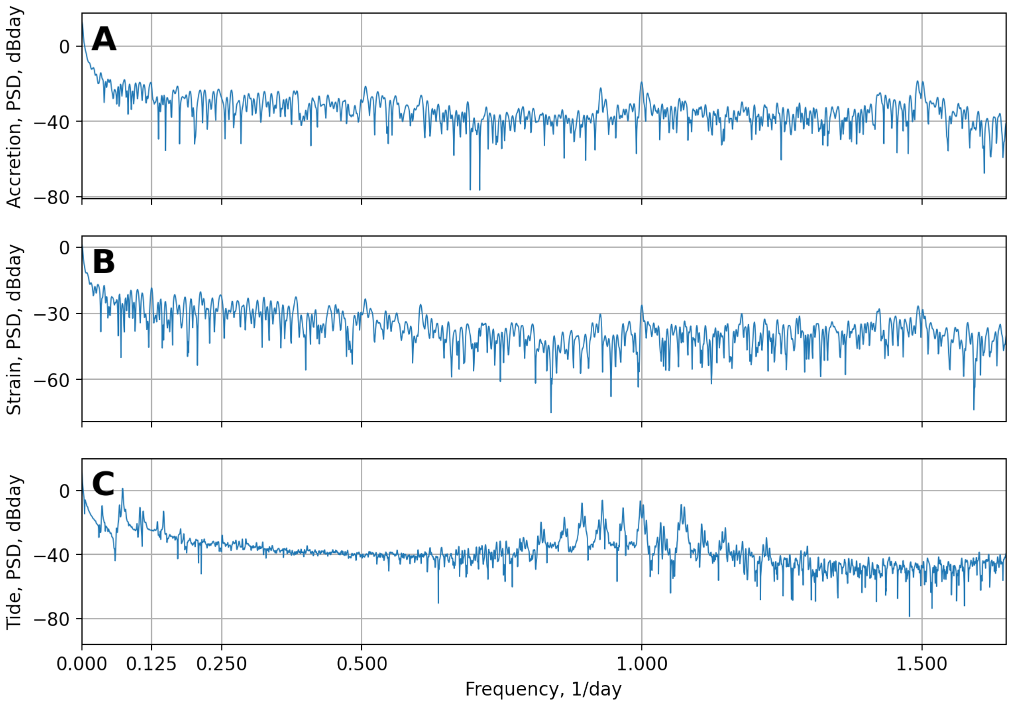

Figure 3.9: The Power Spectral Density (PSD) of apparent accretion (A), strain (B), and estimated tidal magnitude (C) from Padman et al. (2002). Power Spectral Density is calculated by Welch's average periodogram method. A and B are calculated from time series calculated over 28 hour intervals.

The power spectral density (Figure 3.9) of apparent accretion calculated at 28 hour intervals over the entire time series shows diurnal and semidiurnal periodicity with local maximums at frequencies of 0.5, 0.93, 1, 1.42 and 1.5 per day. These correspond to periods of 48, 26, 24, 17 and 16 hours respectively. The power spectrum of strain thickening also has local peaks at these frequencies, and additionally, has local peaks at 0.6 and 1.2 per day which correspond to periods of 20 and 40 hours respectively.

3.3.2 Sliding interval method

Melt rates are calculated from two ApRES observations. These observations must be separated in time to allow for the accurate calculation of strain rates (described in Section 3.2.3). To calculate strain rates we track internal reflectors in the ice, this is only possible if enough time has passed for the reflectors to have moved relative to each other. It follows that a wide window (>1-2 days) is required to calculate strain. Conversely, we aim to capture melt signals at as high a frequency as possible. Calculating melt every 1-2 days would miss semidiurnal tidal periods. It follows that we use a large sliding interval to calculate melt rate, which is wide enough to track strain, but slides in time at a small enough interval to capture high frequencies. In this section we describe this method and validate its usage.

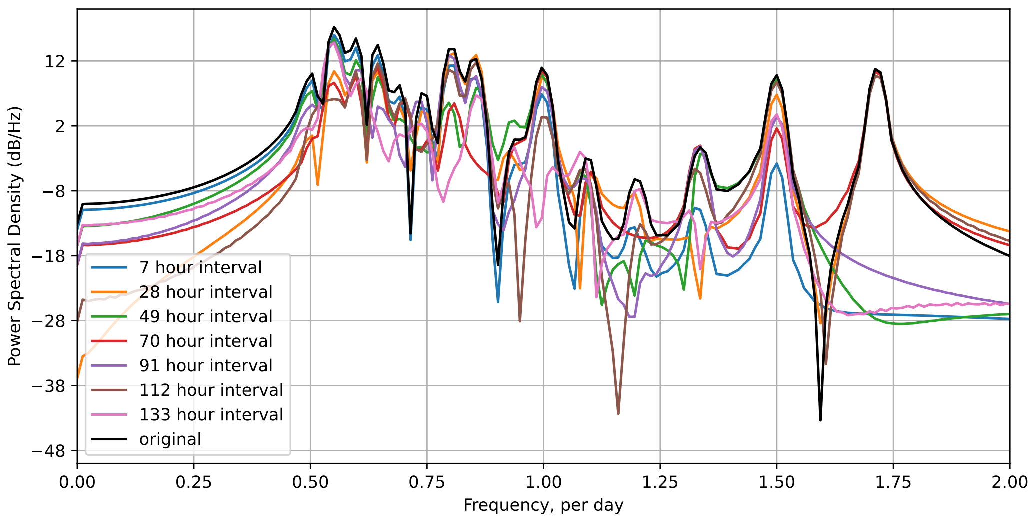

Figure 3.10: In black, the power spectrum of a synthetic time series which is the addition of random sine waves with periods from 14 to 50 hours. Colours show power spectrum of the time series resampled over different intervals as $y[n] = (x[n - w/2] + x[n + w/2])/2$ where x is the original time series, y is the resampled time series and w is the interval length.

Calculating strain and melt over larger intervals has the effect of smoothing the apparent accretion (Figure 3.5). The effect of a large interval on frequencies is similar to that of a comb filter. The output of the filter periodically drops to a local minimum at multiples of the interval frequency $1/2T_w, 3/2T_w, 5/2T_w \cdot$, where T_w is the interval width. The distortion to frequencies is therefore specific to and different for each interval length. Figure 3.10 shows the effect of interval size on a synthetic time series. The time series is a random sum of sine waves with periods from 14 to 50 hours, which we resample using a sliding average of two points to simulate our melt rate calculations. The sliding average is defined as $y[n] = (x[n - w/2] + x[n + w/2])/2$ where x is the original time series, y is the resampled time series and w is the interval length. The resampled time series show similar patterns of frequency distributions though the amplitudes of certain frequencies change. Longer intervals show the most distortion, filtering out frequencies greater than 1.5 1/day, and showing less fidelity than shorter intervals for frequencies greater than 1.5 1/day. Intervals of 7 and 28 hour demonstrate good fidelity.

We compare the power spectrums (Figure 3.11) of the ApRES melt and strain thickening time series with a range of interval sizes. Figure 3.11 shows which frequencies are consistently dominant over different length intervals. In particular, a diurnal signal is dominant regardless of the interval size. This shows that the increase in uncertainties in strain caused by smaller (7 and 28 hour) intervals does not introduce artefacts in the power spectrum which have caused these frequencies to be dominant. This justifies the

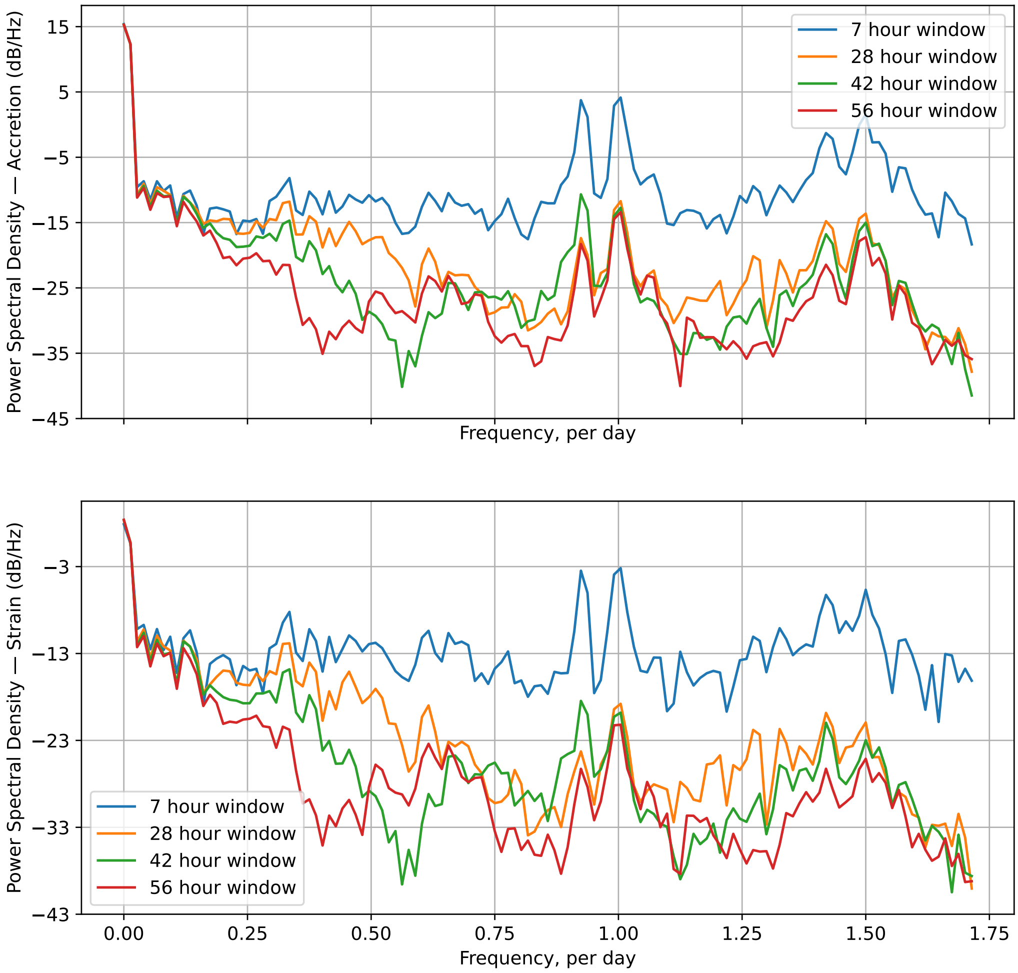

Figure 3.11: Power spectrum of ApRES time series for apparent accretion (top) and strain (bottom) for a range of different sampling intervals, shown by different colours.

sliding interval method of calculating melt rates, described next.

3.3.3 Amplitudes

A time series of return amplitude over 2020 (Figure 3.12) shows a negative trend in the amplitude of the basal reflector, from -35.0 dB to -38.6 dB. The gradient is steepest in January, and sees the most variability from April to October. No spikes in amplitude exceed 2 dB. The basal mass balance calculated from tracking the amplitude of the basal reflector matches the apparent accretion, which is the basal mass balance calculated from phase. The changing range to the amplitude of the basal reflector is shown in Figure 3.7. The amplitude based basal mass balance displays significantly more noise than the phase

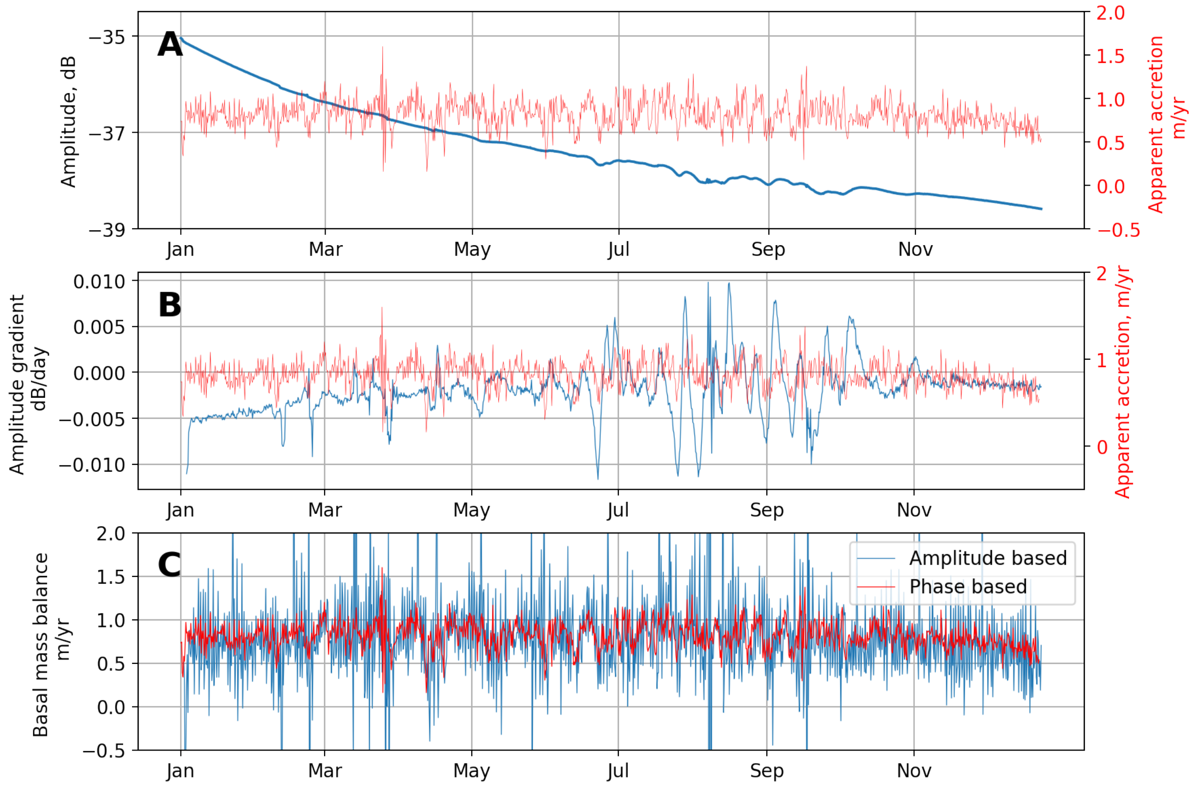

Figure 3.12: A) Time series of amplitudes of basal reflector in blue overlay estimated apparent accretion in red. B) Amplitude gradient C) Amplitude based and phase based (conventional method) estimates of basal mass balance.

derived basal mass balance. The mean of the amplitude based basal mass balance is 0.78 m/yr, slightly less than the mean of phase-based apparent accretion which is 0.81 m/yr.

3.4 Discussion

3.4.0.1 What does the observed apparent accretion represent?

We suggest that for the duration of the time series presented (Figure 3.5), the base of the ice shelf below the ApRES instrument consists of a layer of marine ice, which has accreted to the bottom of glacial ice. Evidence for a basal marine ice layer comes from ApRES observations of consistent apparent accretion throughout the time series (Figure 3.5 A). Consistent apparent accretion rules out the possibility that the base is purely glacial ice, which can only exist under active melting or zero mass balance. In addition, the amplitude of apparent accretion (Figure 3.12) shows a smooth change throughout the time series, gradients do not exceed 0.01 dB/day, implying no sharp change in the properties of the dominant reflector (Vaňková et al., 2021b). This confirms that basal conditions are consistent throughout the time series, confirming the existence of basal ice. Previous work by Vaňková et al. (2021b) suggests that the temporal change from a base of glacial ice to a base of marine ice, or vice versa, causes a sharp change in the amplitude ($\gtrapprox$0.25 dB/day) of an ApRES reflection.

The apparent accretion displayed throughout the time series (Figure 3.5 A), shows a consistently changing dominant reflection from the ice base. This is most likely caused by a consistent change in the marine ice layer. Assuming there is a layer of marine ice present at the base of the ice shelf, we expect the ApRES to return a strong reflection from the glacial/marine–ice boundary due to the strong dielectric contrast and possibly a second, weaker reflection from the marine–ice/sea boundary (as in Fricker et al. (2001)). Apparent accretion shows that the apparent range, the distance from the ApRES instrument to the main reflector, is increasing (Figure 3.5). This is likely caused by a change in the interference of reflections from the glacial/marine–ice interface and the marine–ice/sea interface. The interference of reflections is likely causing a phase shift which appears as an increase in the range to the resulting reflection (Vaňková et al., 2021b). It is unlikely that the increase in apparent length is caused directly by an increase in length caused by accretion because it is unlikely that the main reflection is at the marine–ice/sea boundary, which has a weaker dielectric contrast than the glacial/marine–ice boundary. The change in interference of the two reflections could be caused by accretion, or melt, and/or a change in the electromagnetic properties of the marine ice. Depending on the thickness and properties of the marine ice, accretion or melt could increase the apparent length (Vaňková et al., 2021b).

Following the work of Vaňková et al. (2021b), due to the unknown potentially changing properties of the accreted marine ice layer, we cannot be certain as to whether the basal interface is melting or accreting. Vaňková et al. (2021b) modelled relationships between the change in thickness of the accreted layer and change in phase shift and basal amplitude. They found that for an observed change in apparent length, there are many different possible solutions. The apparent length is a function of the thickness, the dielectric constant, and the electrical conductivity of the marine ice layer. The relationships between these variables and apparent thickness also depend on the frequency of the radar signal. Vaňková et al. (2021b) found that it is not always possible to constrain apparent accretion rates without a better understanding of the thickness and properties of the marine ice layer.

We suggest there are three potential explanations for the observed apparent accretion (Figure 3.5). The most likely is the simplest explanation that ice is actively accreting throughout the time series. The consistent apparent accretion is probably caused by consistent accretion as in Vaňková et al. (2021b), where the accuracy of switches between apparent accretion and melt were confirmed by the growing and disappearing of a marine ice layer. Both phase and amplitude based apparent accretion (Figure 3.12 C) show a consistent positive basal mass balance throughout the time series, suggesting that phase changes are caused by a change in the range, and not by changes in the dielectric contrast of the boundaries. This supports the explanation that the observed apparent accretion is caused by basal accretion.

The second possibility is that the ApRES site may have had thick marine ice before the time series, and during the time series, the layer is actively melting resulting in signals which appear as apparent accretion. This would require the peak and phase to be distorted by destructive interference from multiple reflections. If one of the reflections had a shift in polarity, then a decrease in range (caused by melt) to the marine ice base could combine with the stable reflection from the glacial/marine ice boundary to show an increase in the range of the dominant reflector (showing apparent accretion). We deem this less likely due to the consistent change in amplitude of the basal reflection (Figure 3.12). This would imply that the base has gone through different periods of accretion and melt and that the time series caught a snapshot of just the melt period. The consistently negative mass balance would eventually melt through the marine ice to glacial ice, which we do not see. If outflow through the channel is episodic, large floods of subglacial water passing through (as suggested in Chapter 2) could cause the accumulation of thick marine ice on the bottom of the ice shelf. This marine ice layer may have been consistently melting for the year of 2020.

Thirdly, it is feasible that basal ice is metamorphosing in a way which steadily changes its electromagnetic properties through the time series. If true, basal ice metamorphosing must be influenced by tidal forces, as we can see tidal signals in the apparent accretion. This scenario is improbable. Additionally, it is unlikely that changing electromagnetic properties of the basal layer would result in consistent basal mass balance estimates from both phase and range (Figure 3.12). This possibility is difficult to support or rule out, as we know little about the changing electromagnetic properties of metamorphosing marine ice. However, thermal changes in the ice would not occur at the tidal timescales observed.

3.4.1 Drivers of mass balance variability

The apparent accretion time series shows diurnal periodicity (Figure 3.5 A) which we attribute to the tidal influence on circulation and melt in the channel. Specifically, periods of 26 and 24 hours are dominant in both the apparent accretion time series (Figure 3.9 A) and the estimated tidal velocity time series (Figure 3.9 C). 50km from the ApRES location at 'KIS1' (Figure 1.5), Robinson et al. (2020) estimated a basal melt rate time series from oceanographic observations, and found that basal melt rates closely followed diurnal tides. Additionally, internal tidal waves between layers in the cavity like those described by Robinson et al. (2020) likely promote mixing. Because the channel is constricted, the tide is expected to behave differently from the larger Ross Ice Shelf cavity. The shape of the channel is similar to a converging (upstream narrowing) estuarine river mouth, which generally enhances tidal amplitude (van Rijn, 2011).

Lindbäck et al. (2019) similarly found diurnal basal melt fluctuations using ApRES on the Nivlisen Ice Shelf, and attributed these to tide–driven circulation. Makinson et al. (2011) modelled circulation under the Filchner-Ronne Ice Shelf, and showed that tides increase basal melt by enhancing cavity circulation, increasing both the outflow of cold water and inflow of warm saline water. They found that the presence of tides doubled estimated basal melting under the Filchner-Ronne Ice Shelf. While both of these examples show melt of the base of an ice shelf, melt in basal channels is thought to occur from similar processes, through meltwater plumes (Sergienko, 2013) and the circulation and recycling of melt water with warmer saltier water.

3.4.2 Strain thickening

Observations of consistent positive strain thickening over the ice column (Figure 3.5 D) suggest a viscous response to localised basal melt. While our observations at the ApRES location reveal basal marine ice, and potential thickening, the channel shape (shown in Figure 2.7) indicates the location previously saw more than 300 m of ice melt. Ice is likely flowing towards the centre of the channel to compensate for the melt driven formation of the channel. Ice, like any fluid, flows to flatten perturbations. This observation supports the numerical modelling experiments of Wearing et al. (2021) who modelled ice flow towards the centre of a channel from its sides, predicting that strain causes the closure of channels. In theory, this strain thickening will not cause crevassing like that observed by strain thinning (e.g. Vaughan et al., 2012). If anything, the strain thickening will cause the closing of crevasses. We discount significant active flexing as a cause of strain, as the effect of flexure on strain would be thickening in the upper half of the ice column and thinning in the lower half (Vaughan et al., 2012), which is not observed (Figure 3.4 shows strain thickening throughout the entire ice column). In comparison to 4.6 x 10^{-4} / yr at our site Alley et al. (2018) finds that the along flow strain rate in the area is positive and

$< 1 \times 10^{-6}$/yr, and the transverse strain rate is close to zero, $< 1 \times 10^{-6}$/yr.

Apparent accretion is the rate of change in range to the basal reflector minus the strain thickening rate. While strain thickening contributes to just 24% of the apparent accretion estimates over the whole time series, variation in apparent accretion is closely related to strain thickening. This is evident when comparing zoomed in apparent accretion and strain thickening in Figure 3.6, and is also shown by the similar spectrograms of Figure 3.9 A and B. While this close correlation could be caused by errors in the melt rate calculation method, there is no clear evidence of such errors. Calculated strain thickening rate errors are small relative to the signal. These errors are calculated by the quality of fit as shown in Figure 6.7, which confirms we have a linear strain profile, and the linear fit is reasonable. Using larger intervals (up to 100 hours) to calculate strain thickening rates results in a similar close correlation of oscillations between strain thickening and melt rate, with similar dominant frequencies (Figure 3.11). This suggests that the length of our interval is robust, and is not corrupting strain thickening rate calculations. The close correlation between strain thickening and melt rates is most likely due to the fact both melt and strain thickening are principally driven by the same external forces. In this case, external forces such as tides drive apparent accretion and strain thickening to vary in sync. Alternatively, the correlation could be due to the dependence of melt rate on strain thickening rates or vice versa. For example, feedbacks may stabilise the basal elevation, resulting in a basal mass balance which essentially cancels out the strain thickening. This is an unlikely explanation, as melt and accretion feedbacks caused by changes in the strain, or the converse, are unlikely to occur at the same time scales.

3.4.3 Implications for channel dynamics

The existence of a layer of basal marine ice implies that the ApRES location has experienced positive basal mass balance in the past. Either supercooled water accretes directly to the ice at the site, or frazil ice carried by currents accumulates and builds a layer of marine ice (Vaňková et al., 2021b). Accretion is likely driven by a meltwater plume as described by Hewitt (2020). Subglacial discharge initiates a meltwater plume which flows up the face of the ice, melting ice, becoming fresher and more buoyant. The upward plume entrains warm salty water from the ocean depths to the ice face, enhancing melt. Plume theory (as in Jenkins (2011)) predicts melt for a certain distance downstream from the start of the plume, after which the plume is predicted to lose energy and cause accretion. Our dataset provides constraints on the length scales over which a melt water plume loses energy, in that accretion can occur 3 km downstream from the inception of the channel.

The formation of marine ice immediately downstream from the melt region adds constraints to our conceptual model of the channel formation discussed in Chapter 2 (where we suggested that the channel had formed through the upstream step–wise migration of a subglacial plume). The ApRES location spot was likely a focus of basal melt at some time in the past when the surface basin formed, but now is downstream of the active melting part of the channel and is thickening. This implies that melt is relatively focused at the tip of the channel, and suggests this has been the case throughout the channel formation. This reinforces the theory that a retreating subglacial plume has formed the channel because localised melt must move to form a linear feature like the channel.

Additionally, we have theorised that for the duration of the year-long time series there is a consistent basal mass balance. If we assume that accretion rates are influenced by a subglacial plume triggered by subglacial drainage, it follows that there are no major changes in subglacial drainage for the period surveyed. We would expect changes in subglacial drainage to be associated with changes in basal mass balance at the ApRES location. Kim et al. (2016) found the subglacial lakes beneath the Kamb Ice Stream flood over a period less than a year long. It follows that the time series we present does not show the channel in a subglacial flood period. This implies that the channel is consistent for a year, and constrains a potential period of invariability in the channel. If the observed accretion is driven by the melt water plume, we can also deduce that the melt water plume at the inception of the channel experiences tidal variability. This suggests that the plume has strong connections to the ocean.

3.5 Conclusion

We have presented a time series of Autonomous Phase-sensitive Radio-Echo Sounder (ApRES) observations taken at the apex of a sub–ice–shelf channel at the grounding line of the Kamb Ice Stream. The time series spans most of 2020, and shows basal marine ice for the entirety of the period. This is confirmed with analysis of the amplitudes of the basal reflection, which show no sharp changes through the time series. We interpret the consistent apparent accretion observed by the ApRES as a consistent basal mass balance with a marine ice layer underlying glacial ice. We are unable to confidently constrain the mass balance as melt or accretion due to the unknown, potentially changing properties of the marine ice layer, though suggest that mass balance is most likely positive. Mass balance has a strong diurnal signal, which we attribute to tidally–driven circulation. The estimated strain is consistently thickening in the area, which corresponds to a viscous response to the previous incision of the basal channel.

Chapter 4

Subglacial drainage variability drives basal channel growth at Kamb Ice Stream's grounding line

4.1 Introduction

The strength and condition of an ice shelf affects its capacity to buttress the flow of grounded ice from the Antarctic continent (Gagliardini et al., 2010). When ice shelves lose thickness through submarine melt, buttressing is reduced, and increased flow of grounded ice causes sea level rise (Pritchard et al., 2012). Ice shelf melt is therefore a crucial measurement in forecasting future sea level rise (Liu et al., 2015; Scambos et al., 2017). While ice shelf melt is largely controlled by ocean circulation in the sub–ice–shelf cavity (Rignot et al., 2013), the cavities beneath Antarctic ice shelves are among the least observed parts of the climate system (Stevens et al., 2020). Although remote sensing can measure present basal melt rates of ice shelves (e.g Rignot et al., 2013; Mankoff et al., 2012; Goldberg et al., 2019), predicting future melt rates requires an understanding of ocean circulation processes.

Most observations of ocean circulation under ice shelves occur at the ice front (e.g. Arzeno et al. (2014) or Smethie Jr and Jacobs (2005)). Observation points in ice shelf cavities are sparse (e.g. Begeman et al., 2018; Stevens et al., 2020; Foster, 1983), as direct access requires a large drilling operation. Because direct observations are limited, ocean modelling is an especially important part of ice shelf science. Ocean models are used to understand ocean conditions at a higher resolution by interpolating between drilling points. They are based on continuity equations and are calibrated to the ocean cavity environment (e.g. Millgate et al., 2013; Holland et al., 2003a).

Basal channels incised into the base of ice shelves have been identified across Antarctica. Ice shelf thinning occurs at higher rates at channels (e.g. Marsh et al., 2016). Autonomous Phase-sensitive Radio-Echo Sounder (ApRES) measurements at and around channels show that melt rates can increase from near zero beside a basal channel to around 20 m/yr at the channel (Stanton et al., 2013; Marsh et al., 2016). Estimates of melt rates from satellite altimetry measurements around channels have replicated these findings on a broader scale (e.g Chartrand and Howat, 2020; Rignot and Steffen, 2008), confirming that average sub–ice–shelf cavity conditions are not representative of conditions in channels. (Le Brocq et al., 2009; Alley et al., 2016). The proposed mechanism to explain these higher melt rates is that channels foster a buoyant melt–enhancing plume (described in Chapter 1).

At least two field campaigns have drilled through an ice shelf to directly observe ocean conditions in basal channels. Stanton et al. (2013) drilled into the Pine Island Glacier to find a buoyant melt–water plume at the ice–ocean boundary. The plume moved at 11-15 cm/s, had a salinity of 33.85 g/kg, and was around 1.4 °C warmer than the freezing point. Similarly, Rignot and Steffen (2008) drilled into a 300 m deep channel at the Petermann Glacier in Greenland to find a fresh boundary layer with salinity and absolute temperature of 32.6 g/kg and -1.9 °C (Figure 4.1). The water column increased in temperature and salinity with depth to 0.0 °C and 34.6 g/kg at the ocean floor 660 m deep (see Figure 4.1).

Most descriptions of channel conditions are based on outputs from numerical models. Ice shelf channels have been modelled using a variety of ocean modelling techniques (e.g. Millgate et al., 2013; Gladish et al., 2012; Sergienko, 2013; Payne et al., 2007). Some channel descriptions assume that a buoyant subglacial plume is the dominant process, so use a plume model to describe channel melt (e.g. Gladish et al., 2012; Sergienko, 2013). The majority of these descriptions are based on the formulation found in Jenkins (2011) and described in detail by Hewitt (2020). The Jenkins (2011) one dimensional plume model is based on conservation equations for mass, momentum, heat and salt, whereby melt rate is described in terms of plume thickness, speed, salinity, and temperature. This model forms the basis of sub–ice–shelf plume theory. Various configurations or scalings of the model can provide insights into plume behaviour. For example, if subglacial discharge is included in the model, the buoyancy flux driven by basal melt is negligible near the outlet. The one dimensional model has been used to approximate melt from subglacial outlet flux (e.g. Gourmelen et al., 2017) or outlet flux from melt rate ((e.g. Marsh et al., 2016)).

Holland and Feltham (2006) extended this model to two horizontal dimensions, with depth–integrated conservation equations. In this model, the ocean is represented as a two-layer system consisting of a buoyancy-driven plume layer at the ice interface, which overlies a static ambient layer with horizontally uniform stratification. This two layer system is typical of Greenlandic fjords (Hewitt, 2020). Later, Gladish et al. (2012); Dallaston et al. (2015) and Sergienko and Hindmarsh (2013) coupled the model to the Glim-

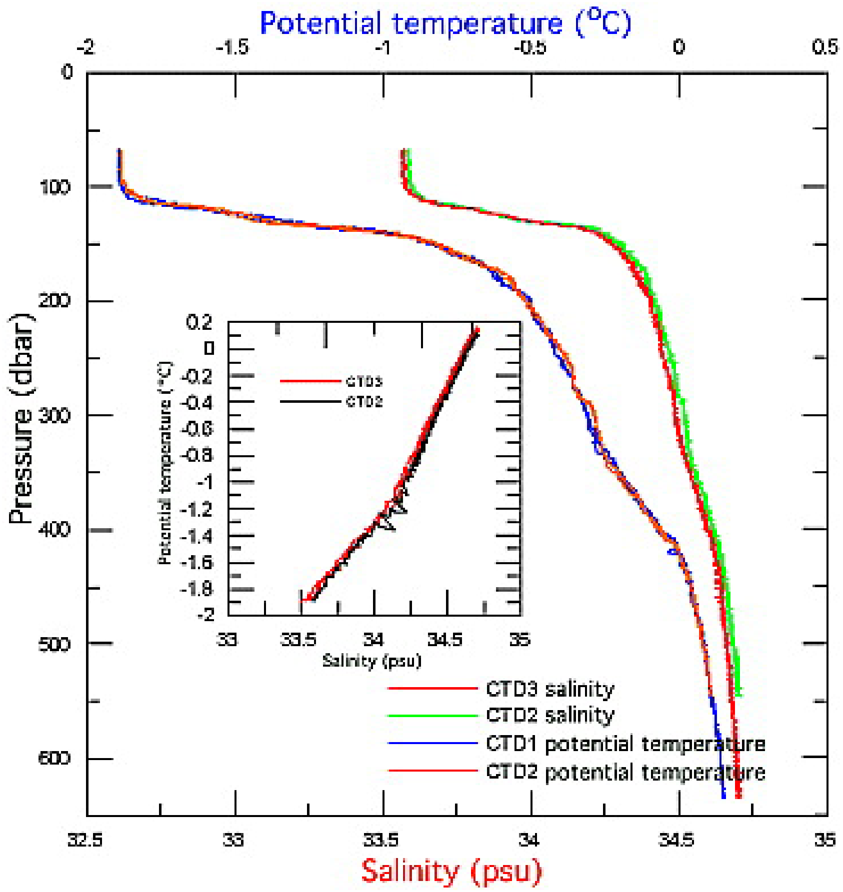

Figure 4.1: Temperature and salinity profiles beneath a channel in the Petermann Glacier in Greenland Rignot and Steffen (2008). A CTD instrument is measured the salinity, temperature, and pressure of water. 1 dbar = 1 meter of sea water.

mer Community Ice-Sheet Model (Rutt et al., 2009) to model basal channel formation in the presence of an advecting ice shelf. Gladish et al. (2012) used the coupled models to describe the effect of basal channels on ice shelf melt rates. They imposed two wavelengths of cross-flow roughness upstream of the grounding line to simulate topographic features. These features introduce grooves in the ice bottom that initiate melt channels downstream. Gladish et al. (2012) suggest that ocean-induced melting, combined with rapid ice flow, deepened the existing channels and reproduced similar channelised basal morphology to that observed at the Petermann Glacier Ice Shelf in Greenland. In these model runs, introducing narrow channels suppressed melting at broader spatial scales, ultimately reducing the total amount of basal melt. The same coupled ice–plume model was used by Sergienko (2013) to explore the conditions conducive to channel formation. Their simulations suggest that channels form in response to melt water plume flow initiated at the grounding line if there are relatively high melt rates and if there is variability in ice shelf thickness transverse to ice flow.

Alternatively, Millgate et al. (2013) used the full three dimensional Massachusetts Institute of Technology general circulation model (MITgcm, described in detail in Section

4.3.3.1) to look at the impact of channels on melt rates on the Peterman Glacier tongue. They considered an idealised static ice shelf boundary and used an ice shelf basal mass balance package (Losch (2008), described in Section 4.3.3.2) to approximate ice shelf melt. By simulating multiple model ice shelves with different numbers of channels, Millgate et al. found that having more channels reduced larger scale circulation which in turn reduced average melt rates under the glacier tongue. To model ice shelf melt Millgate et al. (2013) used an ice shelf basal mass balance package ('shelfice') developed by Losch (2008). This package has been used both to estimate ice shelf melt on real–world ice shelves (e.g. Goldberg et al., 2019), and as a laboratory to better understand ice–ocean processes (e.g. Xu et al., 2012). MITgcm functions on a large range of scales, for example, Xu et al. (2012) used high resolution grid cells of 20 m wide to model an ice shelf front, wheras Naughten et al. (2021) use grid cells up to 50 km to model the Filchner–Ronne Ice Shelf.

A sensitivity analysis of MITgcm and 'shelfice' found that the combination can successfully reproduce melt rates estimated using satellite altimetry (Goldberg et al., 2019). In Goldberg et al. (2019), melt rates at the grounding zone were found to be highly sensitive, in particular to bathymetry. Accurate bathymetry was important for reproducing melt rates around the grounding zone because bathymetry impacted the transport of warm salty bottom water to the ice shelf. When comparing melt parametrisation, a velocity-independent melt model successfully reproduced the high melt rates observed near the grounding line, however, this parametrisation was believed to oversimplify melt when fast velocities were important, such as strong channelisation or subglacial discharge.

Carroll et al. (2017) used MITgcm to model a fresh water plume driven by subglacial discharge in a fjord. Similar to a sub–ice–shelf channel, this featured a laterally confined domain and estuarine flow with tides simulated by imposing an oscillating velocity on the open ocean boundary. Carroll et al. (2017) found that in wider fjords ($\approx$ 10 km) circulation cells develop which increase the residence time of subglacial outlet water.

In this chapter, we aim to better understand and constrain ocean processes in a basal channel at the grounding zone of the Kamb Ice Stream, using an ocean model to extrapolate from the existing knowledge of the channel shape and channel melt (described in Chapter 2), and nearby oceanographic observations (described in Section 4.2). Firstly, we aim to better constrain subglacial discharge, which we assume causes the formation of the channel (Chapter 2). Secondly, we aim to better describe meltwater plume dynamics by modelling melt without first assuming that a plume is driving melt. Lastly, we aim to understand how the channel is interacting with the ocean, constraining the connection between the channel cavity and the larger Ross Ice Shelf cavity.

To address these goals, we use MITgcm to model a channel with a domain shape based on its surveyed bathymetry (described in Chapter 2). Ice-ocean interaction is modelled with the 'shelfice' package, whereby the ice boundary is considered static. We run seven experiments using different boundary conditions (Section 4.3.2), as well as an eighth experiment which uses a contrived domain shape and has an ice shelf boundary which is adaptive in time. The term 'cavity' is used to describe the channel cavity described in Chapter 2, not the larger Ross Ice Shelf cavity, unless specified. The Ross Ice Shelf cavity, as a relatively large ocean body, is referred to as the 'ocean' when describing exchange with the channel cavity.

We start by describing the domain shape used to model the surveyed channel (Section 4.3.1). We next describe the different model setups (Section 4.3.2), before explaining the MITgcm set up, and its treatment of the ocean (Section 4.3.3.1 and ice shelf (Section 4.3.3.2). We outline the process followed to model active melt in the adaptive domain (Section 4.3.5) Next, we describe the model outputs one by one: 'Control' (Section 4.4.1), 'Weak inflow' (Section 4.4.2), 'Medium inflow' (Section 4.4.4), 'Surge inflow' (Section 4.4.5), 'More ocean connection' (Section 4.4.6), 'Fast inflow' (Section 4.4.7), and 'Adaptive domain' (Section 4.4.8). In these model runs, our initial and boundary conditions are based on direct oceanographic observations of the ice shelf cavity nearby.

4.2 Study area

Here, we present a study of ice–ocean interaction in a basal channel at the grounding zone of the Kamb Ice Stream (location in Figure 4.2). The channel extends 6 km upstream of the previously estimated grounding line of the stagnant Kamb Ice Stream, and incises up to 50 % of the ice thickness. The channel is manifest on the ice surface as a 10,000 x 3000 x 20 m valley, and is visible from the ground and in satellite imagery. Because the channel sits at the outlet of estimated subglacial drainage paths (Chapter 2), the channel is likely formed by a buoyant meltwater plume triggered by subglacial discharge (Le Brocq et al., 2009; Kim et al., 2016; Alley et al., 2016).

While there are no observations of ocean conditions in the channel beneath the Kamb Ice Stream, two drilling campaigns have accessed the ocean cavity nearby. Fifty kilometres away from the channel at the field camp, 'KIS1' oceanographic instruments were deployed through a hole drilled through the 580 m thick ice shelf in 2019-20 (Robinson et al., 2020). The 30 m deep water column had two distinct layers (Figure 4.3). The top 18 m had temperature and salinity of -2.25 °C and 34.75 g/kg (Figure 4.3). The bottom 12 m had a temperature and salinity of -2.0 and 34.84 g/kg. 250 km along the coastline, Begeman et al. (2018) accessed the 10 m deep ocean cavity at the Whillans Ice Shelf. Similarly, temperature and salinity profiles (Figure 4.4) show two distinct layers. A 2 m deep fresh, cool layer with temperature and salinity of -2.3 °C and 34.73 g/kg was found above a layer with temperature and salinity of -2.0 °C and 34.87 g/kg. While these observations inform the set up of the model runs, melt rate and subglacial discharge estimates inform the model interpretation. In Chapter 2, we estimated melt rates to be more than 20 m/yr

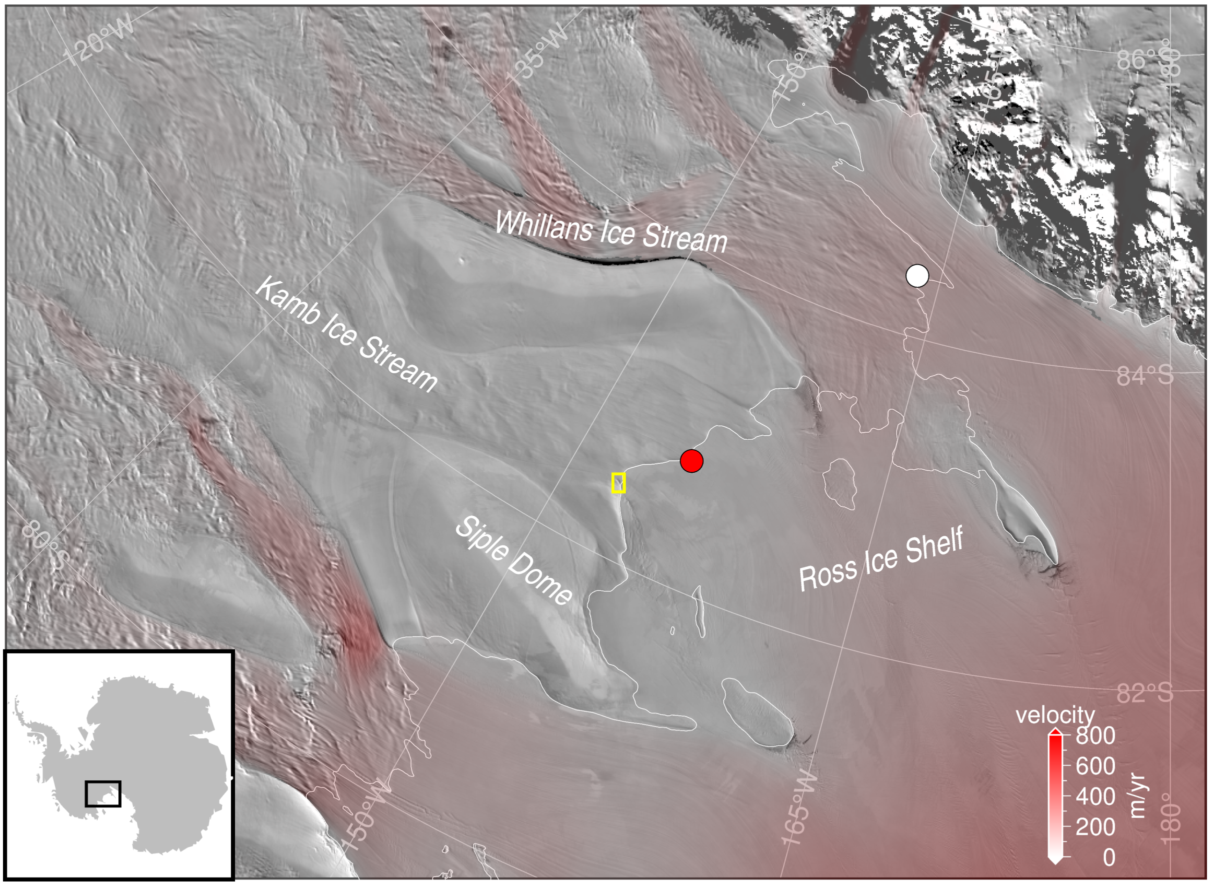

Figure 4.2: Locations of direct access near the grounding line of the Siple Coast. Drilling at 'KIS1' shown by red circle (Figure 4.3). Drilling at Whillans Ice Stream shown by white circle (Figure 4.4). Yellow square outlines channel and future drilling location.

over a 200 m x 1.5 km basal area at the head of the channel. Three and a half kilometres downstream, we found accretion across the channel, peaking at the channel apex, and melt on either side of the channel profile. Nearby at Whillians Ice Stream, Marsh et al. (2016) found melt of 22.2 ± 0.2 m/yr in a channel. Lastly, subglacial discharge from above grounding line was estimated by Le Brocq et al. (2009) to be 23.9 m^3/s.

4.3 Method

4.3.1 The prescribed domain

To investigate water circulation in the subglacial channel we considered a model domain based on the interpolated ice base map (Section 2.4.1.2), simplified for the constraints of a numerical ocean model. A smoother shaped cavity is easier to solve computationally. To construct the model domain, all radar lines crossing the channel were resampled spatially from the channel apex to both sides of the channel. Equivalent points from each line were then interpolated downstream with a weighted B–spline. The upstream–most

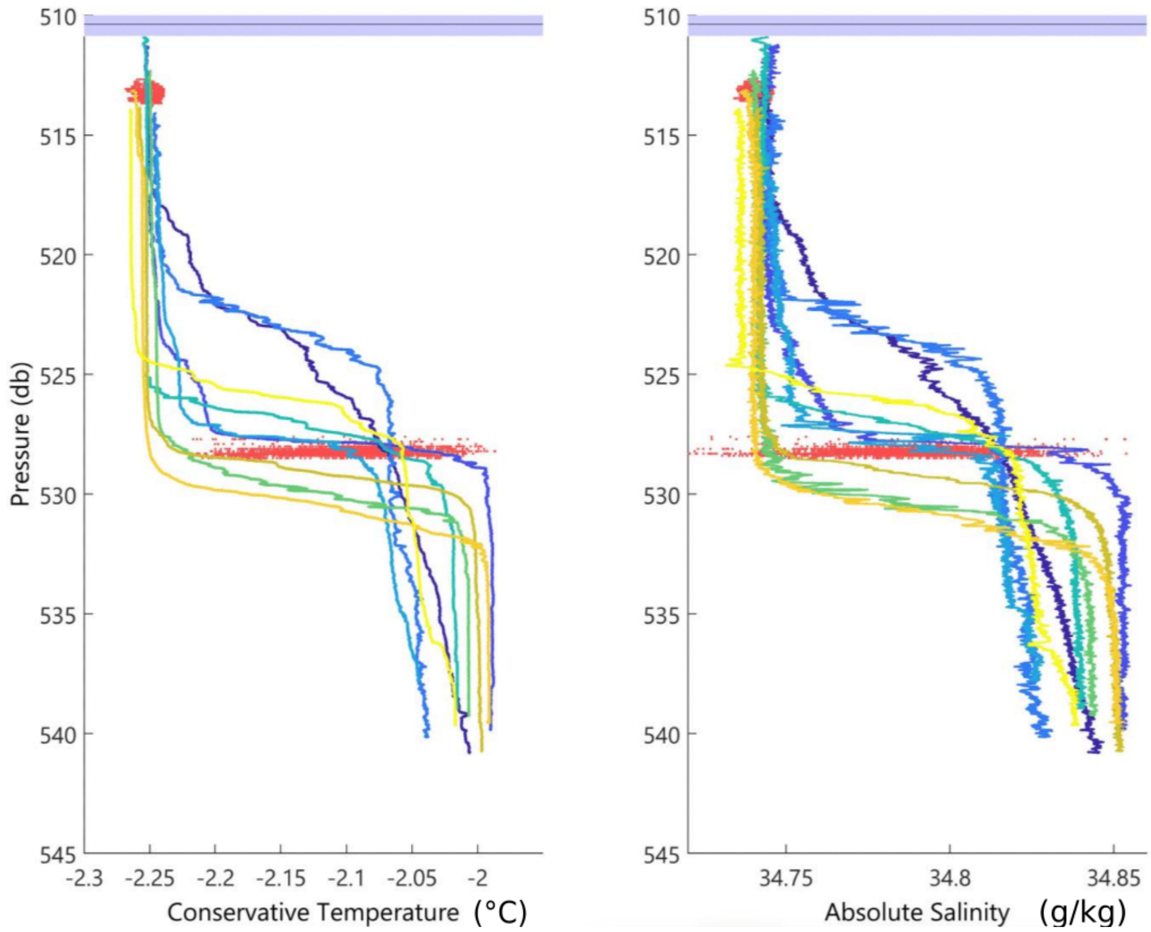

Figure 4.3: Figure from Robinson et al. (2020) showing temperature and salinity profiles beneath the Ross Ice Shelf at 'KIS1', 50 km from the channel study location. Different colors show profiles from different times over a two week long period. Location of direct access shown in Figure 4.2 as a red circle.

cross channel line was weighted 1 to constrain the channel inception then downstream points were weighted 0.1. This gave a smoother ice base map than that described in Section 2.4.1.2, with a standard deviation of the misfit in the vertical direction of 10 m. Additionally, the B–spline was smoothed such that $\Sigma((w(z-g))^2) <= 50$ where x is distance downstream, w is the weight given to a point, z is height and $g = g(x)$ is the smoothed interpolation of (x, z). The interpolated channel area was then cropped onto a flat plane at the level of mean ice base elevation, representing the model ground. The resulting shape was then rotated, and interpolated using nearest neighbours onto a regular grid so that the x direction was down channel and y direction was across the channel. Lastly, the shape was smoothed with an order zero convolution with a Gaussian kernel, with a standard deviation for the Gaussian kernel of 1. The channel length was cropped to exclude the upstream-most 8 m of the channel and 4 m of the downstream-most section. This created larger open boundaries, as the channel narrows at both ends. The domain was represented on a cartesian grid with (x, y, z) extent of (200, 100, 136)

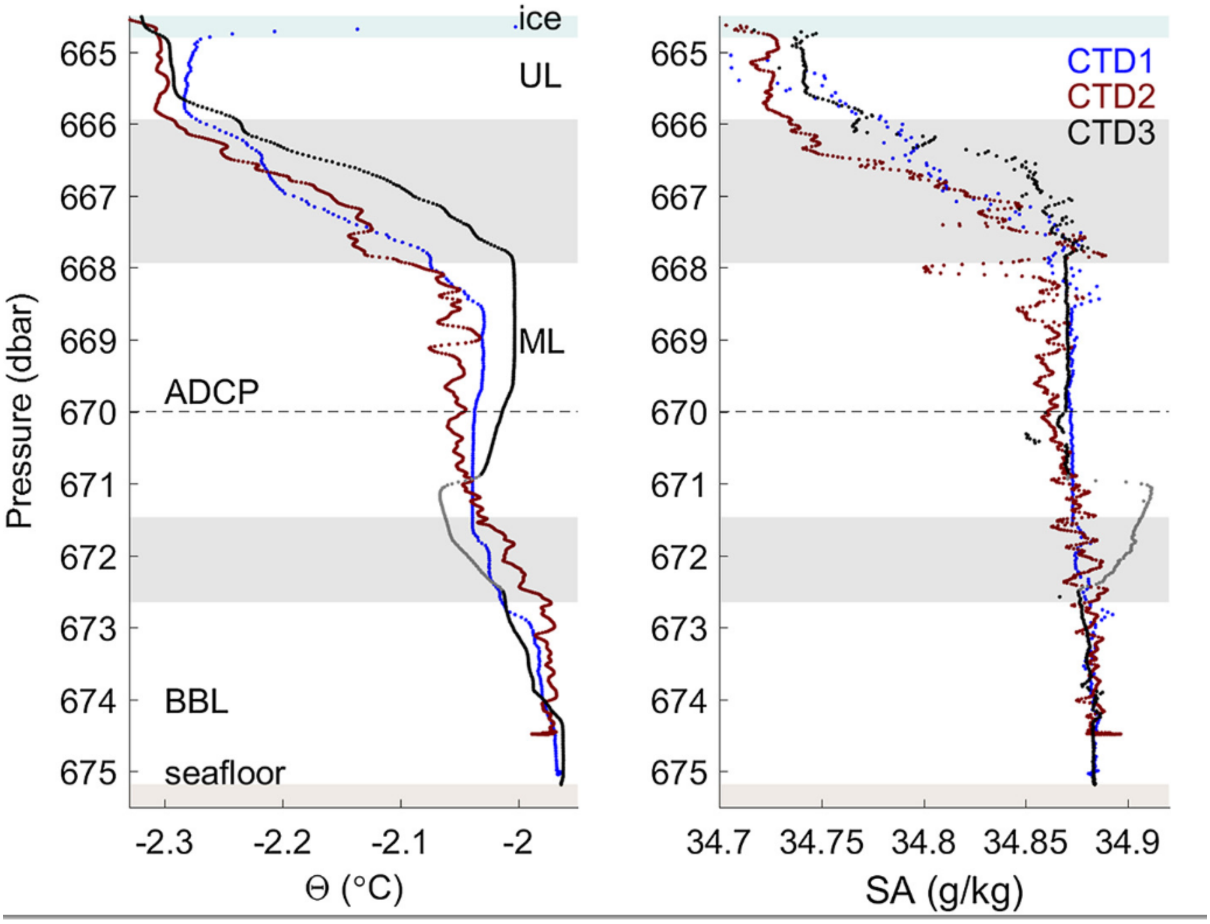

Figure 4.4: Figure from Begeman et al. (2018) shows temperature (θ) and salinity (SA) profiles beneath the Ross Ice Shelf at the grounding zone of the Whillans Ice Stream. Location of direct access shown in Figure 4.2 as a white circle.

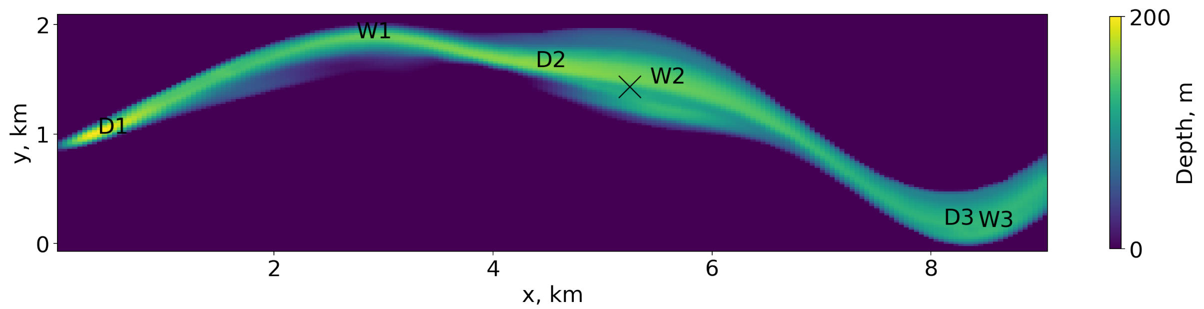

Figure 4.5: Domain shape used in model experiments. Colour shows the depth of the water column or height of the cavity ceiling. An ocean cavity bounded by ice spans 9.2 km between the upstream and downstream boundaries. W1-W3 are locally wide areas of the channel and D1-D3 are locally deep areas of the channel. X is the location of profiles shown Figures 4.8 and 4.15

respectively. Cells edges measure (45.4 m, 21.8 m, 4.0 m) respectively.

The resulting domain is 9.2 km long and 2.1 km wide (Figure 4.5 and 6.8). The sea–water filled channel is bounded by ice on its walls and roof, and an ice–free sea floor -675 m below sea level. The upstream boundary is designed to represent subglacial discharge entering the channel, and the downstream boundary represents the connection with the ocean. In this chapter, we use the terms upstream, downstream, true left, and true right for describing horizontal locations in the ocean cavity. True left and right are facing downstream. The terms top and bottom refer exclusively to vertical position in the water column.

Following down the apex of the channel, the ice roof of the cavity has local maxima in thickness of the water column of 200, 165 and 135 m at $x = 0.55$, 4.5, and 8.7 km which we name D1, D2 and D3 respectively (Figure 4.5). The channel is narrowest (130 m wide) at the upstream boundary. Downstream, the channel features three wide areas we name W1, W2, and W3 which are 460, 900, and 525 m wide at $x = 2.9$, 5.6, 8.6 km respectively (Figure 4.5). These wide areas correspond with bends in the channel. Between wide sections the channel narrows to around 300-350 m.

For each model run, the upstream boundary was prescribed with a constant temperature, salinity and velocity. At the downstream boundary, temperature (T), salinity (S) and the x–component of velocity (U) were prescribed with a logarithmic profile dependent only on height. This was calculated as a logspace which spans from the bottom (B) to top (T) of the downstream boundary (labelled V^d_B and V^d_T where d denotes downstream) along the height of the boundary, as follows, where $V \in \{T, S, U\}$,

$$\left(V^d_B \ldots V^d_T\right) = \begin{cases} 10^{(log_{10}|v_0|\ldots log_{10}|v_n|} + V^d_B - v_0, & \text{if } V^d_T - V^d_B > 0 \\ -10^{(log_{10}|v_0|\ldots log_{10}|v_n|)} + V^d_B - v_0, & \text{if } V^d_T - V^d_B < 0, \end{cases}$$

and all operations are element–wise. The vector $(v_0 \ldots v_n)$ is linearly increasing, and spans v_0 to v_n where $v_n = V^d_B - V^d_T - v_0$ and $v_0 \ll 1$. The parameter v_0 is used to tune the gradient of the profile, and $n - 1$ is the numer of cells which span the open boundary. Values $\left(T^d_B, T^d_T\right)$, $\left(S^d_B, S^d_T\right)$ and U^d_T were prescribed, then U^d_B was calculated so that flux out of the downstream boundary is equal to that flowing in through the upstream boundary. The area of the upstream boundary of the model domain is 5270 m^2. Boundary velocities of 0.0004, 0.01 and 0.1 m/s correspond to flow rates of 2.1 m^3/s, 52.6 and 526 m^3/s respectively.

4.3.2 Model run descriptions

The model was run with 5 second time steps, and was first spun up for 55 days with the run 'Control'. The run 'Control' had no prescribed flux, temperature or salinity at the boundary (it has Neumann boundary conditions), and an initial temperature and salinity of -2.0°C and 34.73 g/kg. All other model runs had initial conditions from 'Control' at 55 days, except 'Fast inflow' which had initial conditions from 'More ocean connection' at 8 days, and 'Adaptive domain' which is described in Section 4.3.5.

The model was run with different boundary conditions described in Section 4.1. The downstream boundary replicates ocean conditions from the Ross Ice Shelf cavity, with values taken from sub–ice–shelf observations made nearby by (Robinson et al., 2020). Temperature at the bottom and top of the downstream boundary are set to -2.0 °C and -2.25 °C and salinity at the bottom and top are set to 34.75 g/kg and 34.64 g/kg respectively. The upstream boundary simulates subglacial discharge, which is likely fresh or at least relatively fresh depending on how far upstream ocean water mixes with the discharge. The model run 'Fresh inflow' and 'Adaptive domain' have discharge with no salinity and at the pressure melting point. With these conditions the model cannot numerically converge with more than 0.4 mm/s velocity inflow at the upstream boundary (corresponding to a flow of 2.1 m^3/s). Most model runs have temperature and salinity of -1.213 °C and 16.46 g/kg which are halfway between the bottom water conditions of -2.0 °C, 34.75 g/kg and the pressure melting point. This represents a partially mixed subglacial discharge. Because its not fully fresh we can run the model with much higher velocities without the model failing. The model run 'Fast inflow' has a upstream boundary 3/4 of the way towards the pressure melting point from -2.0 °C, 34.75 g/kg. 'More ocean connection' and 'Fast inflow' have fresher output water on the downstream boundary on the ice-ocean boundary.

	T^u	S^u	U^u	T^d_T	S^d_T	U^d_T	v_0
Control	–	–	–	–	–	–	–
Weak inflow	-1.213	16.46	0.0004	-2.25	34.64	0.04	10^{-8}
Fresh inflow	-0.51	0.0	0.0004	-2.25	34.64	0.04	10^{-8}
Medium inflow	-1.213	16.46	0.01	-2.25	34.64	0.04	10^{-8}
Surge inflow — pre/post–surge	-1.213	16.46	0.0004	-2.25	34.64	0.04	10^{-8}
Surge inflow — surge	-1.213	16.46	0.01	-2.25	34.64	0.04	10^{-8}
More ocean connection	-1.213	16.46	0.01	-1.21	16.46	0.04	10^{-4}
Fast inflow	-1.61	25.6	0.1	-0.82	7.3	0.1	10^{-4}
Adaptive domain	-0.51	0.0	0.0004	-2.25	34.64	0.04	10^{-8}

Table 4.1: Subscript ^{u} and ^{d} denote upstream and downstream boundaries respectively. Superscript $_T$ denotes top of the water column. (T,S,U) have units of (°C,g/kg, m/s)

4.3.3 Model description

4.3.3.1 Ocean treatment

The MIT general circulation model (MITgcm) (Marshall et al., 1997a,b) is used to model the ocean and its interaction with the ice shelf in the ice bounded cavity. MITgcm is equipped to model metre length scale processes like turbulence and convection (Xu et al., 2012, e.g.). Because we are interested in sub-kilometre length scales we use a nonhydrostatic configuration with a free surface. Our configuration of MITgcm is based on ISOMIP experiments (Ice-Shelf Ocean Model Intercomparison Project) (Holland et al., 2003b). In each model timestep, MITgcm algorithms solve the Boussinesq form of the Navier Stokes equations for an incompressible fluid, with a spatial finite-volume discretization on a cartesian grid. The Boussinesq equations can be written as,

Conservation of momentum

$$\frac{\partial \mathbf{v_h}}{\partial t} = \mathbf{G_{v_h}} - \nabla_h p \tag{4.1}$$

$$\frac{\partial w}{\partial t} = \mathbf{G_w} - \frac{\partial p}{\partial z} \tag{4.2}$$

Continuity

$$\nabla \cdot \mathbf{v} = 0 \tag{4.3}$$

Heat

$$\frac{\partial T}{\partial} = G_T \tag{4.4}$$

Salt

$$\frac{\partial S}{\partial} = G_S \tag{4.5}$$

Equation of state

$$\rho = \rho(T, S, p), \tag{4.6}$$

Where the (x, y, z) components of velocity $(\mathbf{v})$ are $(u, v, w) = (\mathbf{v_h}, w)$, and $\mathbf{G_v} = (G_u, G_v, G_w)$ and (G_S, G_T) represent inertial, Coriolis, metric, gravitational and forcing terms. Pressure, from resting sea-level is p, T is potential temperature, S is salinity. These equations are solved on an Arakawa C–grid in the horizontal direction (Figure 4.6), and a Lorentz grid in the vertical (Adcroft et al., 1997). This leads to a tidy discretization of the incompressible continuity equation (Equation 4.3),

$$A^u_{east} u_{east} - A^u_{west} u_{west} + A^v_{north} v_{north} - A^v_{south} v_{south} + A^w_{up} w_{up} - A^w_{down} u_{down} = 0 \tag{4.7}$$

where $A_{heading}$ are the cell faces and (u, v, w) are the (x, y, z) components of $\mathbf{v}$. The horizontal momentum equation is solved with the projection method (operator splitting), in which the discretized equation (Equation 4.1) solves the pressure forces and viscous

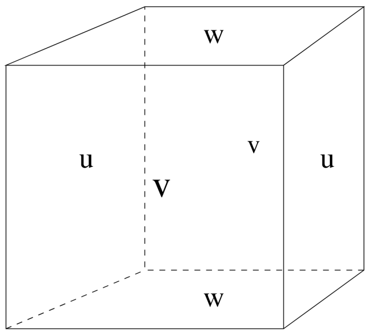

Figure 4.6: Three dimensional staggering of velocity components. (u, v, w) are the (x, y, z) components of velocity respectively. Each component of velocity is calculated on the cell boundary normal to the component direction. This facilitates the natural discretization of the continuity and tracer equations.

forces separately in two half steps.

$$\frac{\mathbf{v}^* - \mathbf{v}^n}{\Delta t} = G_{v_h} \tag{4.8}$$

$$\mathbf{v}^{n+1} = \mathbf{v}^* - \Delta t \, \nabla p^{n+1} \tag{4.9}$$

In the first half step (Equation 4.8), steps velocity $\mathbf{v}$ forward to find an intermediate velocity $\mathbf{v}^*$ by ignoring the pressure gradient term. In the second half step (Equation 4.9), the intermediate velocity is corrected to obtain the final solution of the time step $\mathbf{v}^{n+1}$. Substituting the two momentum equations (Equation 4.1 and 4.2) into the depth integrated conservation of mass equation (4.3) results in an elliptic equation which is solved for pressure. The algorithms used in this process are outlined in Marshall et al. (1997a) and Marshall et al. (1997b). Next we outline the model treatment of ice–ocean interation.

4.3.3.2 Ice shelf treatment

Ablation and accretion at the ice–ocean interface were paramerized by the MITgcm 'shelfice' package described in Losch (2008). This assumes that the ice shelf is stable and floating. 'Shelfice' solves the following three equations from Hellmer and Olbers (1989), describing the conservation of heat, the conservation of salt, and temperature as a linear function of salinity respectively.

$$\rho_0 c_0 \gamma_T (T - T_b) = m \rho_0 L + \rho_1 c_1 \kappa_1 \left(\frac{T_b - T_I}{H_I} \right), \tag{4.10}$$

$$\gamma_S \left(S - S_b \right) = m S_b, \tag{4.11}$$

$$T_b = a S_b + b + cd, \tag{4.12}$$

where m is basal melt rate (mass balance), H_I is ice-shelf thickness, and T_b and S_b are temperature and salinity at the ice-ocean interface, d is ice draft, and ρ_o is density of the ocean surface layer, with constants outlined in Table 4.2.

Specific heat capacity of water	c_o	53994	J/ kg °C
Specific heat capacity of ice	c_I	52000	J/ kg°C
Latent heat of ice fusion	L	3.34×10^5	J/ kg
Density of the ice shelf	ρ_I	917	kg/m^3
Molecular thermal conductivity of the ice shelf	κ_I	1.541×10^{-6}	m^2/s
Core temperature of the ice shelf	T_I	-20	°C
Linear freezing equation coefficients	a	0.0575	°C/psu
Linear freezing equation coefficients	b	0.0901	°C
Linear freezing equation coefficients	c	7.61×10^{-4}	°C / Pa
Vertical eddy diffusivity	-	5×10^{-6}	m^2s
Vertical eddy viscosity	-	1×10^{-4}	m^2/s
Coriolis parameter	$f0$	-1.446×10^{-4}	s^{-1}

Table 4.2: Table of constants

We used a velocity-dependent parameterization of thermal and haline transfer coefficients from Holland and Jenkins (1999):

$$\gamma_{T,S} = u_* \Gamma^f_{T,S} \tag{4.13}$$

where $u_* = \sqrt{c_d u_0^2}$ is the friction velocity, and $\gamma_T = 0.011$, $\gamma_S = 0.00031$ are the thermal and haline exchange velocities respectively. If the conduction of heat through the ice shelf is ignored, Equation 4.10 shows that the melt rate m can be solved as a product of the friction velocity, u_* and thermal driving $(T - T_b)$ (Holland et al., 2008). Basal melt rate is calculated from the ocean properties in the cell vertically beneath an ice cell (Figure 4.7). This takes the mean temperature and salinity from all cells within a distance dz (4 m) from the ice–ocean boundary, which could include a partial cell and a fraction of the full cell beneath it. In our configuration, partial cells with a minimum height of 30 cm were used.

Our configuration of MITgcm used a vertical eddy diffusivity of 5×10^{-6} m^{2}s and a vertical eddy viscosity of 1×10^{-4} m^2/s unless otherwise stated (Table 4.2). We used a non-linear 7th order advection scheme with a monotonicity preserving limiter. The Coriolis parameter $f0 = -1.446 \times 10^{-4}$ s^{-1} was set to be constant over the domain. This corresponds to the location of the channel, at a latitude of 82.47 S (Chapter 2). In the next section we outline the parameters and boundary conditions used in MITgcm model runs.

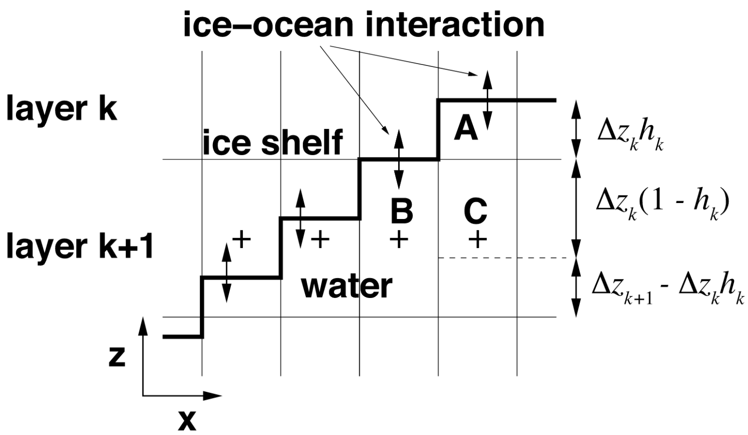

Figure 4.7: Schematic showing the MITgcm package 'shelfice' treatment of partially filled cells at the ice–ocean interface, copied from Losch (2008). Vertical gridlines are thin. The thick line is the model ice shelf base. Pressure gradient is computed at grid centres, marked as + signs. h_k is the fraction of a cell which is ice filled, $h_k \Delta z_k$ is the actual cell thickness.

4.3.4 Model limitations

Firstly, all inflow and outflow from the channel is prescribed. This will strongly influence the model output by constraining channel conditions. The downstream boundary controls the salt water input and fresh water output. The upstream boundary condition controls the initial strength of the meltwater plume, and input of fresh water. All of these are a control on melt rates and circulation in the channel. While both upstream and downstream boundaries are based on the best available data, they are not well constrained despite the fact they will have a strong influence on model results. For this reason, we run the model with a large range of upstream and downstream boundary conditions. Secondly, the channel bathymetry is unknown. As a result, we estimate that the bathymetry is as simple as possible, and assume that the bathymetry is at the base of the ice. This assumption could omit key features which change circulation in the channel, for example there could be gaps between the ice and the ground, or features in the ground topography. Lastly, MITgcm only melts the ceilings of grid cells, not walls. As a result, it is impossible for a plume to form on a vertical wall. This limitation may affect the formation of a meltwater plume and therefore melt and circulation in the channel. This is discussed in more detail in Section 4.5.

4.3.5 Adaptive domain

In a separate experiment, we modelled a simple ice–bounded cavity allowing for the evolution of the cavity in time, simulating basal ablation. The domain shape was different from that described above in Section 4.3.1. The initial cross sectional domain shape was a downwards opening parabola 1.4 km wide with a 56 m deep water column, with an ocean floor at -680 m depth. On the downstream cross section the left half of a downwards opening parabola creates an initial slope from 0 to 56 m above the ocean floor over 2.2 km, followed by a horizontally flat section to $x = 10$ km. The domain is represented on Cartesian grid with (x, y, z) extent of (50, 25, 170) so cells are (204 m, 67 m, 4 m) respectively.

The model was spun up for 7 days with no prescribed flux, temperature, or salinity at the boundaries, followed by a 5 day spin up with boundary condition described in Table 4.1. The model was then iterated over 500 times. At each iteration, the ocean model was run for 10 days with initial conditions as the final timestep of the previous iteration. Next, melt rate was multiplied by 10 days to calculate a basal mass balance over the period. This balance was added to the ice bathymetry and a new domain shape was created. Boundary conditions for the next iteration were recalculated so that they represented the new domain shape.

4.4 Results

4.4.1 Control

After 100 days of simulation, the 'Control' run, with zero flow through boundaries at the entrance and exit of the channel, has developed a steady circulation pattern. Water flows down the true right side of the cavity and up the cavity on the true left, with highest velocities (≈ 1 cm/s) at wide sections of the channel W1, W2 and W3, where circulation cells have formed. Two circulation cells form in each wide section of the cavity, separated at the local maximum in width. At W1, W3 and the upstream cell of W2, these cells move anticlockwise. In contrast, at W2 the downstream cell is moving weakly against background flow in the clockwise direction. At this point in time, temperature and salinity profiles are linear with depth. Temperature ranges from -2.15 °C at the top of the cavity to -2.0 °C at the bottom. Salinity increases from 34.68 g/kg to 34.72 g/kg from the top to bottom. Basal ablation is generally low, median ablation is 0.04 m/yr. Ablation is greatest (≈0.5 m/yr) in the bottom sections of the water column at the flanks of W1, W2 and W3, where ice is in contact with warmer saltier water.

4.4.2 Weak inflow of fresh water

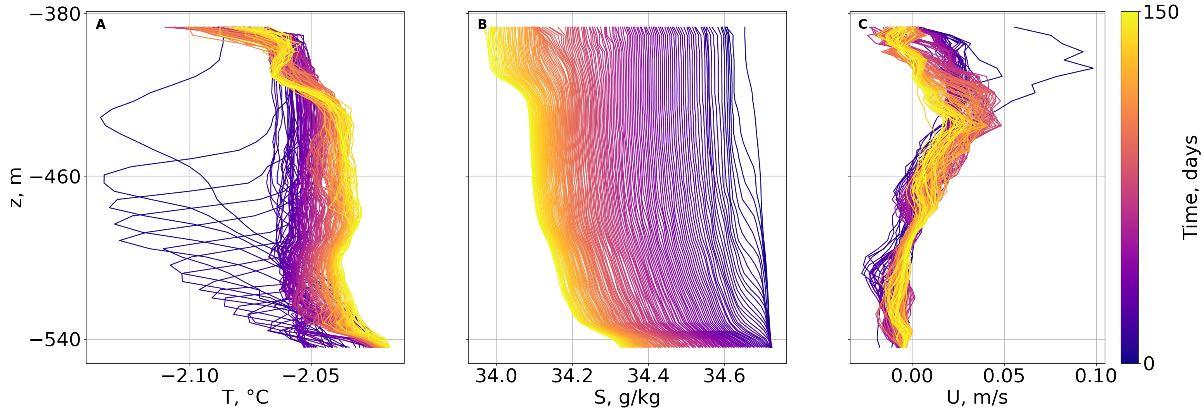

Figure 4.8: Vertical profiles of temperature (T), salinity (S) and x–component of velocity (U) over 150 days of the model run 'Weak inflow'. Location of the profile is shown by the black 'X' in Figure 4.5

The model run 'Weak inflow' (detailed in Section 4.3.2) features an upstream boundary condition with relatively fresh water flowing into the cavity at 0.4 mm/s (corresponding to a flow of 2.1 m^3/s). The cavity's initial temperature and salinity are from the spun up 'Control' run. The weak inflow of relatively fresh water from the upstream boundary introduces a fresh layer to the cavity. The layer flows downstream at 5 cm/s at the top of the water column and has temperature and salinity of -2.05 °C and 34.62 g/kg respectively. Underneath this layer, water is unchanged from initial conditions taken from

'Control' (Section 4.4.1). After one day, the fresh layer spans from the roof of the cavity to a depth of -475 m, at D1 and -425 m at D2 and but does not reach as far downstream as D3. It takes six days for the layer to extend downstream to the downstream boundary. By day six the layer has a horizontally uniform bottom boundary at -500 m.

The layer boundary is shown in Figure 4.8 A as the sharp corners to the true left of the plot. Over time this corner descends the water column, showing the thickening of this layer. This bottom boundary continues to lower until at around 20 days the inflow has flooded the cavity and stabilised, and no remnant of the initial conditions are visible. The inflow of fresh water corresponds to a region of strong basal ablation, initially up to 7 m/yr at the upstream boundary of the channel and 1 m/yr over larger regions in the channel centre at D2 and D3. By day six ablation has reduced to 0.75 m/yr at the upstream boundary. After around 20 days, ablation decreases in magnitude in the centre of the channel. Subsequently, ablation is strongest in the deeper ice at the flanks of the cavity. For the next 150 days ablation slowly decreases, with an upper decile 0.6 m/yr as the cavity water freshens with an inflow of fresher water (Figure 4.9).

By day 20 the salinity profile is smooth from 34.5 g/kg at the top of the water column to 34.7 g/kg at the bottom across the water column. There are no distinct layers with the exception of pockets of freshwater which accumulate at the ice boundary first at D3 then after more time at D2. After 150 days these pockets of fresh water are 40 and 15 m thick, and 34.0 g/kg and 34.1 g/kg at D2 and D3 respectively. After day 20 the cavity's temperature is relatively homogeneous, but starts to develop three layers. These layers become more distinctive over time. At 150 days water adjacent to the ice is relatively cool, -2.08 °C and -2.05 °C at D2 and D3 respectively. Beneath this cool layer, a warm layer (-2.03 °C) associated with the downstream flowing layer mentioned below sits between -410 m and -480 m. The bottom layer's temperature increases smoothly with depth from around -2.04 °C to -2.02 °C at the ocean floor at -545 m.

Circulation after 150 days is dominated by a downstream flowing layer moving at 2-5 cm/s in the top true right of the cavities cross section, and upstream flow at a similar speed in the bottom true left. This excludes the top 30 m of water in regions D1 and D2, which have water flowing upstream at around 5 cm/s. A plume has developed on the initial positive gradient of the cavity, with vertical velocities up to 5 cm/s. The plume is initiated from the upstream boundary at -475 m and raises to -425 m where it appears to detach and form the downstream flowing layer. With an inflow of relatively warm fresh water the temperature and salinity over the cavity do not converge but continue to change after 150 days, reaching median values of -2.037 °C and 34.15 g/kg respectively.

4.4.2.1 Model variations

The 'weak inflow' model run was repeated with an increase in vertical eddy diffusivity, which increases vertical mixing. After 150 days this results in a bottom layer 0.05 g/kg fresher than the model run with smaller vertical eddy diffusivity. This is the only noticeable effect of this change other than a general smoothing of conditions in the model output.

Additionally, the model was repeated with a downstream boundary condition designed to simulate estuarine flow with tidal variations. Velocities at the top of the boundary oscillated with a tidal period ranging from strong outflow to very weak inflow. Velocities at the bottom of the boundary were selected so that the downstream boundary had a net outflow of water to conserve mass with the upstream boundary flow. This boundary condition change had no noticeable affect on the model cavity.

4.4.3 Fresh inflow of water

The model run 'Fresh inflow' is similar to the run 'Weak inflow' except that the inflow of water at the upstream boundary has zero salinity (detailed in Section 4.3.2). Results are very similar to that described in Section 4.4.2, except that the model ocean cavity gets more fresh in less time. The initial fresh layer has temperature and salinity of -2.05 °C and 34.5 g/kg respectively. By day five the layer has horizontally uniform bottom boundary at -500 m, and it takes around 15 days for the layer to flood the cavity.

Basal ablation is as high as 9 m/yr at the downstream boundary of the channel, with a top decile of 1.5 m/yr. This ablation covers large regions in the channel centre around D2 and D3. By day five the top decile of ablation is reduced to 1 m/yr, and over the next 150 days slowly decreases to 0.7 m/yr as the cavity water freshens (Figure 4.9). The temperature and salinity profiles follow the same trend as described in Section 4.4.2, though with slightly fresher profile. By day 150 salinity ranges from 33.5 g/kg to 33.9 g/kg at depth, with a large pocket of relatively cool water developing at the channel ceiling. This layer ranges from 33.4 g/kg at D2 to 33.3 g/kg at D3 (Figure 4.10. Circulation is indistinguishable from that described in Section 4.4.2. With an inflow of relatively warm fresh water the temperature and salinity over the cavity do not converge but continue to change after 150 days, reaching values of -2.02 °C and 33.6 g/kg respectively.

4.4.4 Medium velocity inflow

The model run 'Medium inflow' (detailed in Section 4.3.2) features inflow water at the same temperature and salinity as 'Weak inflow' (-1.2 °C and 16.5 g/kg), but with a faster velocity, of 1 cm/s at the upstream boundary (corresponding to 52.7 m^3/s). The change in velocity of the boundary forms an initial plume with much greater melt rates, and

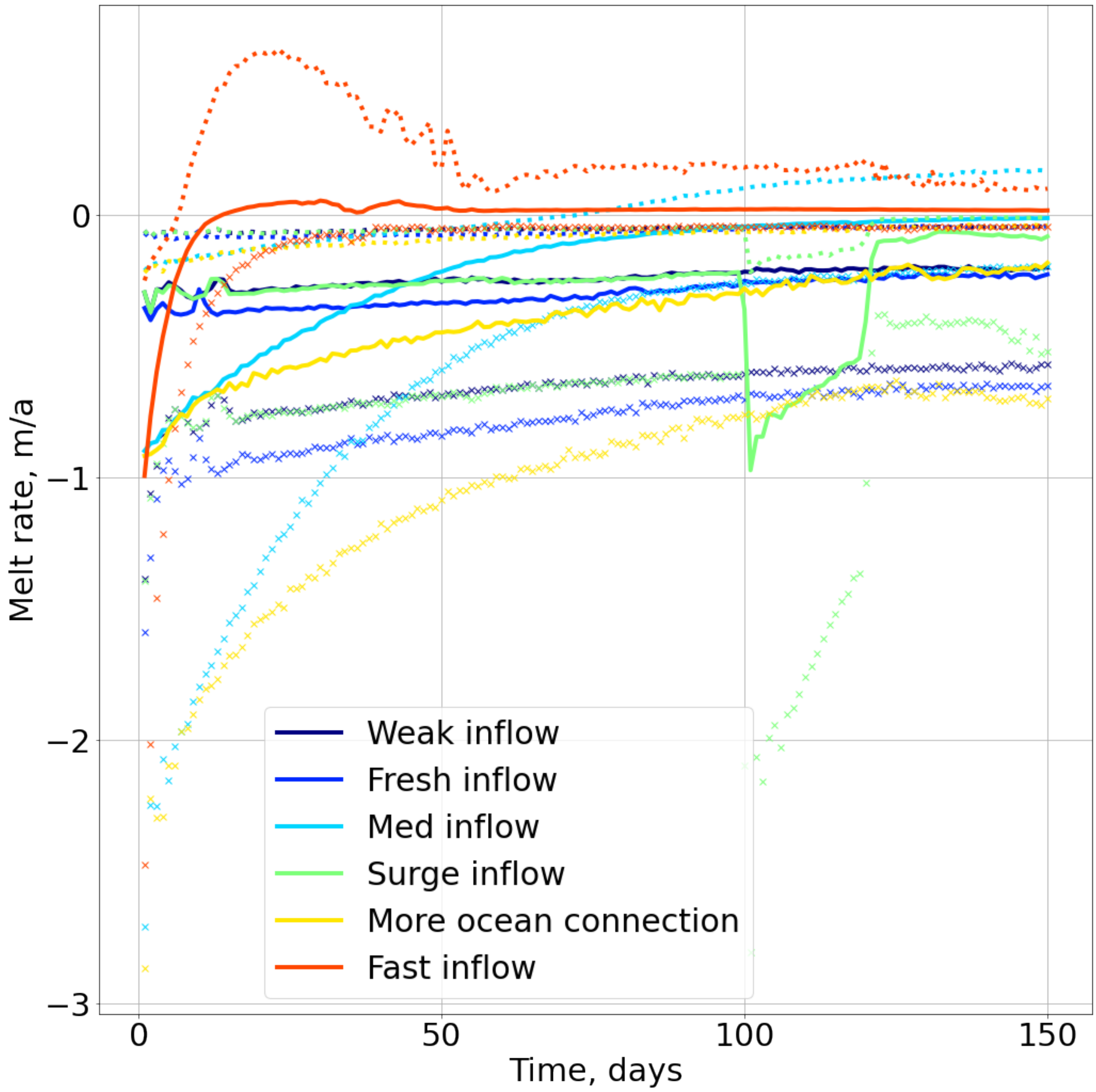

Figure 4.9: Time series of basal mass balance over the domain for each model run. Negative melt is accretion. Model run colour shown in legend, dotted lines with squares and x's show the lower and upper deciles for basal mass balance respectively. Solid lines show median mass balance.

the cavity freshens much faster, to the extent that accretion occurs in the channel centre (Figure 4.9 and Figure 4.11).

The initial inflow of water forms a fresh layer with temperature and salinity of -2.02 °C and 33.6 g/kg, which takes 2-3 days to reach the downstream boundary of the model. By day 7, this inflow has flooded the cavity. For this initial period, a plume causes ice ablation of up to 20 m/yr over a small area at the downstream boundary. The top decile of ice ablation is 3 m/yr of melt which is focused around the centre of the channel and extends down the length of the channel. As the cavity freshens, ablation decreases until it plateaus after around 80 days, with a top decile of 0.3 m/yr (Figure 4.9). This coincides

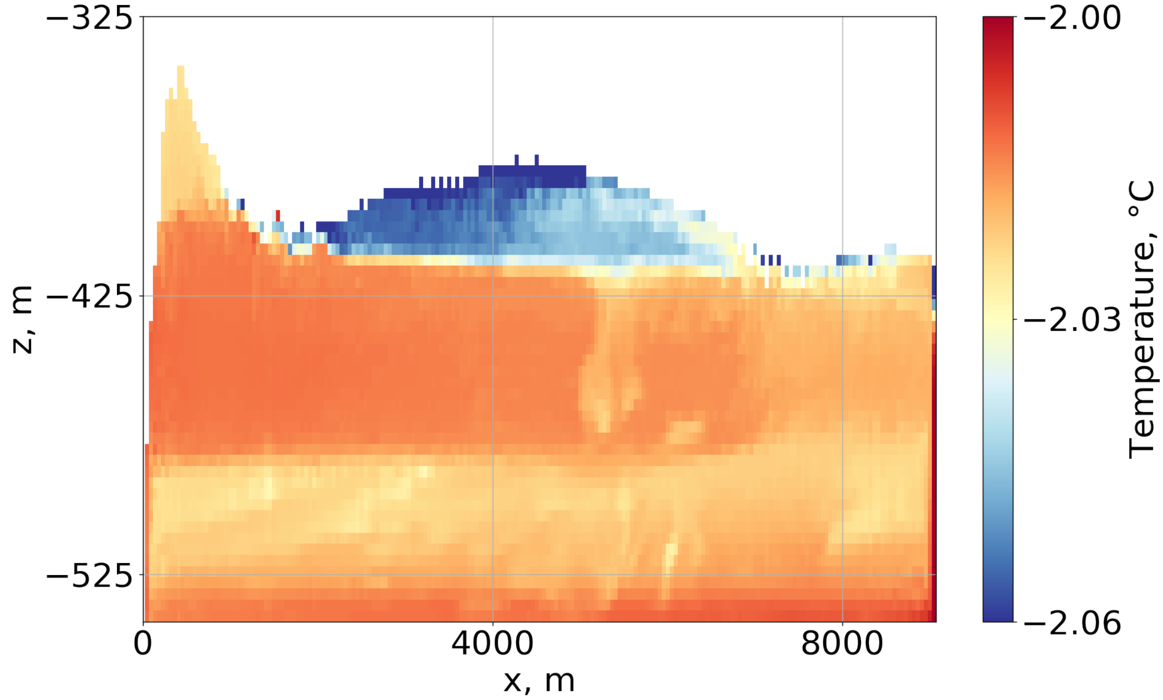

Figure 4.10: Temperature for 'Fresh input' model run at day 150 profiling the apex of the channel. Note this is not a linear profile, but winds along the channel downstream, each point is the maximum height along a lateral transect

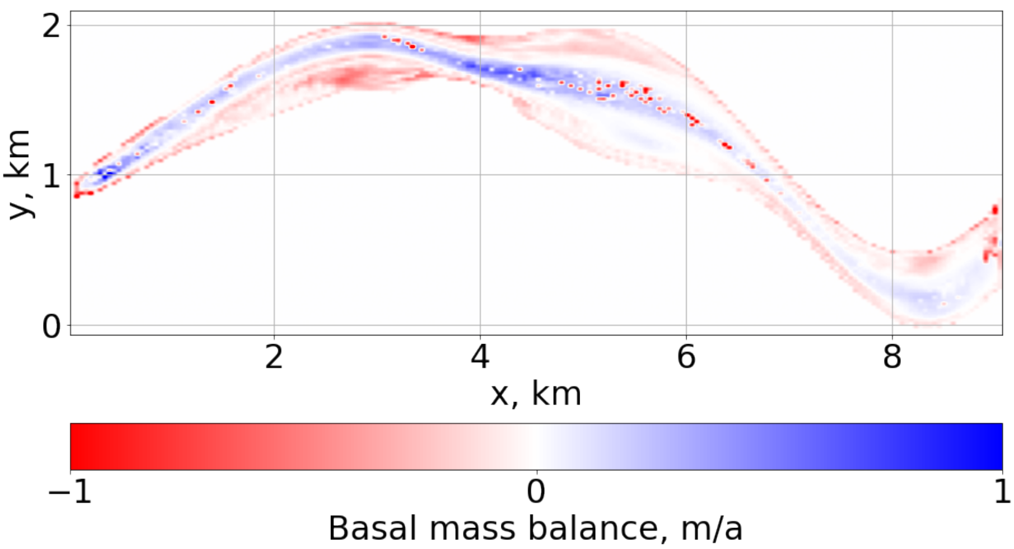

Figure 4.11: Ice shelf basal mass balance from 'Medium inflow' at 150 days

with water freshening to the pressure melting point at the top of the channel. At this time, basal accretion starts to occur, and by 150 days accretion of up to 1.4 m/yr occurs at inception of the channel. Accretion is focused (Figure 4.11) at the top of the water column at the centre of the channel 90-200 wide down the whole channel length. Local variability is shown by small regions of melt at the apex of the channel, within the region of accretion (Figure 4.11). This region is represented by the top decile of basal accretion which is 0.3 m/yr. Ablation continues to occur on the deeper parts of the ice on either side of the channel, and is up to 2 m/yr. Despite accretion occuring, net basal mass balance is positive after 150 days.

Circulation for 'Medium inflow' is shown in Figure 4.12, and is typical of most model runs. In the upstream half of the cavity, water flows downstream in the top half of the cavity (-350 m to -475 m depth) at around 3-5 cm/s and flows back upstream at the bottom half. In the downstream half of the cavity, at the wide parts of the cavity W2 and W3, weak horizontal convection cells form. The downstream flow trends to the top true left side of the cavity and water flows upstream at the top true right. In the narrow section of channel between W2 and W3 the top half of the water column flows uniformly downstream. The bottom layer of the cavity mostly flows upstream, but it also features weak horizontal convection cells at W2 and W3 with a clockwise flow at -510 m and an anticlockwise flow at -535 m deep.

Temperature and salinity through the cavity do not converge but continue to change after 150 days. Temperature and salinity do not show any layers, varying from -1.43 °C and 21 g/kg at the top to -1.5 °C 21.8 g/kg at the bottom.

4.4.5 Surge inflow

The model run 'Surge inflow' runs for 100 days with boundary conditions the same as 'Weak inflow' followed by a 20 day surge period with boundary conditions from 'Medium inflow'. At 100 days, the model looks like 'Weak inflow', and the top decile of ablation is 0.6 m/yr (Figure 4.9). Water is around -2.04 °C, except for a cool layer at the top and a layer 0.02 °C warmer in the bottom 10-20 m. Salinity is stable with depth, a fresh layer 10-20 m deep sits on top of a layer smoothly increasing from 34.2 g/kg to 34.4 g/kg at the sea floor. Water moves downstream in the top half of the water column at up to 4 cm/s and upstream in the bottom half at up to 2 cm/s (Figure 4.13).

The surge of fresher, warmer water takes two days to fill the length of the channel, at which point basal ablation reaches up to 17 m/yr over a small area at the head of the channel and a top decile of 2.8 m/yr (Figure 4.9) representing ablation down the centre of the channel (Figure 4.14). Velocities as high as 20 cm/s and 8 cm/s flow downstream in the top half and upstream in the bottom half of the cavity respectively. After 5 days these velocities weaken by around 25%. After 2 days of the surge, the top half of the water column is filled with water around -2.01 °C and 33.5 g/kg. This layer is fresher and warmer closer to the upstream boundary the channel. Cooler saltier water remains

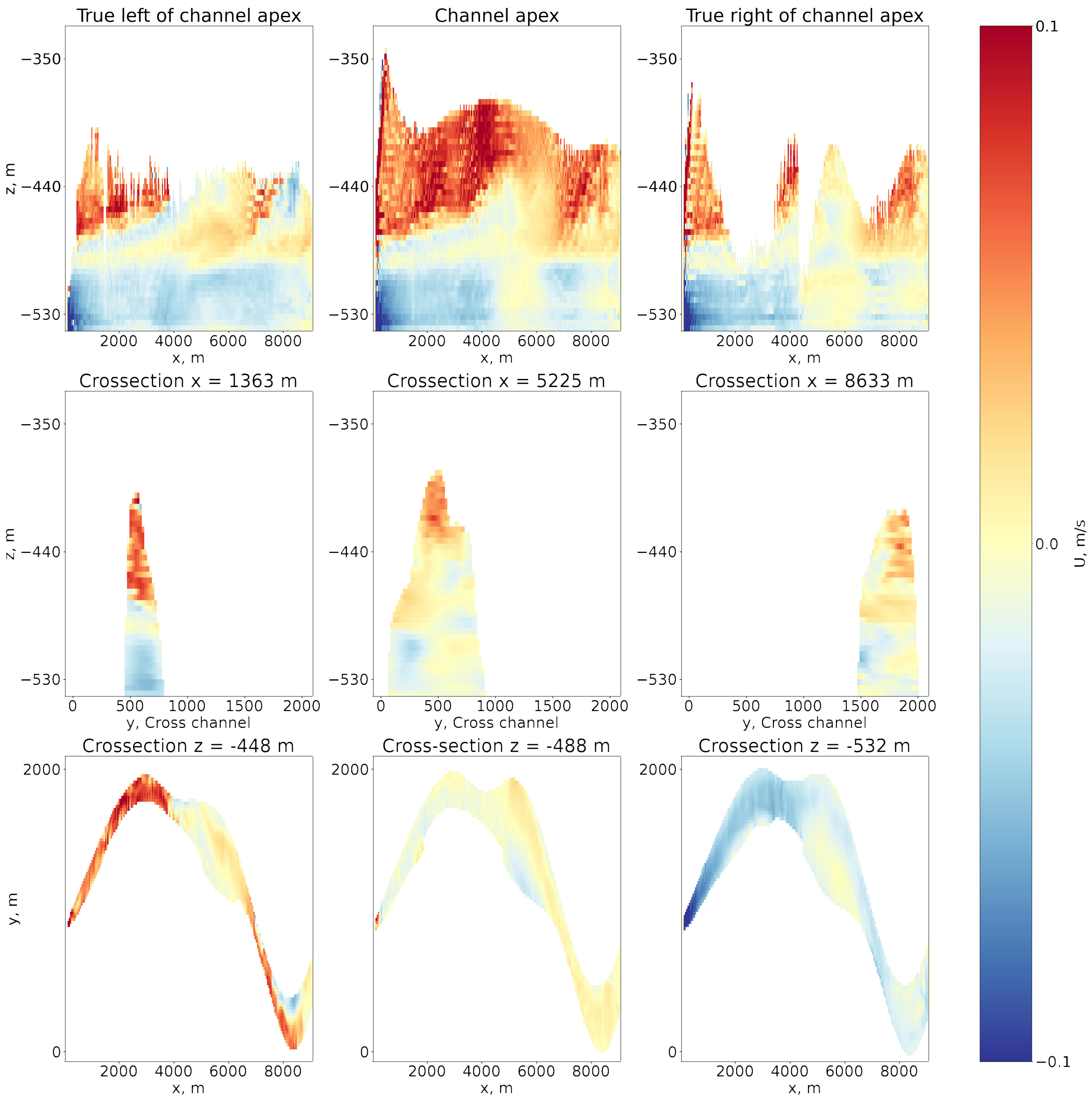

Figure 4.12: U (x–component of velocity) from 'Medium inflow' at 150 days. Note that axes are not equal scale.

beneath the layer. After 5 days of surge the distinctive bottom layer is not visible. For the remainder of the surge, the ocean conditions become more homogenous. After 20 days of surge, the water column smoothly increases in salinity from 32.0 g/kg at the sea floor and converges to 30.5 g/kg at the top of the water column. Temperature warms from -1.9 °C at depth to -1.95 °C (Figure 4.15).

When the surge stops, velocities shrink to near zero at the top of the water column, triggering a drop in melt rates. The top decile of melt rates drops from around 1.4 to 0.4 m/yr (Figure 4.9). A weak flow around 3 cm/s circulates water in a layer that spans from -450 to -540 m deep. Over the 30 days post-surge, the gradient in temperature and salinity of the bottom water shrinks as the salty bottom half of the water column

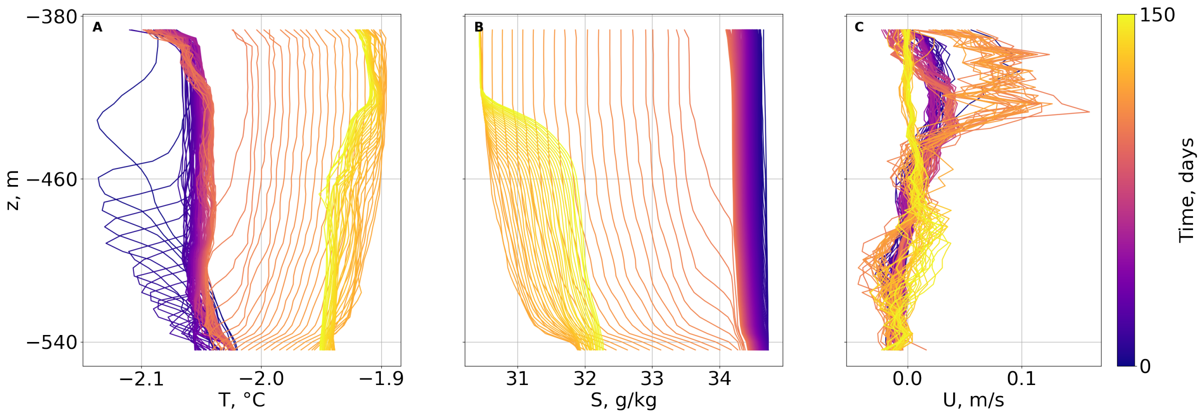

Figure 4.13: Vertical profiles of temperature (T), salinity (S) and x–component of velocity (U) over 150 days of the model run 'Surge inflow'. Location of the profile is shown by the black 'X' in Figure 4.5

becomes more homogeneous. The gradient in temperature and salinity of the top section of the water column increases as water near the top of the water column becomes fresher. Maximum and minimum temperatures and salinity at the top and bottom of the water column remain roughly the same as described above. A distinct layer forms at the top 30-40 m of the water column with temperature increasing with depth and a constant salinity of 30.5 g/kg.

4.4.6 More ocean connection

The model run 'More ocean connection' has the same conditions as 'Medium inflow' (described in Section 4.4.4) except the downstream boundary condition simulates more circulation with the larger Ross Ice Shelf cavity. Flux is stronger both outwards at the top of the boundary where water is fresher, and inwards at the bottom of the boundary where water is saltier (Table 4.1). This has the effect of slowing the decrease in salinity in the cavity, which is caused by the inflow of fresher water from the upstream boundary. Because the inflow of fresh water in 'More ocean connection' is identical to that in 'Medium inflow', the first part of the model runs are indistinguishable. The longer term (100 days) trajectory of runs are different (Figure 4.9 and 4.15).

Unlike the run 'Medium inflow', temperature and salinity converge to a value constant in time. At day 150, the converged temperature and salinity vary from -1.8 °C and 28 g/kg at the top of the water column to -1.85 °C 30.5 g/kg at the bottom (Figure 4.15). At this time, downstream flow is concentrated in a layer between -435 and -480 m. This layer is around 0.05 °C warmer than water above and below. This differs from 'Medium inflow', where downstream flow is at the top of the cavity for the duration of the model run (Figure 4.15).

The top decile of ablation, representing large areas first in the centre channel and

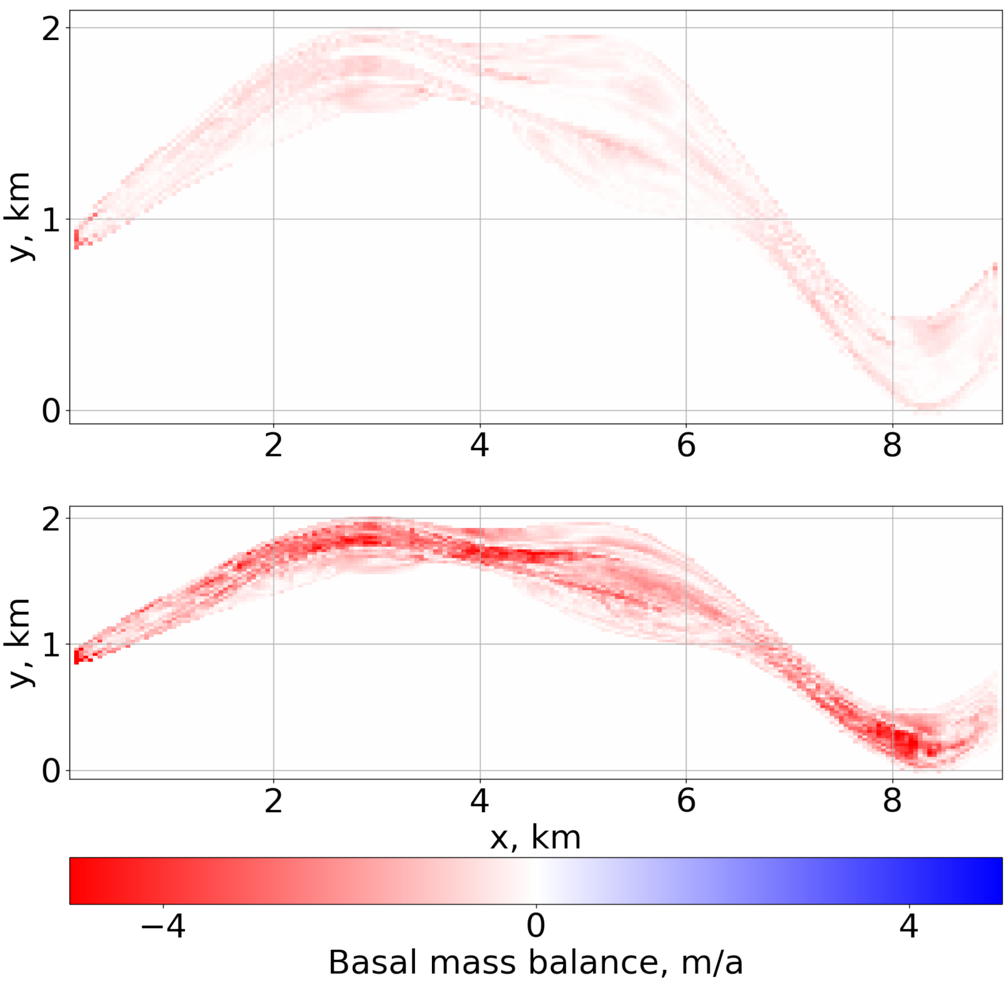

Figure 4.14: Basal mass balance of the model ice shelf showing 'Surge inflow'. Top: Basal mass balance at 99 days before the surge in inflow velocity. Bottom: Basal mass balance at 101 days during the surge in inflow velocity. See Figure 4.9 for time series of median melt over the surge.

later moving to the sides of the cavity, eventually converges to 0.75 m/yr (Figure 4.9). No accretion occurs in the model run. Circulation differs from 'Medium inflow' in that by 150 days the convection cells which develop early in the model run largely break down. The cavity develops downstream flow at the top half and upstream flow at the bottom half (Figure 4.15).

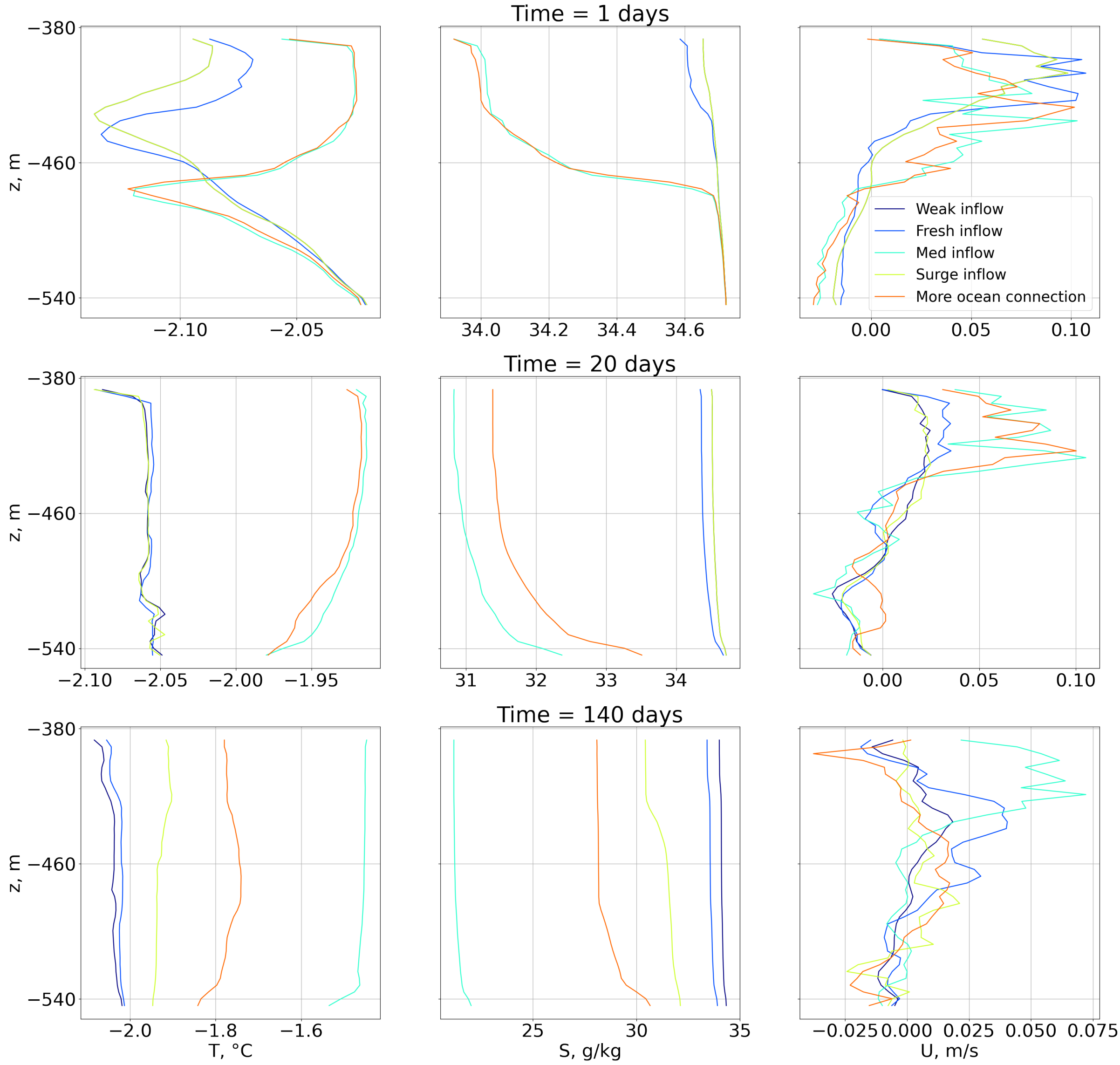

Figure 4.15: Vertical profiles of temperature, salinity and x–component of velocity for all model runs at 3 points in time.

4.4.7 Fast inflow

The model run 'Fast inflow' features a 10 cm/s inflow of relatively fresh water from the upstream boundary (detailed in 4.3.2). This run differs from other runs, in that initial conditions are taken from 'More ocean connection', not from the 'Control' run. The cavity starts with relatively fresh warm water, with a median of 30 g/kg and -1.85 °C. Despite this, initial melt is high, with maximum basal ablation of 15 m/yr and a top decile of 2.5 m/yr (Figure 4.9). Temperature and salinity profiles initially vary from -1.75 °C and 27 g/kg to -1.9 °C and 32.0 g/kg from top to bottom. The upper half of the cavity is cooler and fresher close to the upstream boundary and the bottom half is homogeneous. The water column then stabilises after little time. The top decile of accretion peaks at 0.6 m/yr around 20 days (Figure 4.9). From around 30 days, temperature is relatively constant with depth, at -1.3 °C and 25.7 g/kg respectively. Between day 40 and day 45, the top 60 m develops distinct pockets of fresher cooler water which sit on top of a homogeneous layer (as in Figure 4.10). While the top layer continues to cool and freshen for the next 100 days, the bottom layer is relatively constant at around -1.2 °C and 16.5 g/kg. As in other model simulations, (Figures 4.15 and 4.12) the cavity shows a downstream flow at approximately 5 cm/s in the top half of the water column and upstream flow in the bottom half. However, distinct from other models, at 40 to 45 days this layer collapses and flows under the top layer left of the channel at around 3-5 cm/s, and the top of the cavity cross section shows weak upstream flow.

4.4.8 Adaptive domain

'Adaptive domain' has a different domain shape (Figure 4.16 T=0) to other model runs. Unlike all other runs, the modelled ice boundary can ablate, changing the shape of the domain through time. The upstream boundary condition has a slow influx of fresh water identical to 'Fresh input'. The spun up 'Adaptive domain' features a downstream flowing layer which flows up the sloped roof at the upstream side of the cavity, flowing at up to 20 cm/s. At -640 m depth, the downstream flowing layer stops flowing up the sloped roof and detaches from the ice. It then flows horizontally down the length of the domain at around 10 cm/s, trending to the true left wall. Below this downstream flowing layer, water flows upstream. Above this downstream flowing layer, water is stagnant and relatively fresh, at 28-30 g/kg. Below this stagnant layer, salinity increases smoothly and linearly with depth from around 30.2 g/kg to 31.2 g/kg. The bottom of the downstream flowing layer does not correspond to a change in salinity. Temperature varies only slightly over the domain. While the downstream flowing layer is slightly warmer at -2.0 °C, the background temperature is -2.02 °C. The initial ice ablation pattern in the cavity shows ablation up to 4 m/yr on the upstream ramp and at the sides of the channel. Ablation is slightly stronger on the true left side than the true right. The centre top of the cavity where the stagnant fresh water sits shows accretion of around 0.1 m/yr.

When the ice walls and roof are ablated over time, the domain changes in shape to become more square (Figure 4.16 T=400). Ablation is strongest closer to the upstream boundary, so the lower portion of the sloped roof is ablated first, losing its slope (Figure 4.16 T=100). As the leading boundary of the cavity ablates upwards, the ablation rate immediately downstream follows, because the deepest ice generally shows strongest ablation. As a result, the slope uniformly ablates upwards until it forms a flat roof (Figure 4.16 T=100). With stronger ablation on the sides of the cavity, the cross sectional shape also becomes more square (Figure 4.16 T=400). This is partially due to limitations in the model, the model cannot ablate sides of cells, only the cell tops. The cavity takes around three years to ablate to a square shape. The front roof of the cavity then continues to

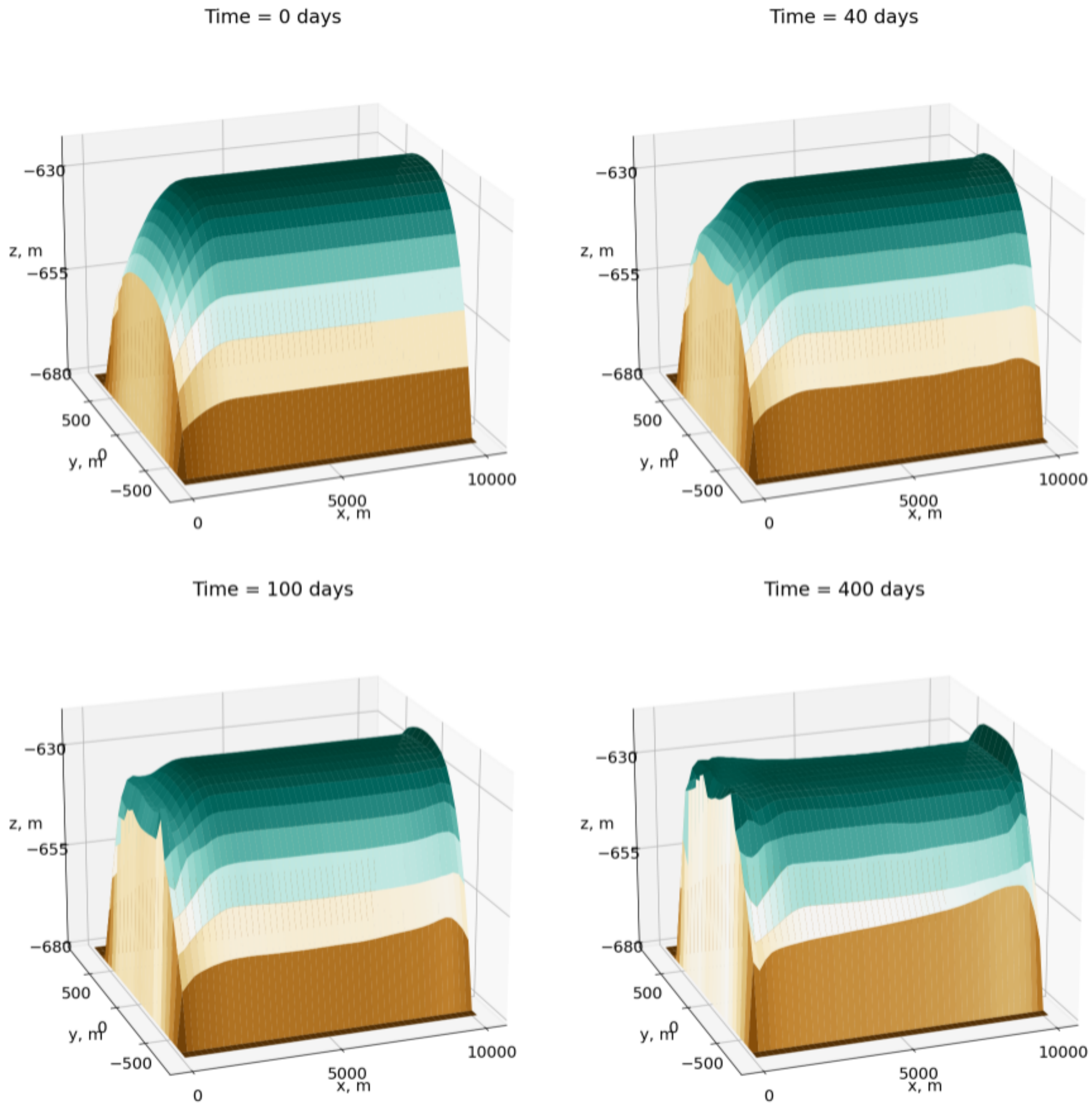

Figure 4.16: The shape of a model cavity 'Adaptive domain' at different points in time. Colour depicts depth.

ablate, forming a negative gradient in the roof.

4.5 Discussion

4.5.1 Constraining ocean processes

This chapter aims to better constrain the cavity conditions, using the MITgcm ocean model to extrapolate from the observations described in Chapter 2. In particular, we aim to better constrain subglacial discharge, meltwater plume dynamics and the connection between the channel and the ocean.

In Chapter 2, we identified a 200 m x 1.5 km region of basal ablation around the inception of the channel. We estimated the region to have ablation rates over 20 m/yr. While the model runs showing the strongest ablation successfully reproduce rates of 20 m/yr, they only do so over a small 200 x 50 m area. Through all model runs, ablation rates are significantly lower over an area this large. The model run 'Surge inflow' has the highest ablation rates (Figures 4.14 and 4.9). In 'Surge inflow' ablation peaks at 20 m/yr over a very small region, and is around 4 m/yr over a region of comparable size to that in Chapter 2. In this section, we discuss the discrepancies between these results and theorise ocean processes which could explain the observations and model predictions.

4.5.1.1 Subglacial discharge

We suggest that high basal ablation rates are associated with pulses of subglacial discharge, such as those observed by Kim et al. (2016). Basal ablation is a function of velocity, temperature and salinity, though, at the cool temperatures present in the model cavity, changes in salinity largely drive changes in basal ablation. In all model runs presented, the highest ablation was at the start of a pulse of subglacial discharge. As each model run progresses, the basal ablation rates decrease due to a reduction in salinity over the model run. Inflow from the upstream boundary triggers a plume to form on the initial slope of the channel (Figure 4.12), where the highest basal ablation rates are shown (Figure 4.14). The plume flows downstream and up the channel ceiling through the majority of the cavity and ablates the ice shelf base through entraining salty water from the deeper ocean. Because the modelled channel is enclosed, the fresher plume eventually mixes with existing cavity water until it homogenizes the channel. This first reduces basal ablation because less salty bottom water is transported to the grounding line. Secondly, basal ablation is reduced by the freshening of the cavity. Thirdly, pockets of freshwater from basal ablation pool on the ceiling of the cavity (Figure 4.10), these pockets are cool and cause basal accretion (as in Figure 4.11).

While strong subglacial discharge is needed to trigger strong basal ablation, strong discharge also causes a reduction in basal ablation in the long term due to a freshening of the cavity. We therefore suggest that to experience the high ablation rates observed, the cavity experiences fluctuating basal ablation via the following process: 1. A strong pulse of subglacial discharge drives a plume, basal ablation spikes by entraining salty bottom water. 2. The top of the water column freshens to the extent that basal ablation stops. 3. The pulse of subglacial discharge stops and the channel mixes with the ocean over time, becoming salty.

In step 2 described above, once the cavity gets fresh enough, accretion occurs at the apex of the channel. The accretion map shown in Figure 4.11 follows a similar lateral pattern as ApRES observations detailed in Chapter 2. Accretion peaks in the centre of the channel and ablation is strongest away from the centre. In the model output, accretion transitions to ablation within the cavity, whereas ApRES observations show this transition at the edge of the cavity. This discrepancy could be due to the low horizontal spatial resolution of ApRES repeat measurements, and the fact ApRES cannot measure melt on steep walls due to off nadir reflections (Vaňková et al., 2021a). We do not directly compare modelled accretion rates with observations. While the ApRES can observe accretion, quantifying the rate is problematic due to the occurrence of multiple reflections from both the glacial/marine ice interface and also from the marine ice/water interface (Vaňková et al., 2021b).

Our model run 'Fast inflow' is at the limit of where the model will converge to produce an output and only runs when spun up from 'Medium inflow' which has already freshened. As a result, it does not test high velocity basal ablation with high salinity initial conditions. We estimate the ablation rate of 'Fast inflow' if the model run could have run with initial conditions from 'Control'. To do this, we assume that ablation depends only on salinity and linearly interpolate between salinity and the ablation rate in both the maximum and top decile. With a salinity of 34.5 g/kg the top decile of ablation rate is estimated as 5.5 m/yr. This value estimates basal ablation rates assuming we could have started the model with salinity similar to that measured in the larger Ross Ice Shelf cavity by Robinson et al. (2020), and takes the mean over 200m x 1.5km of pixels with the highest basal ablation rate.

Boundary velocities of 0.0004 m/s ('Weak inflow', 'Fresh inflow', 'Pre-surge inflow'), 0.01 m/s ('Medium inflow', 'Surge inflow', 'More ocean connection') and 0.1 m/s ('Fast inflow') correspond to flow rates of 2.1 m^3/s, 52.6 and 526 m^3/s respectively. In comparison, flow rates estimated by Le Brocq et al. (2009) are 21 m^3/s. Kim et al. (2016) estimate flood flow rates of 8 m^3/s by looking at draining and filling of lakes. We do not see an order-of-magnitude increase in melt rates by increasing velocities by an order of magnitude, and flow rates of 526 m^3/s are likely too large to be realistic. It is therefore likely that subglacial discharge fluxes are not the dominant factor in driving the higher melt rates we observe. High velocities may be restricted to a smaller channel cross section further upstream, so do not correspond to such large melt rates. Future modelling could restrict the size of the upstream boundary so that velocities are high without corresponding to high flux which inundates the channel with fresh water.

Previous studies have also suggested that the Kamb Ice Stream may see episodic discharge events. Kim et al. (2016) observed rapid draining and filling of subglacial lakes and Horgan et al. (2017) observed stepped, disjointed relict channel features, and theorised that either episodic drainage or stepwise grounding line retreat caused these features to form. Episodic discharge may cause the majority of ice–ocean processes such as melting plume formation or sliding to take place over small periods, through step–like change. To observe and model step–like processes, it is necessary to have a high temporal resolution. Current modelling of ice and ocean processes in the area (e.g. Holland et al., 2003b) uses low spatial resolution (>1 km) and assume that steady state processes dominate activity. Focusing on background processes risks underestimating the average activity by missing episodic events.

4.5.1.2 Meltwater plume dynamics

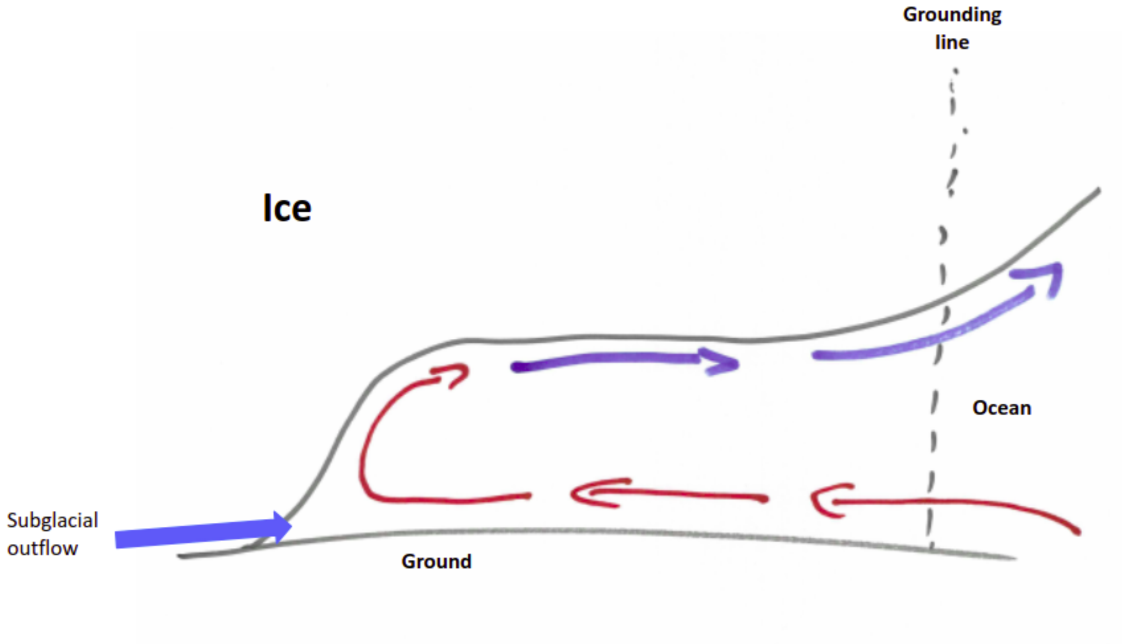

Figure 4.17: Schematic describing ocean circulation in the channel, based on model results. The schematic depicts a cross section down the apex of the channel. Red arrows describe the inflow of saltier water, which mixes with subglacial outflow to form a meltwater plume. As the plume melts and ascends it freshens and flows out to sea, depicted by blue arrows.

In accordance with subglacial plume theory, the model estimates the strongest basal ablation to be on the steepest slopes which have positive gradients in the downstream direction. In Figure 4.14, ablation is strongest at x=0, 4000 and 8000 m. Figure 4.12 shows these points are associated with positive downstream slopes. Unlike classic plume models which flow up a slope with a certain thickness (e.g. Hewitt, 2020), our model shows the plume has no solid bottom boundary but flows horizontally away from the ice as well as up. We can see this flow through the entire length of the channel (Figure 4.12). Downstream flow slows in locations in front and beneath negative downstream roof slopes. This suggests that the buoyant plume flow helps to drive downstream flow in the upper half of the water column (Figure 4.12).

These results indicate that the meltwater plume feedback is compatible with and enhanced by estuarine flow and vice versa (Figure 4.17). The estuarine flow of cool fresh water downstream along the top of the water column is propelled and driven by a meltwater plume, and the estuarine flow of salty water upstream at the bottom layer increases the connection with the ocean, replacing warm salt water and enhancing the melt plume feedback (Figure 4.12, 4.17). Additionally, we see that lateral effects of the channel shape are important in plume and estuarine flow development. The meltwater plume can be enhanced by a narrower channel which sees restricted lateral circulation, or slowed by a wider channel when circulation develops (Figure 4.12). These findings imply that topographical channelisation of a meltwater plume has a large effect on its behaviour, and as a result, a 1D plume model such as the Jenkins (2011) model generally used in channels (e.g. Marsh et al., 2016) is likely inadequate for predicting channelised plume flow. Because plume melt in channels behaves differently from unchannelised plumes, models should incorporate the dynamics of channelisation to accurately model ocean circulation and melt under ice shelves. This requires a much higher spatial resolution than is typically used in ice shelf cavity ocean models (e.g. Holland et al., 2003a).

4.5.1.3 Melt pattern

MITgcm outputs show that changing plume dynamics cause a change in the basal ablation rate pattern (e.g. Figure 4.14). In all model runs, basal ablation is initially at the top (ceiling) of the channel. After the plume has reached equilibrium with the channel (around 20 days), ablation weakens at the top but remains stronger lower on the channel walls (as in Figure 4.14). This is due to the existence of higher salinity water lower in the water column. This basal ablation pattern evolution has two implications. Firstly, for ablation to occur on the ceiling, plume water must be fresh relative to the cavity, suggesting it is episodic. Secondly, between surges of basal ablation, the channel will widen. This may explain the presence of wide parts of the channel. While the basal ablation rate pattern is similar to traditional plume models (e.g. Jenkins, 2011), in that accretion occurs downstream of the channel inception, it differs by showing the lateral variability of basal ablation rates.

These results indicate that the flow rate and change in flow rate influence the evolution of the shape of a channel. A constant flow or low flow concentrates melt in deeper water widening and slackening of the channel wall gradients. This would smooth channel shape, reducing its prominence and opposing the feedback between ice slope and plume melt (Figure 4.14). Alternatively, a high or non constant flow is shown to cause melt at the apex of the channel and cause an increase in the channel growth rate. These results suggest that episodic flow is an important part of the ice slope and plume melt feedback, in that a deep channel can only be incised with intermittent resalinification of the water.

The basal ablation generally has a pattern which squares the domain shape (Figure 4.16). While steep walls of the model output are similar to those observed in Chapter 2, they are partially caused by the model setup which cannot ablate sideways. The adaptive domain model shows that certain model shapes are more stable than others. In particular, a flat roof is relatively stable while a downstream slope produces a plume that ablates. Large changes can happen quickly and be followed by slow changes (Figure 4.16 100 and 400). Following this, we could see slower accretion, and widening of the channel from an ocean regime with melt lower in the water column as in Figure 4.11.

4.5.1.4 Ocean connection

Ocean conditions in the model outputs are atypical of sub–ice–shelf conditions. Because the area is enclosed and circulation with the ocean is limited, conditions in the cavity are dominated by the subglacial drainage processes. Results from this chapter show that the circulation pattern in the cavity affects basal ablation rates. With more circulation with the ocean, basal ablation rates are higher. Ocean exchange includes more incoming salty bottom water, and more outgoing fresh water as shown in Figure 4.17. This is shown by the lower ablation rates of 'Medium inflow' relative to 'More ocean connection', which are caused by less fresh water output—the two model runs are otherwise identical (Figure 4.9). Results show that in all model runs two layers develop with downstream flow on the upper layer and upstream flow on the lower layer, similar to estuarine flow. This flow pattern is conducive to replacing fresh cavity water with salty. This pattern appears especially strongly in the narrow sections of the cavity (Figure 4.12), but breaks down in the wide section W2, where cross flow circulation cells develop (Figure 4.5). It follows that we expect the wide section to slow the replacement of sea water and therefore reduce basal ablation rates. This is similar to findings of Carroll et al. (2017), whose model outputs show that wide fjords see slower replacement rates due to cross–fjord circulation. Additionally, a narrow channel with one–way flow could potentially enhance a plume by evacuating and efficiently replacing fresh plume water with salty bottom water.

Our results suggest that connection with the ice shelf cavity is important in driving melt due to the fact melting is enhanced by warm salty water found at the bottom of ice shelf cavities (as discussed by Goldberg et al. (2019)). This implies that bathymetry and ice base topography are important in modelling ice shelf mass balance, especially close to the grounding line where the shape of the ocean cavity controls the inward flow of bottom water. Most observed ice shelf basal channels form downstream of the grounding line (Alley et al., 2016), and are incised into a floating ice shelf above a body of ocean water (the ice shelf cavity). These channels are likely better connected to the ocean than the channel we model, which is flanked by grounded ice, and bounded by ground underneath. Close to the grounding line where channels exist above a small water column, there is likely similarly reduced connection to a larger body of ocean water. Additionally, because vertical transport of water is minimal in modelled channels, basal channels likely largely rely on horizontal movement of water masses to supply heat and salt required for melting. This would imply that basal channels above an ocean cavity are not necessarily better connected to an ocean than the channel which we model.

4.5.2 Limitations

4.5.2.1 Ocean exchange

It is feasible that the model is missing processes which allow basal ablation to cover a larger area or at a higher rate. Firstly, our model domain may underestimate the initial channel slope, therefore underestimating the initial plume strength. In Chapter 2 the initial channel slope was constrained as at least 45 degrees. We then smoothed the domain, resulting in a 35 degree downstream slope which may reduce buoyancy–driven feedbacks which produce a meltwater plume. Secondly, we may be under–representing the channel cavity to ocean exchange. More inflow would increase modelled basal ablation by reducing the freshening of the cavity and increasing the supply of salt to the ice base. While the observed cavity may have a larger inflow through the downstream boundary, there is no clear mechanism to cause this. It is unlikely that we under–prescribed the plume–driven outflow at the downstream boundary, as velocities at the downstream boundary were greater than that caused by the ambient channel cavity. Other processes like ocean currents or tidal currents could increase cavity to ocean exchange. There is no evidence for or against the existence of ocean currents are much larger than the maximum velocities of 10 cm/s used in the model runs. Nearby at 'KIS1', currents were measured to peak at around 10 cm/s and were dominated by tides (Robinson et al., 2020). We suggest that the most likely possibility of strong cavity to ocean exchange is through estuarine flow. Estuarine flow in rivers can be higher than 1 m/s (Nepf and Geyer, 1996) depending on local bathymetry, and distance from the open ocean. As part of the model run 'Weak inflow,' we simulated tidal flow by imposing an oscillating downstream boundary condition. With a magnitude of 5 cm/s we saw no clear effects of this boundary condition.

Alternatively, our approximation in sealing the bottom corners of the cavity to the ocean floor may miss an important flux of bottom water from the shelf. This approximation was made in the absence of better data. Bed elevation is needed to calculate the ocean depth beneath the ice. Radar cannot penetrate seawater so we cannot tell the ocean floor elevation, only the ice base shape. Available bed map products (Fretwell et al., 2013, e.g.) are too coarse to use for this purpose, and show the area as completely flat. We can get an idea of which part of the channel is floating from the distance from equilibrium shown in Figure 2.11. This shows that only a small downstream portion of the channel has sides which are not resting on the ocean floor, justifying our choice in sealing the ocean walls. Additionally, with limited vertical movement of water in our model, it is unlikely that large flux came from under the channel. However, in combination with another mechanism such as a plume or tidal pumping, vertical influx remains a possibility.

It is possible that pumping of water due to the tidal flexure of the ice shelf causes mixing in the cavity which is not modelled by our model. Walker et al. (2013) found that ice flexure can cause up to 1 km of horizontal ice liftoff which could pump water. On the other hand, our GNSS station over the channel (Chapter 2), shows very little tidal movement in the ice as far upstream as the channel suggesting tidal flexure is minimal.

4.5.2.2 No wall basal ablation

Because MITgcm's 'shelfice' cannot model vertical wall ablation (Section 4.3.3.2), it is worth questioning whether the package is an appropriate tool to model buoyant plume processes. The end member, a vertical wall, can not develop a plume. (Xu et al. (2012) modified the 'shelfice' package to model vertical walls.) Most applications of the package (e.g. Goldberg et al., 2019; Schodlok et al., 2012) model a shallow ice base slope. With a shallow ice base slope, it is reasonable to use the package as the roof area dominates the wall area. In our domain, the initial slope of the cavity is around 35 degrees from the horizontal. This smoothly slackens and by 270 m downstream does not exceed a downstream gradient of 3 degrees. A single pixel pair has a downstream gradient of 35 degrees. Because the vertical resolution is high, the step–like grid reasonably approximates a sloped surface. If we assume that basal ablation should be represented as a diagonal slope instead of the horizontal roofs of stepping cells, at this point basal ablation may be underestimated by up to 26%. This could push maximum basal ablation rates to 25 m/yr over the upstream 50 m of the channel in the model run 'Surge inflow'. Over the initial slope of the channel, the median underestimation of a downstream pixel pair's basal ablation is 7 %, so this is not a dominant error. While it is possible that the initial slope is underestimating basal ablation and therefore failing to trigger a positive feedback in the buoyant plume, this appears to not be the case. Some model runs like 'Fast inflow' have high inflow rates, and do not trigger any enhanced feedback. A downstream plume is likely not hindered by the model setup, however the cross channel walls, which are much steeper, likely see less realistic basal ablation rates.

4.6 Conclusion

We have modelled ice–ocean interaction in the ocean cavity observed in Chapter 2 with a range of configurations designed to simulate potential interaction between subglacial drainage, the cavity, and the larger Ross Ice Shelf cavity. Key results show that fluctuations in subglacial drainage are necessary to get significant rates of basal ablation, and show that freshening of the cavity can lead to accretion in the channel centre as observed.

Unlike most observed channels the cavity exists upstream from previos estimations of the grounding line (Depoorter et al., 2013), and so has enclosed walls. This results in low rates of exchange between the cavity and the ocean. Significant rates of basal melting were only observed when stronger subglacial drainage (1 cm/s) flowed into a cavity at equilibrium with the ocean. This scenario represents episodic drainage events. While the subglacial drainage drives strong melting in the channel, it also freshens the cavity which slows melting. Additionally, while the cavity freshens, buoyant fresh water pools on the cavity ceiling, particularly where it is trapped by a topographic high. On model runs which became very fresh, accretion occurred at these locations. These modelled phenomena were caused due to the lack of simulated salt replacement between the channel cavity and the ocean. We found that exchange between the channel cavity and the ocean could be enhanced by a narrower channel which promotes an estuary flow pattern with chimney–like outward flow on the top half of the water column and inward flow on the lower half. This flow pattern was inhibited at wide areas of the channel which developed cross-channel circulation, increasing the residence time of water in the channel. Lastly, we find that the melt rate pattern produced generally favours strong ceiling melt when subglacial outflow has recently increased and trends to weak wall melt over time. As a result, we expect narrow, tall, steep walled channels to develop relatively quickly while wide channels take more time.

Chapter 5

Synthesis

In this chapter, we first discuss key findings from the thesis, links between these findings, and their implications (Section 5.1). Additionally, we outline discrepancies in results and suggest ideas for future work which could follow from the research presented. In Section 5.2 we summarise and unify the theoretical models presented in this thesis. This unified model is the theoretical description of the channel and processes associated with the channel which are most likely, based on results from the thesis and existing theories.

5.1 Findings and implications

5.1.1 Steep subglacially sourced plume

The basal channel was most likely incised by a subglacially–sourced meltwater plume (discussed in Section 2.5.1.2). This is supported by evidence that the channel's location corresponds to a subglacial discharge outlet (Alley et al. (2016); Le Brocq et al. (2009), Figure 2.1). Describing melt in the channel as driven by a subglacial plume (as described by Jenkins (1991)) is consistent with observations of the steep channel shape, and localised active surface lowering.

In Section 2.4.1.1 the temporal gradient in ice surface topography was mapped across the study area with remote sensing data (Figure 2.7 D). This revealed an active region of surface lowering at the channel inception, which was likely the surface expression of ongoing subglacial melt (Figure 2.7 D). Finding active localised surface lowering was instrumental in better understanding modern processes in the basal channel, and informed our theories of conceptual models of plume dynamics in the channel, as well as ocean modelling experiments that described ocean circulation in the channel (Chapter 4).

The region of surface lowering is focused around a small area at the inception of the channel. We attribute the surface lowering to basal melt from a meltwater plume that ascends the sloped basal channel. Radar surveys showed that the basal channel is steep at its inception (Figure 2.8). A meltwater plume likely flows downstream up the gradient of the ceiling of the channel. As the plume ascends it melts ice, becoming more fresh and buoyant. The upward plume drives circulation, entraining warm salty water from the ocean depths to the ice face, enhancing melt. Plume theory predicts that melt is strongest where a plume starts to ascend and decreases in strength as it continues to ascend (Jenkins, 1991). We suggest that because the channel is steep at its inception the meltwater plume does not travel far downstream over its ascent, resulting in the small horizontal area of melt that we observe.

We suggest that a steep plume developed through feedbacks as described by Sergienko (2013), and in Section 2.2. Such feedbacks between a steepening slope and plume melt will continue until basal slope, and the plume flow, is vertical (described in more detail in Section 2.5.1.2). Future work could solve the plume model presented in Jenkins (2011), adapted to have a time–evolving domain shape. The shape resulting from plume melt in the absence of advection could be compared to the observed shape of the channel.

In Chapter 4, ocean modelling results using MIT Global Circulation Model (MITgcm) showed the strongest melt in the channel domain was consistently at the inception of the channel (Figure 4.14). This independently supports our theory that the steep channel and localised surface lowering are caused by melt from a plume and shows that the MITgcm model setup is successfully modelling some plume processes. Because modelled melt was focused over just a few grid cells at the inception of the channel, MITgcm likely failed to reproduce plume processes accurately (Section 4.5). The channel would be best modelled in future with an adaptive grid with very high resolution at the inception of the channel and modifications to the melt model to allow for melting of vertical cell walls (as discussed in Section 4.5).

5.1.2 Intermittent upstream channel migration

In Chapter 2, satellite imagery showed that the channel has migrated upstream in the last 40 years (Figure 2.6). We theorise that the focused plume melt location had moved upstream over time to form the length of the channel (Section 2.5). Topographic maps revealed multiple basins on the surface, which are the expressions of wide sections of the basal channel (B1-3, Figure 2.7). We suggest that the oscillations in channel width were caused by intermittent melt (Section 2.5.1.1), and that wide sections of the channel correspond to regions where the plume was focused for more time. Results from ocean modelling (Chapter 4) strongly support the theory that subglacial drainage is intermittent, and imply that episodic flow is an important part of the ice slope and plume melt feedback that forms the channel, in that a deep channel could only be incised with a strong plume which only develops after the channel is replaced with more saline water. Due to the long and skinny shape of the channel, a full overturning of water required some time (Section 4.4.5). High melt rates, closer to those estimated in Chapter 2, were only modelled with strong intermittent drainage which flushed the channel and was replaced by salty ocean water in quiescent times. Melt was only found along the apex of the channel at the beginning of drainage events, after which, accretion would occur at the apex. This corresponds to ApRES observations from Chapter 2 which showed accretion at the apex of the channel on a base of marine ice, suggesting that the plume was not strong during the period. It follows that active surface lowering is likely representative of quiescent phase melt, and melt which we infer from surface lowering occurs lower in the water column, on channel walls, not at the highest apex of the channel.

We outline two constraints on the time scale of intermittency of the plume. Firstly, using a continuously recording ApRES radar we chronicled changes at the ice base over 2020 (Chapter 3). The ApRES time series showed a relatively stable basal mass balance over one year. Assuming that the consistency in mass balance was caused by the same plume dynamics that caused melt at the inception of the channel shown by surface lowering, we infer that melt at the inception of the channel was steady for a year-long period. Secondly, in Section 2.5 the active surface lowering was shown to be similar when calculated over 2012-2016 and over 2019-2020, suggesting that the melt plume was consistent over the entire period from 2012 to 2020. This suggests that the theorised episodic nature of melt can have long periods (>10 years) of stability. The intermittent melt and drainage which we suggested was important to forming the channel must therefore have a periodicity larger than the stable time periods, but smaller than the ≈ 150 years it took the channel to form. Therefore it is possible that the intermittent drainage oscillates with multi–decadal periodicity.

Future research can improve our understanding of the channel's formation by monitoring the channel growth with modern, high–resolution remote sensing products. With a few more decades of observations, the rate of inland migration of the channel and the degree of variability in the rate will likely become clear.

5.1.3 Ocean connection

Plume driven melt in the channel was found to be strongly dependent on the availability of saltwater (Section 4.5). A stronger connection (more exchange of water) to the larger Ross Ice Shelf cavity increased basal ablation rates. Ocean exchange increased the salinity in the channel through the inflow of salty bottom water (as described by Goldberg et al. (2019)), as well as more outgoing fresh water. In Chapter 4, model results predicted that two layers of water develop in the cavity similar to estuarine flow, with fresh downstream flow in the upper layer and salty upstream flow in the lower layer. This flow pattern is conducive to replacing fresh cavity water with salty ocean water.

Ocean modelling (Chapter 4) also revealed a relationship between the strength of the ocean connection and the changing width of the channel (described in Chapter 2).

The strong estuarine circulation with outflow layered on top of inflow was shown to break down in wide sections of the channel, where crossflow circulation cells developed (Section 4.5). Therefore, we expect the existence of wide sections of the channel to slow the replacement of seawater and reduce basal ablation rates at the plume. The ApRES time series (Chapter 3) provided additional evidence of an active connection between the channel and the ocean, showing that the tide influences basal processes. Assuming that this accretion was caused by the same plume dynamics that cause melt at the inception of the channel shown by surface lowering, we infer that the subglacial plume is influenced by tides. It follows that melt may be tidal at the channel inception. This observation described a connection between the plume processes and ocean processes, and therefore provided evidence to support the modelling–based prediction that melt rates and plume processes are influenced by the channel's connection to the larger Ross Ice Shelf cavity.

5.1.4 Melt rate estimation

In Chapter 2 the ice base topography and the temporal gradient in ice surface topography were combined to estimate a lower bound of ≈ 20 m/yr on basal melt rate (Section 2.5). This bound was used as a key constraint when modelling ocean circulation in the channel in Chapter 4. In these model experiments, the domain shape was constrained by the ice base estimation from Chapter 2, and the key variable used in the experiment was water exchange in and out of the model domain, through the upstream and downstream boundaries. Model outputs included temperature, salinity, velocities and melt rates, the latter of which were compared to the melt rate bounds estimated in Chapter 2. While the model meltwater plume expelled fresh water along the top of the channel, warm salty water flowed upstream at the bottom. In model runs, this upstream salt flux was necessary to drive significant melt rates. The ocean circulation model did not reproduce the high basal melt rates (≈ 20 m/yr) estimated in Chapter 2. We attribute this to the inability of the model to solve for a strong subglacial drainage at the upstream boundary, or the inability of the model to develop focused melt. While results from Chapter 2 suggest melt was strongly focused at the inception of the channel, model outputs showed a more distributed melt pattern. This discrepancy may have been solved by extending the domain further upstream and increasing the horizontal resolution to more accurately resolve processes at the inception of the channel. Identifying and bounding modern melt processes highlights and guides opportunities for future work. For example, through the oceanographic observations taken in the 2021–2022 drilling project, future work can attempt to better constrain plume dynamics and subglacial drainage which cause the observed surface lowering.

5.1.5 Accretion spatial pattern

Plume theory (as described by Jenkins (2011)) predicts melt to occur over a certain distance downstream from the origin of a plume. After that distance, the plume is predicted to lose energy and become supercooled, first ceasing to melt, then further downstream causing accretion. Accretion downstream from the predicted plume was observed in ApRES basal surveys presented in Chapters Two and Three. Basal accretion or marine ice was found along two perpendicular tracks (Figure 2.14). The track along the apex of the basal channel showed accretion on the edge of the region of surface lowering (Figure 2.3, and 2.8). These results, supported by plume theory (Jenkins, 1991), suggest that melt likely only occurs in the channel as the plume ascends, and over a small distance downstream the plume starts to accrete ice. The surface expression (Figure 2.7) does not show raising of ice immediately downstream of the melt, suggesting that the melt signal dominated and hid the nearby accretion. In Chapter 3 an ApRES survey chronicled changes at the ice base over 2020 (Figure 3.5), downstream from the region of surface lowering. This identified basal marine ice over the whole period and found that the ice base was changing consistently, most likely through accretion (Section 3.4). These results showed that melt does not occur down the length of the channel apex, confirming that melt is concentrated at the inception of the channel for a period of at least one year. This aligns with modelling results in Chapter 4 which showed accretion at the apex of the channel downstream from the inception (Figure 4.11). Rather than showing a supercooled plume, modelling results gave an alternative explanation for conditions that cause accretion, predicting that accretion would occur when pockets of fresh water developed on the ceiling of the channel. These buoyant pockets of meltwater were stable and therefore isolated from the cavity circulation. Water in the stable pockets continued to cool and accreted ice. The formation of these isolated pockets of fresh water is highly dependent on bathymetry and relies on local highs in the ice ceiling (Figure 2.7). The ice base map from Section 2.4.1.2 showed slight highs in the estimated ice ceiling where we would likely see pooling of fresh water and accretion. The location of the ApRES time series (Figure 2.3), was near the centre of the basin B1 (Figure 2.8) which was estimated to correspond to a local high in the ice base, suggesting that the observed marine ice could be forming in a pocket of trapped fresh water.

5.1.6 Surface and basal topography

The basal and subaerial surface topography around the channel were mapped using radio echo sounding and remote sensing respectively (Chapter 2). These results were instrumental in directing subsequent research. Firstly, we used the basal map as a basis for modelling experiments in Chapter 4. Secondly, the map was used to direct field research, including two field campaigns to the channel. In the 2020–2021 field season an ApRES was installed at a location guided by the ice base map, at the intersection of the apex of the channel (Figure 2.3) and the region of surface lowering (Figure 2.7 D). In the 2021–2022 field season, the ice base map guided drilling through the ice to the channel cavity, where a large range of observations were made including oceanographic observations, sediment cores and a submarine survey (Horgan and Stevens, 2022). The ice base map will continue to guide future remote sensing work or any future field studies of the channel. Knowledge of the basal shape will allow surface observations to be better linked to basal channel processes. We recommend that future studies revisit the radar data used in Section 2.3.2.1 using techniques to attempt to map the properties of basal ice as attempted in MacGregor et al. (2011). Using this radar data, it may be possible to reveal areas of marine ice or spatial changes in the ice base which could inform models of plume dynamics.

Observations of surface and basal topography in Chapter 2 displayed that the surface valley is not a direct reflection of the basal channel, and bridging stresses cause basal features to be smoothed or without surface expression. In particular, the basal channel extends further upstream than the surface valley, and the surface valley is wider than the basal channel. The surface expression of basal melt is similarly smoothed to cover an area wider than the channel, and overlaps observed accretion.

5.1.7 Inconsistencies

5.1.7.1 Melt pattern

Modelling experiments in Chapter 4 revealed that due to the high salinity of bottom water, the channel generally experiences greater melt lower in the water column. This implies that the channel likely experiences melt along the walls, effectively widening the channel. This is inconsistent with surface and basal observations from Chapter 2 which did not find wall melt. The ApRES survey crossing the channel showed a trend similar to wall melt with lower magnitudes of accretion at the sides of the channel relative to the centre (Figure 2.14). However, the ApRES cannot measure melt on steep walls due to off nadir reflections, which may also contribute inaccuracies to lateral trends in basal mass balance.

In Chapter 2 we discussed surface observations which suggest that the channel was migrating to the left, similar to a channel described by Chartrand and Howat (2020). We attributed this movement to the asymmetry of circulation caused by the Coriolis force. This was not supported by modelling experiments in Chapter 4 which showed the Coriolis force had little effect on circulation in the channel and did not show a lateral (left–right) bias in melt and accretion. Additionally, in Chapter 2 we predicted that ledges were growing in the channel through accretion, similar to a channel described by Dutrieux et al. (2014). However, this result was again not supported by modelling results which showed accretion only occurring in the top section of the water column, where water was more fresh.

There is an overall trend in the discrepancies between observations and the modelling results. Generally, modelling results showed the most variability in melt processes laterally and showed less variability in the downstream direction. On the other hand, observations imply there is more downstream variability in melting. We suggest that much of these discrepancies are caused by the smoothing of the expression of basal mass balance at the surface. Because the channel is not very wide, lateral variability will hardly be expressed at the surface due to bridging. The lack of downstream variability in modelling experiments may be due to the lack of resolution to resolve plume dynamics at the inception of the channel.

5.1.7.2 Accretion rates

The ApRES derived accretion rates of ≈ 0.8 m/yr presented in Chapter 3 are different to the accretion rates ≈ 3 m/yr presented in Chapter 2, the former of which is more accurate. Accretion rates in Chapter 2 were calculated from repeat surveys one–year apart, over which internal reflectors had moved too much to track accurately. This resulted in an inaccurate strain estimate. The ApRES transect across the channel (Figure 2.14 A) was surveyed on 07-12-2019, 21-12-2019, and 23-12-2020, whereas the transect along the channel apex (Figure 2.14 A) was surveyed only on the latter two dates. The comparison across all ApRES repeat surveys in Chapter 2 was therefore made over the one year time frame for consistency. The inaccuracies of the accretion rates do not affect any other results or conclusions made for two reasons. Firstly, when compared to rates calculated over 20 days, the cross-channel transect shows accretion rates ≈ 0.8 m/yr, but has the same pattern of relative accretion to that displayed in Figure 2.14 A. Secondly, because the magnitude of accretion is likely not representative of the actual accretion due to interference from multiple reflectors, no conclusions were made based on absolute accretion rates.

5.1.8 Implications

This thesis was the initial detailed exploration of the sub–ice–shelf channel, which is the subject of a much larger body of research. The main implications of this thesis are to guide future research, outlined above. Additionally, our observations and constraints, such as the melt rate bounds, channel shape, or theories of plume migration can be used as a case study to further constrain theories of channel formation and growth. Future attempts to model ice shelf channels can use these observations as constraints.

5.2 Unified theoretical model

Based on the results presented in this thesis, we have theorised a description of the channel and processes associated with the channel. In plain terms, we have tried to answer the fundamental questions ‘what is it?’ and ‘how does it work?’ In this section, we present a unified theory describing the channel and associated processes based on results and literature. References will be provided to parts of the thesis which explain theories in more detail.

5.2.1 Description of the present channel

The basal channel shape is described by the ice base map (Figure 2.7). An initial slope between 0-45 degrees rises to the highest part of the channel apex (Figure 2.8). This upstream part of the channel is very narrow (200 m), so has little or no surface expression as it is supported by bridging stresses (Section 2.5.0.1). The apex of the channel decreases in height downstream, after which it follows for 8 km at a consistent height. The basal channel has three bends. At each bend, the channel is wider (Figure 2.7). The surface expression of the basal channel (surface valley) starts downstream from the inception of the basal channel (Section 2.7). The surface valley is wider than the basal channel as it is smoothed by the lateral distribution of stress in the ice. Wide parts of the channel provide less buoyancy and are incompletely bridged so correspond to basins on the surface (Section 2.5.0.1). Melt is focused at the inception of the channel over a small area, as shown by localised surface lowering (Figure 2.7), the steep channel inception (Figure 2.8), and ApRES observations (Figure 2.14). Again, due to bridging stresses in the ice, this melt appears as a larger region extending around the channel, and does not appear directly over the narrow channel tip (Figure 2.7 D). The observed melt is driven by the supply of salt from the larger Ross Ice Shelf cavity (Section 4.5), to a meltwater plume at the inception of the channel. A circulation cell dominates channel circulation, with upstream movement of warm salty water from the ocean at the bottom, and downstream flow of cooler fresh meltwater above this layer (Figure 4.12). Downstream from the melt region, accretion occurs (Figure 2.14). Accretion is especially strong on the true right of the channel, where surface observations reveal surface raising coincident with ledges in the ice base (Figure 2.7 D).

5.2.2 Formation

The formation of the channel occurred subsequent to the retreat of the Kamb Ice Stream grounding line to its present location (Section 2.5.1.1). Effective pressure at the base at the grounding line is zero, meaning the creep closure of the drainage channel no longer counteracted the melting of the channel walls, and it grew unabated (as described by Drews (2015)). When the grounding line initially retreated, there was a subglacial drainage outlet where B3 is currently situated (Figure 2.8). Buoyant subglacial drainage met the ocean triggering a meltwater plume which incised into the ice shelf above (as described by Hewitt (2020)). Melt rates were strongest at the bottom of the plume, closer to the source of entrainment and saltier bottom water, and as a result, the downstream cross–sectional shape developed a more negative change in gradient downstream until the incised channel was steep above B3 (Section 2.5.1.2). The plume continued to melt the steep ice wall above the channel and incised into the ice upstream creating an embayment, which allowed for salty water to flow up the channel at the seafloor, providing energy to the plume for melt (Section 4.5).

When large pulses of subglacial meltwater from a flood upstream drained (Section 2.5.1.1), the plume ascended higher, and the channel melted higher (Section 4.5.1.1). When there was less meltwater, the plume melted the walls at a lower elevation, widening the channel. The widening and narrowing of the channel correspond to periods of low and high discharge rates respectively (Section 4.5.1.1).

5.3 Closing statement

The primary goals of this thesis were to describe a subglacial channel and its evolution on the Siple Coast, Antarctica, and to better understand ice, ice-ocean, and ocean processes around the channel. These goals were addressed by combining results from surface based geophysical observations, remote sensing observations, model predictions, and existing theory. The findings of this thesis enabled a drilling operation into the channel in 2021-22. Observations from this operation will continue to better constrain our theories and estimations of ice and ocean dynamics at the river mouth.

Chapter 6

Appendix

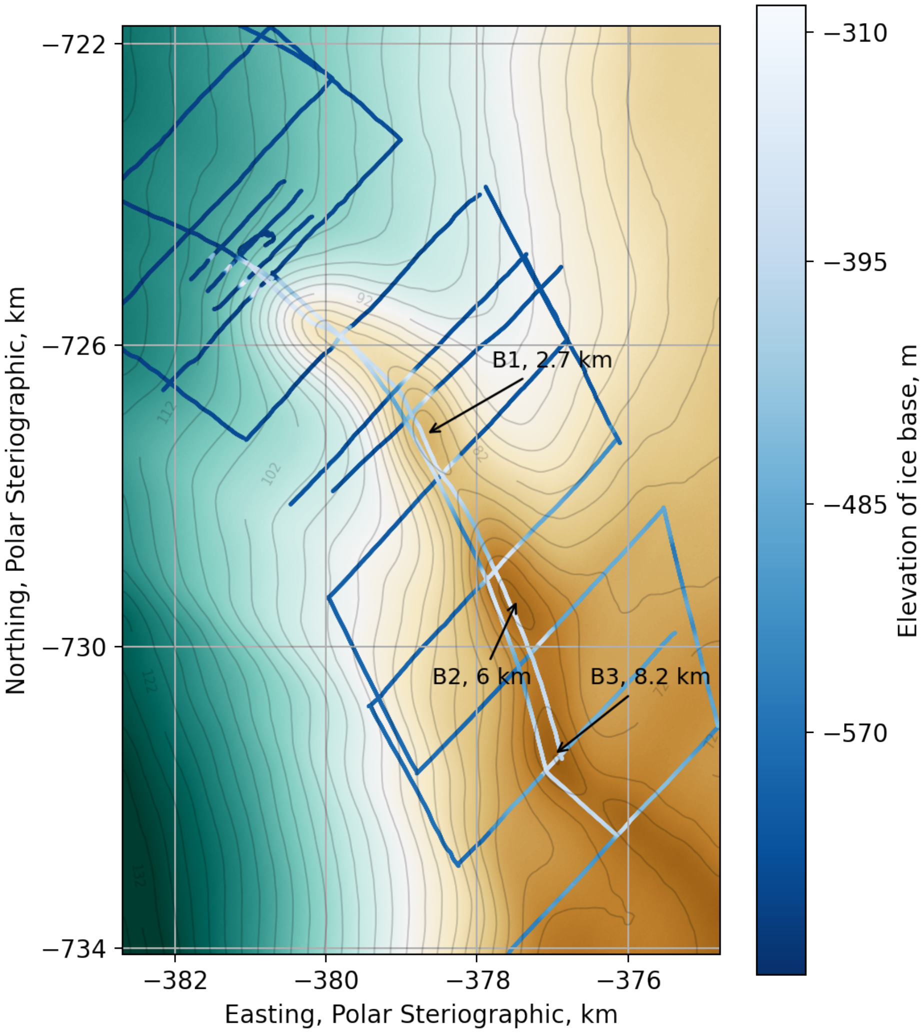

Figure 6.1: Ice depths picked from processed radar data. Note that the channel forms over a short distance. Background image and contours show surface elevation.

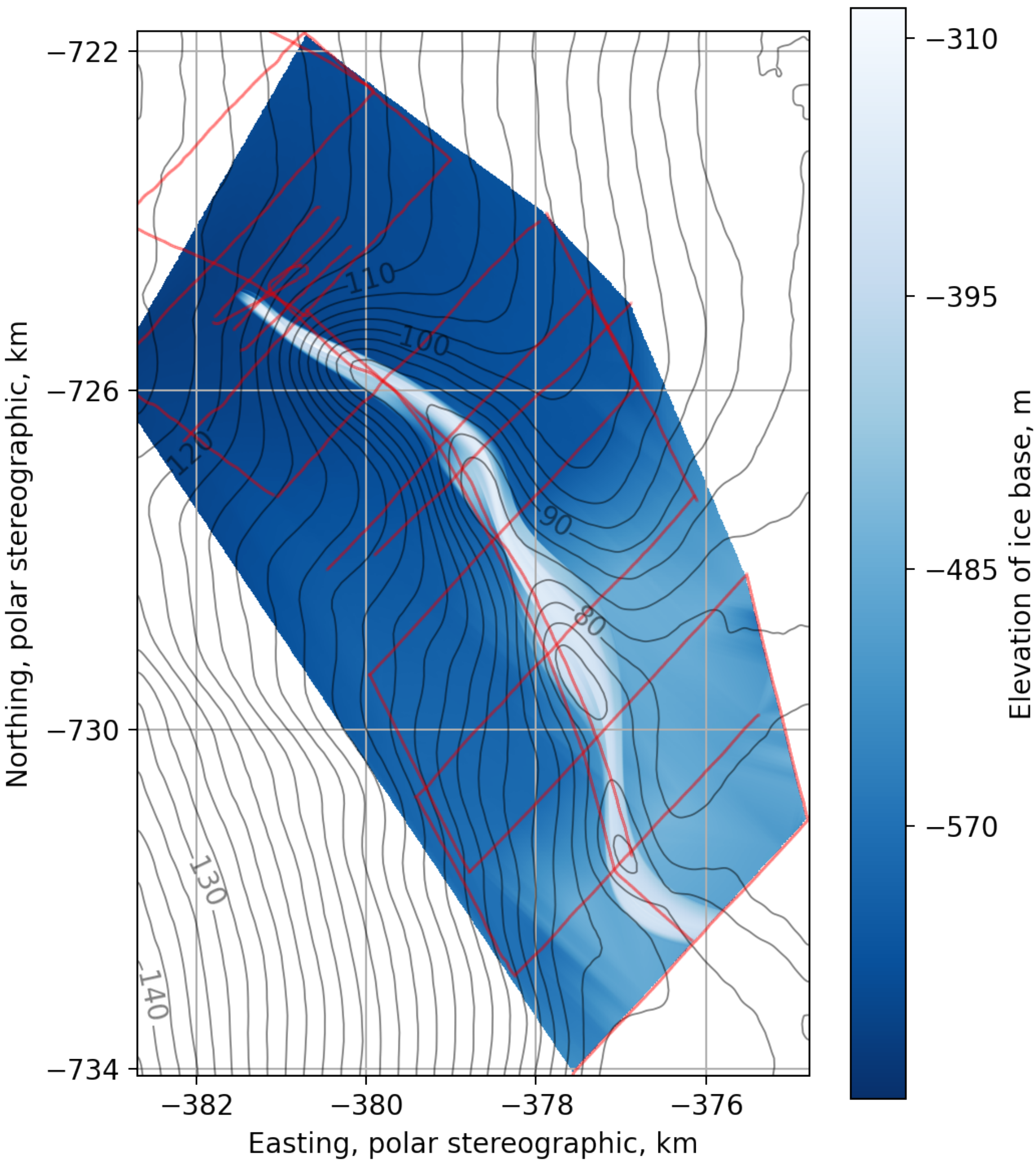

Figure 6.2: Image shows ice base elevation estimated using downstream interpolation described in Section 2.2.2. Red lines show location of radar data collection which informed the interpolation. Contours are REMA ice surface elevation Howat et al. (2019).

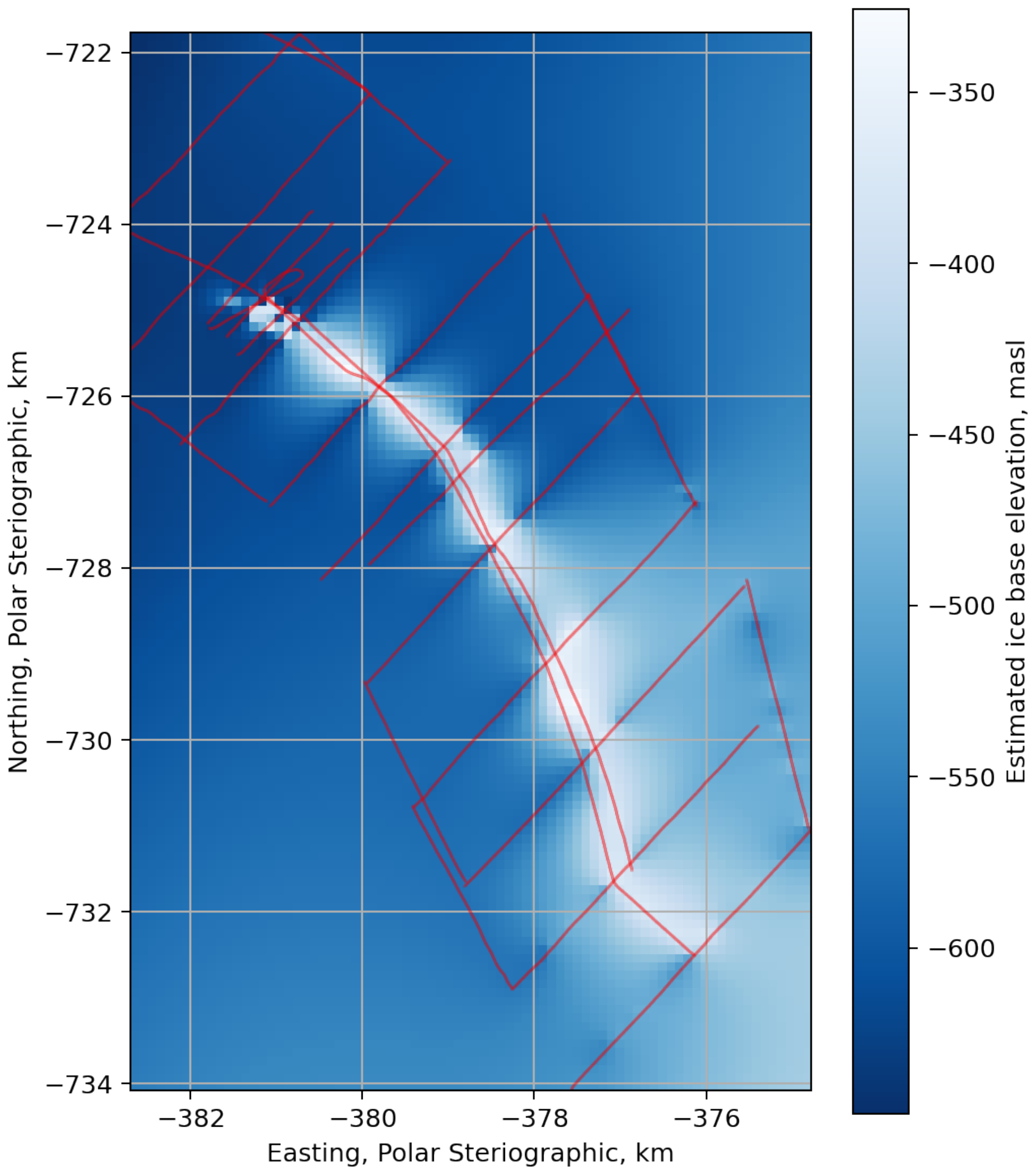

Figure 6.3: Ice base elevation estimated using continuous curvature spline interpolation. Red lines show radar data which was interpolated. The interpolation does not produce a good result, showing clear bias to surveyed locations.

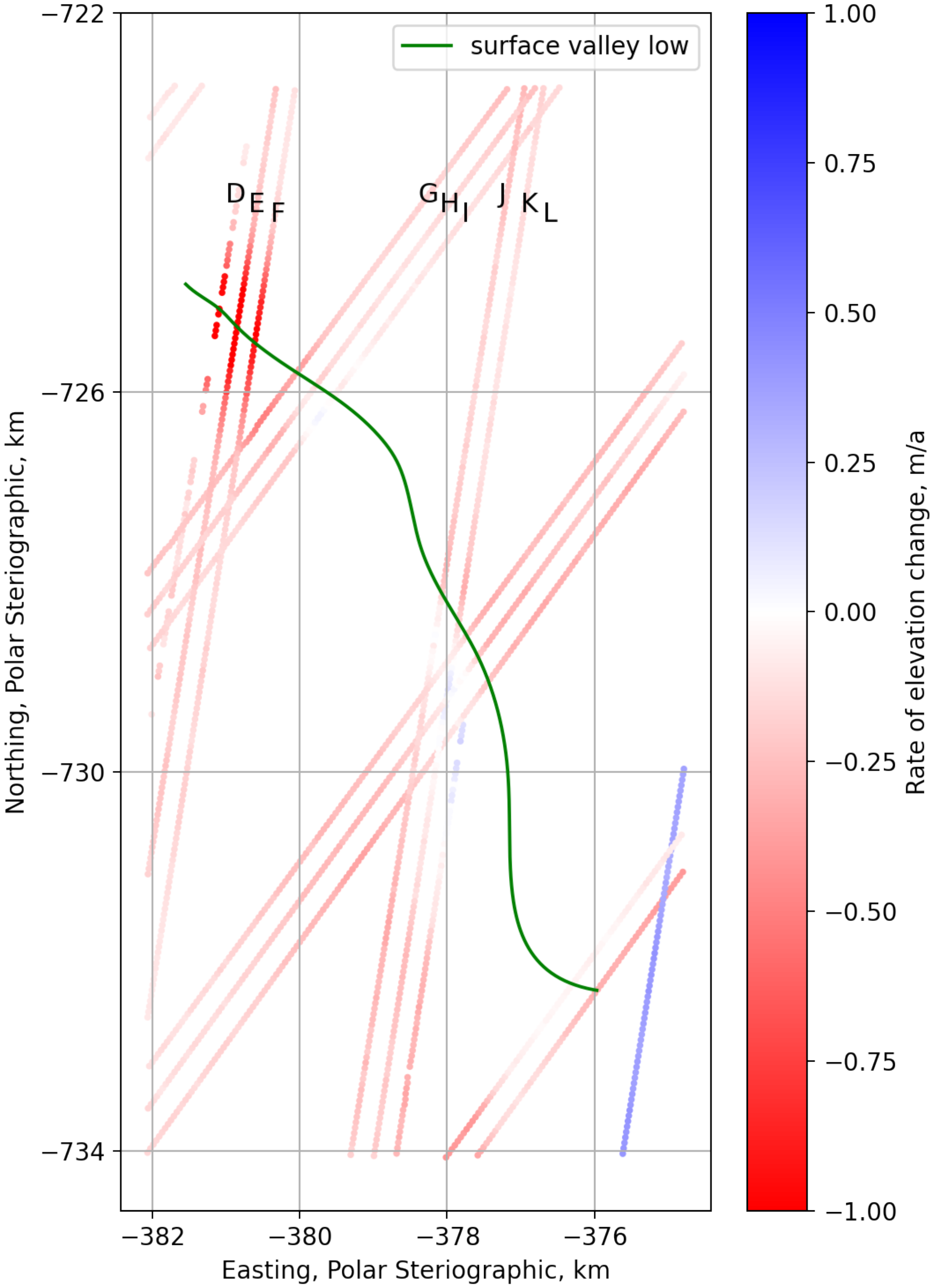

Figure 6.4: Map showing surface elevation changes with ICESat–2 data. Letters D-L refer to the locations of cross sections shown in Figure 10.

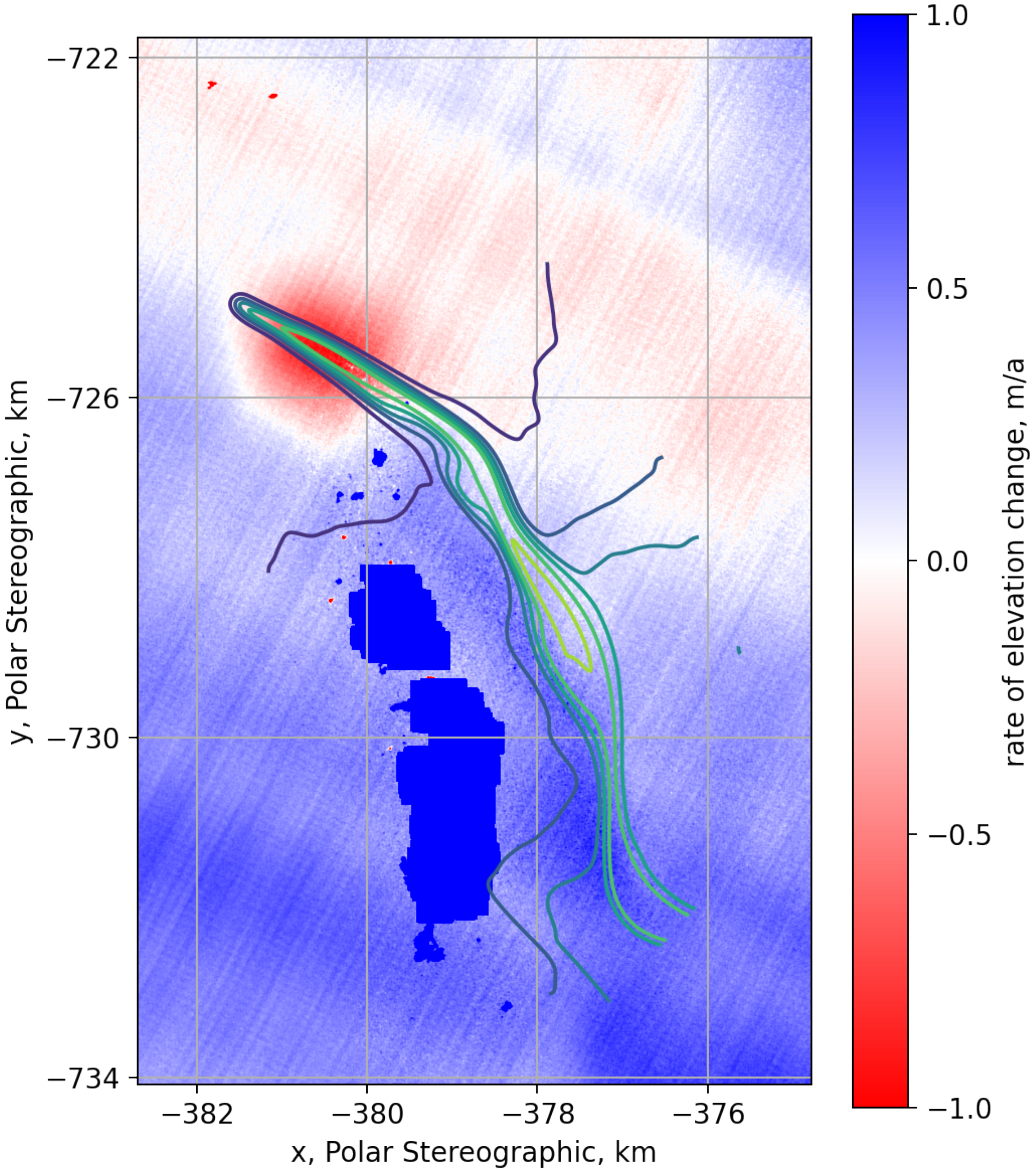

Figure 6.5: Difference between REMA elevation from 2012-12-24 to 2016-11-09, contours show estimated ice base. Dark blue spots to the true–right of the channel are artefacts.

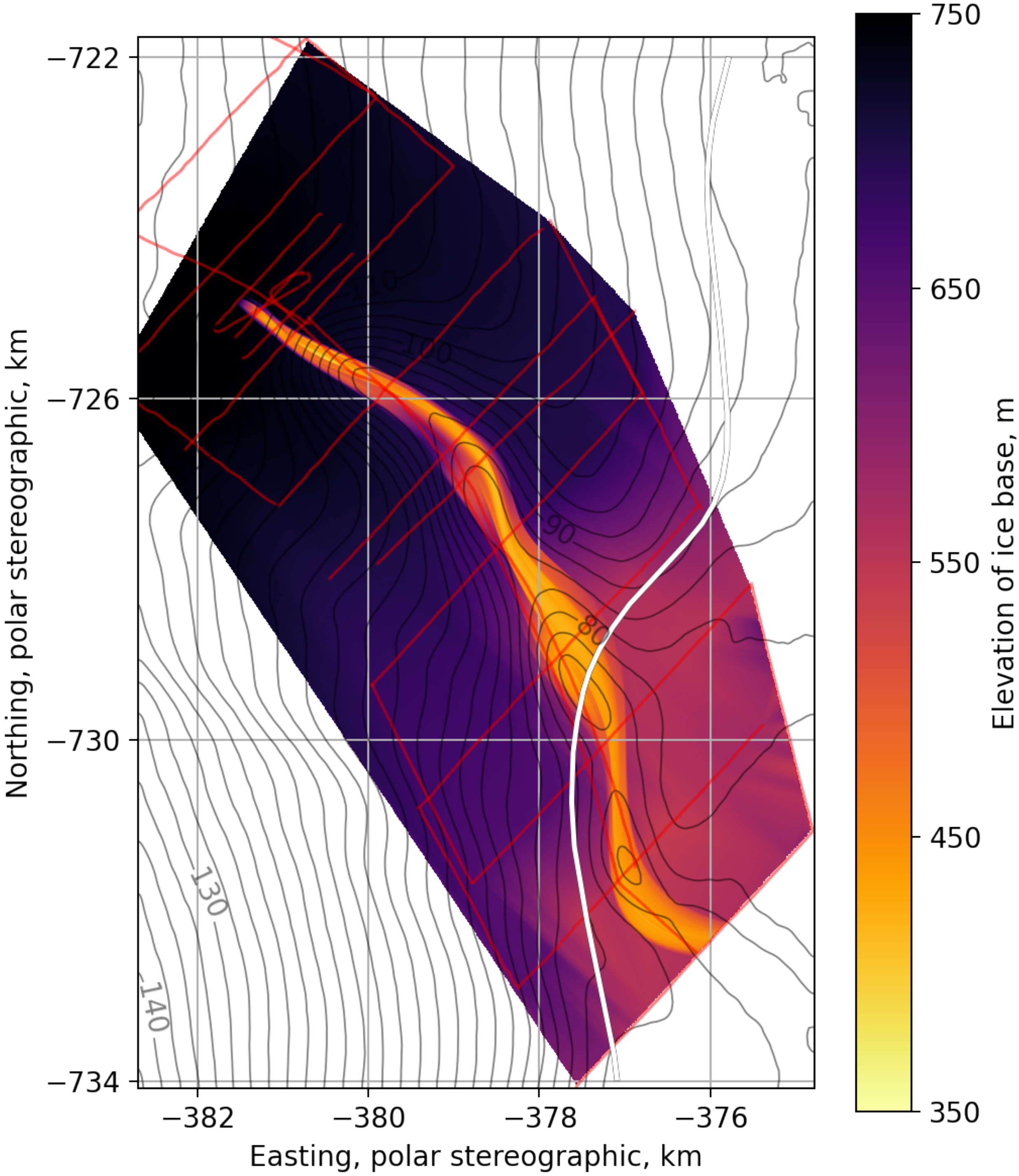

Figure 6.6: Image shows ice thickness estimated using downstream interpolation described in Section 2.2.2. Red lines show location of radar data collection which informed the interpolation. Contours are REMA ice surface elevation Howat et al. (2019).

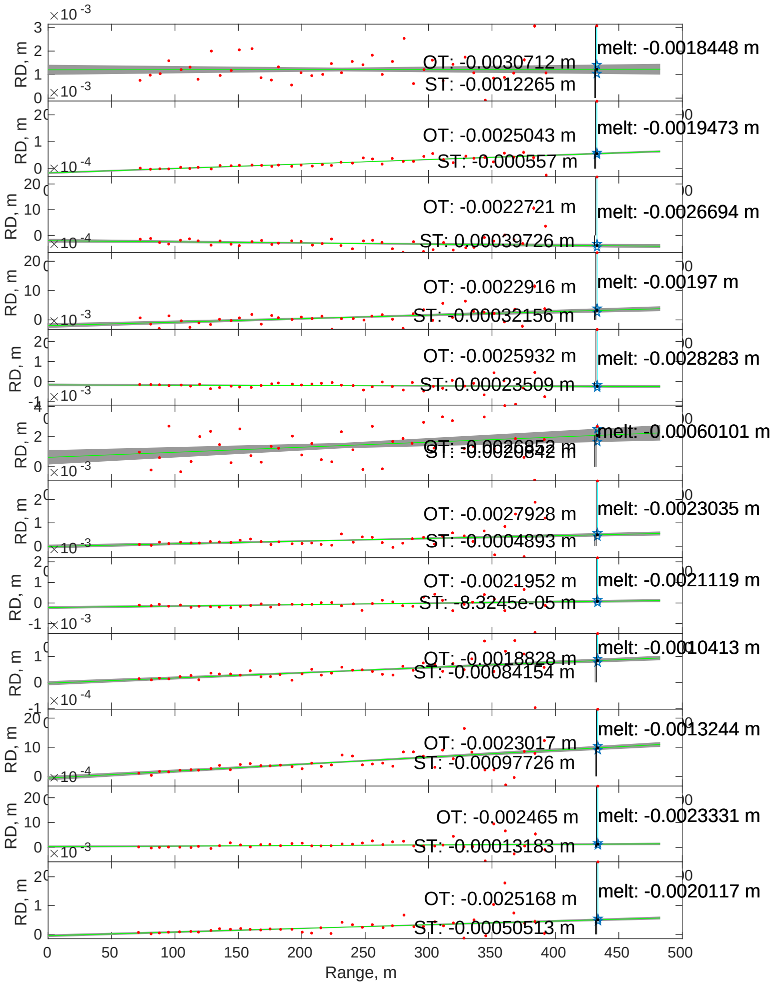

Figure 6.7: As in Figure 3.7, 12 separate ApRES observations are shown over 12 months of 2020. Range difference of internal reflectors (red points) over a 28 hour interval centred on the 1st of each month of 2020. Top plot is from January, bottom plot from December. RD (y-axis) is range difference, OT is observed thinning, ST is strain thinning. Green area shows one standard deviation of a linear fit of the internal reflectors. Melt is the negative of apparent accretion.

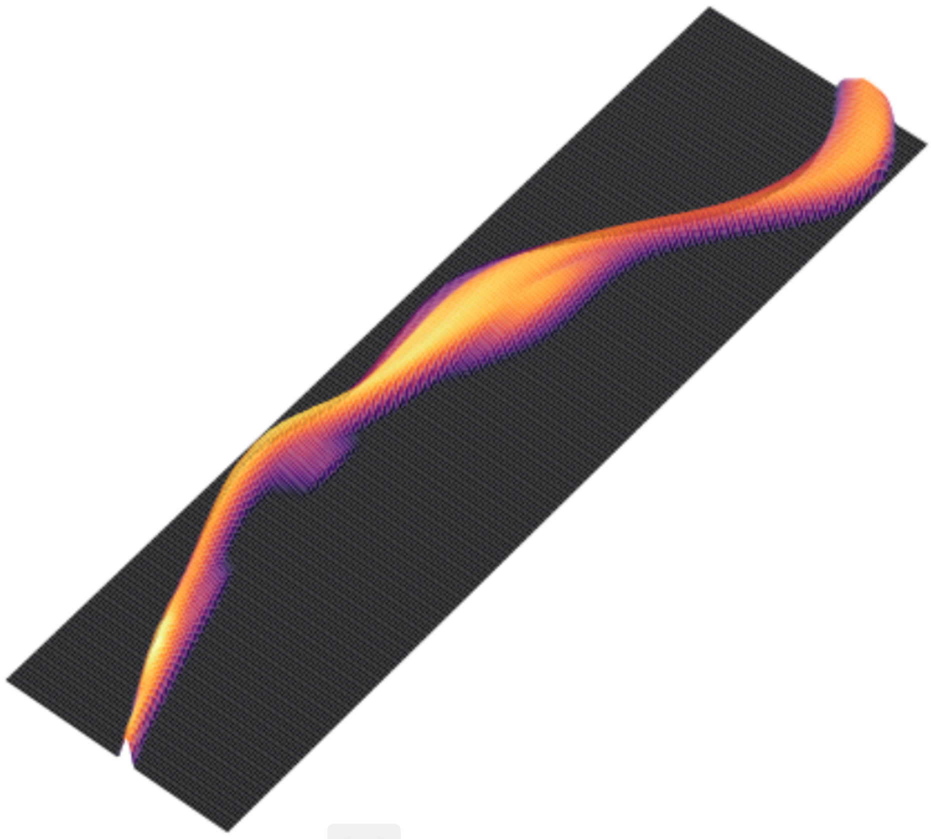

Figure 6.8: To scale, 3D depiction of the domain shown in Figure 4.5. The upstream boundary is at the bottom left and to the top right is the downstream boundary.

References

Adcroft, A., Hill, C., and Marshall, J. 1997. Representation of topography by shaved cells in a height coordinate ocean model. *Monthly Weather Review*, 125(9):2293–2315.

Alley, K. E., Scambos, T. A., Siegfried, M. R., and Fricker, H. A. 2016. Impacts of warm water on Antarctic ice shelf stability through basal channel formation. *Nature Geoscience*, 9(4):290–293.

Alley, K. E., Scambos, T. A., Anderson, R. S., Rajaram, H., Pope, A., and Haran, T. M. 2018. Continent-wide estimates of Antarctic strain rates from Landsat 8-derived velocity grids. *Journal of Glaciology*, 64(244):321–332.

Alley, K. E., Scambos, T. A., Alley, R. B., and Holschuh, N. 2019. Troughs developed in ice-stream shear margins precondition ice shelves for ocean-driven breakup. *Science advances*, 5(10):eaax2215.

Alley, R. 1989. Water-pressure coupling of sliding and bed deformation: I. Water system. *Journal of Glaciology*, 35(119):108–118.

Alley, R., Blankenship, D., Bentley, C. R., and Rooney, S. 1987. Till beneath ice stream B: 3. Till deformation: evidence and implications. *Journal of Geophysical Research: Solid Earth*, 92(B9):8921–8929.

Alley, R., Anandakrishnan, S., Bentley, C., and Lord, N. 1994. A water-piracy hypothesis for the stagnation of Ice Stream C, Antarctica. *Annals of Glaciology*, 20:187–194.

Alley, R. B. 1996. Towards a hydrological model for computerized ice-sheet simulations. *Hydrological Processes*, 10(4):649–660.

Anandakrishnan, S., Voigt, D., Alley, R., and King, M. 2003. Ice stream D flow speed is strongly modulated by the tide beneath the Ross Ice Shelf. *Geophysical Research Letters*, 30(7).

Anandakrishnan, S. and Alley, R. B. 1997. Stagnation of ice stream C, West Antarctica by water piracy. *Geophysical Research Letters*, 24(3):265–268.

Anderson, J. B. and Fretwell, L. O. 2008. Geomorphology of the onset area of a paleo-ice stream, Marguerite Bay, Antarctic Peninsula. *Earth Surface Processes and Landforms: The Journal of the British Geomorphological Research Group*, 33(4):503–512.

Arnold, E., Leuschen, C., Rodriguez-Morales, F., Li, J., Paden, J., Hale, R., and Keshmiri, S. 2020. CReSIS airborne radars and platforms for ice and snow sounding. *Annals of Glaciology*, 61(81):58–67.

Arzeno, I. B., Beardsley, R. C., Limeburner, R., Owens, B., Padman, L., Springer, S. R., Stewart, C. L., and Williams, M. J. 2014. Ocean variability contributing to basal melt rate near the ice front of Ross Ice Shelf, Antarctica. *Journal of Geophysical Research: Oceans*, 119(7):4214–4233.

Bamber, J. L., Vaughan, D. G., and Joughin, I. 2000. Widespread complex flow in the interior of the Antarctic ice sheet. *Science*, 287(5456):1248–1250.

Begeman, C. B., Tulaczyk, S. M., Marsh, O. J., Mikucki, J. A., Stanton, T. P., Hodson, T. O., Siegfried, M. R., Powell, R. D., Christianson, K., and King, M. A. 2018. Ocean stratification and low melt rates at the Ross Ice Shelf grounding zone. *Journal of Geophysical Research: Oceans*, 123(10):7438–7452.

Berger, S., Drews, R., Helm, V., Sun, S., and Pattyn, F. 2017. Detecting high spatial variability of ice shelf basal mass balance, Roi Baudouin Ice Shelf, Antarctica. *The Cryosphere*, 11(6):2675–2690.

Berthier, E., Scambos, T. A., and Shuman, C. A. 2012. Mass loss of Larsen B tributary glaciers (Antarctic Peninsula) unabated since 2002. *Geophysical Research Letters*, 39 (13).

Blankenship, D. D., Bentley, C. R., Rooney, S., and Alley, R. B. 1986. Seismic measurements reveal a saturated porous layer beneath an active Antarctic ice stream. *Nature*, 322(6074):54–57.

Bombosch, A. and Jenkins, A. 1995. Modeling the formation and deposition of frazil ice beneath Filchner-Ronne Ice Shelf. *Journal of Geophysical Research: Oceans*, 100(C4): 6983–6992.

Bougamont, M., Christoffersen, P., Price, S., Fricker, H., Tulaczyk, S., and Carter, S. 2015. Reactivation of Kamb Ice Stream tributaries triggers century-scale reorganization of Siple Coast ice flow in West Antarctica. *Geophysical Research Letters*, 42(20):8471–8480.

Brennan, P. V., Lok, L. B., Nicholls, K., and Corr, H. 2014. Phase-sensitive FMCW radar system for high-precision Antarctic ice shelf profile monitoring. *IET Radar, Sonar & Navigation*, 8(7):776–786.

Bronselaer, B., Winton, M., Griffies, S. M., Hurlin, W. J., Rodgers, K. B., Sergienko, O. V., Stouffer, R. J., and Russell, J. L. 2018. Change in future climate due to Antarctic meltwater. *Nature*, 564(7734):53–58.

Brunt, K., Neumann, T., and Smith, B. 2019. Assessment of ICESat-2 ice sheet surface heights, based on comparisons over the interior of the Antarctic ice sheet. *Geophysical Research Letters*, 46(22):13072–13078.

Budd, W., Keage, P., and Blundy, N. 1979. Empirical studies of ice sliding. *Journal of glaciology*, 23(89):157–170.

Carroll, D., Sutherland, D. A., Shroyer, E. L., Nash, J. D., Catania, G. A., and Stearns, L. A. 2017. Subglacial discharge-driven renewal of tidewater glacier fjords. *Journal of Geophysical Research: Oceans*, 122(8):6611–6629.

Carter, S. P., Blankenship, D. D., Peters, M. E., Young, D. A., Holt, J. W., and Morse, D. L. 2007. Radar-based subglacial lake classification in Antarctica. *Geochemistry, Geophysics, Geosystems*, 8(3).

Carter, S. P., Blankenship, D. D., Young, D. A., and Holt, J. W. 2009. Using radar-sounding data to identify the distribution and sources of subglacial water: application to Dome C, East Antarctica. *Journal of Glaciology*, 55(194):1025–1040.

Carter, S. and Fricker, H. 2012. The supply of subglacial meltwater to the grounding line of the Siple Coast, West Antarctica. *Annals of Glaciology*, 53(60):267–280.

Case, E. and Kingslake, J. 2022. Phase-sensitive radar as a tool for measuring firn compaction. *Journal of Glaciology*, 68(267):139–152.

Castagno, P., Falco, P., Dinniman, M. S., Spezie, G., and Budillon, G. 2017. Temporal variability of the Circumpolar Deep Water inflow onto the Ross Sea continental shelf. *Journal of Marine Systems*, 166:37–49.

Chartrand, A. and Howat, I. 2020. Basal Channel Evolution on the Getz Ice Shelf, West Antarctica. *Journal of Geophysical Research: Earth Surface*, 125(9):e2019JF005293.

Christianson, K., Jacobel, R. W., Horgan, H. J., Alley, R. B., Anandakrishnan, S., Holland, D. M., and DallaSanta, K. J. 2016. Basal conditions at the grounding zone of Whillans Ice Stream, West Antarctica, from ice-penetrating radar. *Journal of Geophysical Research: Earth Surface*, 121(11):1954–1983.

Conway, H., Hall, B., Denton, G., Gades, A., and Waddington, E. 1999. Past and future grounding-line retreat of the West Antarctic Ice Sheet. *Science*, 286(5438):280–283.

Corr, H. F., Jenkins, A., Nicholls, K. W., and Doake, C. 2002. Precise measurement of changes in ice-shelf thickness by phase-sensitive radar to determine basal melt rates. *Geophysical Research Letters*, 29(8):73–1.

Crameri, F., 2018. Scientific colour maps.

Craven, M., Warner, R., Galton-Fenzi, B., Herraiz-Borreguero, L., Vogel, S., and Allison, I. 2014. Platelet ice attachment to instrument strings beneath the Amery Ice Shelf, East Antarctica. *Journal of Glaciology*, 60(220):383–393.

Craven, M., Allison, I., Fricker, H. A., and Warner, R. 2009. Properties of a marine ice layer under the Amery Ice Shelf, East Antarctica. *Journal of Glaciology*, 55(192): 717–728.

Dallaston, M., Hewitt, I., and Wells, A. 2015. Channelization of plumes beneath ice shelves. *Journal of Fluid Mechanics*, 785:109–134.

Damsgaard, A., Suckale, J., Piotrowski, J. A., Houssais, M., Siegfried, M. R., and Fricker, H. A. 2017. Sediment behavior controls equilibrium width of subglacial channels. *Journal of Glaciology*, 63(242):1034–1048.

Das, I., Padman, L., Bell, R. E., Fricker, H. A., Tinto, K. J., Hulbe, C. L., Siddoway, C. S., Dhakal, T., Frearson, N. P., Mosbeux, C., et al. 2020. Multidecadal basal melt rates and structure of the Ross Ice Shelf, Antarctica, using airborne ice penetrating radar. *Journal of Geophysical Research: Earth Surface*, 125(3):e2019JF005241.

Davis, P. E. and Nicholls, K. W. 2019. Turbulence observations beneath Larsen C ice shelf, Antarctica. *Journal of Geophysical Research: Oceans*, 124(8):5529–5550.

Davis, P. E., Jenkins, A., Nicholls, K. W., Brennan, P. V., Abrahamsen, E. P., Heywood, K. J., Dutrieux, P., Cho, K.-H., and Kim, T.-W. 2018. Variability in basal melting beneath Pine Island Ice Shelf on weekly to monthly timescales. *Journal of Geophysical Research: Oceans*, 123(11):8655–8669.

De Angelis, H. and Skvarca, P. 2003. Glacier surge after ice shelf collapse. *Science*, 299 (5612):1560–1562.

De Santis, L., Colleoni, F., Bergamasco, A., Rebesco, M., Accettella, D., Kovacevic, V., Gales, J., Sookwan, K., and Olivo, E. 2018. Exploring the unknown of the Ross Sea in sea ice–free conditions. *Eos*, 99. doi: https://doi.org/10.1029/2018EO106159.

DeConto, R. M. and Pollard, D. 2016. Contribution of Antarctica to past and future sea-level rise. *Nature*, 531(7596):591.

Depoorter, M. A., Bamber, J. L., Griggs, J., Lenaerts, J. T. M., Ligtenberg, S. R. M., van den Broeke, M. R., and Moholdt, G. 2013. Antarctic masks (ice-shelves, ice-sheet, and islands),. *Nature*. doi: 10.1594/PANGAEA.819147. URL `https://doi.org/10.1594/PANGAEA.819147`. In supplement to: Depoorter, MA et al. (2013): Calving fluxes and basal melt rates of Antarctic ice shelves. Nature, 502, 89-92, https://doi.org/10.1038/nature12567.

Depoorter, M. A., Bamber, J. L., Griggs, J. A., Lenaerts, J. T., Ligtenberg, S. R., van den Broeke, M. R., and Moholdt, G. 2013. Calving fluxes and basal melt rates of Antarctic ice shelves. *Nature*, 502(7469):89–92.

Dinniman, M. S., Klinck, J. M., and Smith Jr, W. O. 2011. A model study of Circumpolar Deep Water on the West Antarctic Peninsula and Ross Sea continental shelves. *Deep Sea Research Part II: Topical Studies in Oceanography*, 58(13-16):1508–1523.

Dowdeswell, J., Batchelor, C., Montelli, A., Ottesen, D., Christie, F., Dowdeswell, E., and Evans, J. 2020. Delicate seafloor landforms reveal past Antarctic grounding-line retreat of kilometers per year. *Science*, 368(6494):1020–1024.

Dowdeswell, J. A. and Evans, S. 2004. Investigations of the form and flow of ice sheets and glaciers using radio-echo sounding. *Reports on Progress in Physics*, 67(10):1821.

Drews, R., Schannwell, C., Ehlers, T., Gladstone, R., Pattyn, F., and Matsuoka, K. 2020. Atmospheric and oceanographic signatures in the ice-shelf channel morphology of Roi Baudouin Ice Shelf, East Antarctica, inferred from radar data. *Journal of Geophysical Research: Earth Surface*, page e2020JF005587.

Drews, R. 2015. Evolution of ice-shelf channels in Antarctic ice shelves. *The Cryosphere*, 9(3):1169–1181.

Drews, R., Pattyn, F., Hewitt, I., Ng, F., Berger, S., Matsuoka, K., Helm, V., Bergeot, N., Favier, L., and Neckel, N. 2017. Actively evolving subglacial conduits and eskers initiate ice shelf channels at an Antarctic grounding line. *Nature Communications*, 8: 15228.

Dupont, T. and Alley, R. 2005. Assessment of the importance of ice-shelf buttressing to ice-sheet flow. *Geophysical Research Letters*, 32(4).

Dutrieux, P., Vaughan, D. G., Corr, H. F., Jenkins, A., Holland, P. R., Joughin, I., and Fleming, A. 2013. Pine Island glacier ice shelf melt distributed at kilometre scales. *The Cryosphere*, 7(5):1543–1555.

Dutrieux, P., Stewart, C. L., Jenkins, A., Nicholls, K. W., Corr, H. F., Rignot, E., and Steffen, K. 2014. Basal terraces on melting ice shelves. *Geophysical Research Letters*, 41(15):5506–5513.

Edwards, T. L., Nowicki, S., Marzeion, B., Hock, R., Goelzer, H., Seroussi, H., Jourdain, N. C., Slater, D. A., Turner, F. E., Smith, C. J., et al. 2021. Projected land ice contributions to twenty-first-century sea level rise. *Nature*, 593(7857):74–82.

Engelhardt, H. and Kamb, B. 1997. Basal hydraulic system of a West Antarctic ice stream: constraints from borehole observations. *Journal of Glaciology*, 43(144):207–230.

Engelhardt, H., Humphrey, N., Kamb, B., and Fahnestock, M. 1990. Physical conditions at the base of a fast moving Antarctic ice stream. *Science*, 248(4951):57–60.

Evatt, G., Fowler, A., Clark, C., and Hulton, N. 2006. Subglacial floods beneath ice sheets. *Philosophical Transactions of the Royal Society of London A: Mathematical, Physical and Engineering Sciences*, 364(1844):1769–1794.

Favier, L., Durand, G., Cornford, S. L., Gudmundsson, G. H., Gagliardini, O., Gillet-Chaulet, F., Zwinger, T., Payne, A., and Le Brocq, A. M. 2014. Retreat of Pine Island Glacier controlled by marine ice-sheet instability. *Nature Climate Change*, 4(2): 117–121.

Ferguson, R. 1973. Sinuosity of supraglacial streams. *Geological Society of America Bulletin*, 84(1):251–256.

Flowers, G. E. 2015. Modelling water flow under glaciers and ice sheets. *Proceedings of the Royal Society A: Mathematical, Physical and Engineering Sciences*, 471(2176): 20140907.

Foldvik, A., Gammelsrød, T., Østerhus, S., Fahrbach, E., Rohardt, G., Schröder, M., Nicholls, K. W., Padman, L., and Woodgate, R. 2004. Ice shelf water overflow and bottom water formation in the southern Weddell Sea. *Journal of Geophysical Research: Oceans*, 109(C2).

Foster, T. D. 1983. The temperature and salinity fine structure of the ocean under the Ross Ice Shelf. *Journal of Geophysical Research: Oceans*, 88(C4):2556–2564.

Fowler, A. and Johnson, C. 1996. Ice-sheet surging and ice-stream formation. *Annals of Glaciology*, 23:68–73.

Fretwell, P., Pritchard, H. D., Vaughan, D. G., Bamber, J., Barrand, N., Bell, R., Bianchi, C., Bingham, R., Blankenship, D., Casassa, G., et al. 2013. Bedmap2: improved ice bed, surface and thickness datasets for Antarctica. *The Cryosphere*, 7(1).

Fricker, H. A., Popov, S., Allison, I., and Young, N. 2001. Distribution of marine ice beneath the Amery Ice Shelf. *Geophysical Research Letters*, 28(11):2241–2244.

Fricker, H. A., Scambos, T., Bindschadler, R., and Padman, L. 2007. An active subglacial water system in West Antarctica mapped from space. *Science*, 315(5818):1544–1548.

Fried, M., Hulbe, C., and Fahnestock, M. 2014. Grounding-line dynamics and margin lakes. *Annals of glaciology*, 55(66):87–96.

Fürst, J. J., Durand, G., Gillet-Chaulet, F., Tavard, L., Rankl, M., Braun, M., and Gagliardini, O. 2016. The safety band of Antarctic ice shelves. *Nature Climate Change*, 6(5):479–482.

Gagliardini, O., Durand, G., Zwinger, T., Hindmarsh, R., and Le Meur, E. 2010. Coupling of ice-shelf melting and buttressing is a key process in ice-sheets dynamics. *Geophysical Research Letters*, 37(14).

Gladish, C. V., Holland, D. M., Holland, P. R., and Price, S. F. 2012. Ice-shelf basal channels in a coupled ice/ocean model. *Journal of Glaciology*, 58(212):1227–1244.

Goeller, S., Helm, V., Thoma, M., and Grosfeld, K. 2015. Subglacial hydrology indicates a major shift in dynamics of the West Antarctic Ross Ice Streams within the next two centuries. *The Cryosphere Discussions*, 9(4):3995–4018.

Goldberg, D., Gourmelen, N., Kimura, S., Millan, R., and Snow, K. 2019. How accurately should we model ice shelf melt rates? *Geophysical Research Letters*, 46(1):189–199.

Golledge, N. R., Kowalewski, D. E., Naish, T. R., Levy, R. H., Fogwill, C. J., and Gasson, E. G. 2015. The multi-millennial Antarctic commitment to future sea-level rise. *Nature*, 526(7573):421–425.

Golledge, N. R., Keller, E. D., Gomez, N., Naughten, K. A., Bernales, J., Trusel, L. D., and Edwards, T. L. 2019. Global environmental consequences of twenty-first-century ice-sheet melt. *Nature*, 566(7742):65–72.

Gourmelen, N., Goldberg, D. N., Snow, K., Henley, S. F., Bingham, R. G., Kimura, S., Hogg, A. E., Shepherd, A., Mouginot, J., Lenaerts, J. T., et al. 2017. Channelized melting drives thinning under a rapidly melting Antarctic ice shelf. *Geophysical Research Letters*, 44(19):9796–9804.

Gow, A. J. and Rowland, R. 1965. On the relationship of snow accumulation to surface topography at "Byrd Station", Antarctica. *Journal of Glaciology*, 5(42):843–847.

Gray, L., Joughin, I., Tulaczyk, S., Spikes, V. B., Bindschadler, R., and Jezek, K. 2005. Evidence for subglacial water transport in the West Antarctic Ice Sheet through three-dimensional satellite radar interferometry. *Geophysical Research Letters*, 32(3).

Gudmundsson, G. H. 2003. Transmission of basal variability to a glacier surface. *Journal of Geophysical Research: Solid Earth*, 108(B5).

Gudmundsson, G. H. and Raymond, M. 2008. On the limit to resolution and information on basal properties obtainable from surface data on ice streams. *The Cryosphere*, 2(2): 167–178.

Gudmundsson, G. 2013. Ice-shelf buttressing and the stability of marine ice sheets. *The Cryosphere*, 7(2):647–655.

Haran, T., Bohlander, J., Scambos, T., Painter, T., and Fahnestock, M. 2014. MODIS Mosaic of Antarctica 2008–2009 (MOA2009) image map. *Boulder, Colorado USA, National Snow and Ice Data Center*, 10:N5KP8037.

Haseloff, M. and Sergienko, O. V. 2018. The effect of buttressing on grounding line dynamics. *Journal of Glaciology*, 64(245):417–431.

Hättestrand, C. 1997. Ribbed moraines in Sweden—distribution pattern and palaeoglaciological implications. *Sedimentary Geology*, 111(1-4):41–56.

Hellmer, H. H. and Olbers, D. J. 1989. A two-dimensional model for the thermohaline circulation under an ice shelf. *Antarctic Science*, 1(4):325–336.

Herron, M. M. and Langway, C. C. 1980. Firn densification: an empirical model. *Journal of Glaciology*, 25(93):373–385.

Hewitt, I. J. 2020. Subglacial Plumes. *Annual Review of Fluid Mechanics*, 52:145–169.

Hindmarsh, R. 1996. Stability of ice rises and uncoupled marine ice sheets. *Annals of Glaciology*, 23:105–115.

Hirano, D., Tamura, T., Kusahara, K., Ohshima, K. I., Nicholls, K. W., Ushio, S., Simizu, D., Ono, K., Fujii, M., Nogi, Y., et al. 2020. Strong ice-ocean interaction beneath Shirase Glacier Tongue in East Antarctica. *Nature Communications*, 11(1): 1–12.

Hobbs, W. R., Massom, R., Stammerjohn, S., Reid, P., Williams, G., and Meier, W. 2016. A review of recent changes in Southern Ocean sea ice, their drivers and forcings. *Global and Planetary Change*, 143:228–250.

Hodson, T., Powell, R., Brachfeld, S., Tulaczyk, S., Scherer, R., et al. 2016. Physical processes in Subglacial Lake Whillans, West Antarctica: inferences from sediment cores. *Earth and Planetary Science Letters*, 444:56–63.

Holland, D. M. and Jenkins, A. 1999. Modeling thermodynamic ice–ocean interactions at the base of an ice shelf. *Journal of Physical Oceanography*, 29(8):1787–1800.

Holland, D. M., Jacobs, S. S., and Jenkins, A. 2003a. Modelling the ocean circulation beneath the Ross Ice Shelf. *Antarctic Science*, 15(1):13–23.

Holland, D., Hunter, J., Grosfeld, K., Hellmer, H., Jenkins, A., Morales Maqueda, M., Hemer, M., Williams, M., Klinck, J., and Dinniman, M. The ice shelf-ocean model intercomparison project (ISOMIP). In *AGU Fall Meeting Abstracts*, volume 2003, pages C41A–05, 2003b.

Holland, P. R. and Feltham, D. L. 2006. The effects of rotation and ice shelf topography on frazil-laden ice shelf water plumes. *Journal of physical oceanography*, 36(12):2312–2327.

Holland, P. R., Jenkins, A., and Holland, D. M. 2008. The response of ice shelf basal melting to variations in ocean temperature. *Journal of Climate*, 21(11):2558–2572.

Horgan, H. and Stevens, C. 2022. Exploring Antarctica's hidden under-ice rivers and their role in future sea-level rise. *The Conversation*. URL `https://theconversation.com/exploring-antarcticas-hidden-under-ice-rivers-and-their-role-in-future-sea-level-r`

Horgan, H., Hulbe, C., Alley, R., Anandakrishnan, S., Goodsell, B., Taylor-Offord, S., and Vaughan, M. 2017. Poststagnation Retreat of Kamb Ice Stream's Grounding Zone. *Geophysical Research Letters*, 44(19):9815–9822.

Howat, I. M., Porter, C., Smith, B. E., Noh, M.-J., and Morin, P. 2019. The Reference Elevation Model of Antarctica. *Cryosphere*, 13(2).

Hulbe, C. and Fahnestock, M. 2007. Century-scale discharge stagnation and reactivation of the Ross ice streams, West Antarctica. *Journal of Geophysical Research: Earth Surface*, 112(F3).

Hulbe, C. L. and Fahnestock, M. A. 2004. West Antarctic ice-stream discharge variability: mechanism, controls and pattern of grounding-line retreat. *Journal of Glaciology*, 50 (171):471–484.

Iken, A. and Bindschadler, R. A. 1986. Combined measurements of subglacial water pressure and surface velocity of Findelengletscher, Switzerland: conclusions about drainage system and sliding mechanism. *Journal of Glaciology*, 32(110):101–119.

Jacobel, R. W., Welch, B. C., Osterhouse, D., Pettersson, R., and MacGregor, J. A. 2009. Spatial variation of radar-derived basal conditions on Kamb Ice Stream, West Antarctica. *Annals of Glaciology*, 50(51):10–16.

Jacobs, S., Helmer, H., Doake, C., Jenkins, A., and Frolich, R. 1992. Melting of ice shelves and the mass balance of Antarctica. *Journal of Glaciology*, 38(130):375–387.

Jacobs, S. S., Gordon, A. L., and Ardai, J. 1979. Circulation and melting beneath the Ross Ice Shelf. *Science*, 203(4379):439–443.

Jakobsson, M., Anderson, J. B., Nitsche, F. O., Gyllencreutz, R., Kirshner, A. E., Kirchner, N., O'Regan, M., Mohammad, R., and Eriksson, B. 2012. Ice sheet retreat dynamics inferred from glacial morphology of the central Pine Island Bay Trough, West Antarctica. *Quaternary Science Reviews*, 38:1–10.

Jamieson, S. S., Vieli, A., Livingstone, S. J., Cofaigh, C. Ó., Stokes, C., Hillenbrand, C.-D., and Dowdeswell, J. A. 2012. Ice-stream stability on a reverse bed slope. *Nature Geoscience*, 5(11):799–802.

Jenkins, A. 1991. A one-dimensional model of ice shelf-ocean interaction. *Journal of Geophysical Research: Oceans*, 96(C11):20671–20677.

Jenkins, A. 2011. Convection-driven melting near the grounding lines of ice shelves and tidewater glaciers. *Journal of Physical Oceanography*, 41(12):2279–2294.

Jenkins, A. 2016. A simple model of the ice shelf–ocean boundary layer and current. *Journal of Physical Oceanography*, 46(6):1785–1803.

Jenkins, A., Corr, H. F., Nicholls, K. W., Stewart, C. L., and Doake, C. S. 2006. Interactions between ice and ocean observed with phase-sensitive radar near an Antarctic ice-shelf grounding line. *Journal of Glaciology*, 52(178):325–346.

Jenkins, A., Nicholls, K. W., and Corr, H. F. 2010. Observation and parameterization of ablation at the base of Ronne Ice Shelf, Antarctica. *Journal of Physical Oceanography*, 40(10):2298–2312.

Jeofry, H., Ross, N., Le Brocq, A., Graham, A. G., Li, J., Gogineni, P., Morlighem, M., Jordan, T., and Siegert, M. J. 2018. Hard rock landforms generate 130 km ice shelf channels through water focusing in basal corrugations. *Nature Communications*, 9(1): 1–9.

Joughin, I., Smith, B. E., and Medley, B. 2014. Marine ice sheet collapse potentially under way for the Thwaites Glacier Basin, West Antarctica. *Science*, 344(6185):735–738.

Jourdain, N. C., Asay-Davis, X., Hattermann, T., Straneo, F., Seroussi, H., Little, C. M., and Nowicki, S. 2020. A protocol for calculating basal melt rates in the ISMIP6 Antarctic ice sheet projections. *The Cryosphere*, 14(9):3111–3134.

Katz, R. F. and Worster, M. G. 2010. Stability of ice-sheet grounding lines. *Proceedings of the Royal Society A: Mathematical, Physical and Engineering Sciences*, 466(2118): 1597–1620.

Kim, B.-H., Lee, C.-K., Seo, K.-W., Lee, W. S., and Scambos, T. 2016. Active subglacial lakes and channelized water flow beneath the Kamb Ice Stream. *The Cryosphere*, 10 (6):2971–2980.

Knauss, J. A. and Garfield, N. 2016. Introduction to physical oceanography. Waveland Press.

Langhorne, P., Hughes, K., Gough, A., Smith, I., Williams, M., Robinson, N., Stevens, C., Rack, W., Price, D., Leonard, G., et al. 2015. Observed platelet ice distributions in Antarctic sea ice: An index for ocean-ice shelf heat flux. *Geophysical Research Letters*, 42(13):5442–5451.

Le Brocq, A. M., Payne, A., Siegert, M., and Alley, R. B. 2009. A subglacial water-flow model for West Antarctica. *Journal of Glaciology*, 55(193):879–888.

Le Brocq, A. M., Ross, N., Griggs, J. A., Bingham, R. G., Corr, H. F., Ferraccioli, F., Jenkins, A., Jordan, T. A., Payne, A. J., Rippin, D. M., et al. 2013. Evidence from ice shelves for channelized meltwater flow beneath the Antarctic Ice Sheet. *Nature Geoscience*, 6(11):945.

Lelandais, T., Ravier, É., Pochat, S., Bourgeois, O., Clark, C., Mourgues, R., and Strzerzynski, P. 2018. Modelled subglacial floods and tunnel valleys control the life cycle of transitory ice streams. *Cryosphere*, 12(8):2759–2772.

Lewis, A. R., Marchant, D. R., Kowalewski, D. E., Baldwin, S. L., and Webb, L. E. 2006. The age and origin of the Labyrinth, western Dry Valleys, Antarctica: Evidence for extensive middle Miocene subglacial floods and freshwater discharge to the Southern Ocean. *Geology*, 34(7):513–516.

Lewis, E. and Perkin, R. 1986. Ice pumps and their rates. *Journal of Geophysical Research: Oceans*, 91(C10):11756–11762.

Lindbäck, K., Moholdt, G., Nicholls, K. W., Hattermann, T., Pratap, B., Thamban, M., and Matsuoka, K. 2019. Spatial and temporal variations in basal melting at Nivlisen ice shelf, East Antarctica, derived from phase-sensitive radars. *The Cryosphere*, 13 (10):2579–2595.

Liu, Y., Moore, J. C., Cheng, X., Gladstone, R. M., Bassis, J. N., Liu, H., Wen, J., and Hui, F. 2015. Ocean-driven thinning enhances iceberg calving and retreat of Antarctic ice shelves. *Proceedings of the National Academy of Sciences*, 112(11):3263–3268.

Losch, M. 2008. Modeling ice shelf cavities in az coordinate ocean general circulation model. *Journal of Geophysical Research: Oceans*, 113(C8).

MacAyeal, D. R. 1985. Evolution of tidally triggered meltwater plumes below ice shelves. *Oceanology of the Antarctic continental shelf*, 43:133–143.

MacAyeal, D. R. 1984. Thermohaline circulation below the Ross Ice Shelf: A consequence of tidally induced vertical mixing and basal melting. *Journal of Geophysical Research: Oceans*, 89(C1):597–606.

MacGregor, J. A., Anandakrishnan, S., Catania, G. A., and Winebrenner, D. P. 2011. The grounding zone of the Ross Ice Shelf, West Antarctica, from ice-penetrating radar. *Journal of Glaciology*, 57(205):917–928.

Makinson, K. 2002. Modeling tidal current profiles and vertical mixing beneath Filchner–Ronne Ice Shelf, Antarctica. *Journal of Physical Oceanography*, 32(1):202–215.

Makinson, K., Holland, P. R., Jenkins, A., Nicholls, K. W., and Holland, D. M. 2011. Influence of tides on melting and freezing beneath Filchner-Ronne Ice Shelf, Antarctica. *Geophysical Research Letters*, 38(6).

Malyarenko, A., Wells, A. J., Langhorne, P. J., Robinson, N. J., Williams, M. J., and Nicholls, K. W. 2020. A synthesis of thermodynamic ablation at ice–ocean interfaces from theory, observations and models. *Ocean Modelling*, 154:101692.

Mankoff, K. D., Jacobs, S. S., Tulaczyk, S. M., and Stammerjohn, S. E. 2012. The role of Pine Island Glacier ice shelf basal channels in deep-water upwelling, polynyas and ocean circulation in Pine Island Bay, Antarctica. *Annals of Glaciology*, 53(60):123–128.

Marsh, O. J., Fricker, H. A., Siegfried, M. R., Christianson, K., Nicholls, K. W., Corr, H. F., and Catania, G. 2016. High basal melting forming a channel at the grounding line of Ross Ice Shelf, Antarctica. *Geophysical Research Letters*, 43(1):250–255.

Marshall, J., Adcroft, A., Hill, C., Perelman, L., and Heisey, C. 1997a. A finite-volume, incompressible Navier Stokes model for studies of the ocean on parallel computers. *Journal of Geophysical Research: Oceans*, 102(C3):5753–5766.

Marshall, J., Hill, C., Perelman, L., and Adcroft, A. 1997b. Hydrostatic, quasi-hydrostatic, and nonhydrostatic ocean modeling. *Journal of Geophysical Research: Oceans*, 102(C3):5733–5752.

McKay, R., Dunbar, G., Naish, T., Barrett, P., Carter, L., and Harper, M. 2008. Retreat history of the Ross Ice Sheet (Shelf) since the Last Glacial Maximum from deep-basin sediment cores around Ross Island. *Palaeogeography, Palaeoclimatology, Palaeoecology*, 260(1-2):245–261.

McPhee, M. G., Maykut, G. A., and Morison, J. H. 1987. Dynamics and thermodynamics of the ice/upper ocean system in the marginal ice zone of the Greenland Sea. *Journal of Geophysical Research: Oceans*, 92(C7):7017–7031.

Merino, N., Jourdain, N. C., Le Sommer, J., Goosse, H., Mathiot, P., and Durand, G. 2018. Impact of increasing antarctic glacial freshwater release on regional sea-ice cover in the Southern Ocean. *Ocean Modelling*, 121:76–89.

Millgate, T., Holland, P. R., Jenkins, A., and Johnson, H. L. 2013. The effect of basal channels on oceanic ice-shelf melting. *Journal of Geophysical Research: Oceans*, 118 (12):6951–6964.

Moholdt, G., Padman, L., and Fricker, H. A. 2014. Basal mass budget of Ross and Filchner-Ronne ice shelves, Antarctica, derived from Lagrangian analysis of ICESat altimetry. *Journal of Geophysical Research: Earth Surface*, 119(11):2361–2380.

Morlighem, M., Seroussi, H., Larour, E., and Rignot, E. 2013. Inversion of basal friction in Antarctica using exact and incomplete adjoints of a higher-order model. *Journal of Geophysical Research: Earth Surface*, 118(3):1746–1753.

Mouginot, J., Rignot, E., and Scheuchl, B. 2019. Continent-wide, interferometric SAR phase, mapping of Antarctic ice velocity. *Geophysical Research Letters*, 46(16):9710–9718.

Naish, T., Powell, R., Levy, R., Wilson, G., Scherer, R., Talarico, F., Krissek, L., Niessen, F., Pompilio, M., Wilson, T., et al. 2009. Obliquity-paced Pliocene West Antarctic ice sheet oscillations. *Nature*, 458(7236):322–328.

Nakayama, Y., Menemenlis, D., Zhang, H., Schodlok, M., and Rignot, E. 2018. Origin of Circumpolar Deep Water intruding onto the Amundsen and Bellingshausen Sea continental shelves. *Nature Communications*, 9(1):1–9.

Nakayama, Y., Manucharyan, G., Zhang, H., Dutrieux, P., Torres, H. S., Klein, P., Seroussi, H., Schodlok, M., Rignot, E., and Menemenlis, D. 2019. Pathways of ocean heat towards Pine Island and Thwaites grounding lines. *Scientific reports*, 9(1):1–9.

Natural Resources Canada. *Natural Resources Canada's online tool Canadian Spatial Reference System-precise point positioning (PPP).* Canadian Geodetic Survey, Ottawa, Ontario, 2016.

Naughten, K. A., Meissner, K. J., Galton-Fenzi, B. K., England, M. H., Timmermann, R., and Hellmer, H. H. 2018. Future projections of Antarctic ice shelf melting based on CMIP5 scenarios. *Journal of Climate*, 31(13):5243–5261.

Naughten, K. A., De Rydt, J., Rosier, S. H., Jenkins, A., Holland, P. R., and Ridley, J. K. 2021. Two-timescale response of a large Antarctic ice shelf to climate change. *Nature Communications*, 12(1):1–10.

Nepf, H. and Geyer, W. 1996. Intratidal variations in stratification and mixing in the Hudson estuary. *Journal of Geophysical Research: Oceans*, 101(C5):12079–12086.

Ng, F. and Conway, H. 2004. Fast-flow signature in the stagnated Kamb Ice Stream, West Antarctica. *Geology*, 32(6):481–484.

Ng, F. S. 1998. *Mathematical modelling of subglacial drainage and erosion*. PhD thesis, University of Oxford.

Nicholls, K. W. *Long-term site setup SS+RMB2*. British Antarctic Survey, Cambridge, United Kingdom, 2018.

Nicholls, K. W., Corr, H. F., Stewart, C. L., Lok, L. B., Brennan, P. V., and Vaughan, D. G. 2015. A ground-based radar for measuring vertical strain rates and time-varying basal melt rates in ice sheets and shelves. *Journal of Glaciology*, 61(230):1079–1087.

Nitsche, F. O., Gohl, K., Larter, R. D., Hillenbrand, C.-D., Kuhn, G., Smith, J., Jacobs, S. S., Anderson, J., and Jakobsson, M. 2013. Paleo ice flow and subglacial meltwater dynamics in Pine Island Bay, West Antarctica. *The Cryosphere*, 7:249–262.

Noh, M.-J. and Howat, I. M. 2015. Automated stereo-photogrammetric DEM generation at high latitudes: Surface Extraction with TIN-based Search-space minimization (SETSM) validation and demonstration over glaciated regions. *GIScience & remote sensing*, 52(2):198–217.

Oerlemans, H. Analytical Models of Ice Sheets and Ice Shelves. In *Glaciers and Ice Sheets in the Climate System*, pages 241–254. Springer, 2021.

Orsi, A. H., Johnson, G. C., and Bullister, J. L. 1999. Circulation, mixing, and production of Antarctic Bottom Water. *Progress in Oceanography*, 43(1):55–109.

Padman, L., Erofeeva, S., and Joughin, I. 2003. Tides of the Ross sea and Ross ice shelf cavity. *Antarctic Science*, 15(1):31–40.

Padman, L., Fricker, H. A., Coleman, R., Howard, S., and Erofeeva, L. 2002. A new tide model for the Antarctic ice shelves and seas. *Annals of Glaciology*, 34:247–254.

Paolo, F. S., Fricker, H. A., and Padman, L. 2015. Volume loss from Antarctic ice shelves is accelerating. *Science*, 348(6232):327–331.

Paterson, W. S. B. 2016. The physics of glaciers. Elsevier.

Pattyn, F. 2008. Investigating the stability of subglacial lakes with a full Stokes ice-sheet model. *Journal of Glaciology*, 54(185):353–361.

Payne, A. J., Holland, P. R., Shepherd, A. P., Rutt, I. C., Jenkins, A., and Joughin, I. 2007. Numerical modeling of ocean-ice interactions under Pine Island Bay's ice shelf. *Journal of Geophysical Research: Oceans*, 112(C10).

Perol, T. and Rice, J. R. Control of the width of West Antarctic ice streams by internal melting in the ice sheet near the margins. In *AGU Fall Meeting Abstracts*, 2011.

Pollard, D. and DeConto, R. M. 2009. Modelling West Antarctic ice sheet growth and collapse through the past five million years. *Nature*, 458(7236):329–332.

Pritchard, H., Ligtenberg, S., Fricker, H., Vaughan, D., Van den Broeke, M., and Padman, L. 2012. Antarctic ice-sheet loss driven by basal melting of ice shelves. *Nature*, 484 (7395):502–505.

Reese, R., Gudmundsson, G. H., Levermann, A., and Winkelmann, R. 2018. The far reach of ice-shelf thinning in Antarctica. *Nature Climate Change*, 8(1):53–57.

Retzlaff, R. and Bentley, C. R. 1993. Timing of stagnation of Ice Stream C, West Antarctica, from short-pulse radar studies of buried surface crevasses. *Journal of Glaciology*, 39(133):553–561.

Rignot, E. and Steffen, K. 2008. Channelized bottom melting and stability of floating ice shelves. *Geophysical Research Letters*, 35(2).

Rignot, E., Mouginot, J., and Scheuchl, B. 2011. Ice flow of the Antarctic ice sheet. *Science*, 333(6048):1427–1430.

Rignot, E., Mouginot, J., and Scheuchl, B. 2017. MEaSUREs InSAR-based Antarctica ice velocity map, version 2. *Boulder, Colorado USA. NASA National Snow and Ice Data Center Distributed Active Archive Center. doi: https://doi.org/10.5067/D7GK8F5J8M8R.*

Rignot, E. and Thomas, R. H. 2002. Mass balance of polar ice sheets. *Science*, 297(5586): 1502–1506.

Rignot, E., Casassa, G., Gogineni, P., Krabill, W., Rivera, A., and Thomas, R. 2004. Accelerated ice discharge from the Antarctic Peninsula following the collapse of Larsen B ice shelf. *Geophysical research letters*, 31(18).

Rignot, E., Bamber, J. L., Van Den Broeke, M. R., Davis, C., Li, Y., Van De Berg, W. J., and Van Meijgaard, E. 2008. Recent Antarctic ice mass loss from radar interferometry and regional climate modelling. *Nature Geoscience*, 1(2):106–110.

Rignot, E., Jacobs, S., Mouginot, J., and Scheuchl, B. 2013. Ice-shelf melting around Antarctica. *Science*, 341(6143):266–270.

Robel, A. A., Wilson, E., and Seroussi, H. 2022. Layered seawater intrusion and melt under grounded ice. *The Cryosphere*, 16(2):451–469.

Robel, A. A., DeGiuli, E., Schoof, C., and Tziperman, E. 2013. Dynamics of ice stream temporal variability: Modes, scales, and hysteresis. *Journal of Geophysical Research: Earth Surface*, 118(2):925–936.

Robin, G. d. Q., Swithinbank, C., and Smith, B. 1970. Radio echo exploration of the Antarctic ice sheet. *International Association of Scientific Hydrology Publication*, 86: 97–115.

Robinson, N., Stevens, C., Hulbe, C. L., Horgan, H. J., Stewart, C., Washam, P., and de Joux, P. Ice Shelf Cavity Estuarine Hydrodynamics at the Kamb Ice Stream Grounding Line. In *AGU Fall Meeting Abstracts*, volume 2020, pages C026–07, 2020.

Robinson, N. J., Williams, M. J., Stevens, C. L., Langhorne, P. J., and Haskell, T. G. 2014. Evolution of a supercooled Ice Shelf Water plume with an actively growing subice platelet matrix. *Journal of Geophysical Research: Oceans*, 119(6):3425–3446.

Rose, K. 1979. Characteristics of ice flow in Marie Byrd Land, Antarctica. *Journal of Glaciology*, 24(90):63–75.

Röthlisberger, H. 1972. Water pressure in intra-and subglacial channels. *Journal of Glaciology*, 11(62):177–203.

Roy, D., Wulder, M., Loveland, T., C.E., W., Allen, R., Anderson, M., Helder, D., Irons, J., Johnson, D., Kennedy, R., Scambos, T., Schaaf, C., Schott, J., Sheng, Y., Vermote, E., Belward, A., Bindschadler, R., Cohen, W., Gao, F., Hipple, J., Hostert, P., Huntington, J., Justice, C., Kilic, A., Kovalskyy, V., Lee, Z., Lymburner, L., Masek, J., McCorkel, J., Shuai, Y., Trezza, R., Vogelmann, J., Wynne, R., and Zhu, Z. 2014. Landsat-8: Science and product vision for terrestrial global change research. *Remote Sensing of Environment*, 145:154–172. ISSN 00344257. doi: 10.1016/j.rse.2014.02.001.

Rutt, I. C., Hagdorn, M., Hulton, N., and Payne, A. 2009. The Glimmer community ice sheet model. *Journal of Geophysical Research: Earth Surface*, 114(F2).

Sayag, R. and Worster, M. G. 2013. Elastic dynamics and tidal migration of grounding lines modify subglacial lubrication and melting. *Geophysical Research Letters*, 40(22): 5877–5881.

Scambos, T. A., Bell, R. E., Alley, R. B., Anandakrishnan, S., Bromwich, D., Brunt, K., Christianson, K., Creyts, T., Das, S., DeConto, R., et al. 2017. How much, how fast?: A science review and outlook for research on the instability of Antarctica's Thwaites Glacier in the 21st century. *Global and Planetary Change*, 153:16–34.

Schodlok, M. P., Menemenlis, D., Rignot, E., and Studinger, M. 2012. Sensitivity of the ice-shelf/ocean system to the sub-ice-shelf cavity shape measured by NASA IceBridge in Pine Island Glacier, West Antarctica. *Annals of Glaciology*, 53(60):156–162.

Schroeder, D. M., Blankenship, D. D., and Young, D. A. 2013. Evidence for a water system transition beneath Thwaites Glacier, West Antarctica. *Proceedings of the National Academy of Sciences*, 110(30):12225–12228.

Sergienko, O. V. and Hindmarsh, R. C. 2013. Regular patterns in frictional resistance of ice-stream beds seen by surface data inversion. *Science*, 342(6162):1086–1089.

Sergienko, O. 2013. Basal channels on ice shelves. *Journal of Geophysical Research: Earth Surface*, 118(3):1342–1355.

Shreve, R. 1972. Movement of water in glaciers. *Journal of Glaciology*, 11(62):205–214.

Siegert, M. J., Ross, N., and Le Brocq, A. M. 2016. Recent advances in understanding Antarctic subglacial lakes and hydrology. *Philosophical Transactions of the Royal Society A: Mathematical, Physical and Engineering Sciences*, 374(2059):20140306.

Siegfried, M. R. and Fricker, H. A. 2018. Thirteen years of subglacial lake activity in Antarctica from multi-mission satellite altimetry. *Annals of Glaciology*, pages 1–14.

Simkins, L. M., Anderson, J. B., Greenwood, S. L., Gonnermann, H. M., Prothro, L. O., Halberstadt, A. R. W., Stearns, L. A., Pollard, D., and DeConto, R. M. 2017. Anatomy of a meltwater drainage system beneath the ancestral East Antarctic ice sheet. *Nature Geoscience*, 10(9):691.

Smethie Jr, W. M. and Jacobs, S. S. 2005. Circulation and melting under the Ross Ice Shelf: estimates from evolving CFC, salinity and temperature fields in the Ross Sea. *Deep Sea Research Part I: Oceanographic Research Papers*, 52(6):959–978.

Smith, B., Dickinson, S., Jelley, B., Neumann, T., Hancock, D., Lee, J., and Harbeck, K. *ATLAS/ICESat-2 L3B Annual Land Ice Height, Version 3*. NASA National Snow and Ice Data Center Distributed Active Archive Center, Boulder, Colorado USA, 2021.

Snodgrass, J. A. Melting and deformation of the Ross Ice Shelf, Antarctica, by Multi-Year Phase Sensitive Radio Echo Sounding. Master's thesis, University of Canterbury, 2021.

Stanton, T. P., Shaw, W., Truffer, M., Corr, H., Peters, L., Riverman, K., Bindschadler, R., Holland, D., and Anandakrishnan, S. 2013. Channelized ice melting in the ocean boundary layer beneath Pine Island Glacier, Antarctica. *Science*, 341(6151):1236–1239.

Stearns, L. A., Smith, B. E., and Hamilton, G. S. 2008. Increased flow speed on a large East Antarctic outlet glacier caused by subglacial floods. *Nature Geoscience*, 1(12): 827–831.

Stevens, C., Hulbe, C., Brewer, M., Stewart, C., Robinson, N., Ohneiser, C., and Jendersie, S. 2020. Ocean mixing and heat transport processes observed under the Ross Ice Shelf control its basal melting. *Proceedings of the National Academy of Sciences*, 117 (29):16799–16804.

Stewart, C., 2021. Personal communication.

Stewart, C. L., Christoffersen, P., Nicholls, K. W., Williams, M. J., and Dowdeswell, J. A. 2019. Basal melting of Ross Ice Shelf from solar heat absorption in an ice-front polynya. *Nature Geoscience*, 12(6):435–440.

Stewart, C. L. 2018. *Ice-ocean interactions beneath the north-western Ross Ice Shelf, Antarctica*. PhD thesis, University of Cambridge.

Sun, S., Hattermann, T., Pattyn, F., Nicholls, K. W., Drews, R., and Berger, S. 2019. Topographic shelf waves control seasonal melting near Antarctic ice shelf grounding lines. *Geophysical Research Letters*, 46(16):9824–9832.

Uieda, L., Tian, D., Leong, W., Toney, L., Schlitzer, W., Grund, M., Newton, D., Ziebarth, M., Jones, M., and Wessel, P. 2021. PyGMT: A Python interface for the Generic Mapping Tools. *Python*.

van Rijn, L. C. 2011. Analytical and numerical analysis of tides and salinities in estuaries; part I: tidal wave propagation in convergent estuaries. *Ocean dynamics*, 61(11):1719–1741.

Vaňková, I., Nicholls, K. W., Corr, H. F., Makinson, K., and Brennan, P. V. 2020. Observations of tidal melt and vertical strain at the Filchner-Ronne Ice Shelf, Antarctica. *Journal of Geophysical Research: Earth Surface*, 125(1):e2019JF005280.

Vaňková, I., Cook, S., Winberry, J. P., Nicholls, K. W., and Galton-Fenzi, B. K. 2021a. Deriving melt rates at a complex ice shelf base using in situ radar: Application to Totten Ice Shelf. *Geophysical Research Letters*, 48(7):e2021GL092692.

Vaňková, I., Nicholls, K. W., and Corr, H. F. 2021b. The nature of ice intermittently accreted at the base of Ronne Ice Shelf, Antarctica, assessed using phase-sensitive radar. *Journal of Geophysical Research: Oceans*, 126(10):e2021JC017290.

Vaughan, D. G. 2008. West Antarctic Ice Sheet collapse–the fall and rise of a paradigm. *Climatic Change*, 91(1):65–79.

Vaughan, D. G., Corr, H. F., Bindschadler, R. A., Dutrieux, P., Gudmundsson, G. H., Jenkins, A., Newman, T., Vornberger, P., and Wingham, D. J. 2012. Subglacial melt channels and fracture in the floating part of Pine Island Glacier, Antarctica. *Journal of Geophysical Research: Earth Surface*, 117(F3).

Walder, J. S. and Fowler, A. 1994. Channelized subglacial drainage over a deformable bed. *Journal of Glaciology*, 40(134):3–15.

Walker, R. T., Parizek, B. R., Alley, R. B., Anandakrishnan, S., Riverman, K. L., and Christianson, K. 2013. Ice-shelf tidal flexure and subglacial pressure variations. *Earth and Planetary Science Letters*, 361:422–428.

Washam, P., Nicholls, K. W., Münchow, A., and Padman, L. 2019. Summer surface melt thins Petermann Gletscher Ice Shelf by enhancing channelized basal melt. *Journal of Glaciology*, 65(252):662–674.

Wearing, M., Stevens, L., Dutrieux, P., and Kingslake, J. 2021. Ice-shelf basal melt channels stabilized by secondary flow. *Geophysical Research Letters*, 48(21):e2021GL094872.

Weertman, J. 1957. On the sliding of glaciers. *Journal of glaciology*, 3(21):33–38.

Weertman, J. 1974. Stability of the junction of an ice sheet and an ice shelf. *Journal of Glaciology*, 13(67):3–11.

Wells, A. J. and Worster, M. G. 2011. Melting and dissolving of a vertical solid surface with laminar compositional convection. *Journal of fluid mechanics*, 687:118–140.

Wessel, P., Luis, J., Uieda, L., Scharroo, R., Wobbe, F., Smith, W., and Tian, D. 2019. The generic mapping tools version 6. *Geochemistry, Geophysics, Geosystems*, 20(11): 5556–5564.

Winberry, J. P., Anandakrishnan, S., Alley, R. B., Bindschadler, R. A., and King, M. A. 2009. Basal mechanics of ice streams: Insights from the stick-slip motion of Whillans Ice Stream, West Antarctica. *Journal of Geophysical Research: Earth Surface*, 114 (F1).

Wingham, D. J., Siegert, M. J., Shepherd, A., and Muir, A. S. 2006. Rapid discharge connects Antarctic subglacial lakes. *Nature*, 440(7087):1033–1036.

Wright, A. and Siegert, M. 2012. A fourth inventory of Antarctic subglacial lakes. *Antarctic Science*, 24(06):659–664.

Xu, Y., Rignot, E., Menemenlis, D., and Koppes, M. 2012. Numerical experiments on subaqueous melting of Greenland tidewater glaciers in response to ocean warming and enhanced subglacial discharge. *Annals of Glaciology*, 53(60):229–234.

Yokoyama, Y., Anderson, J. B., Yamane, M., Simkins, L. M., Miyairi, Y., Yamazaki, T., Koizumi, M., Suga, H., Kusahara, K., Prothro, L., et al. 2016. Widespread collapse of the Ross Ice Shelf during the late Holocene. *Proceedings of the National Academy of Sciences*, 113(9):2354–2359.

Young, D. A., Schroeder, D., Blankenship, D., Kempf, S. D., and Quartini, E. 2016. The distribution of basal water between Antarctic subglacial lakes from radar sounding. *Phil. Trans. R. Soc. A*, 374(2059):20140297.

Young, T. J., Schroeder, D. M., Christoffersen, P., Lok, L. B., Nicholls, K. W., Brennan, P. V., Doyle, S. H., Hubbard, B., and Hubbard, A. 2018. Resolving the internal and basal geometry of ice masses using imaging phase-sensitive radar. *Journal of Glaciology*, 64(246):649–660.

Zotikov, I. A., Zagorodnov, V. S., and Raikovsky, J. V. 1980. Core drilling through the Ross Ice Shelf (Antarctica) confirmed basal freezing. *Science*, 207(4438):1463–1465.